

**Université de Limoges**

**ED 610 - Sciences et Ingénierie des Systèmes, Mathématiques,  
Informatique (SISMI)**

**XLIM – Axe RF ELITE**

Thèse pour obtenir le grade de  
**Docteur de l'Université de Limoges**

Discipline : Electroniques des Hautes Fréquences, Photonique et Systèmes

Présentée et soutenue par  
**Jaakko KYLLÖNEN**

Le 18 décembre 2019

**Design of Frequency Agile Filter and mmWave Antenna for 5G  
Mobile Devices**

Thèse dirigée par Dominique CROS, Olivier PAJONA et Valérie MADRANGEAS

JURY :

Président du jury

Rapporteurs

M. Fabien FERRERO, HDR, Maître de Conférences, LEAT, Université de Nice  
Sophia Antipolis

M. Fabien NDAGIJIMANA, Professeur, G2Elab, Université de Grenoble Alpe

Examineurs

Mme. Christelle AUPETIT-BERTHELEMOT, Professeur, XLIM, Université de  
Limoges

M. Olivier PAJONA, General Manager & Chief Scientist, Ethertronics France SAS

M. Emmanuel PERRIN, Ingénieur, CRT CISTEME

Mme. Valérie MADRANGEAS, Professeur, XLIM, Université de Limoges

Invité

M. Dominique CROS, Professeur, XLIM, Université de Limoges



## Preface

---

This thesis has been written in AVX/Ethertronics R&D center in Antibes France, directed by Mr. Olivier Pajona. I would like to extend my gratitude towards him for giving me this opportunity to write this thesis alongside with my daily work at AVX/Ethertronics.

I want to thank Mme. Valérie Madrangeas and Mr. Dominique Cros, professors at the University of Limoges. Their help and guidance has been invaluable, especially with the filter analysis.

I would also like to thank Mr. Fabien Ferrero from University of Nice Sophia Antipolis and Mr. Fabien Ndagijimana from University of Grenoble Alpe for finding the time in their busy schedules to review my thesis.

Great colleagues make great work place, many thanks to my colleagues for supporting me during my thesis. I would especially like to thank Mr. Mohd Faizal Bin Mohd Zaini for developing the EC686 control software used in the frequency agile filter measurements.

Finally, I would like to thank my parents. Kiitoksia että olette kannustaneet ja tukeneet koulutietäni aina ala-asteelta tänne akateemisen maailman huipulle asti!

## Table of Contents

---

Preface.....	2
General Introduction .....	5
References: .....	10
Chapter I. Frequency Agile Filters for Mobile Devices .....	15
I.1 Requirements for the frequency agile filters for mobile devices .....	15
I.2 Characteristics of CMOS RF switch (EC 686) .....	20
I.3 Low-Temperature Co-fired Ceramic (LTCC).....	24
I.4 Electro-Magnetic-Simulation tools.....	24
I.5 Designing of combline filter by 2.5D and 3D EM-simulations .....	25
I.5.1 Filter synthesis .....	25
I.5.2 Parallel load combline filter .....	30
I.5.2.1 Determining the values of elements $L_1$ and $C_1$ .....	31
I.5.2.2 Determining the values of elements $L_2$ and $C_2$ .....	32
I.6 Frequency agile combline filter .....	36
I.7 Combline filter measurements .....	49
I.8 Conclusions.....	59
References: .....	60
Chapter II. Low Cost Millimeter Wave Antenna Arrays .....	63
II.1 Millimeter Wave antennas for Fifth Generation New Radio .....	63
II.2 Designing of Low Cost Millimeter Wave Antenna Arrays.....	64
II.2.1 Antenna architecture.....	66
II.2.2 Low Loss transmission lines for mmWave.....	67
II.2.3 Antenna Array 3D EM Simulations .....	76
II.2.3.1 Unit element design .....	76
II.2.3.2 Four element linear antenna array design.....	83
II.2.3.3 Design of antenna array in FR-4 substrate .....	90
II.2.3.4 Low loss FPC Antenna Array .....	105
II.3 Conclusions.....	123
References: .....	124

General Conclusions .....	129
Part I: Frequency Agile Filter.....	129
For the future work on the frequency agile filter: .....	131
Part II: Low cost mmWave antenna array .....	132
For the future work on the low cost mmWave antenna array: .....	134
Table of Charts.....	135
Table of Figures .....	138
Table of Tables.....	140

## General Introduction

---

The increased usage of a mobile data has forced the authorities to reallocate more frequency bands for mobile consumer use. Every new mobile communication generation has seen addition of new frequency bands, growing from the Global System for Mobile Communications (GSM) standard's four frequency bands to tens of different frequency bands in the current 4<sup>th</sup> generation Universal Mobile Telecommunication System (UMTS) Long Term Evolution (LTE) standard (4G LTE). The upcoming fifth generation communication standard, the 5G NR (fifth generation New Radio), promises even faster download speeds and lower latency communications than the current 4G LTE standard. To be able to full fill these promises the authorities have allocated more frequency bandwidth in the sub 6 GHz frequency range to accommodate the growing number of users and have introduced new frequency range, the millimeter wave frequencies, to enable fast and low latency communications in the crowded urban areas. Although this increase of available frequency bands helps operators to provide more and faster data services to their customers, it has made the Radio Frequency (RF) front end and antenna design more complicated especially in the mobile devices where the design volume is by nature sparse.

To mitigate the increasing complexity of the RF front end design, frequency agile solutions have been studied and implemented on mobile devices, such as mobile phones and tablets [1], [2], [3], and [4].

Antennas with frequency tunable resonant frequencies has been available for markets from the mid 2000's and are getting more and more common even in the low end mobile devices now a days. The frequency agility is achieved in antennas using antenna tuners, usually CMOS capacitor banks, or implementing band switching using RF-switch in antenna structure and/or antenna's matching circuit [3], [5], [6], and [7].

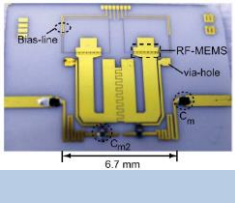
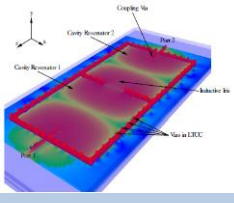
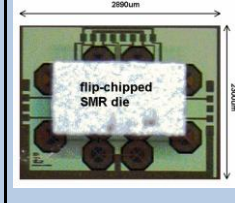
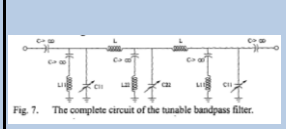
Also frequency agile power amplifiers (PA) and transceivers are more and more available for mobile device developers. PA's and transceivers use voltage controlled oscillators (VCO) and changing IF-frequency to achieve frequency tunability [4], [8], [9], [10], and [11].

The only part in the radio frequency front end chain in mobile devices that is not truly frequency agile is the microwave filters. Current state of the art commercial RF filters for mobile devices are made of using SAW (Surface Acoustic Wave) [12], [13], [14], and [15] and BAW (Bulk Acoustic Wave) technologies [16],[17], and [18]. Both the techniques utilize RF induced acoustic standing waves to form high-Q resonators to filter the signal. The acoustic wave propagates in SAW filters horizontally, i.e. parallel to material surface whereas in BAW filters the acoustic wave propagates vertically through the material thickness. As both technologies rely on acoustic standing waves to create the filter, their frequency tunability is weak [19], [20], and [21].

Frequency tunable filters have existed since the beginning of microwave circuitry, mechanically [22], [23], and [24] and magnetically [22], [24], and [25] tunable microwave filters are well known for RF community. In mechanically tuned filters the dimensions of the filter, e.g. length, volume, or input/output locations are changed to achieve frequency change. In magnetically tuned filters a change of magnetic field in ferromagnetic which compose the resonators changes the filter's resonance frequency. Although both these techniques are well known and widely used their problem is their size. Mechanically or magnetically tunable filters are in same size category as the mobile devices themselves and are thus not a viable solution for mobile devices. Also some sort of frequency agility has been introduced to the microwave filters for mobile devices using SAW/BAW filters. By stacking several SAW/BAW filters parallel with one SPNT RF-switch on each side (input/output) of the parallel filters discrete frequency tunable filter is created [26], and [27]. This does not remove the complexity from the design, but gives limited frequency agility. The down side in addition of the large surface area is that the frequency selectivity is discrete and dependable of the selected filters. In addition two series RF-switch in the RF path add more losses. State of the art RF-switches have at least 0.2 dB losses at the low band (below 1 GHz), and 0.5-0.8 dB losses in high band (1-2 GHz), this is doubled due the two switch design.

To be able to fulfill the market needs for tunable filters researchers have studied new ways to achieve the frequency tunability. The main focus of the latest research for frequency tunable filters has been on microstrip filters, such as combline filters, as the microstrip technology enables easy miniaturization with high dielectric materials and easy integration with the tuning elements, such as varactors and MEMS (Micro Electro Mechanical Systems) switch and capacitors [28] –[32]. Although good tunability and miniaturization of the filter has been achieved with microstrip technology the main problem in mobile device point of view is the need of high control voltages by the varactors and MEMS devices and the nature low Q-value of microstrip filters. Mobile devices normally work on nominal voltage of 3.3 V, dictated by the battery, whereas varactors and MEMS devices need control voltages in 10's V up to 100 V in some MEMS devices. These control voltage levels are not feasible for mobile devices and solutions where the needed voltages are in 3 V level or lower are needed. Other filter technologies in addition of the microstrip technology have been also studied for the frequency tunable filters, such as cavity and lumped component filters, but they usually do not have as wide tuning range as their microstrip counterparts and occupy larger surface area and/or volume [33]-[38]. On table I. some of these frequency agile filters are listed and their performance compared.

Table I. Filter performance comparison

Article	[30]	[35]	[36]	[38]
Picture				 Fig. 7. The complete circuit of the tunable bandpass filter.
Center Frequency [MHz]	2000	15 000	2140	170
Filter Architecture	Microstrip	Cavity	BAW	Lumped components
Insertion loss [dB]	<2.2	5	~7 dB	7-5
Relative bandwidth [%]	9	4.7	5.6	~50
Size in mm	6.7x6.5	20x10	6.65 mm <sup>2</sup>	13 lumped components
Tunability [%]	48	7.2	0.3	45
Tuning technology	MEMS	MEMS	Varactor	BST capacitor

The addition of the millimeter wave (mmWave) spectrum to 5G NR poses new challenges to the mobile device antenna designers. In the current 4G LTE and legacy generation's a single antenna element has been enough to full fill the antenna gain requirements for successful communications. In the mmWave frequencies the free space losses increases significantly compared to the sub 6 GHz range of the 4G LTE. To overcome the increased free space losses new antenna architectures, such as antenna arrays with multiple antenna elements, are needed [39], [40], and [41].

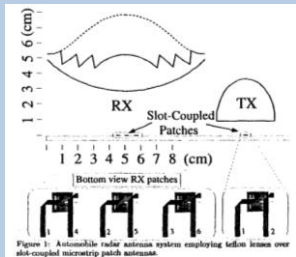
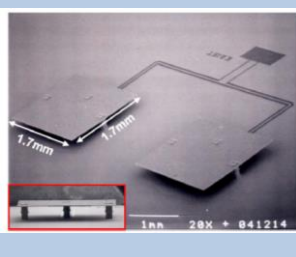
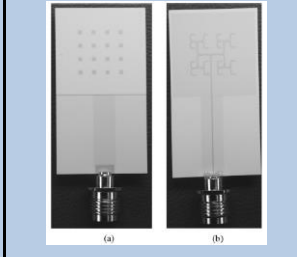
Antenna arrays have been commonly used in military and space applications since 1940's for the radar, scientific measurement, and communication links [42] - [45]. These antenna arrays consist of tens of to thousands of antenna elements and range in frequency from hundreds of MHz of the military early warning radars to hundreds of GHz for missiles and scientific measurement radars and vary in size from tens of meters to few millimeters [42] - [45]. Thus the basic physics of the antenna arrays are widely studied and well understood in the scientific community.

Antenna arrays for mmWave frequencies have been studied for last decades for different use cases, such as automotive radars at 70 GHz [46]-[49]. The main focus of the research has been minimizing the losses due substrate material in the mmWave frequencies and maximizing the gain of the antenna array. This has led to use of complex designs utilizing expensive manufacturing techniques and materials as the antenna array performance has been favorited over the cost effectiveness [46]-[51] as shown on table II. For mass-produced consumer products, such as mobile devices, cheaper solutions for manufacturing the mmWave antenna are needed. The price of a conventional single 4G LTE antenna used in mobile devices is well below 1 € and the mmWave antenna arrays have to meet or at least be close to this price point to be commercially liable for consumer mobile devices.

At the moment there are only few mmWave antenna solutions commercially available for consumer mobile device products. The Qualcomm QTM052 mmWave antenna module (with X50 and X55 RF Front End Modules (FEM)) [52] introduced in 2018 for 28 GHz is the only commercially available antenna array for consumer mobile devices. Other RF FEM and

antenna manufacturers do not offer a “commercial of the self” full antenna solutions, antenna array plus FEM, for the mmWave frequencies at this current moment.

Table II. Millimeter-Wave antenna comparison

Article	[47]	[49]	[50]
Picture			
Center Frequency [GHz]	77	77	60
Antenna type	Patch antenna array with lens	patch antenna array	Patch antenna array
Antenna substrate	Rogers Duroid 5880	Corning Pyrex 7740	LTCC (Ferro A6)
$\epsilon_r / \tan\delta$	2.2 / 0.0009	4.6 / -	5.99 / 0.0015
Antenna bandwidth (-10 dB) [GHz]	-	9	7
Antenna ArraySize in mm	80x80	~5x5	18x18 (substrate length 39 mm)
Peak Gain [dB]	-	6 (Simulated)	15.7
No. of antennas	3	2	16

This thesis has been divided to two different parts. In the first part a frequency agile filter for the sub 6 GHz frequencies is studied and in the second half of the thesis a low cost antenna array is studied for 28 GHz band for the 5G NR..

In this thesis a combline filter is studied with state of the art CMOS RF switch for the mobile device use case for the sub 3 GHz frequencies. The combline filter is studied both in 3D electromagnetic (3D EM) simulations (CST microwave suite) and prototype measurements in LTCC block incorporating the combline filter and the RF switch with all the necessary signal routing and components to achieve the tunability. The CMOS RF switch use control voltages in 3 V level and is thus ideal candidate for a tuning device for frequency tunable filter in mobile devices.

In the beginning of the first chapter the requirements for the frequency agile filter are discussed and a publication study is carried out for frequency tunable filters to find a suitable filter technology. In end of the first chapter a design of a frequency agile filter using 3D EM simulator is shown with the measurement results of the designed frequency agile filter.

The second part of the thesis focuses on a low cost mmWave antenna array for the mobile devices is studied.

In the beginning of the second chapter the requirements of the mmWave antenna array for the latest fifth generation mobile devices are discussed. In end of the second chapter an antenna array and its feeding network are studied on polyamide (PI) substrate which has



better RF performance than the FR-4 substrate and is commercially used in flexible circuit boards (FPC). Also a low loss transmission line, with air-cavity, is studied in conjunction of the low cost array in the PI substrate. And as for the frequency agile filter, the antenna array is studied using 3D EM simulations and prototype measurements.

## References:

- [1] R. Bagheri, A. Mirzaei, S. Chehrazi, and A. A. Abidi, "Architecture and Clock Programmable Basedband of an 800 MHz - 6 GHz Software-Defined Wireless Receiver", IEEE 20<sup>th</sup> International Conference on VLSI Design, 2007.
- [2] Y. Neuvo, "Cellular phone as Embedded Systems", IEEE International Solid-State Circuit Conference, ISSCC, 2004.
- [3] C. Rowell, and E. Y. Lam, "Mobile-Phone Antenna Design", IEEE Antennas and Propagation Magazine, Vol. 54, No. 4, August 2012.
- [4] F. Agnelli et al, "Wireless Multi-Standard Terminals: System Analysis and Design of a Reconfigurable RF Front-end", IEEE Circuits and Systems Magazine, 2006
- [5] O. Kivekäs, J. Ollikainen, P. Vainikainen, "Frequency-Tunable Internal Antenna for Mobile Phones", 12<sup>th</sup> International Symposium of Antennas (JINA 2002), November 2002.
- [6] J. Ollikainen, O. Kivekäs, P. Vainikainen, "Low-Loss Tuning Circuits for Frequency-Tunable Small Resonant antennas", The 13th IEEE International Symposium on Personal, Indoor and Mobile Radio Communications, September 2002.
- [7] Z. Milosavljevic, A. Leskela, Christian Braun, "Adjustable Multiband Antenna and Methods" US Patent US 8564485B2, 2006.
- [8] NXP, Datasheet AFIC901N, "RF LDMOS Wideband Integrated Power Amplifier", 2016, Online [www.nxp.com/docs/en/data-sheet/AFIC901N.pdf](http://www.nxp.com/docs/en/data-sheet/AFIC901N.pdf)
- [9] Analog Devices, Datasheet HMC998APM5E, "GaAs pHEMT MMIC 2 Watt Power Amplifier, DC – 22 GHz", Online [www.analog.com/media/en/technical-documentation/data-sheets/hmc998apm5e.pdf](http://www.analog.com/media/en/technical-documentation/data-sheets/hmc998apm5e.pdf)
- [10] Analog Devices, Datasheet ADRV9009 "Integrated Dual RF Transmitter, Receiver, and Observation Receiver", Online [www.analog.com/media/en/technical-documentation/data-sheets/ADRV9009.pdf](http://www.analog.com/media/en/technical-documentation/data-sheets/ADRV9009.pdf)
- [11] Analog Devices, Data Sheet HMC8411LP2FE, "Low Noise Amplifier, 0.01 GHz to 10 GHz", Online [www.analog.com/media/technical-documentation/data-sheets/HMC8411LP2FE.pdf](http://www.analog.com/media/technical-documentation/data-sheets/HMC8411LP2FE.pdf)
- [12] Qualcomm, Data sheet B8635, "SAW Duplexer for WCDMA / LTE Band 1", Online <https://rffe.qualcomm.com/inf/40/ds/mc/B8635.pdf>

- [13] Qualcomm, Data sheet B8672, "SAW duplexer WCDMA / LTE band 3" , Online <https://rffe.qualcomm.com/inf/40/ds/mc/B8672.pdf>
- [14] Qualcomm, Data sheet B8655, "SAW Rx filter GSM 1800", Online <https://rffe.qualcomm.com/inf/40/ds/mc/B8655.pdf>
- [15] Qorvo, Data sheet 856327 "915 MHz SAW filter", Online [www.qorvo.com/products/p/856327#documents](http://www.qorvo.com/products/p/856327#documents)
- [16] Qorvo, Data sheet TQQ1231, "LTE Band 1 and Band 3 Uplink BAW diplexer", Online [www.qorvo.com/products/p/TQQ1231#documents](http://www.qorvo.com/products/p/TQQ1231#documents)
- [17] Qorvo, Data sheet QPQ1237, "LTE B3/B7 BAW Diplexer", Online [www.qorvo.com/products/p/QPQ1237#documents](http://www.qorvo.com/products/p/QPQ1237#documents)
- [18] Qorvo, Data sheet 885049, "2300-2400 MHz Tx/Rx Filter", Online [www.qorvo.com/products/p/885049](http://www.qorvo.com/products/p/885049)
- [19] K. Hashimoto, S. Tanaka, M Esashi, "Tunable RF SAW/BAW filters: Dream or reality?", 2011 Joint Conference of the IEEE International Frequency Control and the European Frequency and Time Forum (FCS) Proceedings, 2011
- [20] T. Ogami, M Tani et al, "A new tunable filter using love wave resonators for reconfigurable RF", 2014 IEEE MTT-S International Microwave Symposium (IMS2014), 2014.
- [21] H. Lim, A. Z. Kouzani, A. Kaynak, "A study on Tunable Bulk Acoustic Wave Macro Resonators", 2016 IEEE Region 10 Conference (TENCON), 2016.
- [22] G. L. Matthaei, L. Young, E. M. T. Jones, "Microwave Filters, Impedance-Matching Networks, and Coupling Structures", Artech House, 1980.
- [23] R. L. Slevin, "Design of a Tunable Multi-Cavity Waveguide Band-Pass Filter" 1959 IRE National Convention Record, Part 3, pp. 91-112.
- [24] J. Uher and W.J.R. Hoefler, "Tunable microwave and millimeter-wave bandpass filters", IEEE Trans. Microwave Theory Tech., vol. 39, pp. 643—653, 1991
- [25] H. Brand, N. Krause, "Tunable millimetre-wave ferrite bandpass filter with reduced biasing field", Institution of Engineering and Technology (IET), Journal, Vol. 13, Issue 19, 1977.
- [26] Skyworks, Data Sheet SKY13741\_PS\_203469A, Online [www.skyworksinc.com/uploads/documents/SKY13741\\_PS\\_203469A.pdf](http://www.skyworksinc.com/uploads/documents/SKY13741_PS_203469A.pdf)

- [27] Skyworks, Data Sheet SKY13740\_PS\_203470A, Online [www.skyworksinc.com/uploads/documents/SKY13740\\_PS\\_203470A.pdf](http://www.skyworksinc.com/uploads/documents/SKY13740_PS_203470A.pdf)
- [28] CH. ko, K. M.J. Ho, R. Gaddi, and G. M. Reibeiz, "A 1.5 to 2.5 GHz Tunable 4-Pole Filter Using Commercial High Reliability 5-Bit RF MEMS Capacitors", IEEE MTT-S International Microwave Symposium Digest, 2013.
- [29] A. Othman, R. Barrak, M. Mabrouk, "A Tunable RF Filter For Multistandard GSM/UMTS/WiFi/LTE Receiver", Proceedings of 2014 Mediterranean Microwave Symposium (MMS2014), 2014.
- [30] M. A. El-Tanani, G.M. Reibeiz, "High-Performance 1.5–2.5-GHz RF-MEMS Tunable Filters for Wireless Applications", IEEE Transactions on Microwave Theory and Techniques, Vol. 56, 2011.
- [31] T. Jia, J. Ye, Z. Liu, "A RF-MEMS based dual-band tunable filter with independently controllable passbands", 12th IEEE International Conference on Solid-State and Integrated Circuit Technology (ICSICT), 2014.
- [32] X. Mi, O. Toyada, S. Ueda, F. Nakzawa, "Miniaturized Microwave Tunable Bandpass Filters on High-k LTCC with Integrated Resistive Vias as Bias-T", IEEE MTT-S International Microwave Symposium, 2011.
- [33] H. Joshi, H. H. Sigmarsson, D Peroulis, W. J. Chappel, "Highly Loaded Evanescent Cavities for Widely Tunable High-Q Filters", IEEE/MTT-S International Microwave Symposium, 2007.
- [34] W. Gautier, A. Stehle, B. Schoenlinner, V. Ziegler, U. Prechtel, W. Menzel, "RF-MEMS Tunable Filters on Low-Loss LTCC Substrate for UAV Data-Link", IEEE European Microwave Integrated Circuits Conference (EuMIC), 2009.
- [35] B. Schulte, V. Ziegler, B. Schoenlinner, U. PRechtel, H. Schumacher, "RF-MEMS Tunable Evanescent Mode Cavity Filter in LTCC Technology at Ku-Band", IEEE 6th European Microwave Integrated Circuit Conference, 2011.
- [36] S. Rafazimandimby et al, "An Electronically Tunable Bandpass BAW-Filter for a Zero-IF WCDMA Receiver", IEEE Proceedings of the 32nd European Solid-State Circuits Conference, 2006.
- [37] X. Mi, O. Toyoda, S. Ueda, F. Nakazawa, "Miniaturized Microwave Tunable Bandpass Filters on High-k LTCC with Integrated Resistive Vias as Bias-T", IEEE MTT-S International Microwave Symposium, 2011.

- [38] A. Tombak et al, "Tunable RF filters using thin film barium strontium titanate based capacitors", IEEE MTT-S International Microwave Symposium Digest, 2001.
- [39] T. S. Rappaport et al, "Millimeter Wave Mobile Communications for 5G Cellular: It Will Work!", IEEE Access, Vol. 1, 2013.
- [40] A. I. Sulyman et al, "Radio Propagation Path Loss Models for 5G Cellular Networks in the 28 GHz and 38 GHz Millimeter-Wave Bands", IEEE Communications Magazine, 2014.
- [41] A. I. Sulyman et al, "Directional Radio Propagation Path Loss Models for Millimeter-Wave Wireless Networks in the 28-, 60-, and 73-GHz Bands", IEEE Transactions on Wireless Communications, Vol. 15, No. 10, 2016.
- [42] R. J. Mailloux, J. F. Mcllvanna, and N. P. Kernwais, "Microstrip Array Technology" IEEE Transactions of Antennas and Propagation, Vol. AP-29, No. 1, 1981.
- [43] R. J. Mailloux, "Phased Array Theory and Technology", Chapter 4, USA Air Force In-House Report RADC-TR-81-227, 1981.
- [44] R. J. Mailloux, "Phased Array Theory and Technology", Proceedings of the IEEE, Vol. 70, No. 3, 1982.
- [45] J. R. James, P. S. Hall, "Handbook of Microstrip Antennas", Chapters 19 and 23, IEE Electromagnetic Waves Series 28, Peter Peregrinus Ltd., 1989.
- [46] A. S. Cherepanov, A. B. Guskov, Y. P. Yavon, E. F. Zaitsev, "Electronically scanned FDF-antennas for autonomous intelligent cruise control radar applications", 26th European Microwave Conference, 1996.
- [47] B. G. Port, and S. S. Gearhart, "77 GHz Dual Polarized Slot-Coupled Patches on Duroid with Teflon Lenses for Automotive Radar Systems", IEEE Antennas and Propagation Society International Symposium, 1998.
- [48] J. Freese, R. Jakoby, H.-L. Blocher, J. Wenger, "Synthesis of microstrip series-fed patch arrays for 77 GHz-sensor applications ", Asia-Pacific Microwave Conference, 2000.
- [49] H. S. Lee; J.-G. Kim, S. Hong, J.-B. Yoon, "Micromachined CPW-Fed Suspended Patch Antenna For 77 GHz Automotive Radar Applications", European Microwave Conference, 2005.

- [50] A. E. I. Lamminen, J. Säily, A. R. Vimpri, "60-GHz Patch Antennas and Arrays on LTCC With Embedded-Cavity Substrates", IEEE Transactions on Antennas and Propagation, VOL. 56, NO. 9, 2008.
- [51] K.-S. Chin, W. Jiang, W. Che, C.-C. Chang, and H. Jin, "Wideband LTCC 60-GHz Antenna Array With a Dual-Resonant Slot and Patch Structure", IEEE Transactions on Antennas and Propagation, VOL. 62, NO. 1, 2014.
- [52] Qualcomm, "5G NR mmWave Deployment Strategy Presentation", online [www.qualcomm.com/documents/5g-nr-mmwave-deployment-strategy-presentation](http://www.qualcomm.com/documents/5g-nr-mmwave-deployment-strategy-presentation) (Accessed July 2019).

## Chapter I. Frequency Agile Filters for Mobile Devices

---

In the beginning of this first chapter the requirements, electrical and mechanical, for the frequency agile filter are discussed. A comparison of different type of filter technologies is carried out to be able to select the best candidate for the frequency agile filter. After the suitable filter technology has been chosen an analytical filter synthesis is carried out and the frequency tunability is confirmed and optimized. Then a frequency agile filter design with EM simulation is presented, optimizing the filter for LTCC (Low Temperature Co-fired Ceramics) manufacturing technology. In the end of this chapter the experimental results of frequency agile filter build based on the EM-simulations are presented and compared to simulation results.

### I.1 Requirements for the frequency agile filters for mobile devices

A transceiver has filters between the antenna and the baseband to attenuate the unwanted signals from the antenna and also control the harmonics and intermodulation distortions created by the mixers. The number of filters in a modern direct conversion transceiver, shown in figure 1.1 [1], increases rapidly with the increase of the supported communication bands. To solve the problem frequency agile filters, especially for the receiver chain, are currently actively studied to simplify the transceivers architecture. As shown in figure 1.1 the bank of image reject filters in the receiver chain can be replaced with one single frequency agile filter, i.e. tunable filter. By changing to single tunable filter component the complexity of the receiver chain can be reduced by eliminating the two RF-switches and set of passive bandpass filters, one for each supported band.

Designing the frequency agile filters for mobile consumer products such as mobile phones is challenging due the restricted available space inside the device. The battery based power source poses a design limitation for the power consumption and also for the available control voltages. In table 1.1 the mechanical and electrical design criteria's for the frequency agile filter for mobile devices are presented. As seen from the table the most limiting requirements for frequency agile filter are the dimensions, control voltage, and current consumption requirements. Also the insertion loss and band rejection are challenging, as the frequency agile filter should have similar RF performance as the state of the art SAW/BAW filters. In table 1.2 the communication protocols and their respected frequency bands are presented. In table 1.3 the different filter technologies which can be used to design tunable RF filters are listed with the advantages (pros.) and disadvantages (cons.) on mobile device point of view.

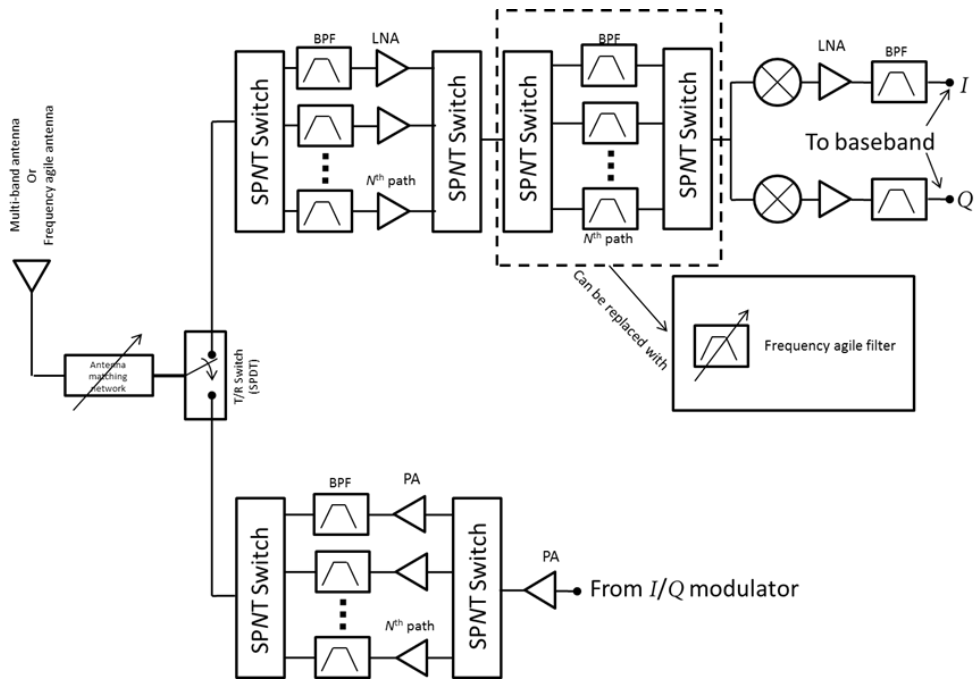


Figure 1.1 Block diagram of multiband transceiver [1]

Table 1.1 Mechanical and electrical specifications for frequency agile filter in mobile devices

Size (LxWxH) mm	9x9x3
Temperature range	-40 to 120° C
Maximum power handling on 50 Ω	35 dBm
Insertion loss	≤ 1.5 dB
Adjacent band rejection	≥ 40 dB
Control Voltage	2.5 to 5 V
Current consumption	<0.5 mA



Table 1.2 Frequency bands for tunable filter

	Protocol		Tx	Rx
Mid-Band	LTE 3	Center frequency [MHz]	1747.5	1842.5
		Bandwidth [MHz]	75	75
		Tx/Rx separation and attenuation	20 MHz/40 dB	
	LTE 2	Center frequency [MHz]	1880	1960
		Bandwidth [MHz]	60	60
		Tx/Rx separation and attenuation	20 MHz/40 dB	
	LTE 1	Center frequency [MHz]	1950	2140
		Bandwidth [MHz]	60	60
		Tx/Rx separation and attenuation	130 MHz/40 dB	
	GSM 1800	Center frequency [MHz]	1747.5	1842.5
		Bandwidth [MHz]	75	75
		Tx/Rx separation and attenuation	20 MHz/40 dB	
	GSM 1900	Center frequency [MHz]	1880	1960
		Bandwidth [MHz]	60	60
		Tx/Rx separation and attenuation	20 MHz/40 dB	
	WCDMA 3	Center frequency [MHz]	1747.5	1842.5
		Bandwidth [MHz]	75	75
		Tx/Rx separation and attenuation	20 MHz/40 dB	
	WCDMA 2	Center frequency [MHz]	1880	1960
		Bandwidth [MHz]	60	60
		Tx/Rx separation and attenuation	20 MHz/40 dB	
WCDMA 1	Center frequency [MHz]	1950	2140	
	Bandwidth [MHz]	60	60	
	Tx/Rx separation and attenuation	130 MHz/40 dB		
LTE 7	Center frequency [MHz]	2535	2655	
	Bandwidth [MHz]	70	70	
	Tx/Rx separation and attenuation	50 MHz/40 dB		

As we can see from the table 1.2 the filters required for the mobile device communication bands have very low relative bandwidths ( $\Delta f/f_0$ ), less than 10% ( $2.6\% < \Delta f/f_0 < 4.3\%$ ). Thus the unloaded quality factor of the resonator has a dominant role to the insertion losses of the filter.

Table 1.3 List of different filter technologies for tunable filters

Filter Technology	Pros.	Cons.
Cavity	+Simple mechanical design for non-tunable filter	-Size, usually double compared to the specification of table 3.1 -Poor tunability
Comblines	+Simple mechanical design for filter part. +Tunability possible achieve with several techniques (MEMS, varactors, SP4T, etc.)	-Insertion Losses? -Size in low band?
Distributed components	+ Good performance even in low frequency +Small size +Tunability possible achieve with several techniques (MEMS, varactors, SP4T, etc.).	-Complicated design with multilayer structures
Microstrip	+ Good performance. +Tunability possible achieve with several techniques (MEMS, varactors, SP4T, etc.).	- Size in low band?
Lumped components	+Tunability possible achieve with several techniques (MEMS, varactors, SP4T, etc.).	- Complicated multiple component designs
SAW/BAW	+Possibility to add the good RF performance of SAW/BAW filters +Tunability possible achieve with several techniques (MEMS, varactors, SP4T, etc.).	- Poor tunability and band selectivity

Table 1.4 Comparison of filter technologies to mechanical specifications (Table 1.1)

Filter Technology	Pros.	Cons.
Volumic technology	Temperature, power handling, insertion loss, adjacent band rejection.	Size, control voltage, current consumption.
Planar technology	Distributed	Insertion losses, size in lower frequencies (with reservation)
	Lumped components	
SAW/BAW	Size, temperature range, power handling, insertion loss, adjacent band rejection.	Control voltage, current consumption.

From the RF performance perspective the cavity and SAW/BAW filters have the best performance, i.e. the lowest insertion loss, of all the filter technologies presented in the table 1.3. Unfortunately cavity filters are large in size in the frequency range in interest for mobile devices. In addition to their size, implementing tunability is difficult and the achieved tuning ratios are small due the high control voltages and large current consumption [2 Chapter 3, 3, 4, and 5] as presented in table 1.4 where the different filter technologies are compared to the mechanical electrical specifications presented in table 1.1.

SAW and BAW filters are more suitable for mobile devices in term of size compared to the cavity filters. Passive, non-tunable, SAW and BAW filters are used extensively in mobile

devices as they provide good RF performance in small form factor. For tunable filters they don't unfortunately fit very well. The high Q-value of the SAW/BAW resonators makes them insensitive for external tuning elements [6]. To be able to introduce tunability to SAW/BAW filter the material properties of the substrate material where the acoustic wave propagates needs to be modified. With the current technologies this is achieved only with high electric- or magnetic fields which are very difficult to create in mobile device environment due the limited power source.

The combine-, distributed component-, and microstrip- filter technologies provides much more suitable media for tunable filters in mobile devices. By using high  $\epsilon_r$  materials the size of these filters can be reduced to suitable size for mobile devices. And with microstrip technology different tuning techniques/technologies can be easily integrated. But the transmission losses are higher than in SAW and BAW filters. The most popular tuning technologies studied in the recent literature are the MEMS-switch and -capacitors and also varactors [7, 8, 9, 10, and 11]. Although good tunability with MEMS and varactor technologies are achieved the available control voltage and power, i.e. current consumption, limits dictated by mobile device battery based power source are not suitable for these tuning technologies. For MEMS tuners, especially tunable MEMS capacitors, high control voltages, even up to 90 V, are required. MEMS RF switches have excellent RF performance with low ohmic losses (and thus high-Q), high linearity, and good power handling to very high frequencies, up to 110 GHz, but just as MEMS capacitors the MEMS switches requires high control voltages. In addition to the high control voltages MEMS based RF switch's switching cycle life time is not with the current technology suitable for consumer products [12 Chapter 2, 13]. Varactors don't necessarily need as high control voltages as the counterpart MEMS tunable capacitors, but they need variable voltage level to change their capacitance, i.e. they are not controllable with digital signal, which makes them difficult to implement in the mobile devices.

CMOS (Complementary Metal Oxide Semiconductor) SOI (Silicon on Insulator) based RF switches such as Ethertronics EC 686 SP4T (Single-Pole Four-Through) offers very attractive tuning solutions for mobile devices. The CMOS switches supply and control voltages are well below the 5 V max voltage limit of the table 1.3. The state of the art CMOS RF switch EC868 needs only 2.8 V supply and control voltages and its current consumption of 90  $\mu$ A is well below the 0.5 mA listed in table 1.3 [14]. Using CMOS for RF circuitry gives also other benefits over the other tuning solutions mentioned above. As the CMOS SOI technology is used also to manufacture digital circuitry, such as micro-controllers or CPUs for computer, the switch control circuitry is easy to integrate to the same silicon die with the RF switch [15]. This on die integration simplifies the use of the CMOS RF switch in the mobile devices as standard digital control signals, such as GPIO, MIPI, or SPI can be used straight from the mobile device baseband without external control circuitry [14].

In this thesis we want to evaluate the possibility of designing a frequency agile combine filter by integrating the Ethertronics CMOS RF SP4T switch (EC 686) for mobile device application.

## I.2 Characteristics of CMOS RF switch (EC 686)

CMOS RF switches use FET (Field Effect Transistor) transistors as a switching element, shown in figure 1.2. In practice these FET transistors are connected both in series and parallel to increase the voltage/power handling of the switch and to minimize the internal losses. In this thesis the selected CMOS RF-switch has only four through state in the switch. But the CMOS technology is not limited only to four through ports. RF switches up to 14 through ports are used in high end mobile devices, and also double-pole switches with separated common ports for low and high bands are used in 4G mobile devices [15]. By increasing number of through ports the supported communication bands is possible to increase without adding a new frequency agile filter(s).

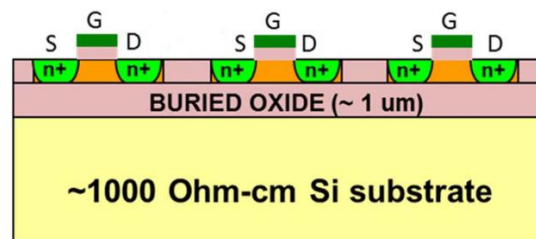


Figure 1.2 Side view of general CMOS N-FET transistors [15]

CMOS RF switches can be configured in different topologies based on the applications but are usually configured in either series or series-shunt configuration as shown in figure 1.3 [16]. Each switch transistor  $M_N$  can be made of several actual FET transistors in series and/or parallel to each other. In a series-shunt configuration the non-activated paths are terminated to ground through their dedicated shunt branches, as shown in figure 1.3 b). By grounding the non-active path(s) the isolation between the RF paths can be improved compared to the series configuration, but the switch losses, especially in higher frequencies, are increased in same time [16]. In figure 1.4 the equivalent circuits of both series and series-shunt topologies are presented for the case where only the  $RF_1$  path is activated. As we can see from figure 1.4 a) only the OFF capacitance ( $C_{OFF}$ ) on the series switch topology are isolating the other paths, whereas in the series-shunt topology the un-used paths are grounded through the ON resistance ( $R_{ON}$ ) of the shunt branch, improving the isolation.

The  $R_{ON}$  resistance of the active RF path(s) is the dominant factor for determining the insertion loss of the switch. The  $R_{ON}$  resistance can be decreased by material selection and increasing the size of the switch transistor. This unfortunately increases the  $C_{OFF}$  capacitance which has an effect to the input impedance and decreases the isolation and the usable bandwidth of the switch. Also the increase of the  $C_{OFF}$  capacitance has an impact to the switching time of switch [15].

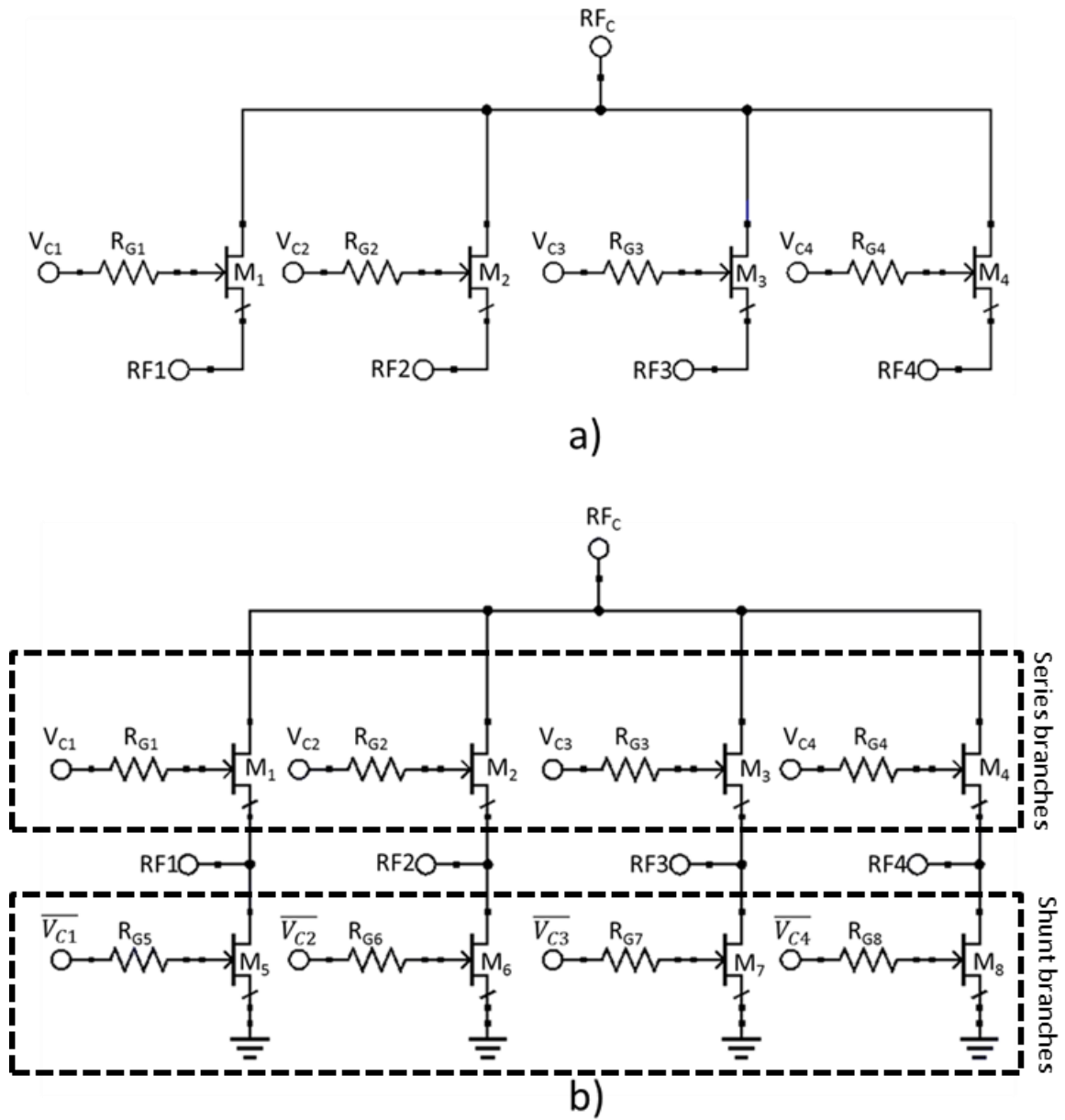
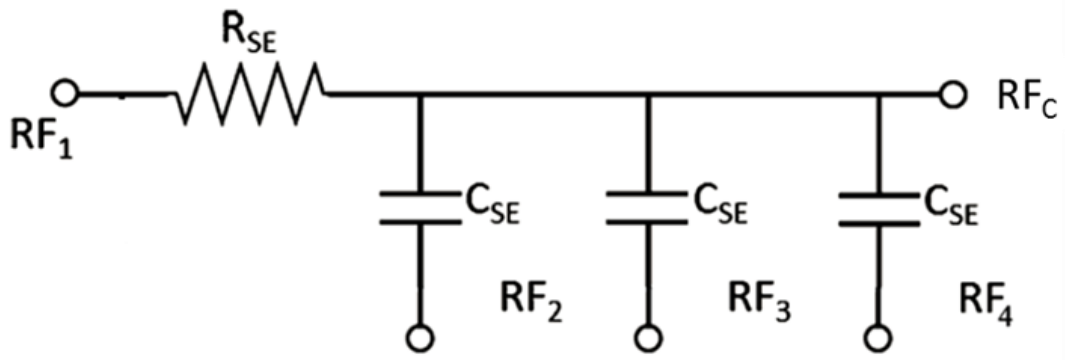
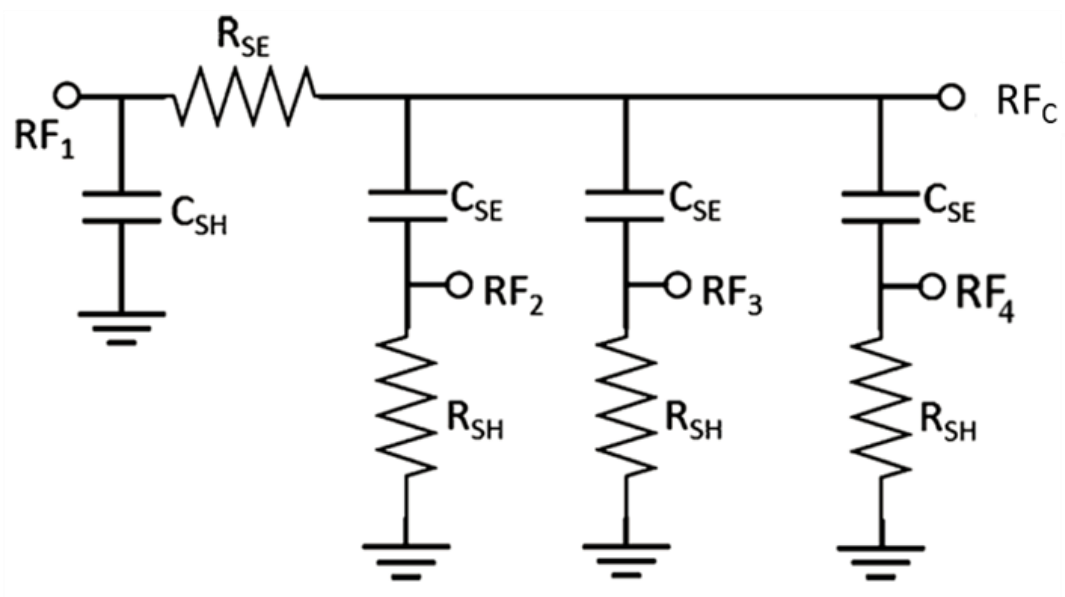


Figure 1.3 Series a) and series-shunt b) SP4T switch topologies



a)



b)

Figure 1.4 Equivalent-circuit models of series a) and series-shunt b) SP4T RF switches, where  $R_{SE}$  and  $C_{SE}$  stands for ON ( $R_{ON}$ ) resistance and OFF ( $C_{OFF}$ ) capacitance of the series branches, respectively,  $R_{SH}$  and  $C_{SH}$  stands for ON ( $R_{ON}$ ) resistance and OFF ( $C_{OFF}$ ) capacitance of the shunt branches, respectively [15]

In table 1.5 and figure 1.5 the characteristics, electrical and mechanical, and the block diagram of the Ethertronics EC 686 SP4T RF switch are presented. As discussed earlier in this third chapter the electrical and mechanical properties, low loss, low control voltage, low power, and small size, of this switch makes it ideal candidate for tunable filters in mobile devices. The EC 686 consist of two parts, digital and RF (SP4T), as shown in figure 1.5. The digital part takes care of providing the chipset's internal bias voltages and controlling the RF state, i.e. witch RF path(s) is activated, of the switch. The RF switch part of the EC 686 is

based on the series topology shown in figures 3.3 a) and 3.4 a) to minimize the insertion losses of the switch.

Table 1.5 The characteristics of EC 686 RF Switch [14]

<b>EC 686 SP4T RF switch</b>	
<b>Frequency range:</b>	700-3000 MHz
<b>R<sub>on</sub>:</b>	0.9 Ω
<b>C<sub>off</sub>:</b>	300 fF
<b>IIP3:</b>	+80 dBm
<b>Supply Voltage (Vdd):</b>	+2.8 V (DC)
<b>Supply Current:</b>	90 μA
<b>Control interface:</b>	SPI, MIPI, GPIO
<b>Operating temperature:</b>	-40 to +80 °C
<b>Size &amp; Package:</b>	2x2x0.5 mm <sup>3</sup> , QFN 16

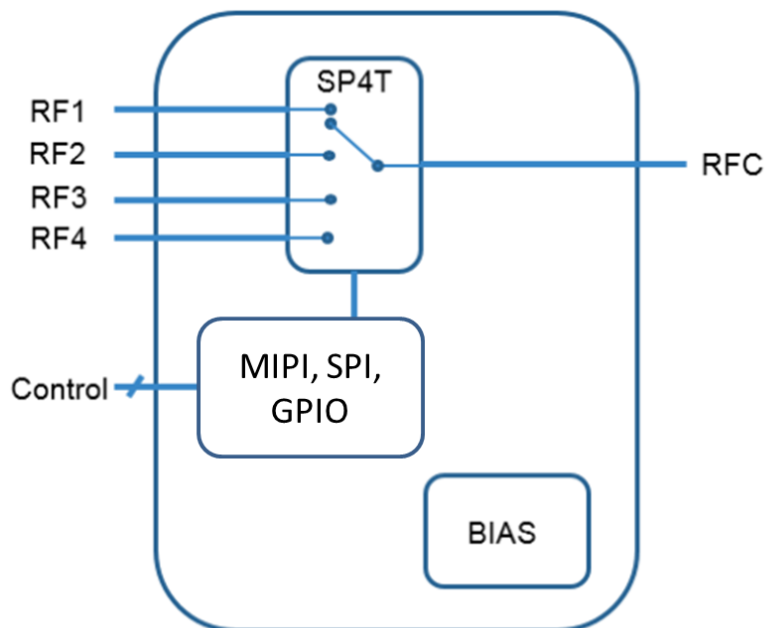


Figure 1.5 The block diagram of the Ethertronics EC 686 SP4T RF switch [14]

In this thesis the frequency agile filter has been chosen to be designed in LTCC technology integrating CMOS switches on microstrip filter topology. The LTCC technology offers good

RF properties, with high  $\epsilon_r$  and low losses, for miniaturizing the filter and doesn't restrict the layout of the metal layers. CMOS switches are chosen over MEMS and varactor diodes, the two popular tuning methods, as CMOS switches supports higher integrations for the controls, don't require high control voltages, and is a mature commercially available technology. For the filter topology microstrip and combline structure was chosen as the integration of the tuning solution (i.e. CMOS switch) and the miniaturizing of the filter is easier than most of the other filter technologies. Comparing to mechanical and electrical targets set on the table 1.1 in the beginning of this chapter the chosen filter topology and tuning technology can fulfill the requirements on size, temperature, power handling, and the power (control voltage and current). Microstrip filters don't have inherently as high Q-values as SAW/BAW and cavity filters and the CMOS switches have more losses than their MEMS counter parts making the set insertion loss target difficult to achieve. Although the losses of the selected tunable filter topology might be higher than single fixed frequency band filter, the total system losses with the frequency agile filter can be smaller as the frequency agile filter simplifies the transceiver architecture and removes other lossy components needed with traditional filters in multi-band transceiver.

### **I.3 Low-Temperature Co-fired Ceramic (LTCC)**

LTCC is a thin film manufacturing technology widely used for microwave circuitry packaging. In LTCC pre-cut metallized layers of ceramic substrates are sintered together below  $1000^\circ\text{C}$  (the exact co-firing temperature depends on the ceramic material) to form circuit boards [17]. Compared to more common electronics circuitry substrate FR-4 the LTCC ceramic substrates offer several advantages. Especially for high frequency and also for loss sensitive applications, such as filters, LTCC offers much more attractive electrical material properties. The losses of the ceramic materials used in LTCC can be 10 to 100 times less than FR-4 based substrates [18]. In addition to better material properties LTCC offers also more freedom for designing electronic circuitry. The layer stack up doesn't restrict the routing of the signal lines and vias between the layers can be placed without any restrictions.

Selecting the correct high  $\epsilon_r$  substrate material for the filter is crucial. In addition of high  $\epsilon_r$  value the substrate material should have also low electrical losses to achieve the best RF performance, which is low insertion loss for filter design. The substrate material should be also easy to handle and manufacture. Ceramic substrates used in LTCC technologies offers all these properties with mass production capability. Kyocera's GL330 LTCC substrate with  $\epsilon_r = 7.8$  and  $\tan\delta = 0.0005$  (at 2 GHz) is chosen as the substrate for this thesis filter as it offers all the qualities of the good substrate material for the RF-filter. For the GL330 LTCC substrate copper with thickness of  $10\ \mu\text{m}$  in the inner layers and  $15\ \mu\text{m}$  in outer layers and sheet resistance of  $3\text{m}\Omega/\text{square}$  is used as a conductor.

### **I.4 Electro-Magnetic-Simulation tools**

The advance of computing power has made 2.5D and 3D EM-simulations tools, such as Momentum integrated in Advanced Design Systems (ADS) and CST, very powerful and



practical tools for RF engineers, especially for antenna, filter, and EMC/EMI engineers. With a modern desktop computer complicated planar and 3D structures, such as mobile phones, can be fully imported and simulated to gain accurate antenna results with the full phone mechanics prior to first prototype device [19]. The two most popular solver methods used in EM-simulations are the frequency- and the transient-solvers (time-domain). Especially for wide frequency band problems such as cellular antennas or tunable filters the transient solver is most suitable. With the frequency-solver the Maxwell's equations are solved in each frequency point in interest, for wide band problems this becomes time consuming and the simulation times becomes unpractical. On contrary with transient-solver the Maxwell's equations in each individual mesh-cell are solved for all the frequency points in interest together until the inserted power pulse in time-domain has been decayed to the desired power level to obtain desired accuracy [19]. Whereas frequency bandwidth is the limitation for frequency-solver, the electrical size of the simulated problem is the limitation for the transient-solver. When the size of the problem becomes significantly big in term of the smallest wave-length in interest, the mesh-cell number rises significantly which then increase the simulation time.

### **I.5 Designing of combline filter by 2.5D and 3D EM-simulations**

Designing a RF-filter has become easier with the 3D EM-simulations tools. With the aid of the EM-simulation tools the filter performance can be easily optimized after the initial physical parameters have been synthesized with the mathematical formulas. In the following chapter 2.5D and 3D EM-simulation tools are used to design and optimize the performance of a frequency agile combline filter.

The combline filter has been implemented in LTCC multi-layer technology to achieve the small form factor required by the mobile devices. To further reduce the size of the combline filter the transmission lines can be folded over each other [20]. In this way the resonators are formed by stripline and microstrip line sections connected by vias. The high permittivity materials can be easily implemented to reduce the size of the filter. From the filter topologies presented in table 1.2 the combline filter is chosen as it with the  $\lambda/8$ -length transmission line length provides the smallest size of all the planar filter topologies.

#### **I.5.1 Filter synthesis**

After the substrate material and the supported communication protocols are selected the design of the combline filter can be started. We will design a Rx (receive) filter covering the middle bands of the 5G NR sub 6 GHz frequencies shown in table 1.2.

In a first step, the synthesis of a filter consists in determining a transfer function (Butterworth or Chebyshev or pseudo-elliptic type transfer function,) and the number of poles making it possible to satisfy the electrical criteria fixed by the specifications. We opted for a 3<sup>rd</sup> order Chebyshev filter, with a ripple of 0.1 dB in the bandwidth. The study of an electrical circuit composed of localized elements whose responses are equivalent to those of the desired filter

then makes it possible to access the values of the couplings between the different resonant elements of the structure ( $k_{n,n+1}$ ) and the couplings between the first and last resonators and the excitation systems (external quality factor ( $Q_e$ )).

The external quality factor  $Q_e$  and inter-resonator coupling factors  $k_{12}$  and  $k_{23}$  can be derived by using the table 1.6 [22] and equations 1.1-1.3 [22]. In the table 1.6 the element values for Chebyshev lowpass prototype filter are presented for 0.1 dB passband ripple ( $L_{Ar}$ ).

Table 1.6 Element values of Chebyshev lowpass filter ( $g_0 = 1, \Omega_c = 1 \text{ rad/s}$ ),  $L_{Ar} = 0.1 \text{ dB}$

Order/element	$g_1$	$g_2$	$g_3$	$g_4$	$g_5$	$g_6$	$g_7$	$g_8$	$g_9$	$g_{10}$
1	0.3052	1.0000								
2	0.8431	0.6620	1.3554							
3	1.0316	1.1474	1.0316	1.0000						
4	1.1088	1.3062	1.7704	0.8181	1.3554					
5	1.1681	1.4040	2.0562	1.5171	1.9029	1.0000				
6	1.1681	1.4040	2.0562	1.5171	1.9029	0.8618	1.3554			
7	1.1812	1.4228	2.0967	1.5374	2.0967	1.4228	1.1812	1.000		
8	1.1898	1.4346	2.1199	1.6010	2.1700	1.5641	1.9445	0.8778	1.3554	
9	1.1957	1.4426	2.1346	1.6167	2.2054	1.6167	2.1346	1.4426	1.1957	1.0000

$$Q_e = \frac{f_0 g_0 g_1}{\Delta f} \quad (1.1)$$

$$k_{1,2} = \frac{\Delta f}{f_0 \sqrt{g_1 g_2}} \quad (1.2)$$

$$k_{2,3} = \frac{\Delta f}{f_0 \sqrt{g_2 g_3}} \quad (1.3)$$

In the table 1.7 the external quality factor ( $Q_e$ ), and coupling factor ( $k_{n,n+1}$ ) are calculated for the lowest and highest filter resonances. The values presented in table 1.7 have to be respected to have a good matching an adequate bandwidth for the filter.

Table 1.7 Calculated external quality factor  $Q_e$  and inter-resonator coupling factor  $k$

GSM 1800 RX	LTE 7 RX
$Q_e = 25$	$Q_e = 39$
$k_{12} = k_{23} = k = 0.037$	$k_{12} = k_{23} = 0.024 = k$

The first studied topology that is often found in the literature is presented in figure 1.6. First, we consider only a stripline structure. The calculations will be performed using a hybrid method coupling an electromagnetic simulation (Momentum) and a circuit simulation (ADS).

A segmented analysis of the filter will make it possible to approximate the length  $l$  of the resonators, the value of capacitor and the distances  $w_g$  and  $d$ . After the first approximation a global simulation will be done to optimize the set of values to meet the desired performance.

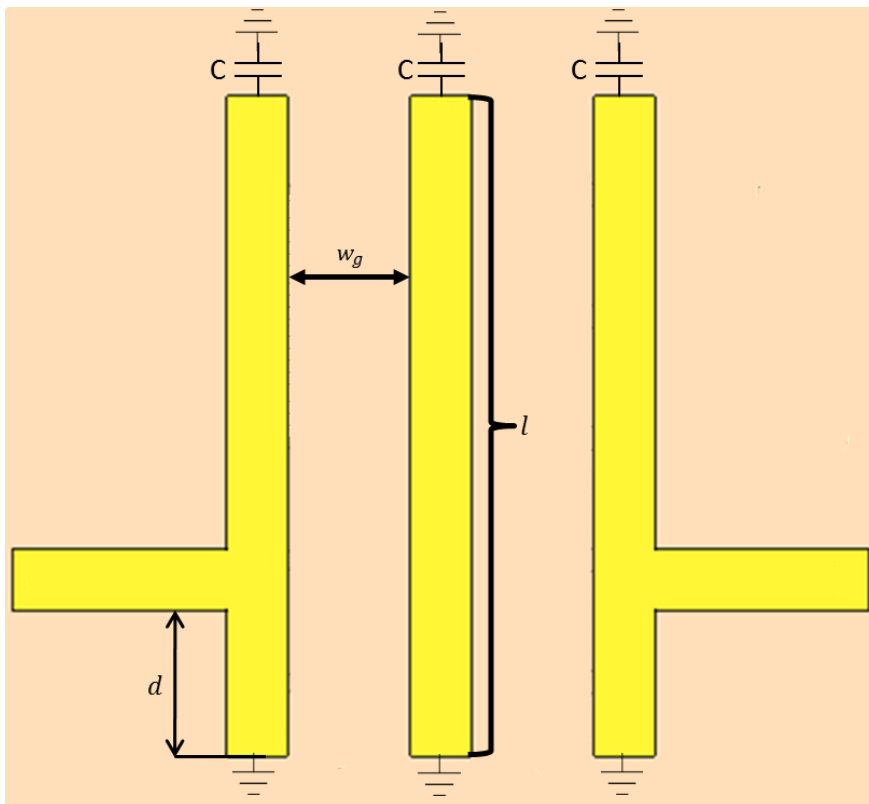


Figure 1.6 Topology of 3rd order combline filter

The length of the transmission line is calculated using the equation 1.4 [21]. For combline filters the length of the transmission line is one eighth of the wavelength. This choice makes it possible to have a good compromise between agility and losses. With the Kyocera GL330 substrate, the  $\lambda/8$  wavelength at 1700 MHz is  $\sim 7.898$  mm.

$$\lambda = \frac{c}{f_c \sqrt{\epsilon_r}} \quad (1.4)$$

where  $c$  = speed of light in vacuum,  $f_c$  = resonant frequency in Hz,  $\epsilon_r$  = permittivity of the substrate.

For the frequency agile filter the capacitance value of the capacitors  $C$  in the end of the combline filter are varied to tune the center frequency of the filter to the desired frequency band. A 2 pF capacitor is needed to create the lowest bands, GSM 1800/WCDMA 3/LTE B3, resonance and a 0.6 pF capacitor for the highest covered band, LTE 7, leading to a tuning ratio of 3.3.

In the table 1.8 and 3.9 the circuit simulated (Momentum and ADS, (Advanced Design System)) external quality factor and coupling factor are shown for the combline filter shown in figure 1.6 with the appropriate capacitance values for GSM 1800 and LTE 7. In the table 1.8 the location ( $d$ ) of the tapped feed and the distance ( $w_g$ ) between the resonators are optimized for GSM 1800 band and in the table 1.9 for the LTE 7 band.

Table 1.8 Simulated  $Q_e$  and  $k$  for the GSM 1800 and LTE 7 with  $d$  and  $w_g$  optimized for GSM 1800 band

	<b>GSM 1800 RX</b>	<b>LTE 7 RX</b>
	<b>C = 2 pF</b>	<b>C = 0.6 pF</b>
<b><math>d = 1800 \mu m</math></b>	<b><math>Q_e = 25</math></b>	<b><math>Q_e = 15</math></b>
<b><math>w_g = 550 \mu m</math></b>	<b><math>k = 0.037</math></b>	<b><math>k = 0.021</math></b>

Table 1.9 Simulated  $Q_e$  and  $k$  for the GSM 1800 and LTE 7 with  $d$  and  $w_g$  optimized for LTE 7 band

	GSM 1800 RX	LTE 7 RX
	<b>C = 2 pF</b>	<b>C = 0.6 pF</b>
<b><math>d = 1100 \mu m</math></b>	<b><math>Q_e = 66</math></b>	<b><math>Q_e = 39</math></b>
<b><math>w_g = 505 \mu m</math></b>	<b><math>k = 0.044</math></b>	<b><math>k = 0.024</math></b>

As we can see from the tables 3.8 and 3.9 it is not possible to respect the external quality and coupling factors defined in table 1.7 just by varying the capacitance value of the tuning capacitors C. With only using tuning capacitors the center frequency of the filter can be modified, but the bandpass bandwidth and the matching of the filter in different center frequencies are not optimal for the different communication bands (chart 1.1).

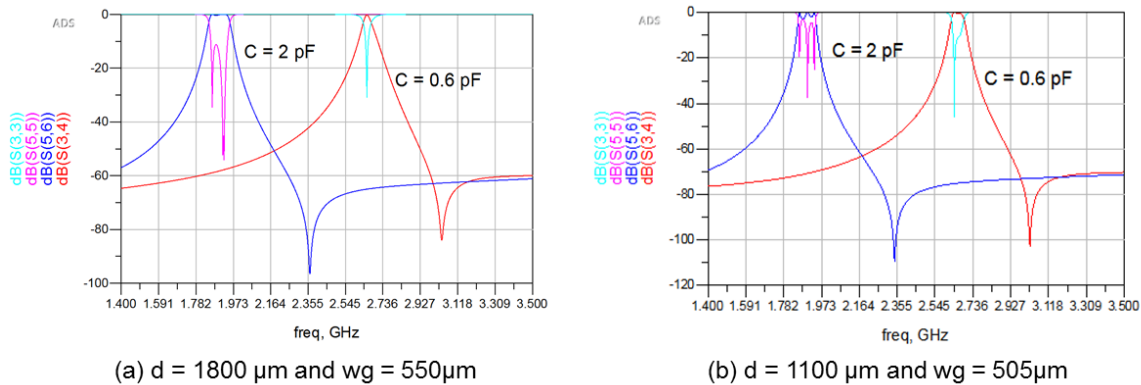


Chart 1.1 Reflection and transmission responses of the filters with  $d$  and  $w_g$  optimized for GSM 1800 band (a) and for LTE 7 band (b)

To obtain the optimal performance for all the center frequencies of the Rx bands of the communication protocols it is necessary to be able to control independently the center frequency  $f_0$  and also the bandwidth  $\Delta f$ . Tunable bandpass filters with constant fractional bandwidth ( $\Delta f/f_0$ ) or absolute bandwidth ( $\Delta f$ ) have been widely studied in the literature. The proposed solutions use distributed capacitive and corrugated couplings lines [23], the mixed electrical and magnetic coupling structures [24], [25], the non-resonant lines [26], and the inductors for input/output coupling [27], [28]. All these methods do not meet our needs and moreover they require designing of complex feeding or de-coupling structures in addition to the filter structure.

### I.5.2 Parallel load combine filter

In this thesis we have studied new filter topology to adjust simultaneously both the center frequency and the bandwidth of the passband without a complex feeding or decoupling structures. The new filter configuration is shown in the figure 1.7. The distributed structure (striplines) is same as in the figure 1.6 but the tuning load is now, instead of just a capacitor, a parallel load made of an inductor and a capacitor. The inductor parallel to the capacitor gives a second degree of freedom to adjust the resonator characteristics when the distributed structure is fixed (length, tapped feed location, and resonator spacing). In a symmetrical structure the  $L_1$  and the  $C_1$  determine the external quality factor and the  $L_2$  and the  $C_2$  determine the inter-resonator coupling  $k_{12} = k_{23}$ . The resonance frequency is determined both by the  $L_1, C_1$  and  $L_2, C_2$  resonators.

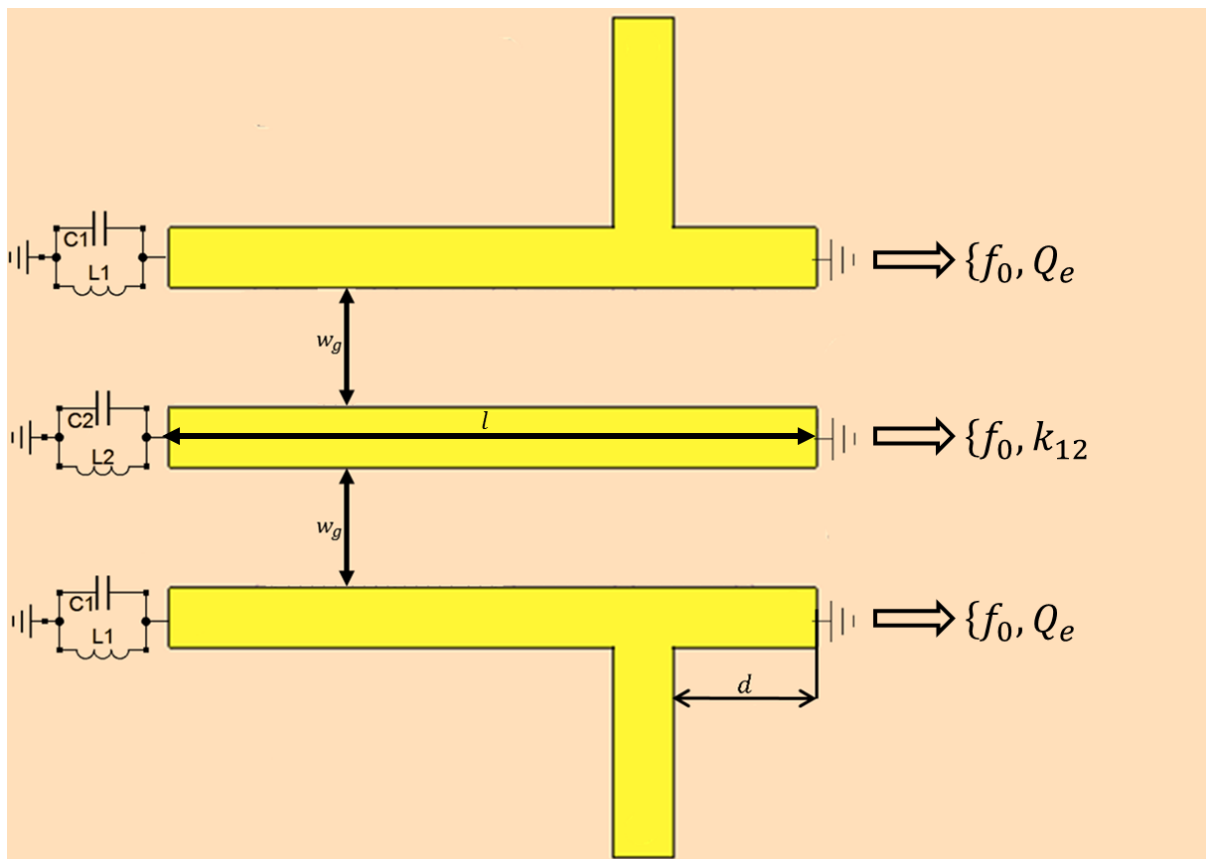


Figure 1.7 Topology of the new proposed filter

As discussed in the second chapter the combine filter needs to have a capacitive load in the open end to be able to form a resonator. Thus the admittance (1.5) of the parallel load in figure 1.7 must be equal to capacitance.

$$Y = j \left( \frac{LC\omega^2 - 1}{L\omega} \right) = j \left( \frac{\frac{\omega^2}{\omega_1^2} - 1}{L\omega} \right) \quad (1.5)$$

where  $\omega_1 = \frac{1}{\sqrt{LC}}$ .

If  $\omega_1 < \omega \Rightarrow \frac{LC\omega^2 - 1}{L\omega} > 0$  the parallel load circuit admittance is equal to a capacitance ( $Y = jC(\omega)\omega$ ). This condition must be verified for all the desired resonance frequencies.

### I.5.2.1 Determining the values of elements $L_1$ and $C_1$

The  $L_1$  and  $C_1$  are determined by the external quality factor  $Q_e$  and the resonant frequency  $f_0$  which are also dependable by the location of the tapped feed (distance  $d$ ). If we fix the value of  $d$  we can determine the values for  $L_1$  and  $C_1$ , while respecting the  $\omega_1 = 2\pi f_1 < \omega$ . In Table 1.10 the simulated values for  $L_1$  and  $C_1$  for the simulation model shown in figure 1.8 are shown for different feeding locations for GSM 1800 and LTE 7 Rx bands. For these simulations realistic value ranges for the capacitance and inductance were used to keep the feed locations realistic. The component value ranges were taken from muRata high-Q capacitor (GJM03) and inductor (LQW03) series components in 0603 (metric) size and the values for the capacitors and inductors are within 0.2-33 pF and 1-15.5 nH respectively.

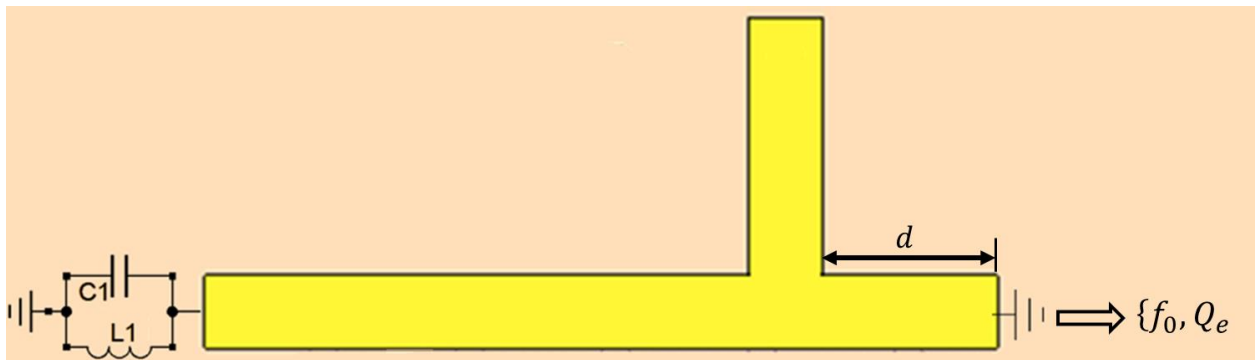


Figure 1.8 Simulation model to determine the values of  $L_1$  and  $C_1$

Table 1.10 Values of  $L_1$  and  $C_1$  for different tapped feed locations for GSM 1800 and LTE 7 Rx bands

Center frequency	$f_0 = 1842.5$ MHz	$f_0 = 2655$ MHz
$d = 1900 \mu\text{m}$	$L_1 > 20$ nH	
$d = 2000 \mu\text{m}$	$f_1 = 0.8$ GHz $L_1 = 14.492$ nH $C_1 = 2.73$ pF $Q_e = 25$	$f_1 = 2.42$ GHz $L_1 = 1.1$ nH $C_1 = 3.92$ pF $Q_e = 39$
$d = 2100 \mu\text{m}$	$f_1 = 0.9$ GHz $L_1 = 10.65$ nH $C_1 = 2.93$ pF $Q_e = 25$	$f_1 = 2.43$ GHz $L_1 = 1.04$ nH $C_1 = 4.125$ pF $Q_e = 39$
$d = 2200 \mu\text{m}$		$L_1 < 1$ nH

From the simulation results we can see that:

- By increasing the distance  $d$  the external quality factor  $Q_e$  decreases.
- Increasing the  $f_1$  will decrease the  $L_1$  and increase the external quality factor  $Q_e$ .

### I.5.2.2 Determining the values of elements $L_2$ and $C_2$

To determine the values for the  $L_2$  and  $C_2$  elements a full filter simulations is needed as the distance between the distributed resonators has an impact to the coupling factor  $k$  and thus to the values of the  $L_2$  and  $C_2$ . In the beginning of the simulations the  $w_g$  is set to arbitrary value and the inductor  $L_2$  and capacitor  $C_2$  values are set to same with the  $L_1$  and  $C_1$  respectively, where  $L_1$  and  $C_1$  are obtained from the previous simulation with a given  $d$ . The correct values for  $L_1$ ,  $L_2$ ,  $C_1$ ,  $C_2$ , and  $w_g$  are obtained by optimization simulations where for  $L_1$ ,  $L_2$ ,  $C_1$ ,  $C_2$ , and  $w_g$  are varied to obtain the optimum matching and passband bandwidth. The center resonator have different inductor and capacitor values from the edge resonators ( $L_2 \neq L_1$  and  $C_2 \neq C_1$ ) due the different resonator topology, the feed lines on the edge resonators have an impact to their resonator characteristics. It's possible to use the same values for  $L_2$  and  $C_2$  as  $L_1$  and  $C_1$  but the distributed central resonator width and length has to be modified accordingly.

In below the procedure to obtain the inductor and capacitor values are shown for the example combine filter shown in figure 1.7. The feed location is set to  $d = 2000 \mu\text{m}$  and the inter resonator distance to arbitrary value of  $w_g = 400 \mu\text{m}$ . The inductor ( $L_1=L_2$ ) and capacitor ( $C_1=C_2$ ) values are taken from the table 1.10. The simulated wideband response of the filter is shown in chart 1.1 and the filter characteristics on table 1.11.



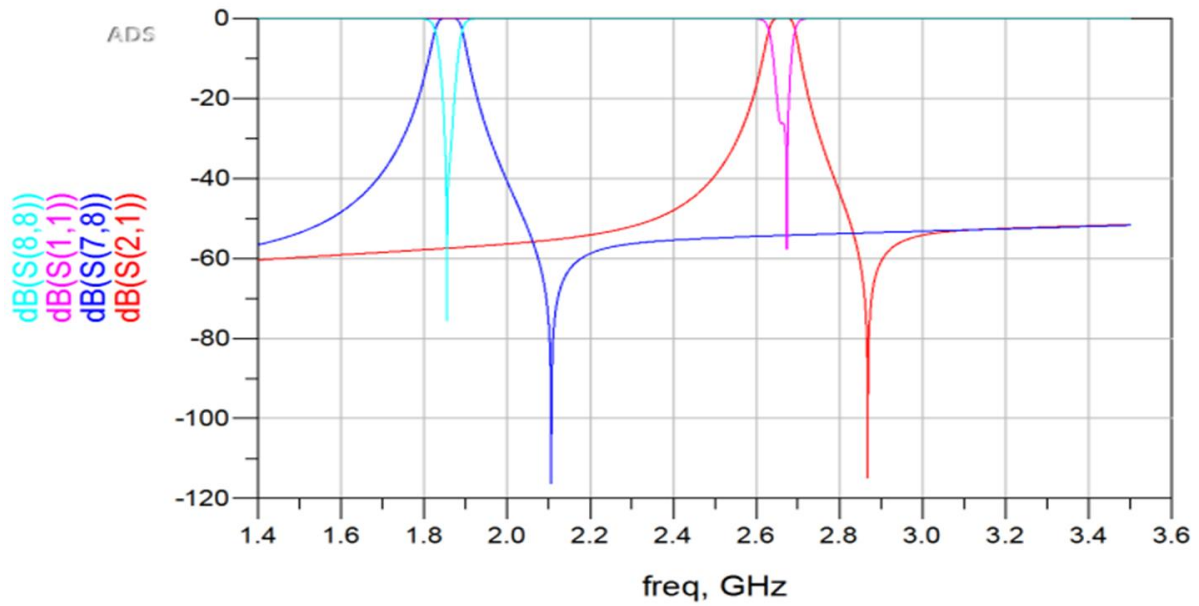


Chart 1.2 Wideband response of the simulated filter

Table 1.11 Filter characteristics,  $d = 2000 \mu m$  and  $w_g = 400 \mu m$

	GSM 1800 Rx	LTE B7 Rx
Center frequency	$f_0 = 1859 \text{ MHz}$	$f_0 = 2663 \text{ MHz}$
Bandwidth	32 MHz	33 MHz
coupling factor	$k_{1,2} = 0.016$	$k_{1,2} = 0.011$

As we can see from the simulated results and comparing them to the table 1.7 the coupling is not strong enough with  $w_g = 400 \mu m$  and the coupling must be increased by decreasing the distance between the distributed resonators ( $w_g$ ).

For the second optimization round the distance is decreased to  $w_g = 280 \mu m$  and the values of the  $L_1$ ,  $L_2$ ,  $C_1$ , and  $C_2$  are optimized. In the charts 1.3 and 1.4 the wideband and passband responses and on the table 1.12 the filter characteristics for the optimized filter are shown.

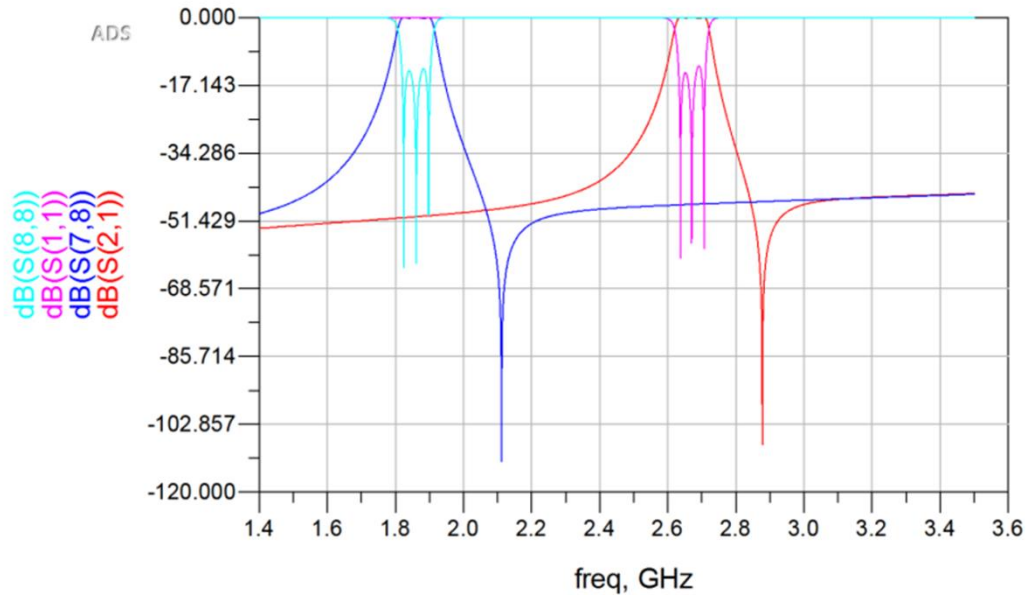


Chart 1.3 Wide band response of the combline filter with optimized parallel load component values

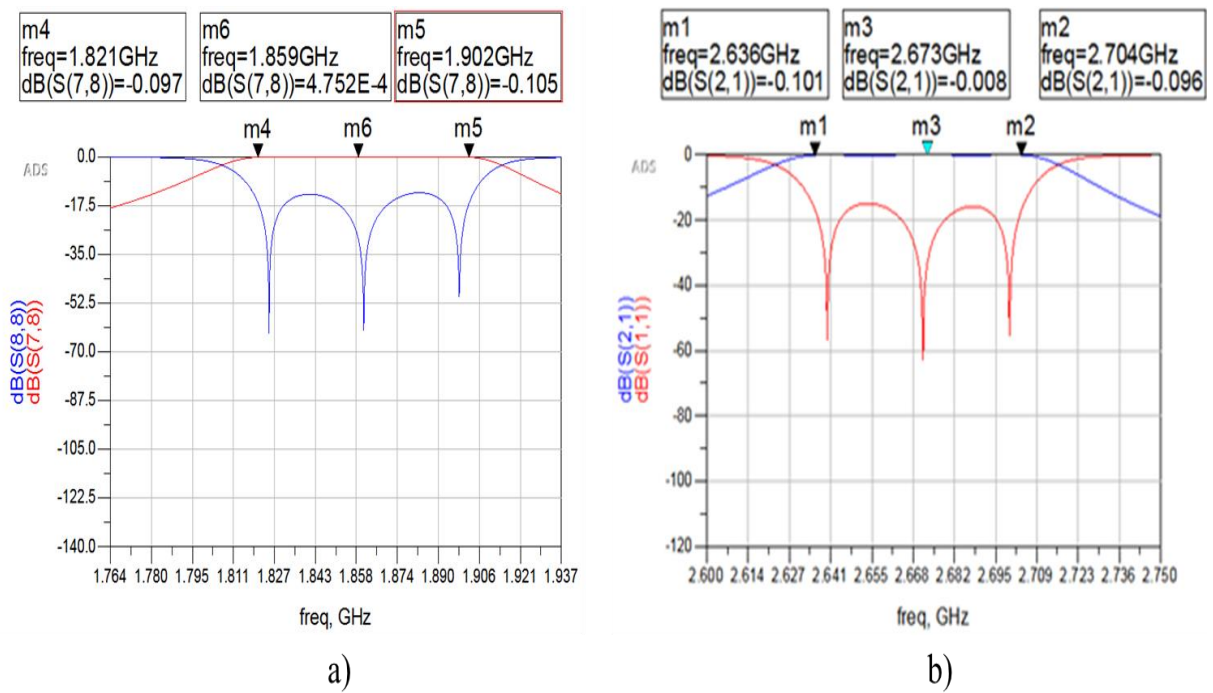


Chart 1.4 Passband responses for a) GSM 1800 and b) LTE 7 for the optimized filter

Table 1.12 Filter characteristics for the optimized parallel load combline filter,  $d = 2000 \mu m$  and  $w_g = 280 \mu m$

	GSM 1800	LTE 7
<b>Edge resonators</b>	$L_1 = 8.58 \text{ nH}$	$L_1 = 1 \text{ nH}$
	$C_1 = 3.02 \text{ pF}$	$C_1 = 4.18 \text{ pF}$
<b>Center resonator</b>	$L_2 = 0.65 \text{ nH}$	$L_2 = 7.19 \text{ nH}$
	$C_2 = 13.41 \text{ pF}$	$C_2 = 1.1 \text{ pF}$
<b>Center frequency</b>	1859 MHz	2663 MHz
<b>Bandwidth</b>	81 MHz	76 MHz

As we can see from the above results the filter characteristics can be controlled with selecting the components values correctly for the parallel load circuit, thus enabling full control of the passband bandwidth for each resonant frequency of the frequency agile filter. The passband bandwidth control is illustrated in more details in the following subchapter with 3D EM simulations in CST.

## I.6 Frequency agile combine filter

After the basic dimensions of the combine filter are synthesized the designing of the frequency agile filter can be started. First the tunability of the filter is verified in EM-simulations. In chart 1.5 the four tuning states for the nine supported communication bands from the table 1.2 are verified for the basic combine design. For the lowest state 2 pF capacitor is needed to cover the GSM 1800/WCDMA III resonance, whereas for the LTE 7 0.6 pF capacitor is needed, giving tuning ratio of 3.3.

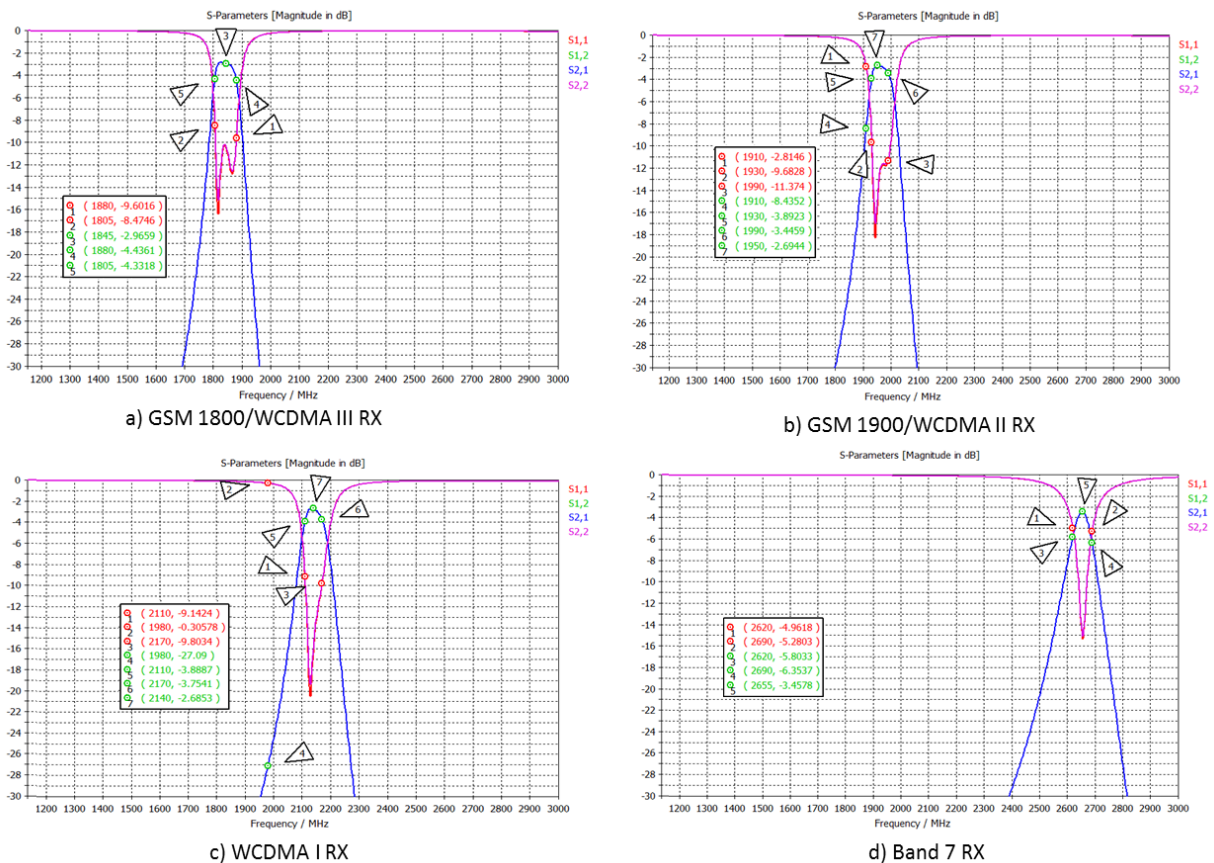
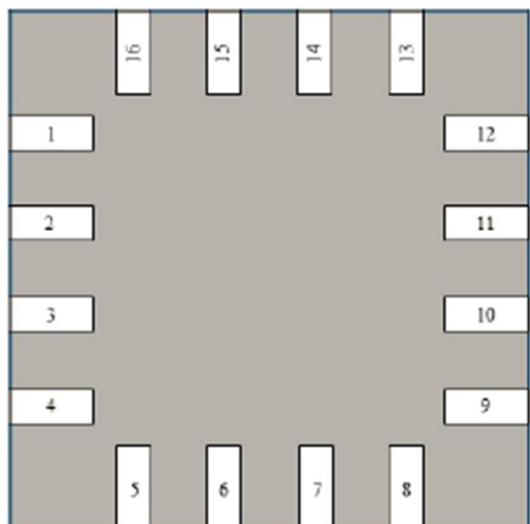


Chart 1.5 The tuning range of the basic combine filter

After the tunability of the frequency agile filter is confirmed the implementation of the tuning element(s) can begin. In this thesis Ethertronics EC 686 SP4T RF switch is used as tuner for the frequency agile filter. It's low  $R_{on}=0.9 \Omega$  resistance and possibility to control each through (RF-port) independently makes it a good tuner candidate [14]. The low  $R_{on}$  resistance means that the losses due the tuner element are low. The independent control of the RF-ports gives the opportunity to combine the discrete tuning components, capacitor or inductor, and enlarge their value range to increase the tuning range. The EC 686 has three different variants. Each variant has identical RF performance but different control protocol. For this thesis MIPI protocol is chosen as it is well supported by the mobile phone basebands and its control lines are easier to route than the GPIO version. The MIPI standard requires four

control lines  $V_{DD}$ , clock, data, and select. The  $V_{DD}$ , clock, and data lines can be shared with the other MIPI devices. Only the select line has to be device specific if independent control is required. In figure 1.9 the pin layout of the EC 686 QFN-16 package is shown with the description of each pin [14].



Pin Number	Pin Name	Pin Type	Description
1	RFC	Input	RF Common Input
2	RFC	Input	RF Common Input
3	NC	No connect	No internal connection, ground in application
4	GND	Ground	Ground
5	VDD	Power	Power Supply
6	DATA	Input/Output	MIPI Data Input/Output
7	CLK	Input	MIPI Clock Input
8	SEL	Input	Chip Select Input (internal pullup)
9	GND	Ground	Ground
10	NC	No connect	No internal connection, ground in application
11	RFC	Input	RF Common Input
12	RFC	Input	RF Common Input
13	RF4	Output	RF Output 4
14	RF3	Output	RF Output 3
15	RF2	Output	RF Output 2
16	RF1	Output	RF Output 1

Figure 1.9 EC 686 QFN-16 package pin description [14]

In the figure 1.10 the three dimensional (3D) perspective projection of the designed frequency agile filter is presented. The designed filter is a three pole folded combline filter, with three EC 686 SP4T switches to control the each comblines independently. The filter dimensions are 9.5 x 8.3 x 2.4 mm including the switches. The height of the LTCC ceramic block itself is 1.9 mm. As seen from the figure 1.10 the combline filter structure is in two separate layers. This folding of the filter structure shrinks the length of the combline filter to almost half making the filter very compact and thus very suitable for mobile devices. Each resonator is formed by stripline and microstrip line sections connected by vias.

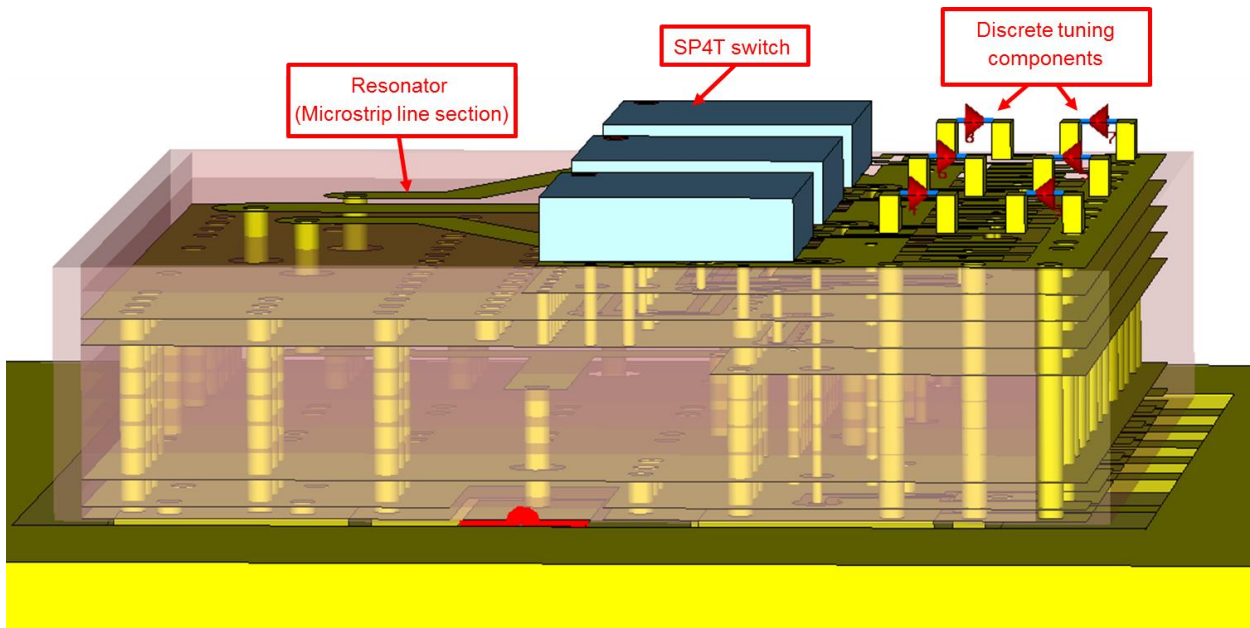


Figure 1.10 Perspective projection of the designed frequency agile filter with three EC868 in CST

In figure 1.11 the ceramic layer stack up of the designed frequency agile filter is shown for the Kyocera GL330 substrate. The ceramic layer 9 (CeL9) is the top ceramic layer of the filter and the three EC 686 RF-switches are positioned on top of ceramic layer 9. The fired layer thickness for layers CeL1 –CeL9 is 0.2 mm whereas the fired thickness of the layer CeL0 is 0.1 mm.

CeL9
CeL8
CeL7
CeL6
CeL5
CeL4
CeL3
CeL2
CeL1
CeL0

Figure 1.11 Ceramic layer stack up of the frequency agile filter

In the figures 1.12 to 1.17 the top view of the metallic layers, hatched in gray color, of each ceramic layer is presented with the ceramic outline starting from the top ceramic layer 9. The red dots represent the metallized vias going through or ending in the specific layer. In figure 1.12 the top metallic layer of the folded combline filter is shown with the three EC 686 and the lumped tuning components, eight per switch. The shared  $V_{DD}$ , data, and clock lines needed for the MIPI protocol are shown in figure 1.14 for  $V_{DD}$  and data (left to right), and for

the clock signal in figure 1.15. As seen from the figures 1.12 to 1.17 the combine structure is fully isolated from the digital control signals to minimize any interference from the digital lines to filter and vice versa. The isolation between the RF- and digital-signals is important. As if not properly shielded the RF signal inserted to the filter can couple to the digital lines and cause interference for the control signals. Especially RF-signal coupling to the clock and data signals can cause corruption of the control signals and in worst case block the control of the switches or make them change their state randomly.

The dashed lines in figures 1.12 a) and 1.17 shows the gold plating areas in the top and bottom copper layers.

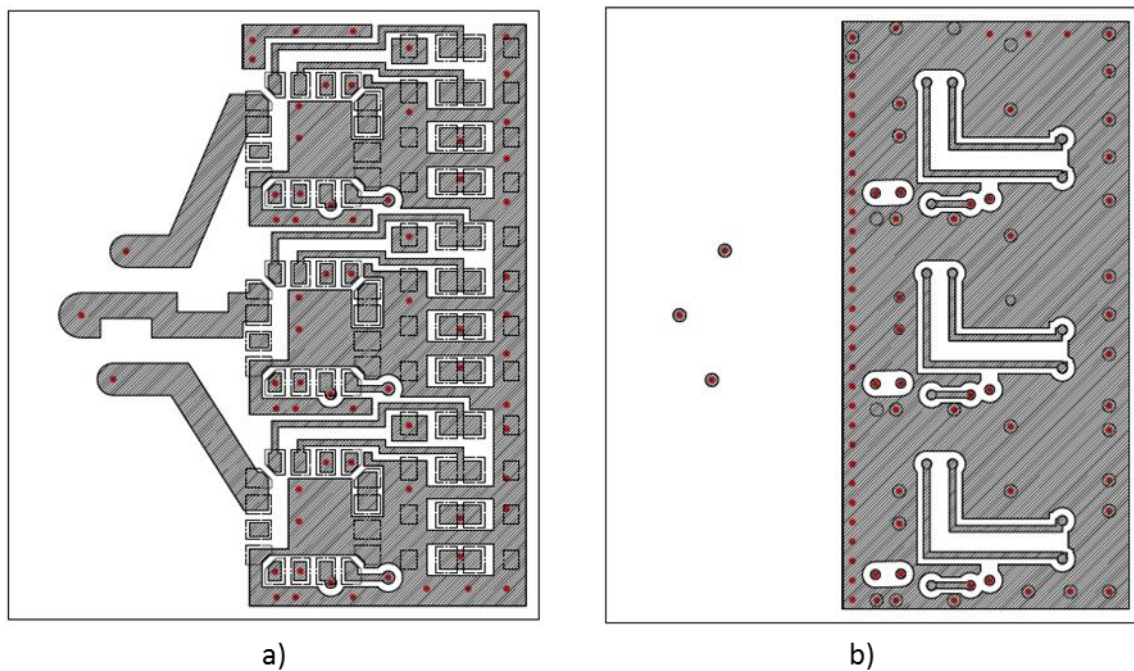


Figure 1.12 The top metallic layers of a) the ceramic layer 9 and b) the ceramic layer 8

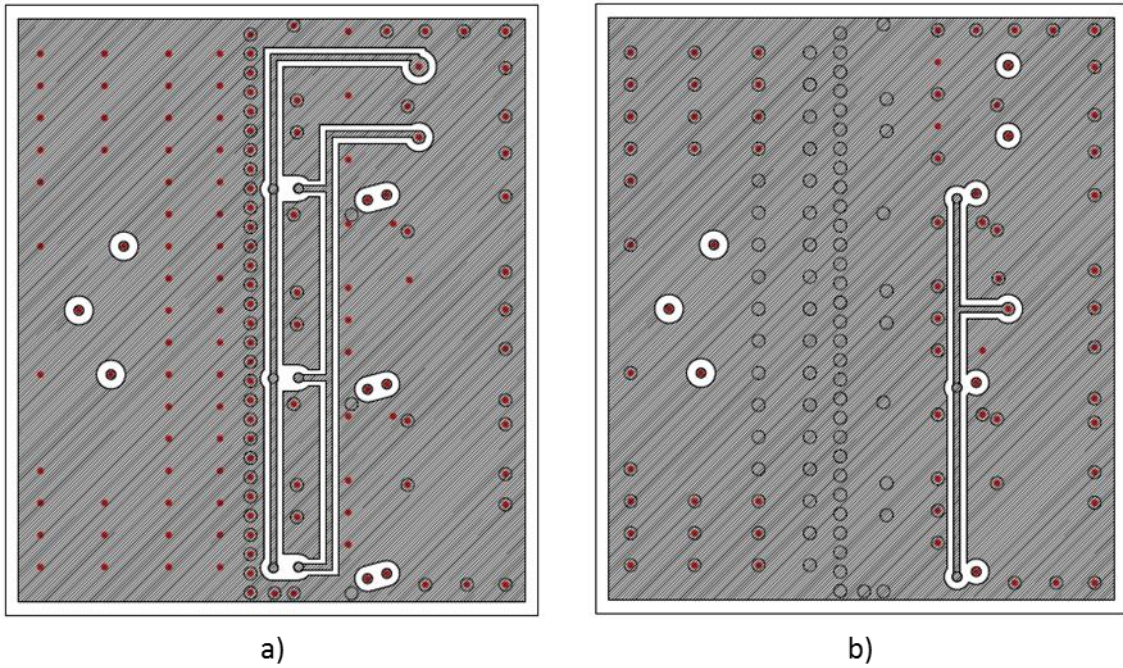


Figure 1.13 The top metallic layers of a) the ceramic layer 7 b) the ceramic layer 6

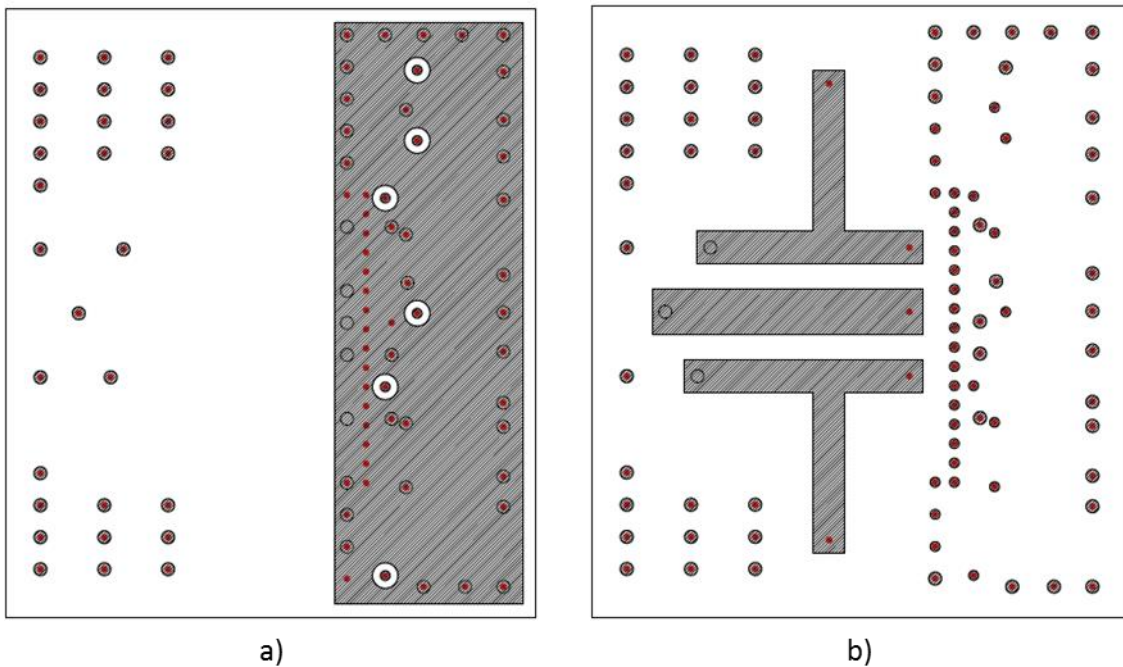


Figure 1.14 The top metallic layers of a) the ceramic layer 5 and b) the ceramic layer 4



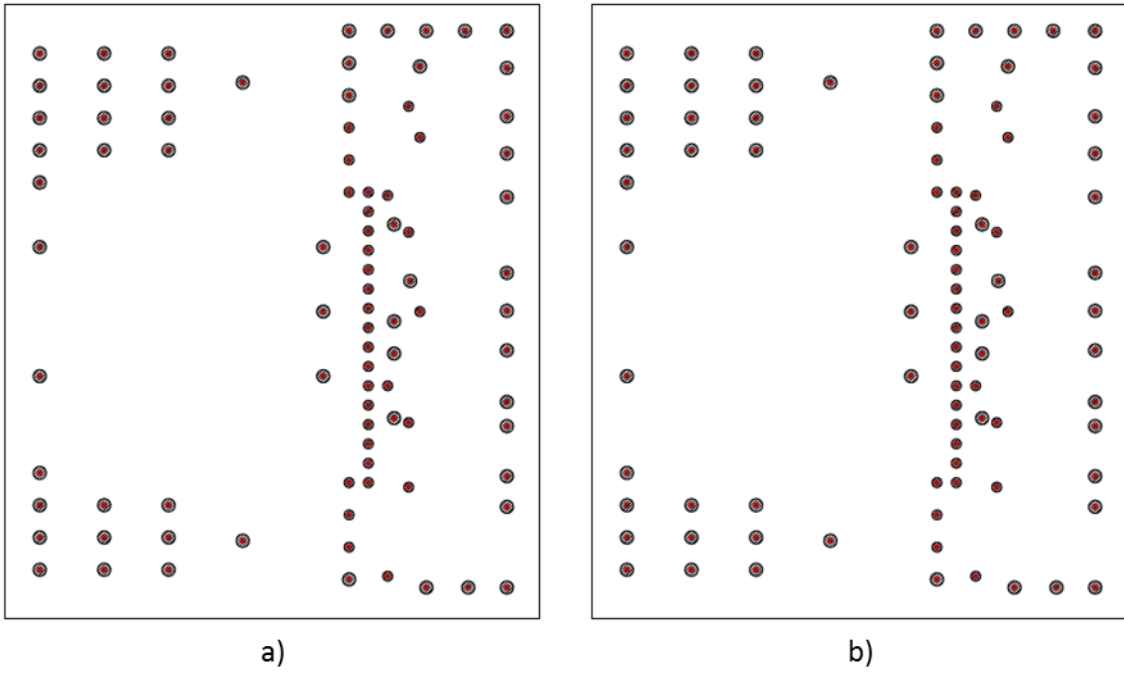


Figure 1.15 The top metallic layers of a) the ceramic layer 3 and b) the ceramic layer 2

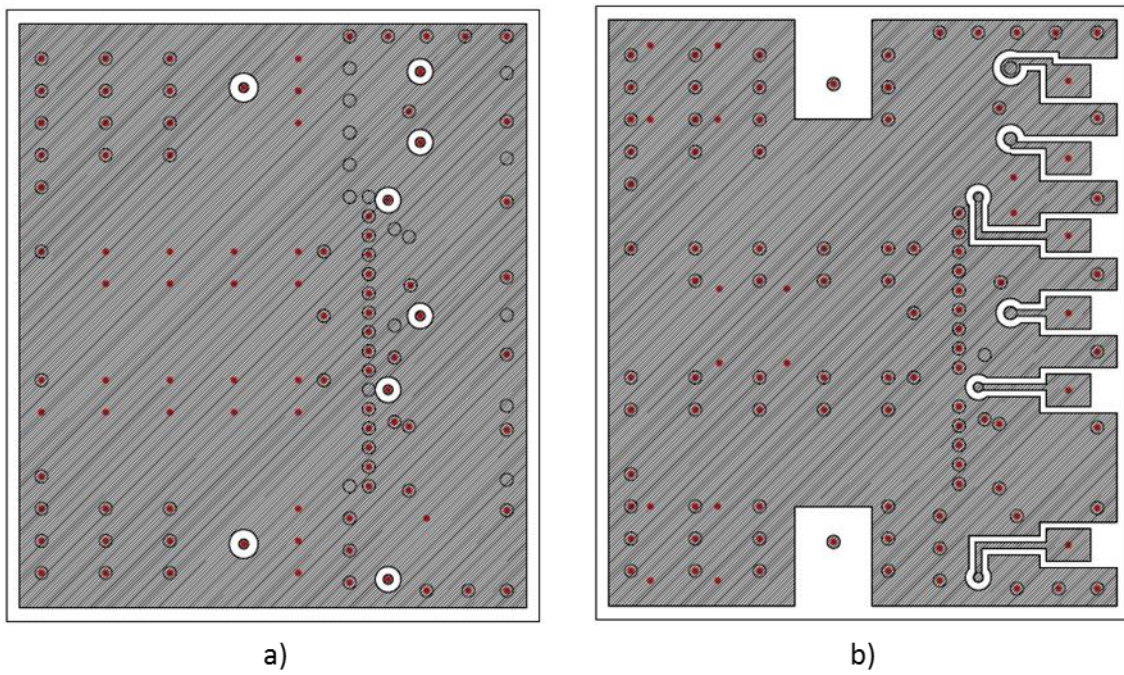


Figure 1.16 The top metallic layers of a) the ceramic layer 1 and b) the ceramic layer 0

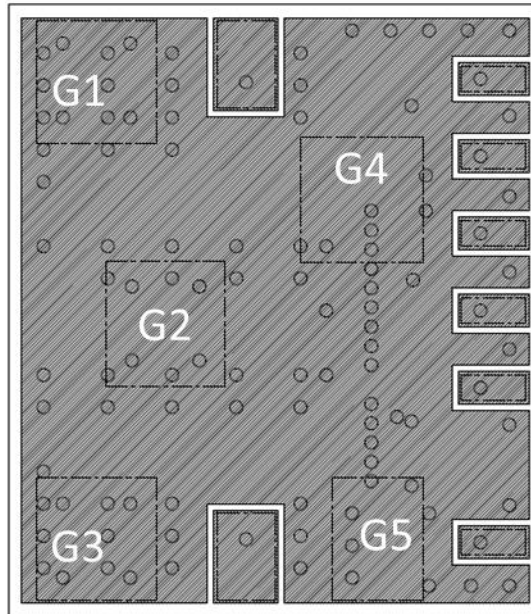


Figure 1.17 The bottom metallic layer of the ceramic layer 0

The center pads on the figure 1.17 are the RF in/out pad of the filter. The pads on the right side of the picture are the control lines for the EC 686, starting from the top to bottom:  $V_{DD}$ , data, select for switch 3, clock, select for switch 2, and select for switch 1. The five larger dashed rectangular areas, denoted by G1-G5, in the figure 1.17 are the locations for grounding areas of the filter to the main PCB.

As seen from the figures 1.10 and 1.12 a), each tuning state of the EC 686 has space for two lumped component, one for capacitive and the second for inductive load. The theoretical analysis for the parallel load for a combline filter has been discussed in the preceding subchapter 1.5.2 and the passband bandwidth control proved in calculations. In the charts 1.6 and 1.7 the effect of the parallel inductor to the bandpass bandwidth is shown. The bandpass bandwidth can be controlled to desired bandwidth with the correct combination of the capacitor and inductor values. Decreasing the inductor value the bandwidth of the filter's bandpass decreases, while the resonance frequency increases. To compensate the increased resonance frequency the capacitance value is increased. From chart 1.7 we can see that adding an ideal inductor parallel to ideal capacitor doesn't change the level of the transmission coefficient.

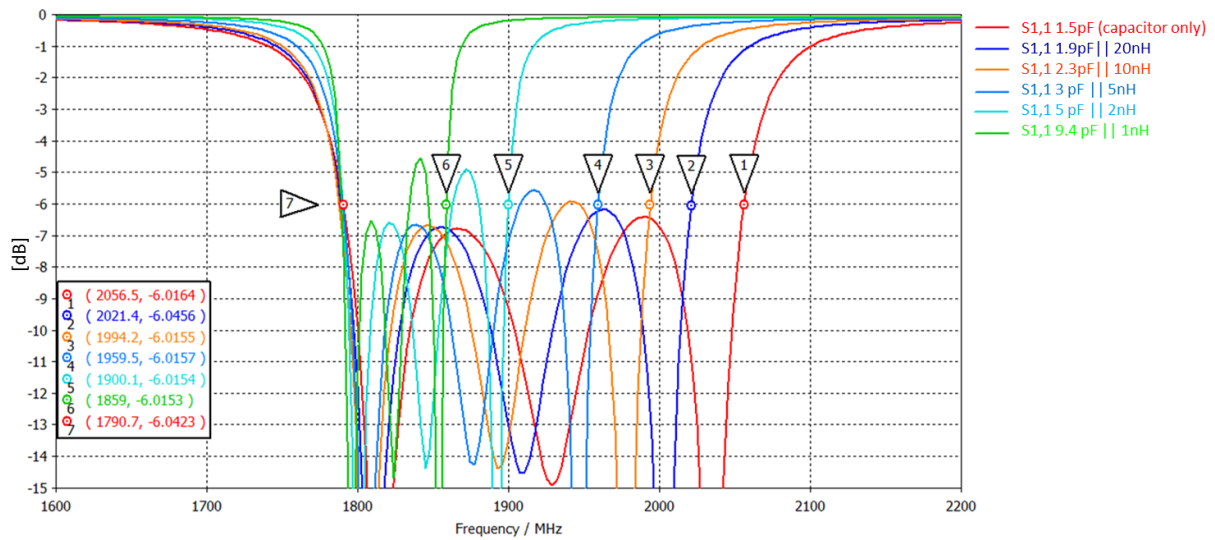


Chart 1.6 Parallel load impact to combine filter bandwidth

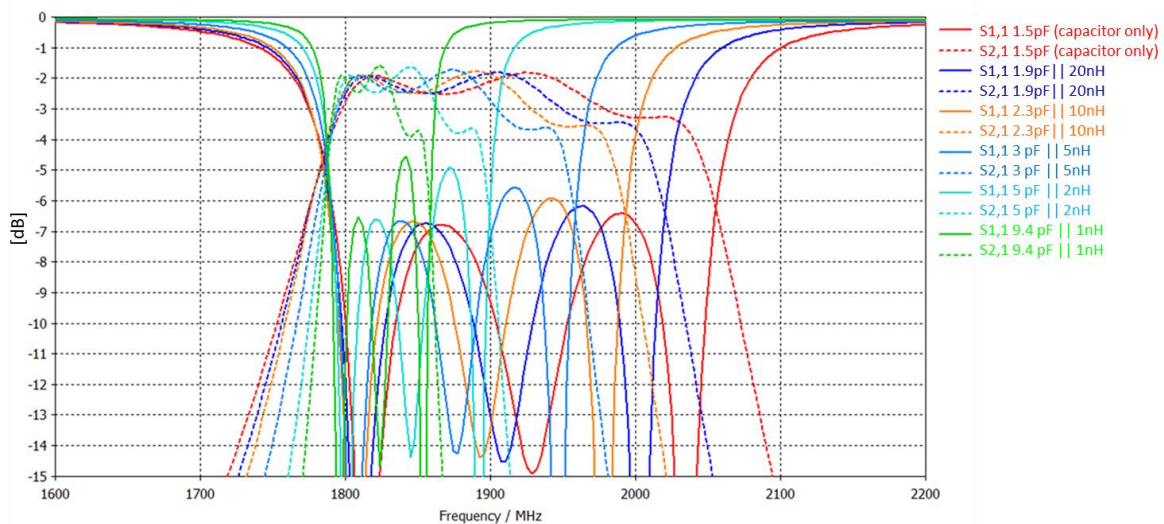


Chart 1.7 Parallel load impact to combine filter bandwidth with transmission response

In chart 1.8 the change of the bandpass bandwidth in different resonant frequencies and the bandwidth compensation with the parallel inductor are shown for filter which mechanical dimensions are optimized for LTE 7. As we can see in the chart 1.8 b) the bandpass bandwidth in GSM 1900 band with capacitance load only is much wider than the needed bandwidth of the Rx band. With the aid of the parallel inductor the bandpass bandwidth can be optimized.

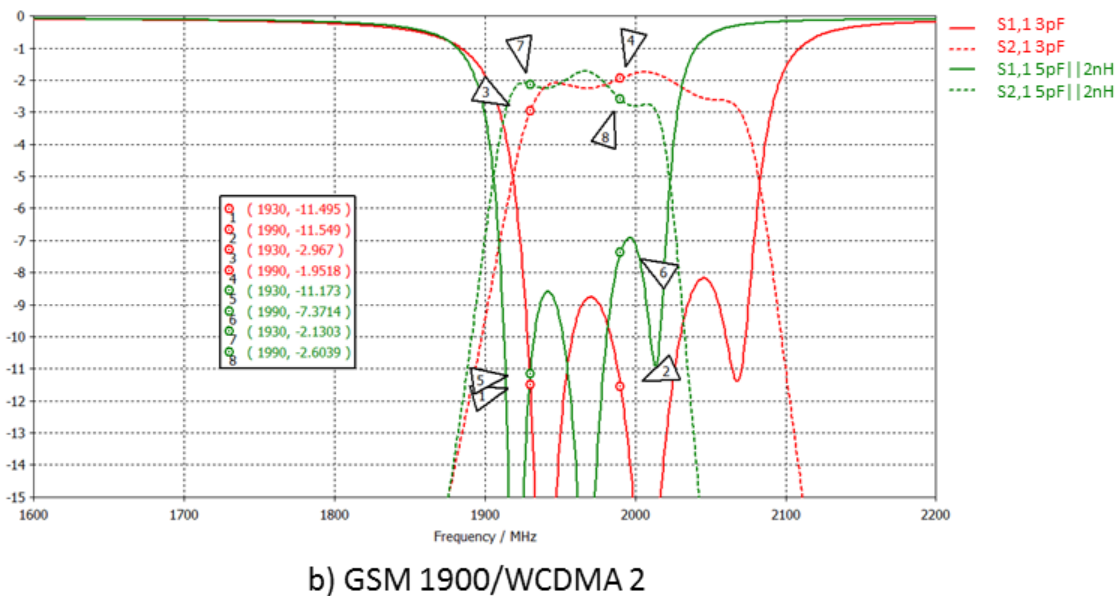
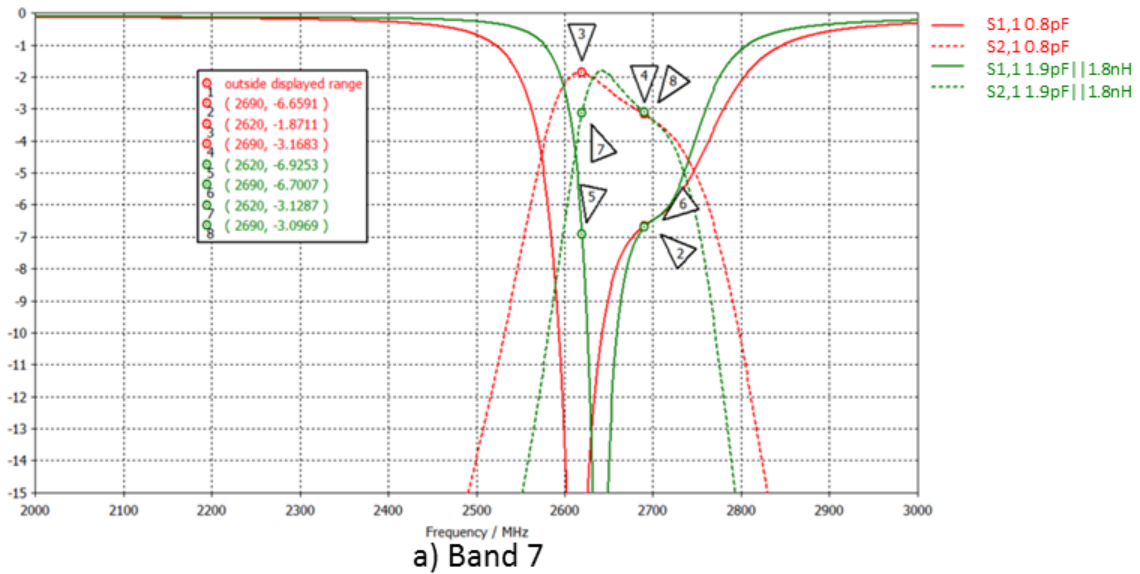


Chart 1.8 Bandpass bandwidth optimization with parallel inductor

So far all the simulation results presented in this thesis are from simulations with ideal switches, without any losses. In reality the CMOS switches have losses due the  $R_{on}$  resistance inherent of the CMOS technology. To be able to predict the real filter performance the  $R_{on}$  resistance has to be included in the simulation model. In the figure 1.18 the filter's updated simulation model of the figure 1.10 is shown with the addition of three extra ports, one port per switch, for modelling the  $R_{on}$  resistance of the CMOS switches. For a conventional combine filter these ports would not have been necessary to add to the model as the  $R_{on}$  resistance could have been added in series with the capacitor in the CST circuit simulator. But in the case of the parallel inductor load the  $R_{on}$  resistance is difficult to model in

the circuit simulator and thus the extra ports are necessary. These extra ports increase slightly the simulation time, as the port number increase from 8 to 11.

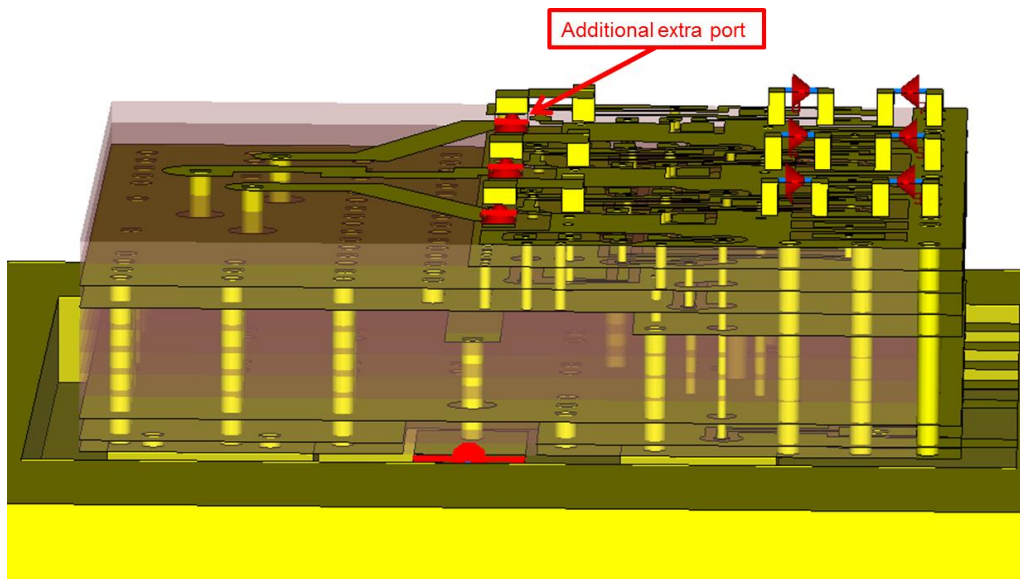


Figure 1.18 The updated filter CST model to take in account the CMOS  $R_{on}$  resistance

The addition of the extra port per switch has only very small effect to the filter's performance as seen from the chart 1.9. The filter's resonance has shifted slightly lower and the filter passband bandwidth slightly decreased.

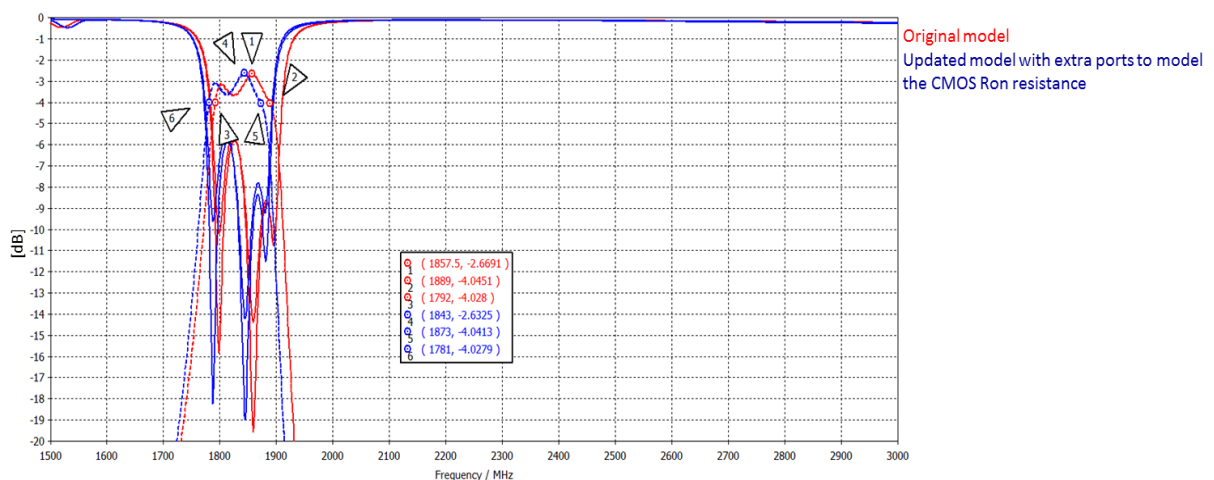


Chart 1.9 Verification of the  $R_{on}$  simulation model

The  $R_{on}$  resistance of the EC 686 RF-switch used in this thesis is  $0.9 \Omega$ , which is state of the art figure for CMOS RF-switches [14]. Even though the RF switch resistance is very low it has a big effect to the filter's performance. As shown in the chart 1.10 the resistance has a big value on the insertion loss, especially in the lower frequencies of the frequency band in interest. In the charts 1.10 a) and b), for states of GSM 1800 and GSM 1900 respectively, the insertion loss increases 2 to 2.5 dB compared to the ideal switch. In the higher frequencies the effect of the  $R_{on}$  resistance is less significant, and the losses due the switch reduce only to 0.5 dB at LTE 7.

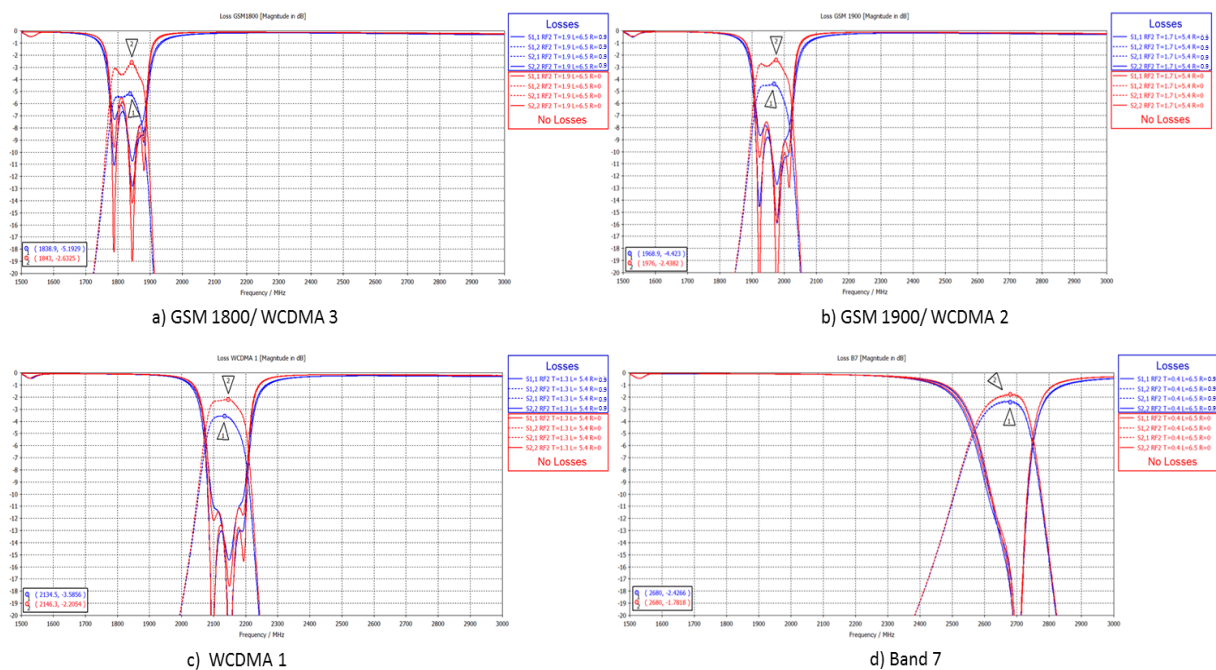
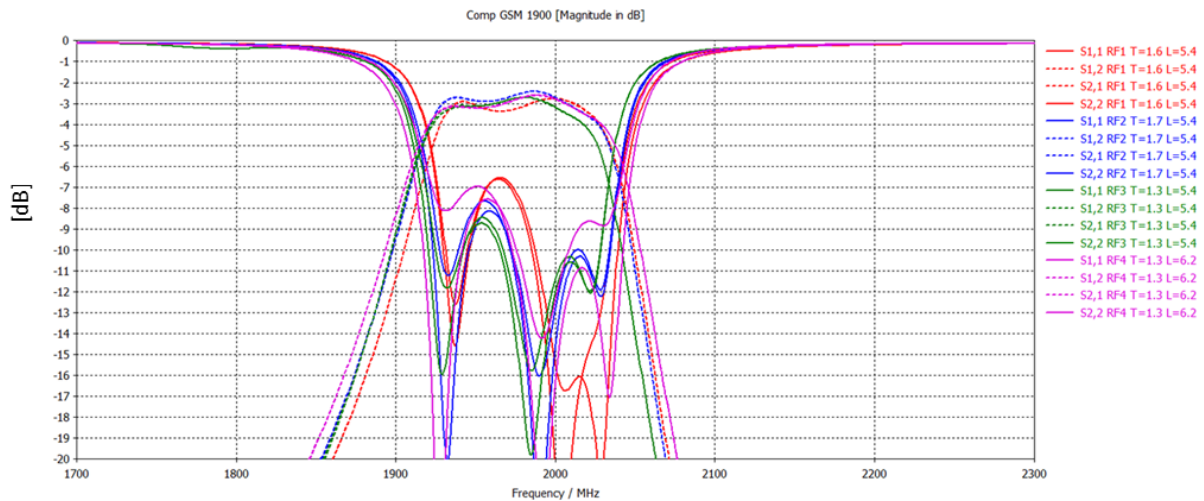


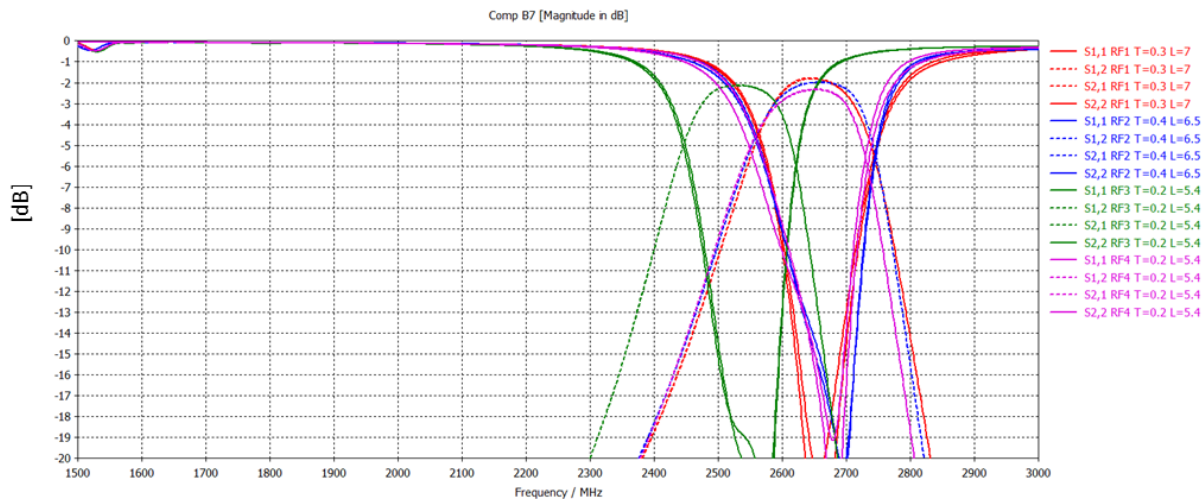
Chart 1.10 The CMOS switch  $R_{on}$  effect to the filter's insertion loss (in dB)

The last verification before the LTCC block can be manufactured is to verify which RF-state of the EC 686 is used for which communication band. From the figures 1.10 and 1.11 we can notice that the transmission lines from the RF-states RF1 and RF2 (figure 1.9) to the parallel tuning loads are routed only on the top metal layer whereas for the transmission lines from the states RF3 and RF4 are routed between the metal layers 7 and 9. The unequal lengths from the RF-switch to the parallel tuning load common pads on each path have an impact to the filter performance. Different values of capacitance and inductance are needed to compensate the length difference. This is visualized in the chart 1.11 where the all the RF-paths are simulated for two communication bands, GSM 1900 in chart a), and LTE 7 in chart b). In the charts the "T" denotes the capacitance in pF and "L" the inductance in nH for each parallel load. From the chart 1.11 a) we can see that to be able to tune the filter's resonance to correct frequency, different capacitance values are needed for the four different paths. The

highest capacitance value is for the RF2-path which has the shortest line and the smallest for the two longest lines, which travels inside the ceramic substrate between metal layers 7 and 9. Noteworthy is the inductance value of RF-path four, where higher inductance value is needed compared to other paths to have large enough bandwidth to support the selected communication protocol. In chart 1.11 b) the importance of verifying the RF-paths performances is well illustrated. Not all the paths are suitable for the highest supported frequency band. The length of the RF3 path is too long to be able to cover the LTE 7 Rx band with the smallest capacitor value available in 0603 (metric) size.



a) GSM 1900



b) Band 7

Chart 1.11 RF-path effect to filter's resonance frequency. Where T denotes the capacitance in pF and L the inductance in nH for each parallel load

In chart 1.12 all the four states with their dedicated RF-paths of the figure 1.18 filter are shown in one chart with the adjacent band isolation marked with the markers. The designed frequency agile filter covers all the four communication bands Rx bands set in the requirements, presented in table 1.2. The insertion loss of the low three lowest state of the filter, with the simulated RF switch losses, are clearly greater than the 1.5 dB set in table 1.1. Only the highest state of the filter has insertion loss which is less than 3 dB. Although the RF performance (insertion loss and band rejection) of the frequency agile filter does not achieve the level of the state of the art SAW/BAW filters, the simulated performance is in acceptable level when taking account that the this simulation model takes in account the switch losses and with this filter several filters and RF switches can be replaced by single component.

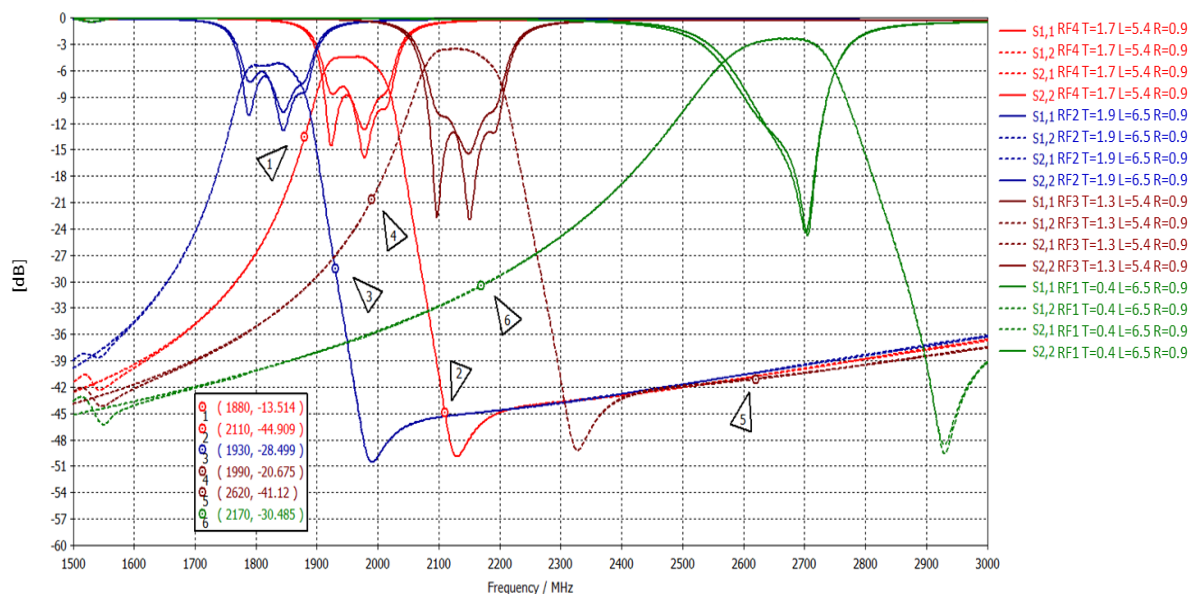
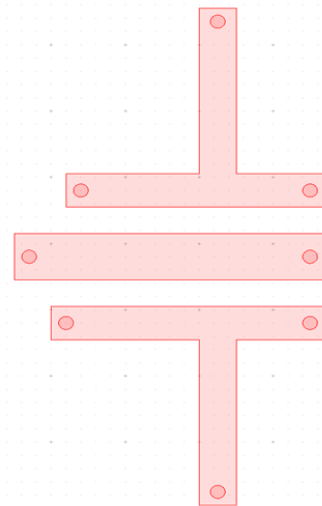


Chart 1.12 All the filter states simulated with their optimized RF-path, where T and L are the parallel load capacitance in pF and inductance in nH, respectively. And the R is the  $R_{ON}$  resistance of the RF switch in  $\Omega$



Table 1.13 Final mechanical dimensions of the simulated filter

Final Filter dimensions	
Resonator spacing	0.4 mm
Edge resonator length	7.8 mm
Feed location (d)	1.03 mm
Center resonator length	8.1 mm
Height (without EC 686)	1.9 mm
Width	8.3 mm
Length	9.7 mm



### I.7 Combine filter measurements

After the filter is designed and optimized in electro-magnetic simulation the ceramic block of the filter is manufactured. In figure 1.19 the top, side, and bottom views of the manufactured LTCC block are shown without the RF-switches and the tuning components. In figure 1.21 a) the gold-plated landing patterns of the three EC 686 switches and their respected tuning components shown where as in figure 1.19 c) the gold plated feed and control pads with five larger grounding pads are shown (G1-G5). The dimensions of the manufactured LTCC block are exactly same as in the EM-simulations (9.5 x 8.3 x 1.9 mm).

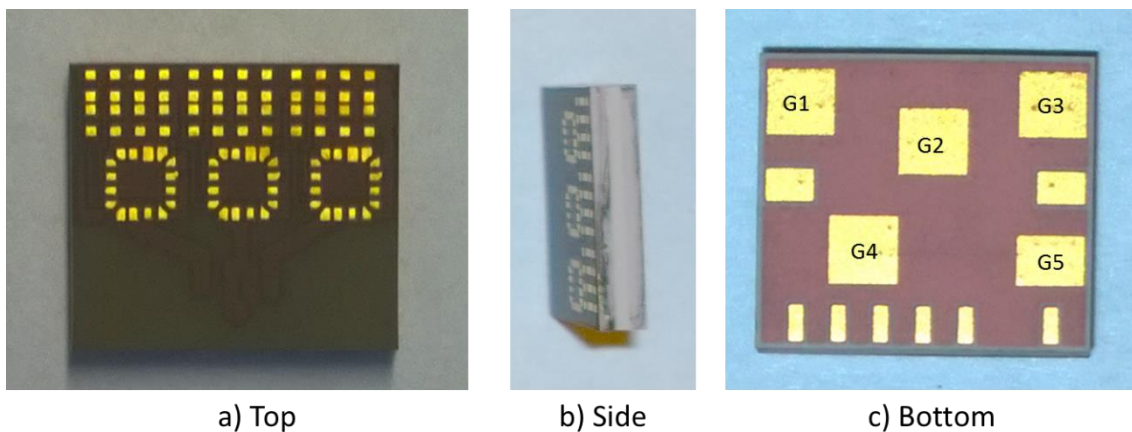


Figure 1.19 The manufactured LTCC block for the frequency agile combine filter

To be able to measure the filter's performance an evaluation PCB is also designed and manufactured. The figure 1.20 illustrates the evaluation PCB, made from a common FR-4

substrate, without the filter and the connectors. The control lines on the top of the PCB are connected to computer through a control PCB, shown in the figure 1.21 on left with the control lines to the evaluation PCB, which enable the control of the three EC 686 MIPI switches through USB port on the computer. The two RF-lines connected to the input/output pins of the filter have SMA-connectors on the edge of the evaluation PCB to be able to connect filter to the VNA for the measurements.

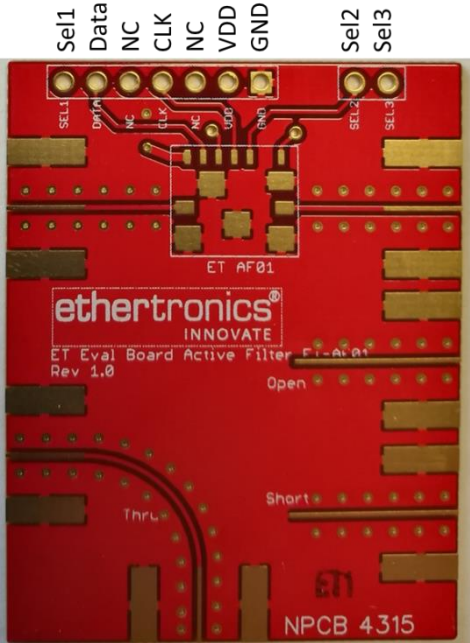


Figure 1.20 The evaluation board for the filter measurements

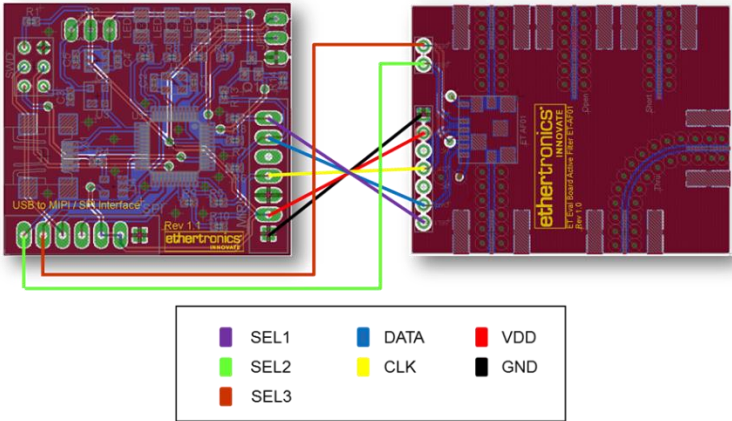


Figure 1.21 The control PCB and the connections to the evaluation PCB

The control of the EC 686 is done with Ethertronics proprietary software which translates the USB series commands to MIPI commands through the control PCB. In figure 1.22 the view of the control software is shown with the RF-switch and RF-state selections highlighted. To set

the RF-state of a switch, the switch to be programmed is selected first from the switch selection dropdown menu. Then the wanted RF-state(s) are activated and the “Apply Config” button is clicked to send the command to switch.

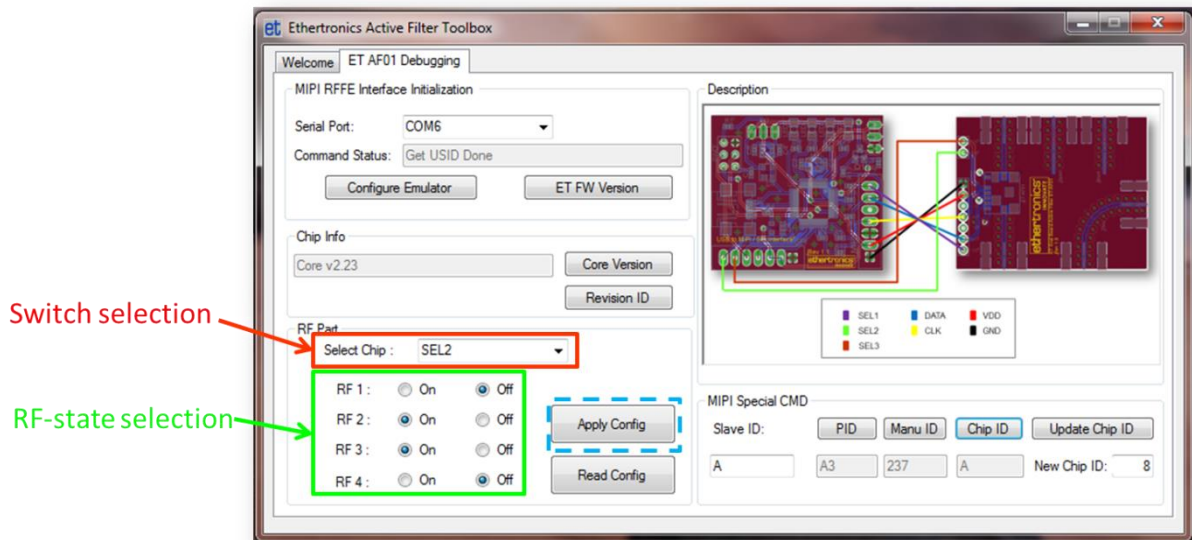


Figure 1.22 The view of the control software for controlling the MIPI switches from computer

The first measurement of the active filter is done with the fully populated LTCC block, shown in the figure 1.23, the tuning capacitors are Murata’s 0603 (metric, 0201 in inch) size high-Q GJM series, and the tuning inductors are Murata’s high-Q LQW series also in 0603 (metric) size. The connector for the select control cables is soldered on the back side of the evaluation PCB.

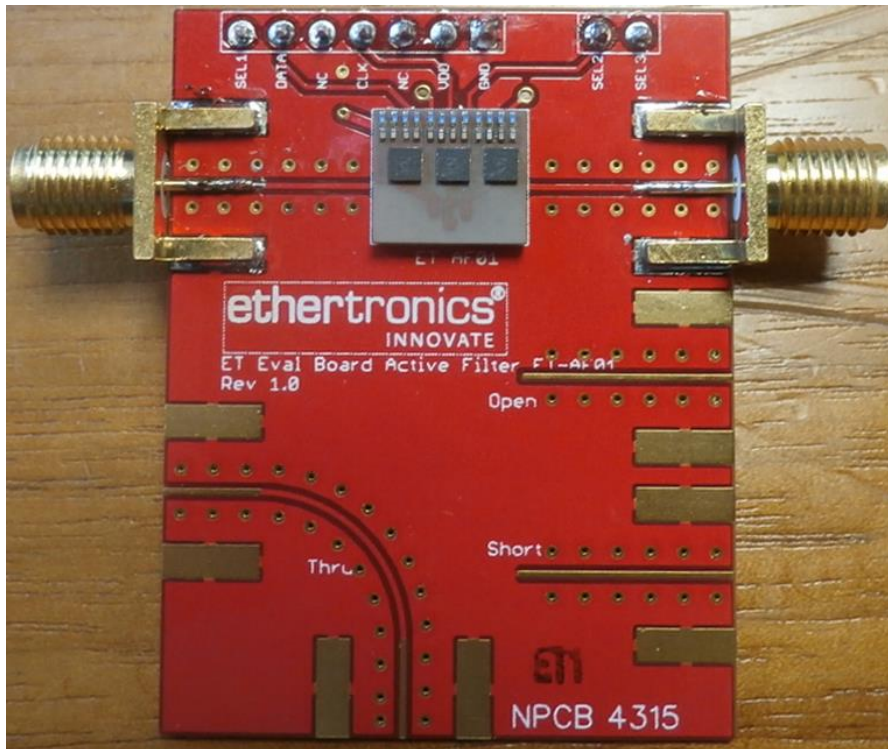
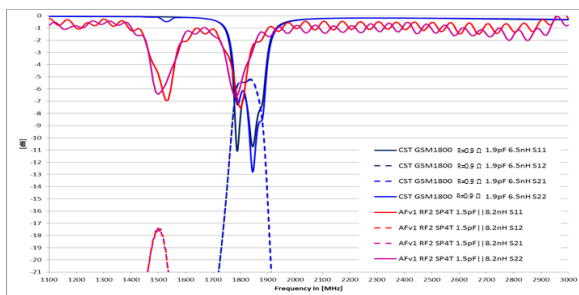


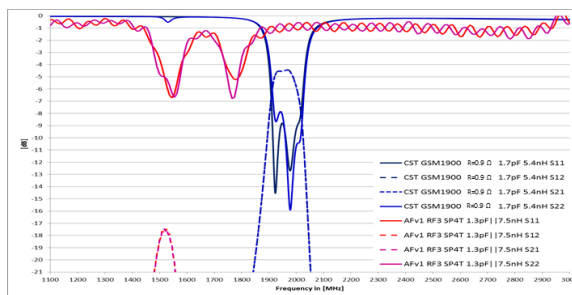
Figure 1.23 The tunable filter on the evaluation board with three EC 686

In chart 1.13 the measured states of the LTCC block are compared to the CST simulations model with the  $0.9 \Omega$  resistor for simulating the RF-switch  $R_{on}$  resistance and with ideal components (capacitor and inductor). The simulations under CST also take into account the metallic and dielectric losses of the distributed structure. The blue lines in the charts 1.13 are the simulated results and the red lines are the measured results. The dashed lines are the insertion loss of the filter. As we can see from the results of the chart 1.13 the measured results do not correlate at all with the simulated filter. The measured filter's responses do not shift in frequency as in the simulations and practically stays in same center frequency in all switch states. This is more clearly illustrated in the chart 1.14 where all the four states of the filter are plotted to single chart. In addition to the loss of tunability also the losses of the switch have increased greatly, from simulated -5 dB to -17 dB rendering the filter to useless. The ripples in the measurement results in reflection coefficient are probably due to calibration problem with the VNA used in these measurements and/or discontinuities related to assemble the filter on evaluation board.

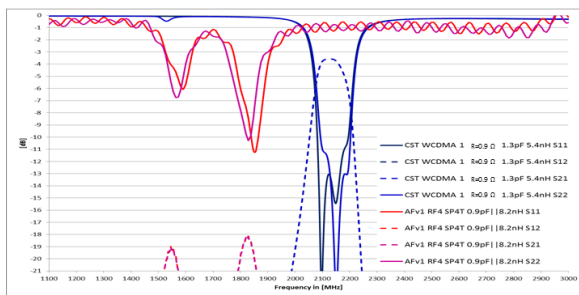
At first, to understand better why the filter center frequency is not changing while the tuning load is modified, two tests are carried out. The two most novel features of this frequency agile filter are the use of parallel load tuning with inductor and the use of the commercial SP4T RF-switches. Although the inductive load parallel with the more conventional capacitive load did not have any effect to the filter's tunability, the use of the inductive load has been never tested before for the best knowledge of the author. The first test is to remove the inductors in the tuning circuitry to recover the tunability.



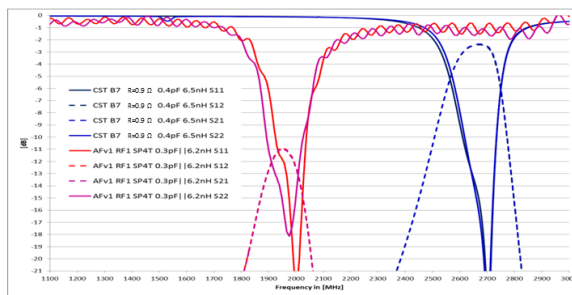
a) GSM 1800/WCDMA 3



b) GSM 1900/WCDMA 2



c) WCDMA 1



d) Band 7

Chart 1.13 CST simulations versus measurements of the frequency agile filter

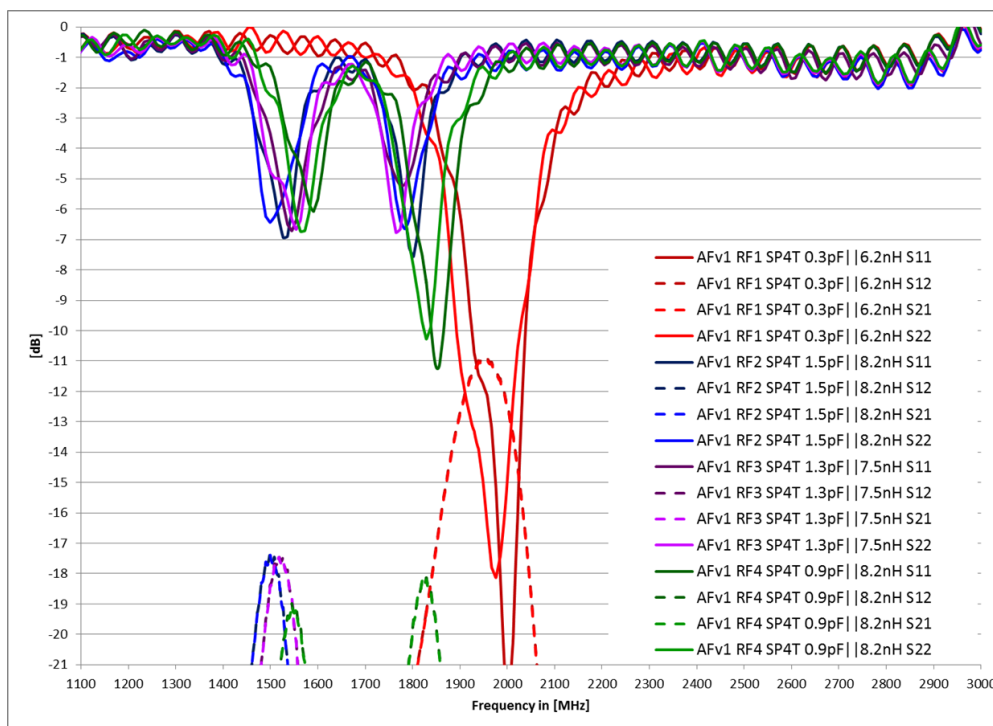


Chart 1.14 All the RF-states of the measured filter

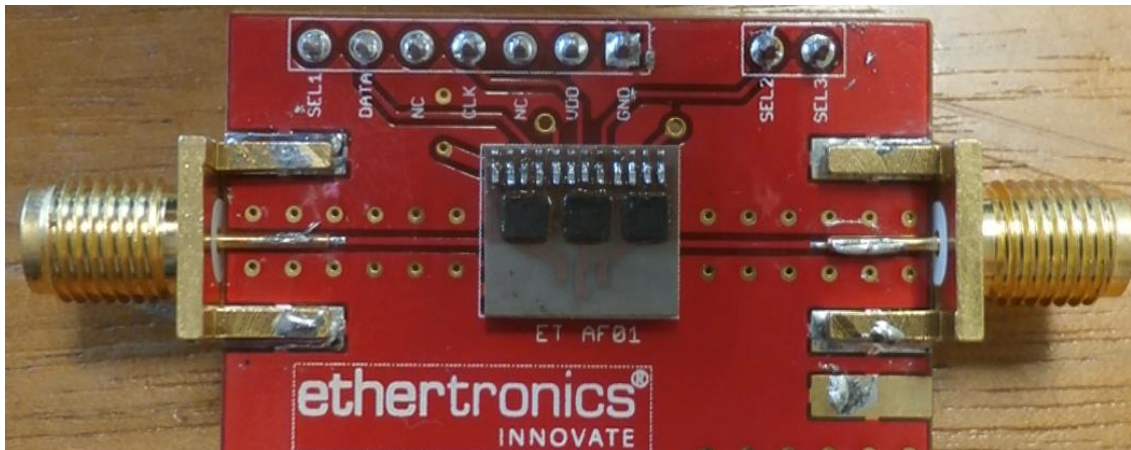


Figure 1.24 Frequency agile filter with only capacitive tuning loads with the EC 686 switches

In figure 1.24 the test setup for the only capacitive load is shown. The inductors are removed from the LTCC block and capacitor values are adjusted so that the filter's center frequency is close the original frequency. In chart 1.15 the results of the non-inductor test are shown. As the inductive load tunes the resonance frequency higher only two states are shown as 0.1 pF capacitor is the smallest commercially available in 0603 size (metric).

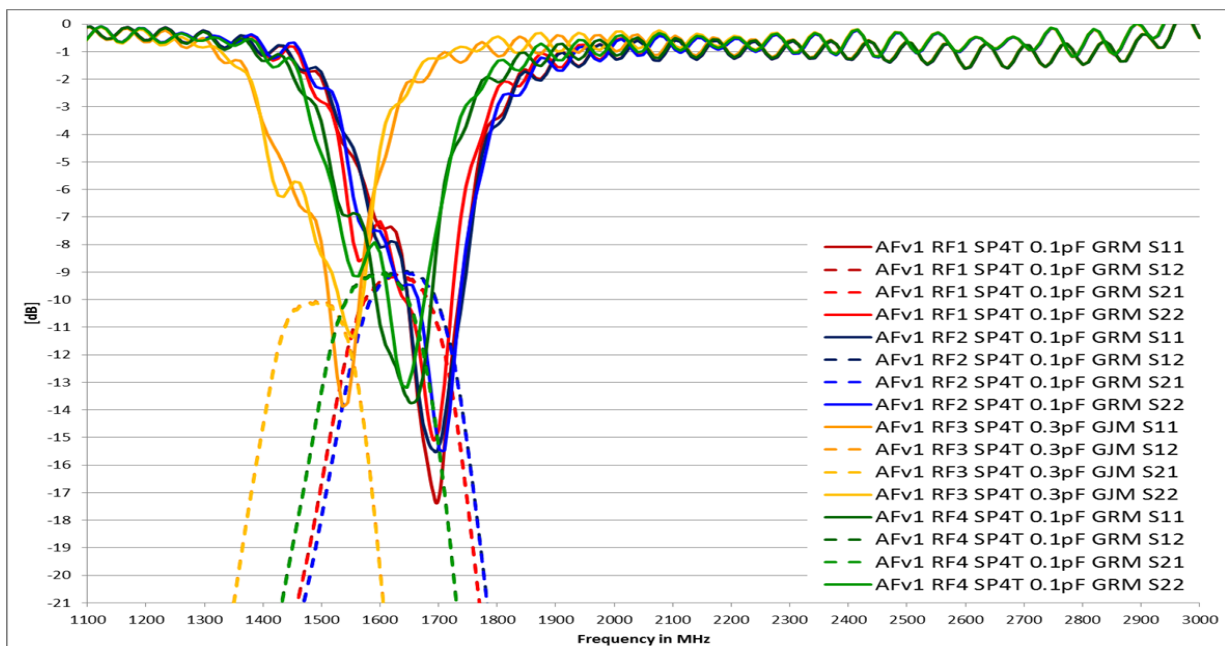


Chart 1.15 Measured filter performance without the inductive load

Removing the inductor from the tuning circuitry doesn't fix the tunability issue of the filter but does improve the insertion loss of the filter. Based on this test the inductive load parallel with the capacitive load induces losses which were not induced in the EM-simulations. To verify

the findings the second novelty of this filter, the SP4T switch, is removed and the filter is measured with and without the parallel inductive load.

To be able to connect the tuning circuitry to the combine filter without the SP4T switch a  $0\ \Omega$  resistor is soldered between the switch common/input RF-pins (pins 1&2, see figure 1.9) and the RF1 path (pin 16, see figure 1.9) as shown in the figure 1.25. Only the RF1-path can be tested with this configuration as the size of the  $0\ \Omega$  resistor does not permit to connect the other RF-paths to the switch RF input pins. This doesn't pose a problem for testing the different bands as the RF1-path has similar performance in the lower and higher frequency in interest as shown previously in chart 1.11. The selection of the filter resonance frequencies are done by manually soldering the new capacitors and inductors values to the load circuit pads on the RF1 path.

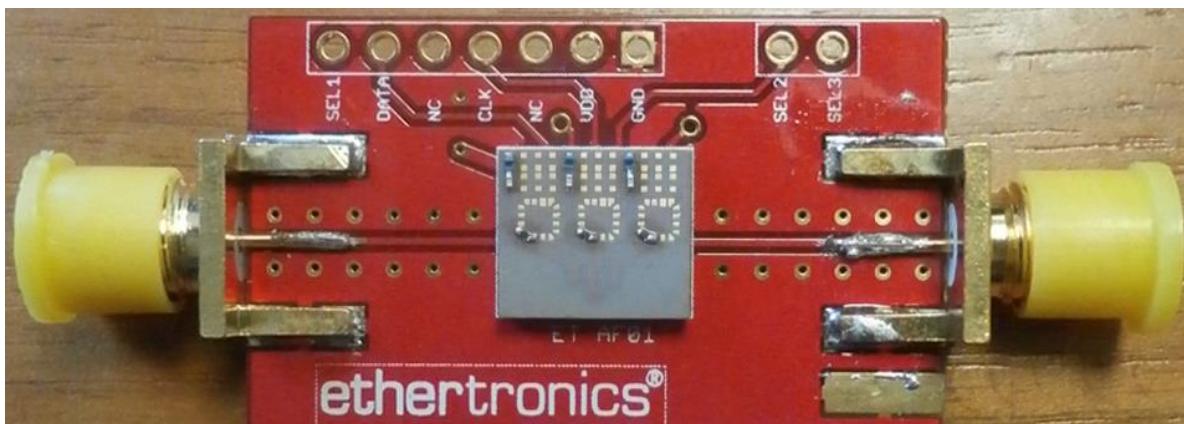


Figure 1.25 Frequency agile filter without the EC 686

In chart 1.16 the results of the filter with the RF-switch replaced with the  $0\ \Omega$  are shown. The tunability of the filter is recovered when the SP4T switch is replaced with the  $0\ \Omega$  resistor. Although the tunability is recovered the losses of the filter are still 3-4 dB higher compared to the results of the EM-simulation model without the  $R_{on}$  resistance. These results indicate that both the parallel inductor and the SP4T switch induce more losses to the filter than anticipated with the EM-simulations. Also the results indicate that the use of the SP4T switch is the root cause for the loss of the tunability of the filter.

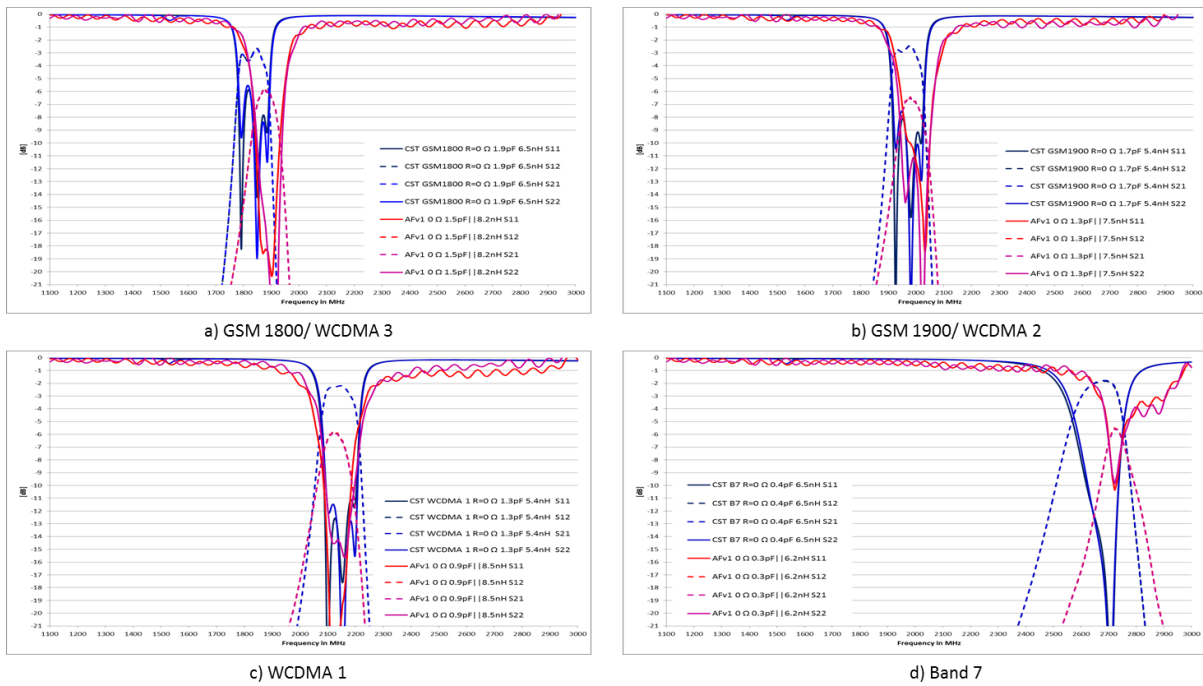


Chart 1.16 Measured performance of frequency agile filter without the three EC 686

To verify if the 3-4 dB higher insertion losses without the switch are due inductor, rather than the LTCC ceramic substrate itself, the inductive loads of the filters without the switch are removed and the filter performance is re-measured only with the capacitive load. As with the case of the only capacitive load with the SP4T switch the capacitance values are adjusted so that the filter center frequencies are in the middle frequencies of the communication bands in interests. In figure 1.26 the test setup for the non-inductive load filter is shown.

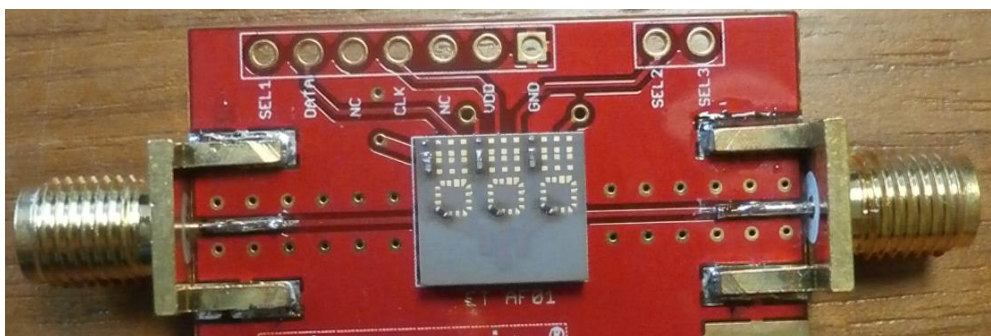


Figure 1.26 Frequency agile filter without the RF-switches and inductive loads

In the chart 1.17 the results of the filter without the parallel inductive load and the RF-switch are shown. Without the inductors and the switch the measured insertion losses are superior 1 dB to those simulated on the GSM1800/GSM1900/WCDMA1 bands. The LTE 7 center



frequency of the measured filter is lower compared to the simulated filter. This is due the missing inductive load which tunes the center frequency higher as shown in chart 1.7. The 0.1 pF is the smallest commercially available capacitor from Murata in 0603 (metric) size and the center frequency cannot be tuned higher without changing the length of the combine transmission lines inside the ceramic substrate. Comparing the measurement results in charts 1.16 and 1.17 the inductive load effect to the bandwidth of the filter can be verified now also in measurements in addition to the EM-simulations.

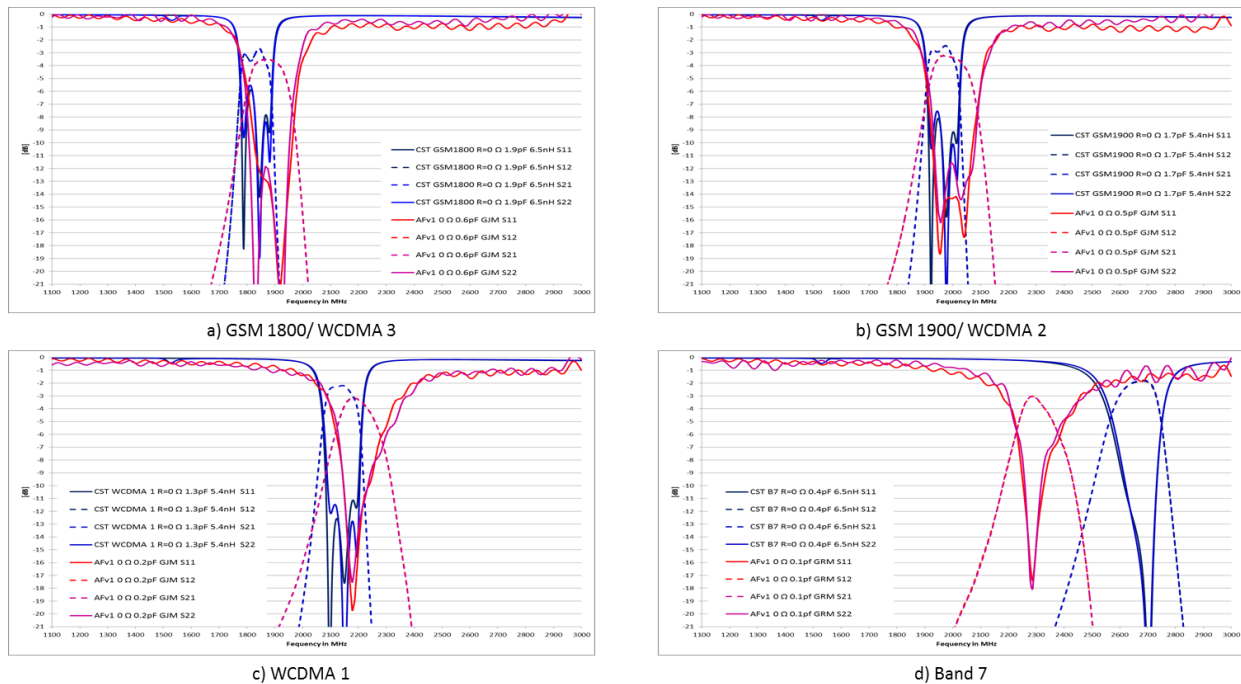


Chart 1.17 Measured performance of frequency agile filter without the three EC 686 and the inductive loads

The effects of the parallel inductor and the RF-SP4T switch were not successfully modelled in the EM-simulations. The RF-switch was modelled in the EM-simulation tool as well as it was reasonable without the real physical model of the CMOS die of the switch. The full layout of the switch landing-pattern with the transmission lines from the switch to the tuning components were included and optimized for the filter in the simulations. The only more accurate model would have been including the real physical model of the switch inside the EM-simulation tool instead of the resistor to simulate the  $R_{ON}$  resistance. Unfortunately it isn't possible to model the behavior of FET transistors inside the 3D EM-simulation tool and the switch physical model in general is not feasible to simulate due the extremely small details inside the CMOS die, in range of nm, without a super computer. For these simulations also no link between the EM-simulation tool and RFIC design tool was available due to licensing problems during the design of the frequency agile filter. Also the benefits of the link between the two simulation tools are not clear. The software link from the RFIC-software doesn't

necessarily give information needed to the EM-simulator, how the channel in the FET transistor behave when RF-signal pass through the transistors, rather than just modelling the losses of the transistor(s).

The amount of losses induced by the parallel inductor load was more unexpected for the author than the effects of the CMOS switch to the tunability of the filter. As both the capacitive and inductive loads were modelled as an independent port inside the 3D EM-simulation tool the effects of the parallel resonator to the filter performance should have been able to correctly modelled in the circuit simulator. The use of ideal components was the main root cause for this discrepancy. It was assumed during the CST simulations that the  $R_{ON}$  of the CMOS would be the main contributor to the losses and the losses of the high-Q lumped components would be negligible. This assumption was proven wrong in the measurements of the prototype filter. After the prototype measurements the filter was simulated once again with the realistic lossy capacitors and inductors (Q-values from muRata webpage [29]) to confirm the findings of the prototype filter measurements. In chart 1.18 the GSM 1800 transmission response is shown both with ideal and realistic components. As we can see from the results the inductor induces most of the losses of the parallel load circuit, close to losses of the switch itself. Thus it is important in future parallel load tuning circuits to take account the inductor losses in the simulations.

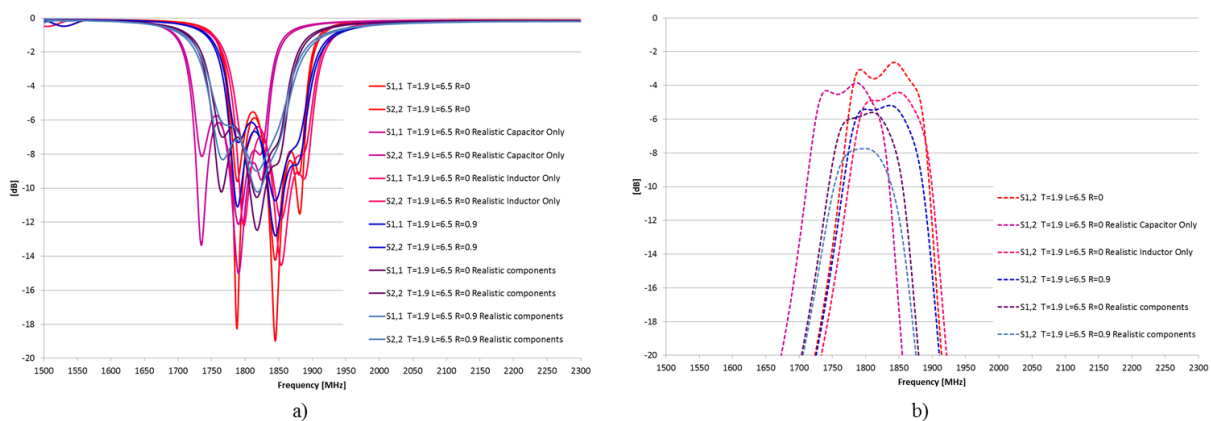


Chart 1.18 Simulation comparison of ideal and realistic lossy (with realistic Q-values) components effect to filter performance a) return loss and b) insertion loss

## **I.8 Conclusions**

It has been shown through the theoretical study and electromagnetic simulations that it is possible to produce frequency agile filters with the possibility of adjusting both the center frequency and the bandwidth simultaneously. The proposed solution is based on the use of parallel resonator load on the combline filter. A combline filter has been realized and tested with a commercial CMOS SP4T RF switch as a tuning element. The responses obtained in measurements show the need to take into account the losses of the localized elements and all the elements of the equivalent diagram of the switch in the optimization of the filter.

## References:

- [1] Sang-June Park "High-Performance RF-MEMS Tunable Filters" Dissertation for Doctor of Philosophy in electronic engineering, University of Michigan, 2003.
- [2] P. Jarry and J. Beneat, "Advanced design techniques and realizations of Microwave and RF filters", John Wiley & Sons, 2008.
- [3] H. Joshi, H. H. Sigmarsson, D Peroulis, W. J. Chappel, "Highly Loaded Evanescent Cavities for Widely Tunable High-Q Filters", IEEE/MTT-S International Microwave Symposium, 2007.
- [4] W. Gautier, A. Stehle, B. Schoenlinner, V. Ziegler, U. Prechtel, W. Menzel, "RF-MEMS Tunable Filters on Low-Loss LTCC Substrate for UAV Data-Link", IEEE European Microwave Integrated Circuits Conference (EuMIC), 2009.
- [5] B. Schulte, V. Ziegler, B. Schoenlinner, U. PRechtel, H. Schumacher, "RF-MEMS Tunable Evanescent Mode Cavity Filter in LTCC Technology at Ku-Band", IEEE 6th European Microwave Integrated Circuit Conference, 2011.
- [6] T. Ogami, M. Tani, K. Ikada, H. Kando, T. Wada, H. Obiya, M. Koshino, M. Kawashima, N. Nakajima, "A New Tunable Filter Using Love Wave Resonators for Reconfigurable RF", IEEE MTT-S International Microwave Symposium, 2014.
- [7] CH. ko, K. M.J. Ho, R. Gaddi, and G. M. Reibeiz, "A 1.5 to 2.5 GHz Tunable 4-Pole Filter Using Commercial High Reliability 5-Bit RF MEMS Capacitors", IEEE MTT-S International Microwave Symposium Digest, 2013.
- [8] X. Mi, O. Toyoda, S. Ueda, F. Nakazawa, "Miniaturized Microwave Tunable Bandpass Filters on High-k LTCC with Integrated Resistive Vias as Bias-T", IEEE MTT-S International Microwave Symposium, 2011.
- [9] A. Othman, R. Barrak, M. Mabrouk, "A Tunable RF Filter For Multistandard GSM/UMTS/WiFi/LTE Receiver", Proceedings of 2014 Mediterranean Microwave Symposium (MMS2014), 2014.
- [10] M. A. El-Tanani, G.M. Reibeiz, "High-Performance 1.5–2.5-GHz RF-MEMS Tunable Filters for Wireless Applications", IEEE Transactions on Microwave Theory and Techniques, Vol. 56, 2011.
- [11] T. Jia, J. Ye, Z. Liu, "A RF-MEMS based dual-band tunable filter with independently controllable passbands", 12th IEEE International Conference on Solid-State and Integrated Circuit Technology (ICSICT), 2014.

- [12] V.M. Srivastava, G. Singh, "MOSFET Technologies for Double-Pole Four-Throw Radio-Frequency Switch", Springer, 2014.
- [13] G.M. Rebeiz, et al, "Tuning in to RF MEMS", IEEE Microwave magazine, October, 2009.
- [14] Ethertronics EC 868 Etherchip data sheet, 2016.
- [15] A. Tombak, M. S. Carroll, D. C. Kerr, J.-B. Pierres, E. Spears, "Design of High-Order Switches for Multimode Applications on a Silicon-on-Insulator Technology", IEEE Transactions on Microwave Theory and Techniques, 2013.
- [16] X. J. Li and Y. P. Zhang "Flipping the CMOS Switch" IEEE Microwave Magazine, February 2010.
- [17] H. Birol, "Fabrication of Low Temperature Co-Fired Ceramic (LTCC)-Based Sensor and Micro-Fluidic Structures" Dissertation for Doctor of Science, École Polytechnique Fédérale de Lausanne, 2007.
- [18] <https://global.kyocera.com/prdct/semicon/semi/ltcc/index.html>
- [19] CST: Electromagnetic field simulation software – Available on [www.cst.com](http://www.cst.com) [accessed 25<sup>th</sup> of September 2019]
- [20] M. Rahman, K. Shamsaifar, "Electronically Tunable LTCC Based Multi-Layer Filter for Mobile Handset Application", IEEE MTT-S International Microwave Symposium Digest, 2003.
- [21] David M. Pozar "Microwave Engineering", John Wiley & Sons, 4<sup>th</sup> Edition 2012.
- [22] J.-S. Hong, Microstrip Filters for RF/Microwave Applications, John Wiley & Sons, Second edition 2011.
- [23] M. A. El-Tanani and G. M. Rebeiz, "High-Performance 1.5 - 2.5-GHz RF-MEMS Tunable Filters for Wireless Applications", IEEE Trans. Microw. Theory Tech., vol. 58, no 6, p. 1629-1637, June 2010
- [24] G. Nicolini, C. Guines, D. Passerieux, P. Blondy, G. Neveu, M. P. Dussauby, W. Rebernak, et M. Giraud, "Constant absolute bandwidth UHF tunable filter using RF MEMS", in European Microwave Integrated Circuits Conference (EuMIC), 2012, p. 687-690

- [25] R. Stefanini, M. Chatras, et P. Blondy, "Compact 2-pole and 4-Pole 1.5-0.9 GHz constant absolute bandwidth tunable filters", in Microwave Symposium Digest (MTT), IEEE MTT-S International, 2012, p. 1-3
- [26] M. Sanchez-Renodo, et all, "Tunable Comblin Filter with Continuous Control of Center Frequency and Bandwidth", IEEE Transactions on Microwave Theory and Techniques, Vol. 53, January 2005
- [27] J.-H. Lee, J.-W. Choi, X.-G. Wang, et S.-W. Yun, « Design of tunable bandpass filter using PIN diode with constant absolute bandwidth », in Asia-Pacific Microwave Conference Proceedings (APMC), 2013, p. 191-193
- [28] L. Cao, G. Li, J. Hu, and L. Yin, "A Miniaturized Tunable Bandpass Filter with Constant Fractional Bandwidth," Progress In Electromagnetics Research C, Vol. 57, 89-97, 2015
- [29] Data sheet of high-Q capacitor (GJM03) and inductor (LQW03) series components in 0603 – Available on: [www.murata.com](http://www.murata.com) [accessed 25<sup>th</sup> of September 2019]

## Chapter II. Low Cost Millimeter Wave Antenna Arrays

---

In this second chapter of this thesis a low cost antenna array is designed. In the beginning of this chapter the needs of the antenna arrays in mobile communication is discussed in the point of view of the fifth generation mobile standard (5G NR, fifth generation New Radio). After understanding better the need of the millimeter wave (mmWave) antenna arrays in 5G NR, a low cost mmWave antenna array is designed using 3D EM simulations and in the end of this chapter the measurement results, return loss and peak gain, of the designed antenna array are presented.

### II.1 Millimeter wave antennas for fifth generation new radio

The upcoming 5G NR coordinated by the ITU (International Telecommunication Union) and 3GPP (3<sup>rd</sup> Generation Partnership Project) is an evolutionary step for the current 4<sup>th</sup> generation mobile communication standard, known as 4G LTE. With the 5G NR the telecommunication industry and regulators try to respond to the continuously increasing demand of mobile data usage. It is estimated that the monthly global data usage will grow up to 77 Exabyte by 2022 from 12 Exabyte in 2017 [1]. To cope this 7 fold expected increase of mobile data usage several novel mobile communication techniques are introduced in to the new standard, including from the use of new frequency spectrum to new encoding techniques [2]. In addition to accommodate the increased data traffic (data usage), the 5G NR also promise faster download speeds and lower latency communications than the older communication standards [2].

From the antenna design point of view the two most interesting new areas are the massive-MIMO and the use of new frequency spectrum in millimeter wave area (30 – 100 GHz). In massive-MIMO large antenna arrays (~ 100 antenna elements) are used in the base station to create user specific antenna radiation patterns to optimize signal path from the base station to the mobile end user and enabling the use of more aggressive encoding techniques and thus faster connections. The addition of the mmWave frequencies in the 5G NR to the old 4G LTE frequency spectrum increase available communication bandwidth at least by factor of two [2]. The increased bandwidth helps accommodate more users in single base station coverage area with faster communication speeds.

The use of the mmWaves for mobile communication has been studied very extensively in last ten years by the research community in 28-, 38-, and 60 GHz frequencies [3]-[7]. Due the high free space (FS) path loss attenuation in mmWave frequencies successful communication requires high gain antennas both from the base station and the end user's mobile devices. Mathematical models based on empirical measurement data gathered from the urban areas indicates that antenna gains up to 24.5 dBi, both in the base station and mobile device, are need at 28 GHz to be able to support cell sites with radius of 200 m [5]. Such a high gain antennas are difficult to obtain in mobile devices with their limited antenna

volume available. Microstrip antenna arrays are practically the only antenna type that can provide high gain antennas in the mobile device form factor. For mobile phones 24.5 dBi gain antennas are very difficult to implement even with microstrip antenna arrays and in practice antennas with much lower gain for mmWave frequencies have to be used in mobile phones.

Until very recently the main focus on the mmWave antenna array research has been on the 60 GHz ISM frequency band (61-61.5 GHz [8]), as it has been the most likely candidate for the 5G NR due the worldwide coverage. In 2018 the 3GPP and United State Federal Communications Commission (FCC) both included the 28 GHz for their 5G NR frequency allocations. In June 2018 3GPP published their latest technical specification, Release 15, for the user end radio transmission and reception [9] and [10]. In [10] the first mmWave bands for the 5G NR were allocated as shown in the table 2.1. In 3<sup>rd</sup> of August 2018 the FCC released a public notice (FCC 18-109) for the auction of two mmWave blocks at 28 GHz band (Block 1: 27.5-27.925, Block 2: 27.925-28.35 GHz) in addition of 7 blocks at 24 GHz (24.25-25.25, each block 100 MHz wide) [11]. The bidding for the 28 GHz and the 24 GHz blocks were closed and the results were announced in June 3<sup>rd</sup> 2019 with two FCC public notices (FCC DA-19-484 for the 28 GHz auction, and FCC DA-19-485 for the 24 GHz auction). The two auctions raised in total ~3.7 billion USD's (United States Dollar) [12], [13]. With the inclusion of the 28 GHz band for both FCC and 3GPP specifications the research for the 5G NR mmWave antenna array will most likely move from 60 GHz to 24- and 28 GHz frequencies.

Table 2.1 3GPP millimeter wave bands in Release 15 [10]

Operating Band	Uplink (UL) operating band BS receive UE transmit	Downlink (DL) operating band BS transmit UE receive	Duplex Mode
	$F_{UL\_low} - F_{UL\_high}$	$F_{DL\_low} - F_{DL\_high}$	
n257	26500 MHz – 29500 MHz	26500 MHz – 29500 MHz	TDD
n258	24250 MHz – 27500 MHz	24250 MHz – 27500 MHz	TDD
n260	37000 MHz – 40000 MHz	37000 MHz – 40000 MHz	TDD
n261	27500 MHz – 28350 MHz	27500 MHz – 28350 MHz	TDD

## II.2 Designing of low cost millimeter wave antenna arrays

As discussed above, majority of the mmWave antenna array studies done in the last ten years have been focused on the 60 GHz ISM band. Only in the last few years papers on 28 GHz antenna arrays have been published as we can see from the sample of the papers from 2005 to 2018 [14]-[26]. Although 28 GHz is significantly lower in frequency compared to the 60 GHz band the challenges of designing antennas in mobile devices are similar in the both mmWave bands compared to the legacy 4G sub 6 GHz frequency bands. Whereas for the 4G bands a single element antennas were sufficient, the gain of monopole-, PIFA-, and loop-antennas, to name few well known antenna types used in 2G, 3G, and 4G communication,



are not sufficient for the mmWave frequencies and thus antenna arrays are needed for the 5G NR devices.

In addition to the change of the antenna type the mmWave frequencies brings new design challenges due the high frequency. In mmWave frequencies, as the name implies, the wavelength of the signal is in millimeter range and many mechanical dimensions of the antennas start to be large in electrical length wise. This leads to physical phenomena, such as surface waves, which didn't have to be considered in the lower frequencies of 4G antennas. Surface waves if not taken account during design can reduce the antenna's efficiency and have destructive effect to the antenna's radiation pattern.

Surface waves can occur if the thickness of the patch antenna's substrate becomes electrically thick enough ( $d \gg 0.05\lambda_0$ ), the electric fields of the microstrip antenna induce surface waves to the dielectric substrate [27]. The surface waves are formed in the boundary layer between the dielectric substrate and air where part of the electric field in the dielectric reflects back. For a grounded dielectric substrate both TM- and TE- surface waves are excited. In high frequencies surface waves are more bounded into the substrate allowing the surface waves to travel in waveguide fashion [28].

The surface waves induced by a single microstrip antenna can be mainly considered as a loss mechanism where part of the energy inserted to the antenna is loss to the non-radiating surface waves. However surface waves can be diffracted from the substrate edges and other discontinuities in the substrate and distort the antenna radiation pattern and polarization characteristics. Surface waves also can deteriorate the isolation between antennas as the energy in the ground plane can be coupled to other antennas [27].

As the power of the surface wave increases when the thickness of the substrate and the dielectric constant are increased, low permittivity substrates are preferred for microstrip antennas to minimize the surface waves [27]. Other methods to reduce the surface waves such as air cavities under the antenna (reduced effective permittivity) and other metamaterial structures have been studied for millimeter wave antenna arrays as the thickness of the substrate becomes electrically thick easily even for physically thin substrates in higher frequencies [16, 21].

Elimination of the surface waves in 60 GHz have been studied using electrical soft surfaces, or EBG (Electronic Band Gap). Although performance improvements between 2 to 4 dB have been reported in papers [22]-[23], the implementation of the EBG surfaces increases the complexity and the size of the design and in most of the antenna array design requires expensive manufacturing technologies, such as LTCC, due the via arrangement.

Compared to the legacy antenna designs also the manufacturing materials have to be reconsidered as the losses due material properties can be higher in millimeter wave frequencies. Commonly used antenna substrates, such as FR-4, can induce much higher losses in mmWave frequencies than in the sub 6 GHz frequencies used in 4G LTE. LTCC (Low Temperature Co-fired Ceramic) have been widely used [14]-[23] in the mmWave research as it provides variety of low-loss substrates for the mmWave frequencies and have less design restrictions than the more common substrates, such as FR-4. The problem of

using LTCC as a manufacturing technology is the price. LTCC substrates are roughly 1.5 to 2 times more expensive than the FR-4. In a cost driven market, as a mobile phones, such an increase of price is problematic and cheaper solution are preferable. In this fifth chapter a solution for low cost antenna array for 28 GHz is investigated using FPC (flexible printed circuit) manufacturing technology. Commercial FPCs uses polyimide (PI, with  $\epsilon_r = 3.5$  and  $\tan\delta = 0.0025$ , at 1 kHz) [29] as substrate material between the metal layers which has significantly lower loss factor ( $\tan\delta$ ) than substrate used in normal FR-4 PCB circuitry ( $\tan\delta = 0.025$ , at 10 GHz). Even though the loss factor ( $\tan\delta$ ) of the PI is reported in very low frequency it remains practically constant up to 45 GHz [30]. Although FPC is slightly more expensive than the FR-4 PCB, it is still cheaper than LTCC and other low loss PCB substrates and thus selected as a substrate for this thesis.

## II.2.1 Antenna architecture

As the antenna arrays used in mmWave frequencies are very directive several different arrays inside a mobile device are needed to have good coverage of the surrounding space. The arrays inside the mobile device can be arranged countlessly different ways but the problem of transferring the data from the antenna arrays to the RF FEM (Front End Module) and MCU/Baseband (Micro Control Unit) still remains. In the below picture two main schemes to transfer data are illustrated, centralized in figure 2.1 a) and distributed in figure 2.1 b).

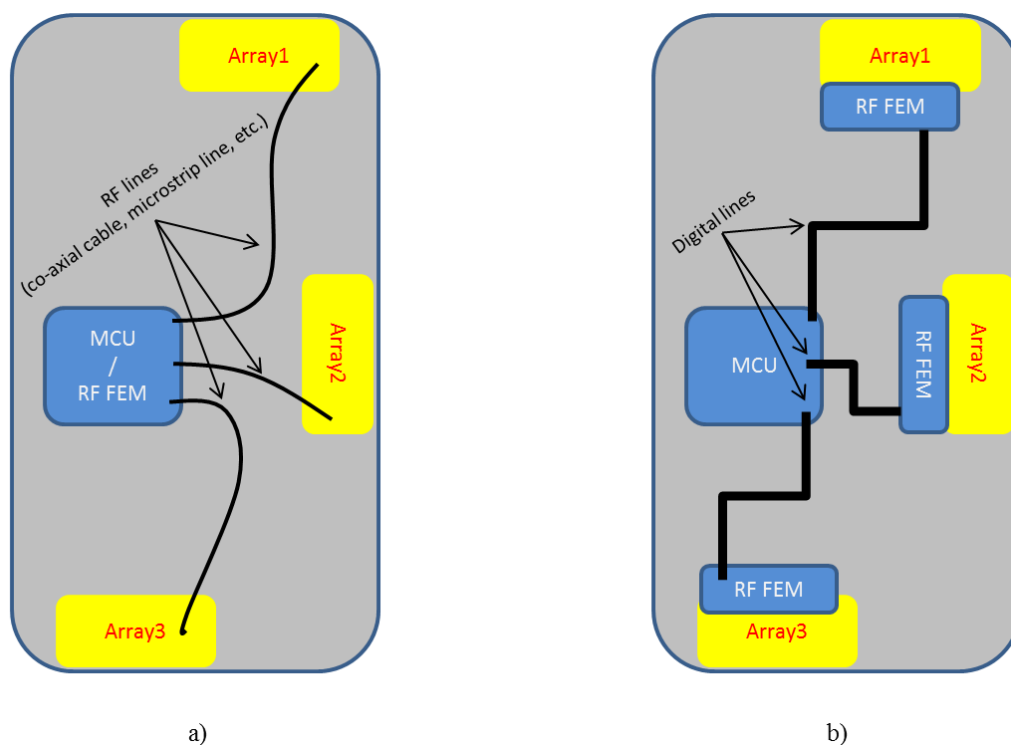


Figure 2.1 a) A centralized and b) a distributed mmWave antenna architecture

In the distributed scheme each array has its own RF FEM module which converts the analog RF signal from the antennas to digital form and the digitalized signal is send to MCU for further processing. This approach will give the best RF performance and agility to control the array as each element can be easily individually controlled but have challenges with the data synchronization in multiple array schemes. It has also a price penalty compared to the centralized RF FEM as each array needs its own RF IC circuitry to convert the analog signal to digital. In the centralized scheme all the arrays are connected to single RF FEM module via RF transmission lines. This solves the data synchronization and price challenges, but has lower RF performances due the losses induced by the long RF connections and less agile control of the array as the phase shift between the antenna elements is fixed by the array design. Thus with the centralized scheme no beam steering is possible.

As the distributed architecture can get easily very expensive solution in multi array systems due the individual FEM's the centralized scheme is a natural choice for the data transfer scheme for a low cost millimeter wave antenna array.

### II.2.2 Low loss transmission lines for mmWave

There are several different transmission line technologies to transfer the millimeter wave RF signal from the antenna arrays to the centralized FEM e.g. waveguides, co-axial cables, microstrip lines etc. For the mmWave frequencies the air filled waveguides have the best RF performance, i.e. lowest loss, of all technologies but are bulky in size and are difficult to integrate to small mobile devices. A microstrip line is the cheapest and easiest transmission line to integrate to the RF circuitry and consume much less space/volume than the other transmission technologies. In a mobile device environment where available space is scarce microstrip lines poses problems. In a microstrip line the upper half of the line is unprotected from the environment and is susceptible for interference from the mechanical parts and spurious signals from in- and out-side of the device. A stripline transmission line, shown in figure 2.2, has a metallic ground plane on both side of the conductor which helps to isolate the center conductor from the interference and offers thus better solution for the mmWave frequencies in mobile devices than microstrip lines and waveguides.

The characteristic impedance of the stripline transmission line can be approximated by the equation (2.1) [28]:

$$Z_0 = \frac{30\pi b}{\sqrt{\epsilon_r}(W_e + 0.441b)} \quad (2.1)$$

where  $W_e$  is the effective width of the center conductor given by the equation (2.2) [28]:

$$\frac{W_e}{b} = \frac{W}{b} - \begin{cases} 0 & \text{for } \frac{W}{b} > 0.35 \\ \left(0.35 - \frac{W}{b}\right)^2 & \text{for } \frac{W}{b} < 0.35 \end{cases}$$

(2.2)

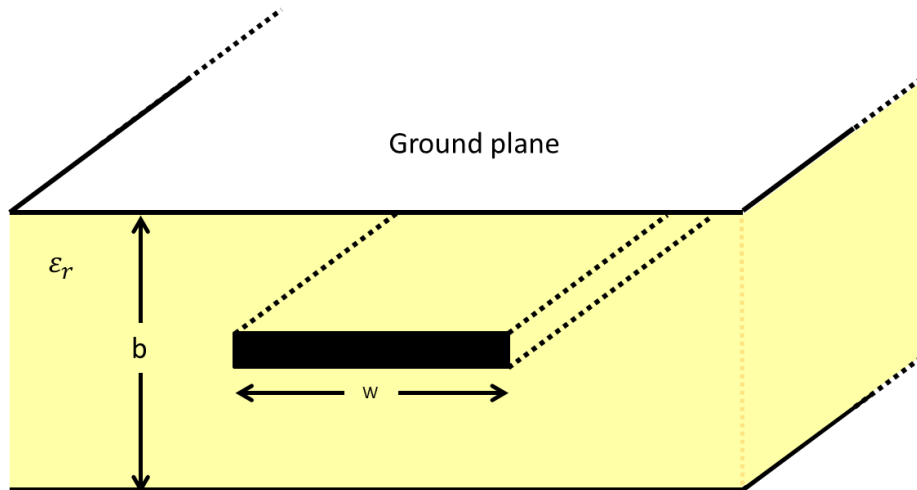


Figure 2.2 Geometry of stripline transmission line.

Compared to microstrip line and wave guide the stripline has more losses as the center conductor is submerged inside the lossy dielectric. In [31] different rectangular co-axial cables manufactured using additive micro-fabrication techniques for mmWaves were tested and studied. One tested topology was a rectangular co-axial cable with bottom half of the rectangular co-axial cable, under the central conductor, was filled with the dielectric and the upper half was left empty i.e. filled with air. With this geometry the losses due the dielectric can be reduced. The data provided in the [31] starts at 35 GHz which is higher than the 28 GHz frequency studied in this thesis. Also the rectangular co-axial cable studied in [31] has slightly different characteristics than the stripline topology, mainly the side wall distance to the center conductor, studied in this thesis. Thus a new study was done.

In figure 2.3 the CST simulation setups are shown for the air cavity study. The stripline without the air cavity is the base line and the microstrip is the target for the strip lines with four air cavity. The substrate in all models is polyimide (PI) with  $\epsilon_r = 3.5$  and  $\tan\delta = 0.0025$ , at 1 kHz) [29], [30], and all the metal surfaces are modelled as an annealed copper from CST library, with electrical conductivity of  $\sigma = 5.8e^{+7} S/m$ . For high frequencies, like mmWave frequencies, the copper conductivity is highly dependable on the surface roughness of the copper, and depending on the roughness can be even one third of the optimal conductivity of the CST library value [33]. But as the copper roughness value for the copper used in the prototype antennas was not available the CST library value was used in the simulations. The electrical conductivity is frequency dependable in CST and reduced in

higher frequencies, but depending on the surface roughness of the used conductor the CST library value can be too optimistic in mmWave frequencies. The center conductors are 40  $\mu\text{m}$  thick and their widths are presented in the table 2.2. The transmission line is excited by discrete face-ports placed on both end of the center conductor lines in the CST model. The length of the center conductor is 150 mm for all the lines, and the air cavity is made for the full length of the transmission line. The length of 150 mm is chosen to represents a possible worst case length scenario where the mmWave antenna is located in the opposite side, in lengthwise, from the RF FEM in a modern large screen mobile phone.

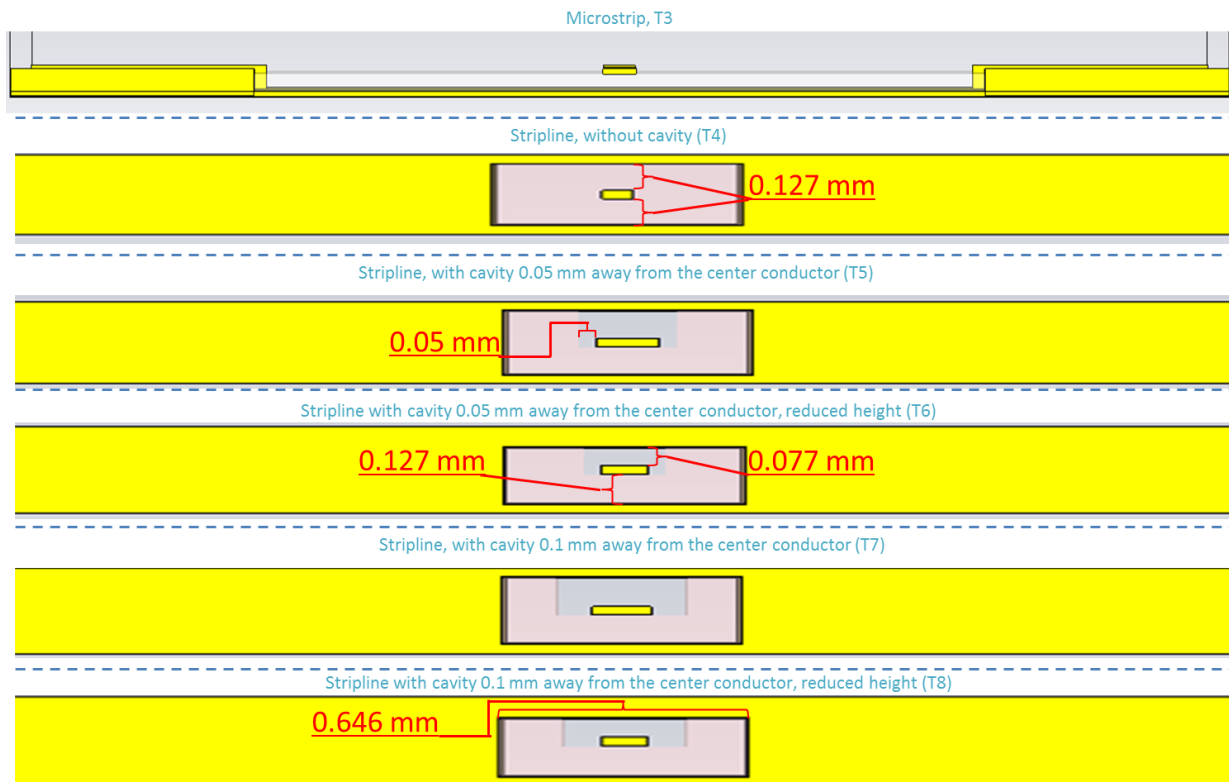


Figure 2.3 Transmission line topologies for the CST simulation

Table 2.2 Center conductor widths

	Center conductor width [ $\mu\text{m}$ ]
Microstrip, (T3)	246
Stripline, without cavity (T4)	80
Stripline, with cavity 0.05 mm away from the center conductor (T5)	157
Stripline with cavity 0.05 mm away from the center conductor, reduced height (T6)	120
Stripline, with cavity 0.1 mm away from the center conductor (T7)	157
Stripline with cavity 0.1 mm away from the center conductor, reduced height (T8)	120

In figures 2.4 and 2.5 the E- and H-fields of all the different transmission lines under study are plotted at 28 GHz. As we can see from the plots the E- and H-fields of the T4 stripline transmission line, the nominal stripline structure, are equally distributed above and under the center conductor. When the air cavity above the center conductor is cut out the fields in the air cavity are slightly stronger around the center connector but the fields are still equally distributed both in the air and in the dielectric. When the height of the air cavity is reduced to 0.077 mm, almost halve of the original height, the fields in the air cavity are stronger than the fields in the dielectric substrate. As most of the fields are now concentrated in the air cavity section of the stripline, the reduced height striplines (T6 and T8) should have the best performance of all the striplines and should be closest to the microstrip line performance.

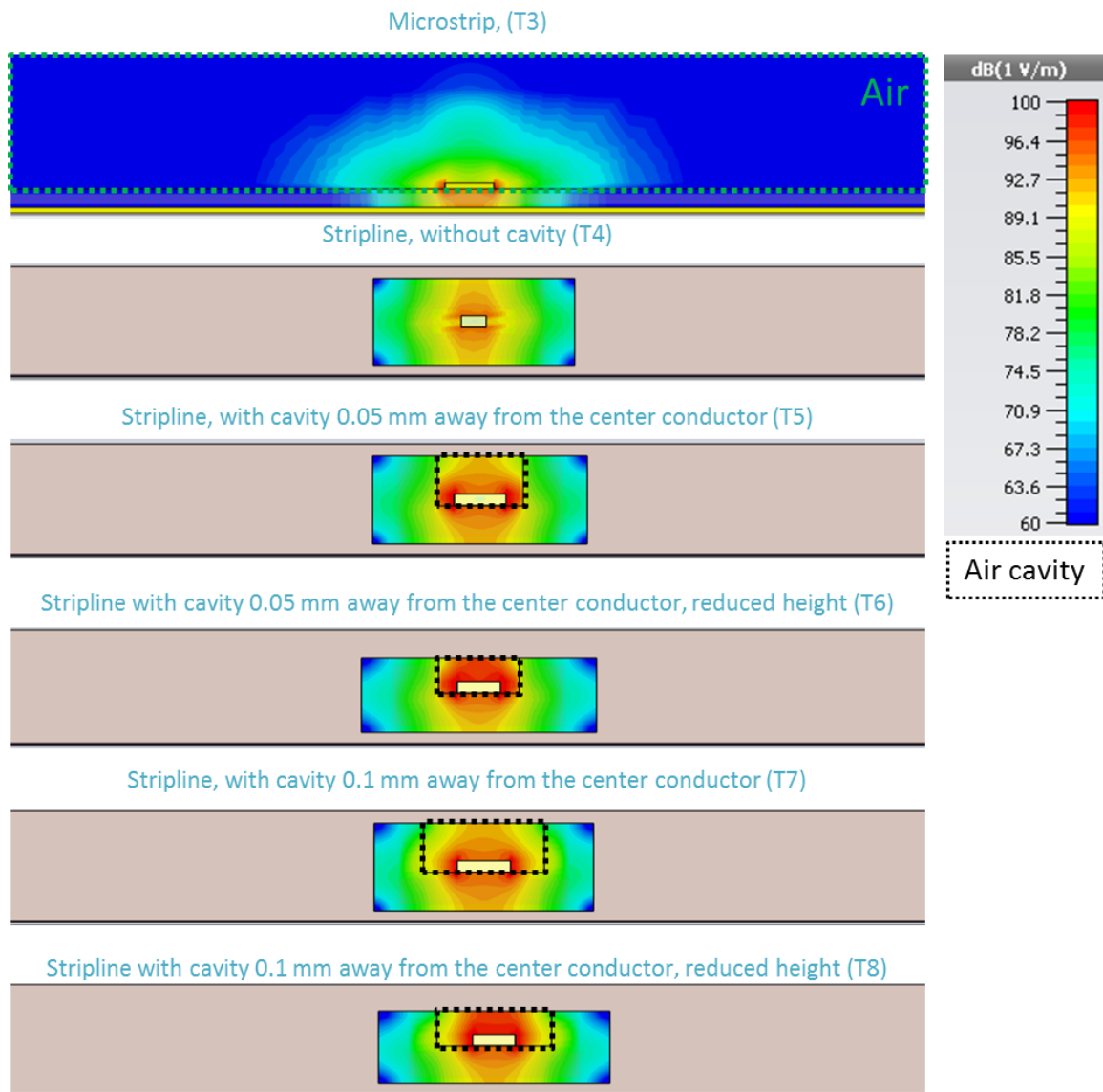


Figure 2.4 E-field distributions in the transmission lines at 28 GHz

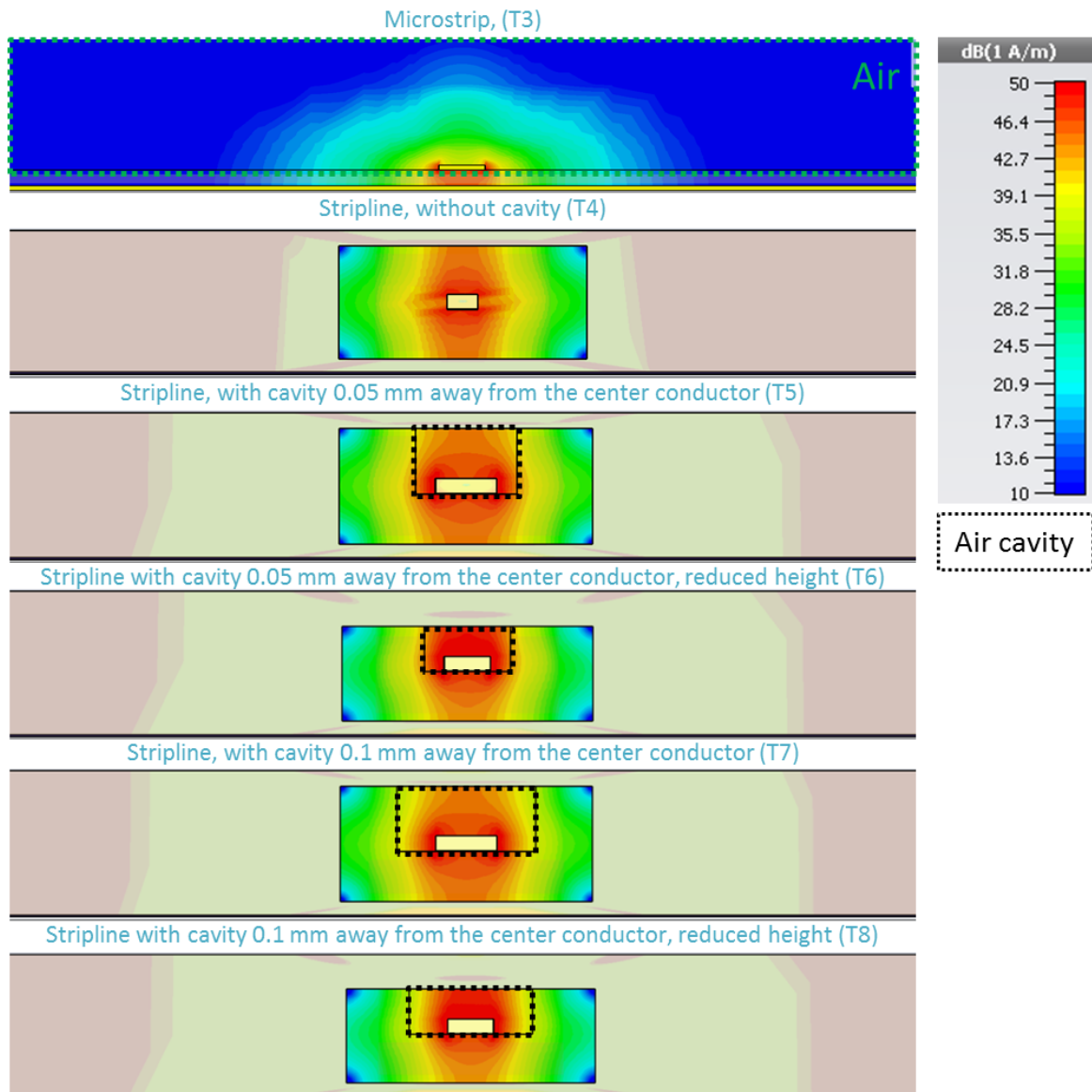


Figure 2.5 H-field distributions in the transmission lines at 28 GHz

In the charts 2.1 to 2.3 the input matching, and insertion are plotted (RH= Reduced Height). As we can see from the chart 2.1 all the transmission lines under the study are matched equally in the whole bandwidth in interest and the results are thus comparable between all the different topologies.



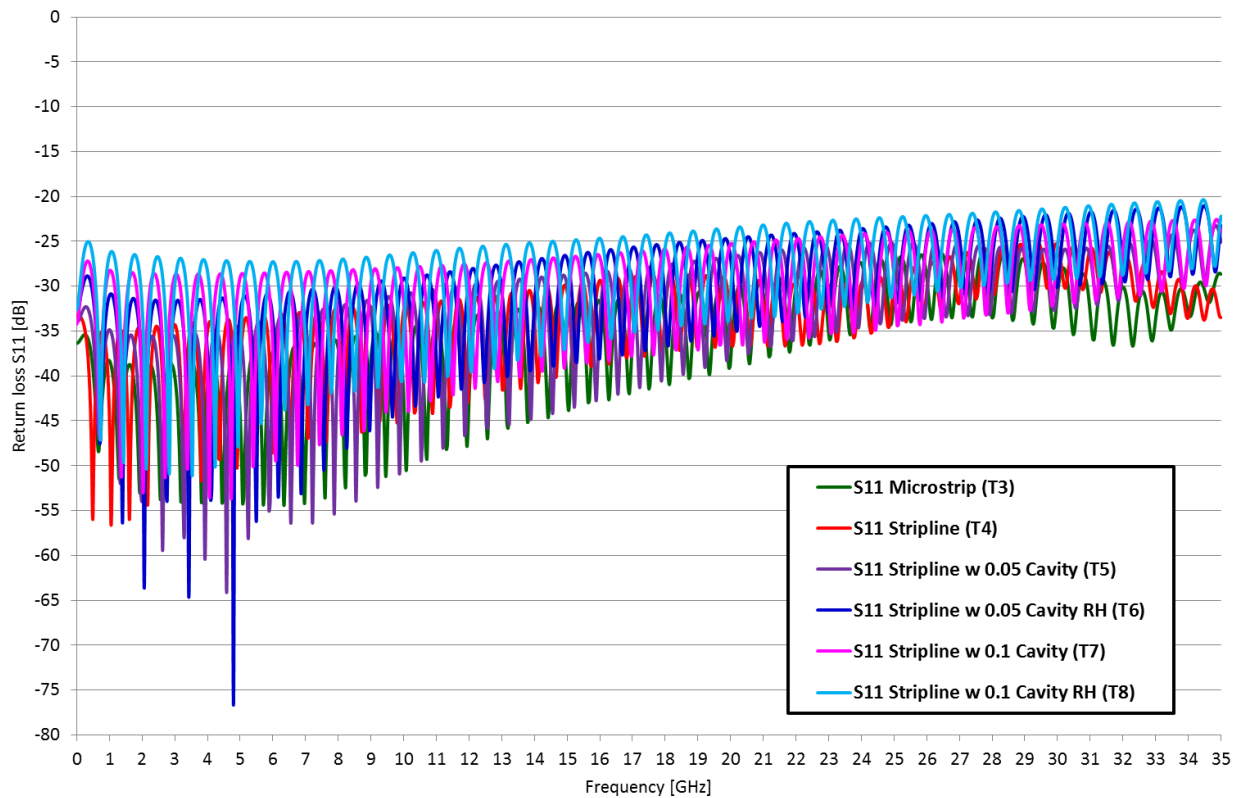


Chart 2.1 Input matching of the transmission lines

In the charts 2.2 and 2.3 the insertion loss, including the losses of the metal and the dielectric substrate, of all the transmission lines are plotted. In chart 2.2 the insertion losses are normalized to one millimeter and in the chart 2.3 the insertion loss of the whole 150 mm line is shown. By comparing the results of the chart 2.2 to the results of [31, figure II.25 and II.27] we can observe that the losses of the nominal stripline (T4) simulated in this thesis are very close to the results of the rectangular coaxial line with fully filled with dielectric (polyimide) at 35 GHz and as the air cavity is added the losses are reduced in both studies. When the results of the charts 2.2 and 2.3 are compared to the figures 2.4 and 2.5 the insertion losses of the reduced height stripline transmission lines are not as predicted from the E- and H-field results. The T6 and T8, the reduced air cavity height samples, are more lossy than their normal air cavity height counterparts, T5 and T7. This is because as the fields are more concentrated between the center conductor and the upper copper ground plane the fields are more coupled to the metal ground plane. And as we can see from the charts 2.4 and 2.5 the losses of the copper are more dominant for T6 and T8 in the whole frequency range than the losses of the dielectric substrate. Although the reduced height have less losses due the dielectric than their normal height counterparts the losses of the copper overrides the benefits of concentrating the fields closer to the center connector. For better conductive metals, such as silver, or more lossy dielectric the height reduction and thus concentrating the fields could bring benefits. It should be also noted that increasing the air cavity width has

small benefits but the main gain is achieved with introducing the air cavity over the center conductor as the fields are strongest above to the center conductor.

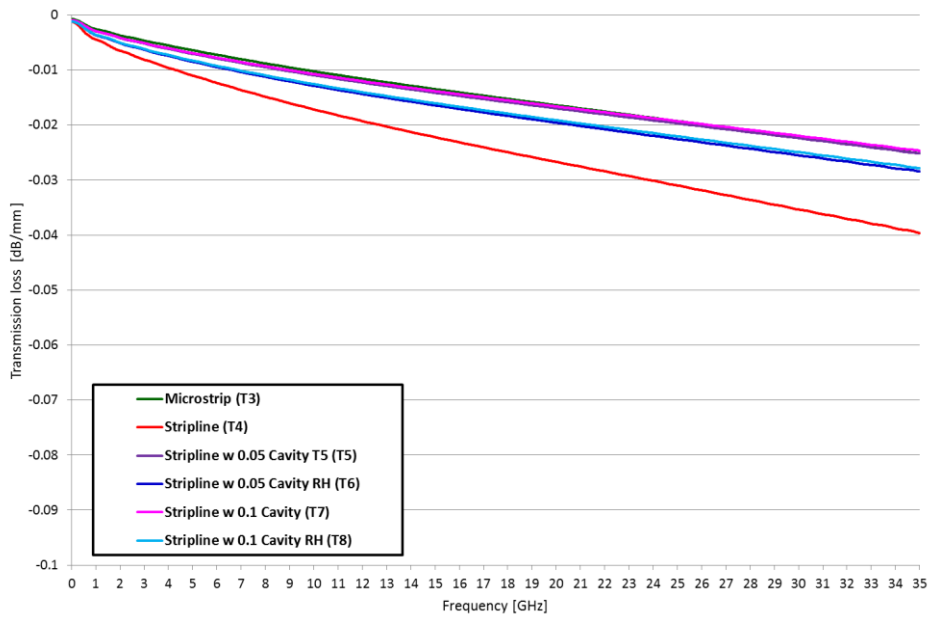


Chart 2.2 Insertion losses per mm of the transmission lines

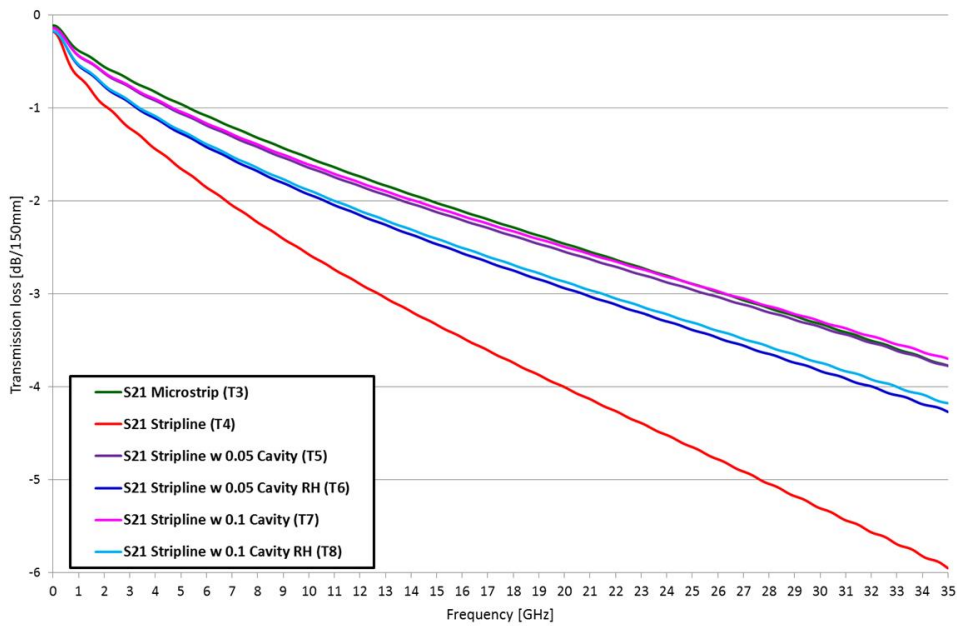


Chart 2.3 Insertion losses of the full length transmission lines

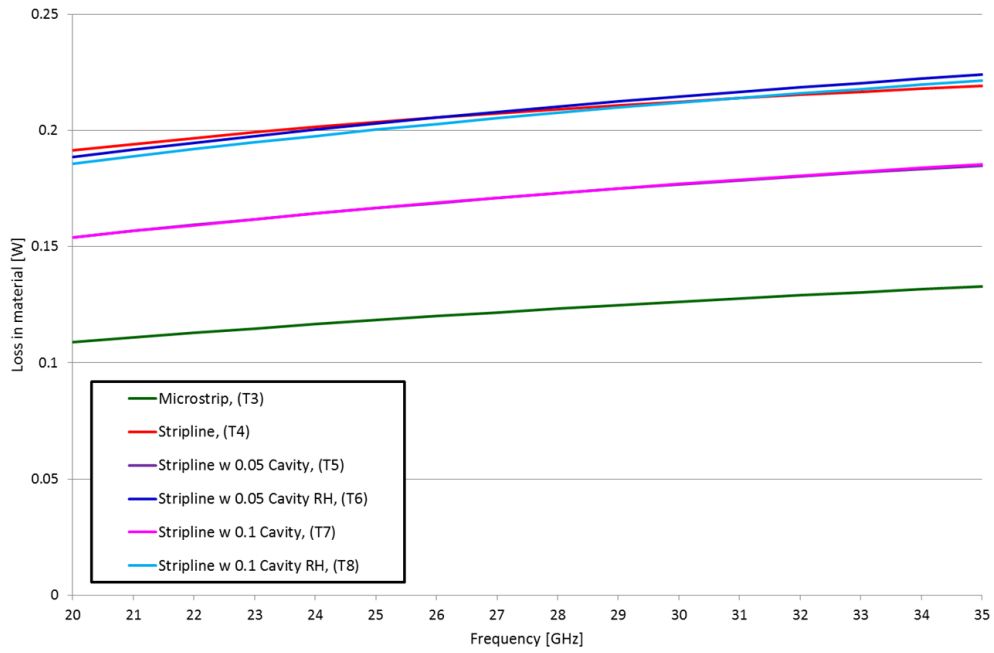


Chart 2.4 Losses due to the copper in the transmission lines

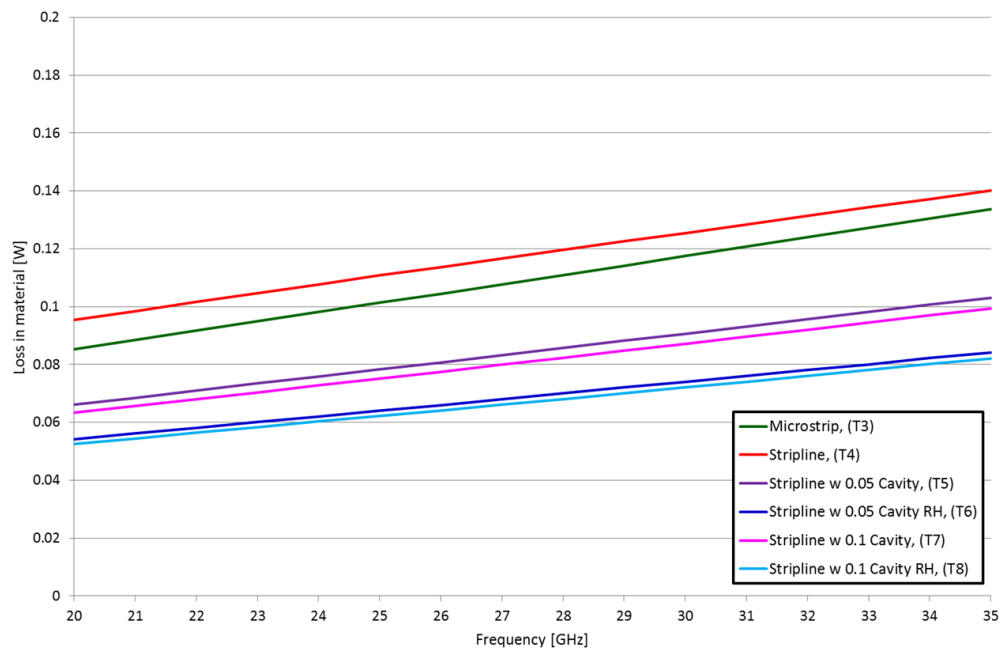


Chart 2.5 Losses due to the dielectric in the transmission lines

## II.2.3 Antenna array 3D EM simulations

### II.2.3.1 Unit element design

An antenna array design starts usually from the designing of the single antenna element, or unit element. After the unit element is designed the antenna array is formed by arranging multiple unit elements in linear or planar pattern depending on the requirements of the antenna array performance [32].

For this thesis a dual polarized patch antenna, with separate feeds for vertical (y-axis) and horizontal (x-axis) polarizations, is chosen for the unit element, shown in the figure 2.6. With both polarizations the antenna can use the different polarizations for multiplexing in line-of-sight communications or combine the two polarizations to form circular and elliptical polarizations if need.

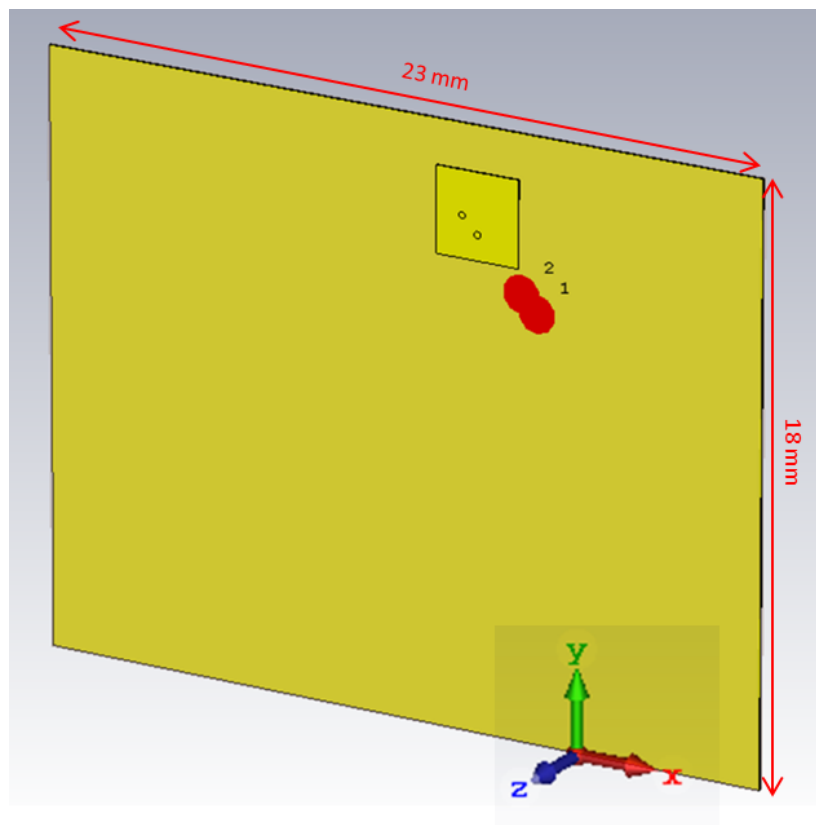


Figure 2.6 Dual polarized patch antenna with the simulation coordinates

The initial dimensions of the square patch can be calculated with the layer thickness of the patch antenna shown in the figure 2.7. by solving equation 2.3 [32]:

$$W = \frac{c}{2f_r} \sqrt{\frac{2}{\epsilon_r + 1}} \quad (2.3)$$

where  $f_r$  is the wanted resonance frequency in Hz,  $c$  is the speed of the light in vacuum, and  $\epsilon_r$  is the dielectric constant of the substrate.

Due the fringing fields, the electrical length of the patch antenna appears to be larger than the physical dimension. The correction factor for the length  $\Delta W$  can be calculated using equation 2.4 [32]:

$$\Delta W = \frac{(\epsilon_{eff} + 0.3) \left( \frac{W}{d} + 0.264 \right)}{(\epsilon_{eff} - 0.258) \left( \frac{W}{d} + 0.8 \right)} d \quad (2.4)$$

where  $d$  is the thickness of the substrate and effective dielectric constant  $\epsilon_{eff}$  is given by the formula 2.5:

$$\epsilon_{eff} = \frac{\epsilon_r + 1}{2} + \frac{\epsilon_r - 1}{2} \left( 1 + 12 \frac{d}{W} \right)^{-\frac{1}{2}} \quad (2.5)$$

After the correction factor for the length is calculated the physical length  $W$  of the patch antenna can be solved using the equation 2.6 [32]:

$$W = \frac{c}{2f_r \sqrt{\epsilon_{eff}}} - 2\Delta W \quad (2.6)$$

With a FPC substrate ( $\epsilon_r=3.5$ ) the equation 2.6 gives the length ( $W = 2.827$  mm) for the square patch antenna for 28 GHz.

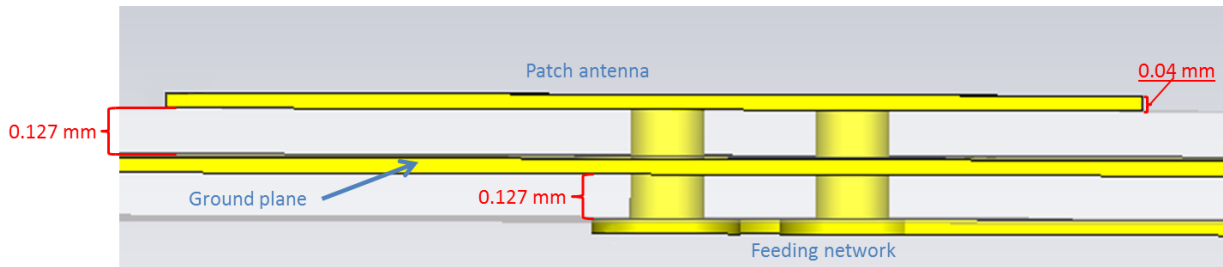


Figure 2.7 The stack up of the 28 GHz dual polarized FPC patch antenna

To be able to excite the two polarizations separately the feed points of the vertical ( $dy$ ) and horizontal ( $dx$ ) polarizations, see figure 2.8, are carefully chosen in the centerline of the patch [34], [35]. The distance of the feed location from the center point of the patch has an impact to the input impedance of the patch antenna and thus the matching of the antenna. The distance between the feed points determine to isolation between the two polarizations. The isolation between the two polarization is very sensitive for the locations of the feeds as can be seen from the chart 2.6 where the isolation between the two feeds of a 28 GHz patch antenna on FPC substrate are plotted. Even a 0.1 mm change in the optimum feeding location ( $dx, dy = 0.5$  mm) has a big impact (12 dB) to the isolation at 28 GHz.

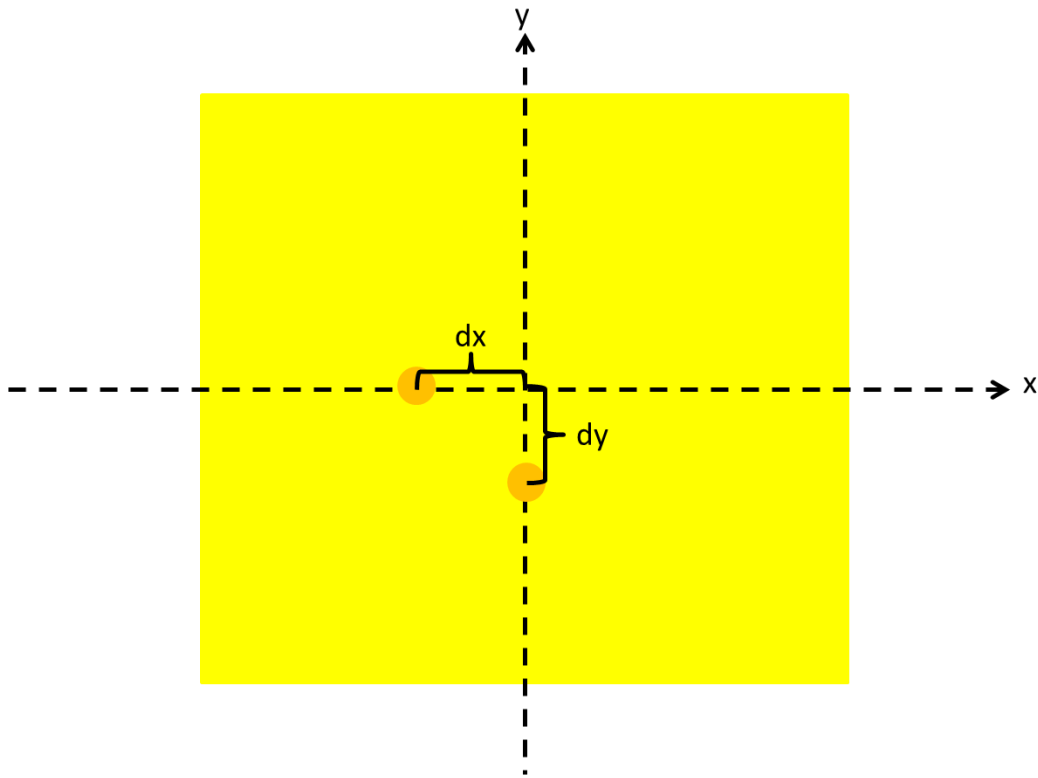


Figure 2.8 Location of the feeding pins for dual polarization patch antenna

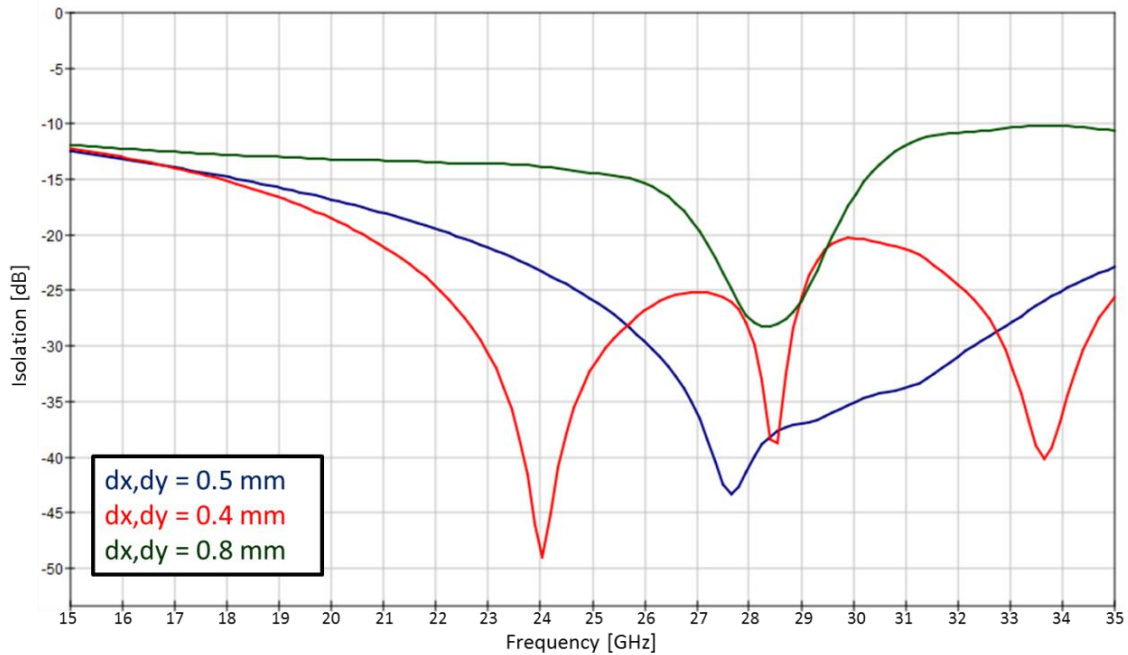


Chart 2.6 Isolation between the feeding probes of 28 GHz square patch

After the initial size and the feeding locations of the square patch antenna are determined the 3D EM simulation model in CST can be built and simulated. In chart 2.7 the return loss and isolation between the two ports are plotted for the final unit element. The resonance frequency of the unit element is designed to be higher in frequency to take account the loading of the adjacent cells in the antenna array which will tune the resonance frequency lower. The final dimension of the square patch is slightly smaller than the initial calculated, the final side length is 2.63 mm and the dx and dy distances of the feed probes are 0.5 mm.

In the charts 2.8 and 2.9 the simulated total efficiency which is the full antenna system efficiency, taking account all the losses in the antenna system, and the peak gain of the unit element are shown for both polarization feeds/ports. As the return loss of the antenna indicated the peaks of the total efficiency and the peak gain are higher in frequency than 28 GHz. The gain patterns of the unit element are shown in the charts 2.10 to 2.12 at 28 GHz. Especially in the charts 2.10 a) and b) the difference of the vertical and horizontal polarizations are clearly shown in the total gain (phi and theta polarizations combined).

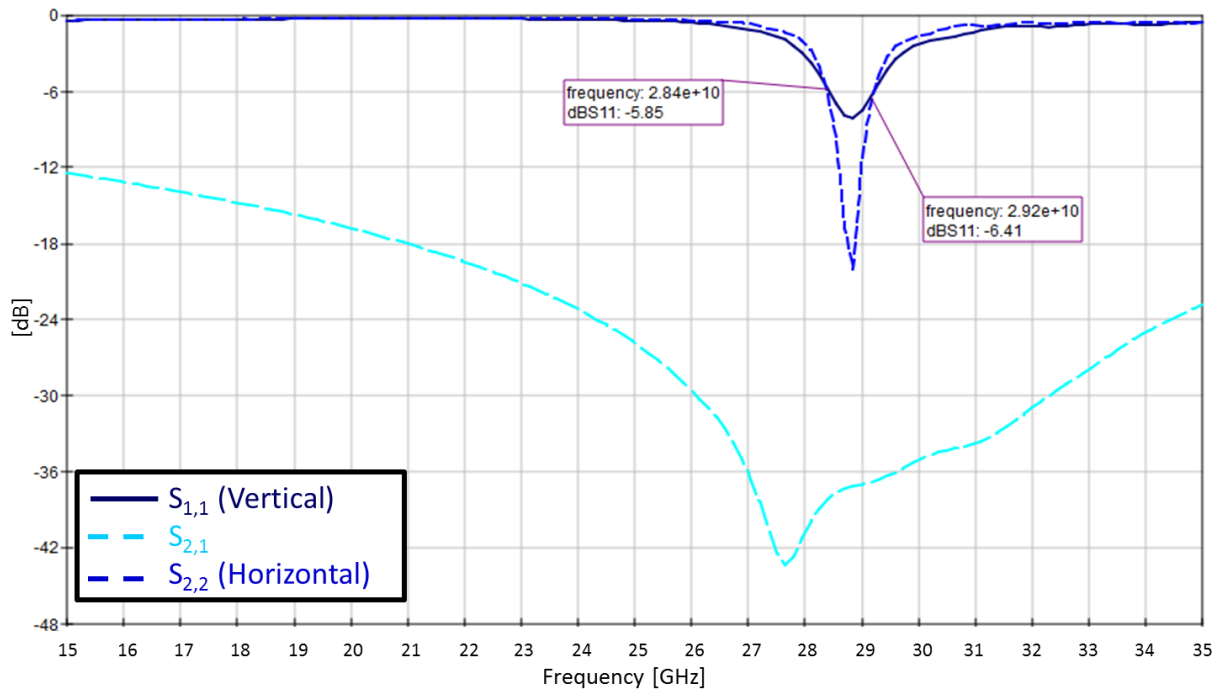


Chart 2.7 The return loss and isolation of the designed unit element of the 28 GHz antenna array

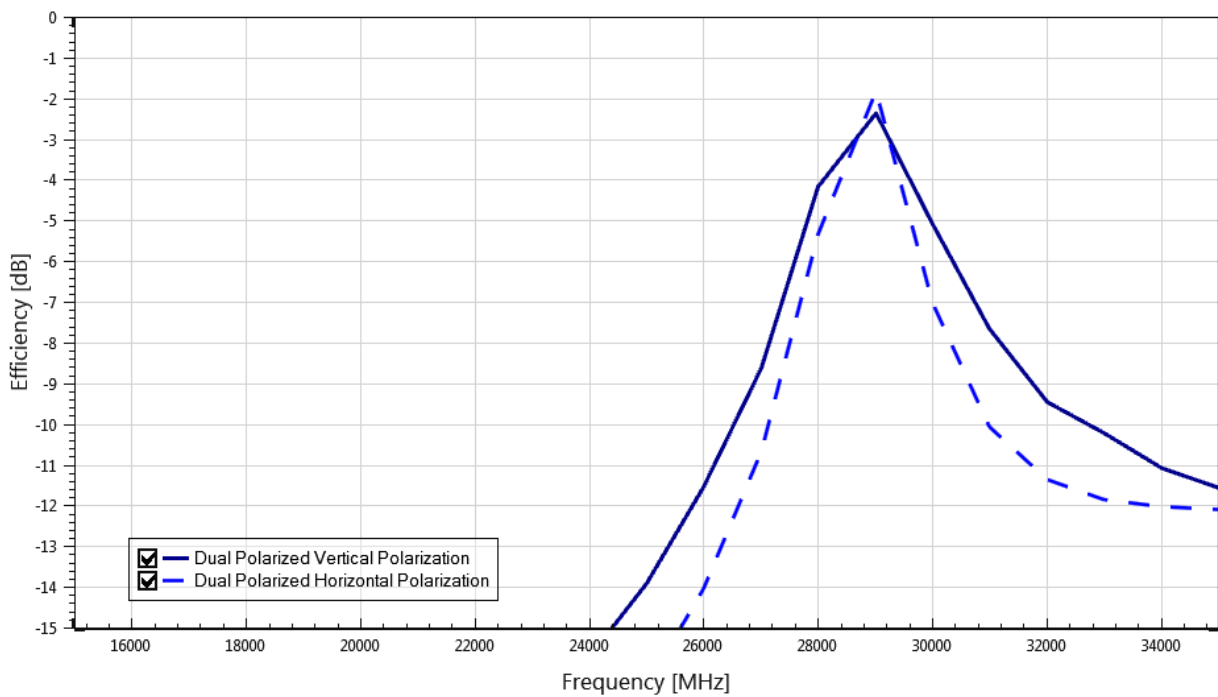


Chart 2.8 The total efficiency of the unit element's both polarization ports



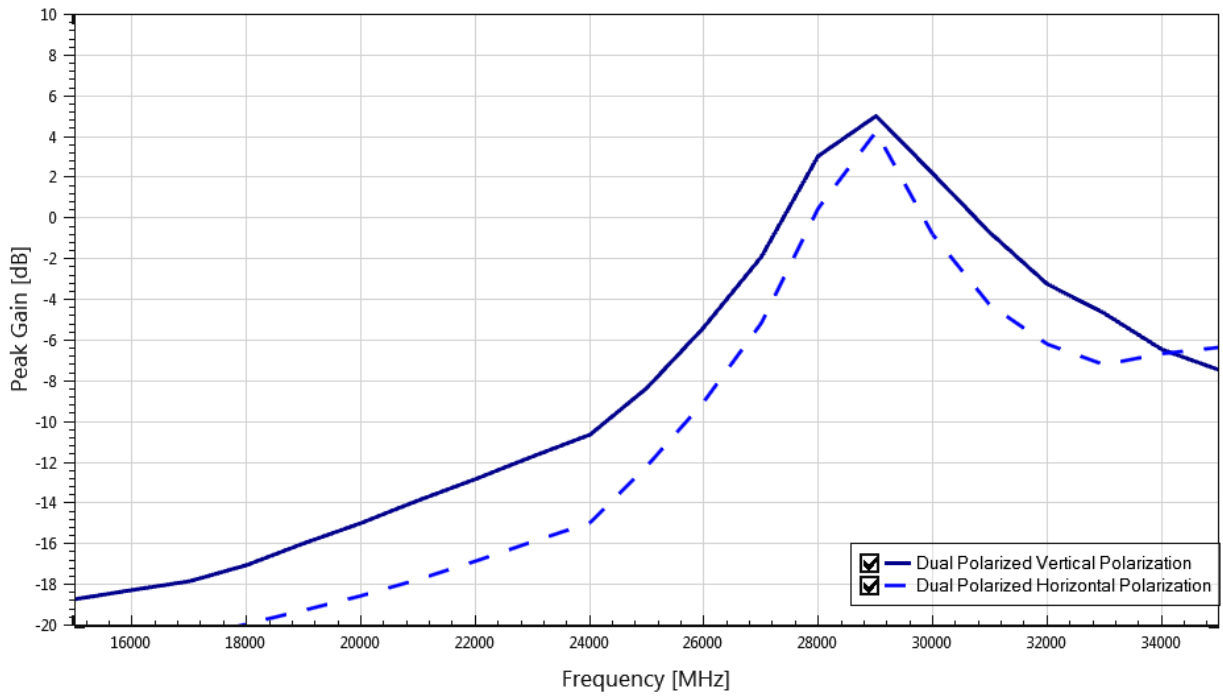


Chart 2.9 The peak gain of the unit element's both polarization ports

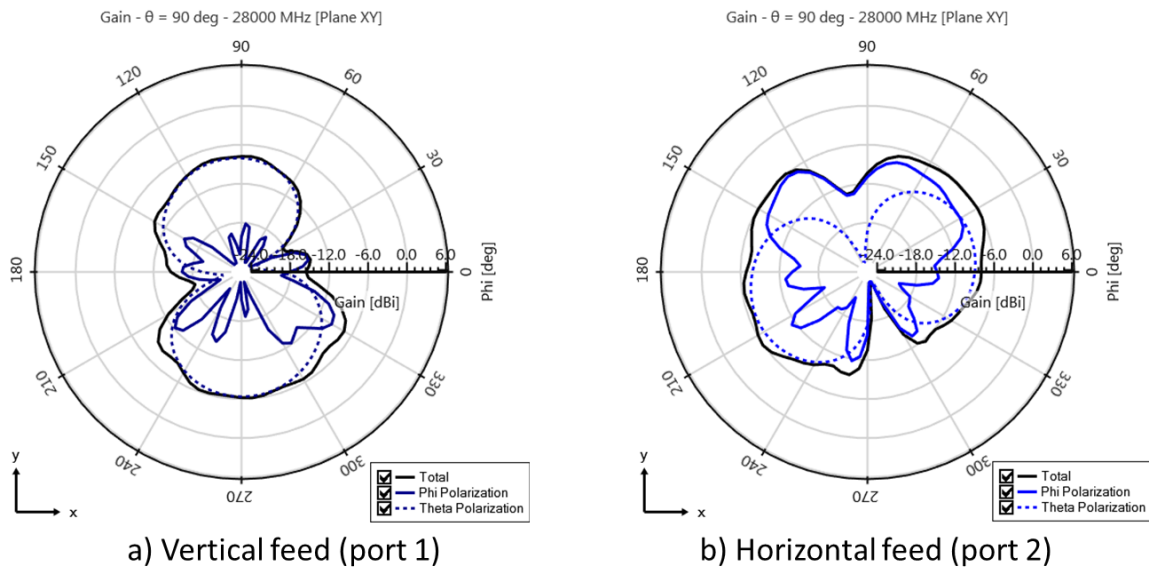
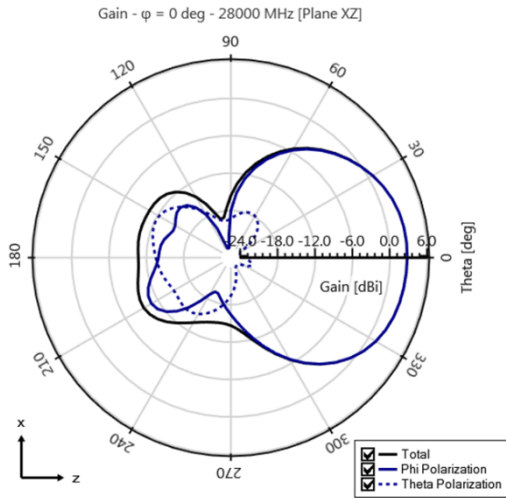
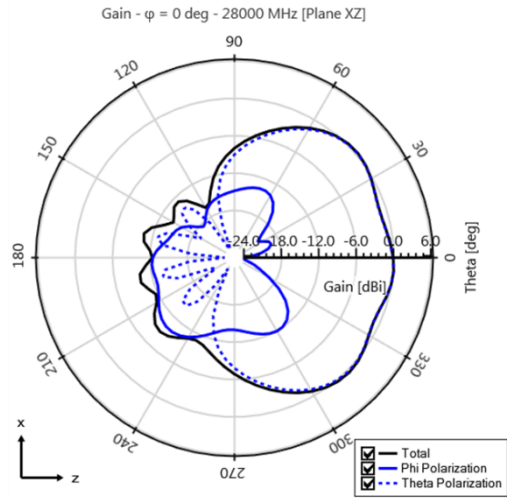


Chart 2.10 The XY-cut of the gain pattern of the unit element's both polarization ports at 28 GHz

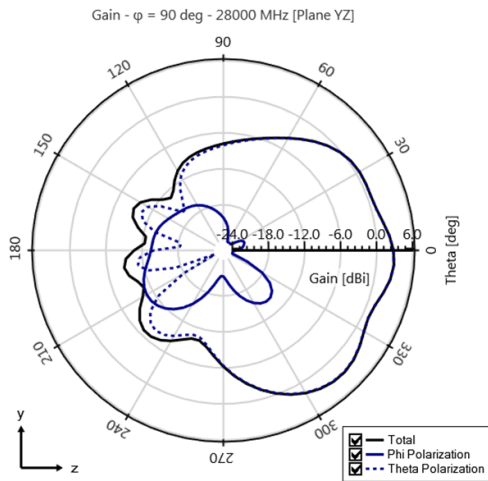


a) Vertical feed (port 1)

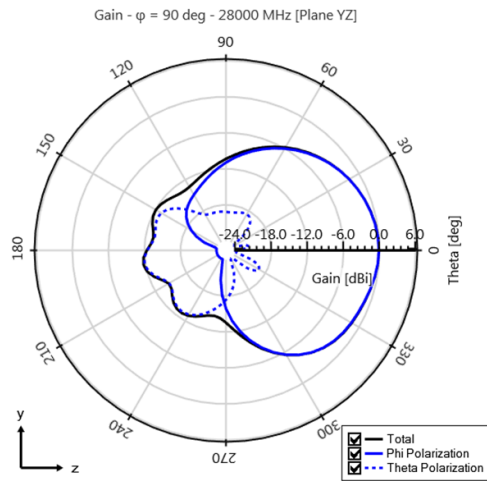


b) Horizontal feed (port 2)

Chart 2.11 The XZ-cut of the gain pattern of the unit element's both polarization ports at 28 GHz



a) Vertical feed (port 1)



b) Horizontal feed (port 2)

Chart 2.12 The YZ-cut of the gain pattern of the unit element's both polarization ports at 28 GHz

### II.2.3.2 Four element linear antenna array design

Now when the unit element is designed with 3D EM simulations in CST the design of the array can be started. For this thesis a linear antenna array is chosen as it has only one row of antenna elements it's easier to implement in side of the thin mobile phones. The drawback of linear arrays compared to the planar arrays is the narrower beamwidth than a planar array.

The final design of the 28 GHz 4 element linear antenna array is shown in figure 2.9 and 2.10. The stack up of the whole array and the element dimensions are same as in the unit element simulations and the element distance, from center to center of the patch antennas, is 5mm or  $0.87\lambda$ . For minimizing the grating lobes the element spacing should be less than one wave length [32]. For PI substrate with  $\epsilon_r = 3.5$  the one wavelength at 28 GHz is 2.73 mm making the spacing of the elements less than one wavelength. In charts 2.13 and 2.14 the return loss of the each patch both polarization feeds and the isolation between the all the feeds are shown.

As we can now see from the return loss results the element resonance has now tune slightly down in frequency due the loading from the adjacent elements and all the elements are now well matched at 28 GHz.

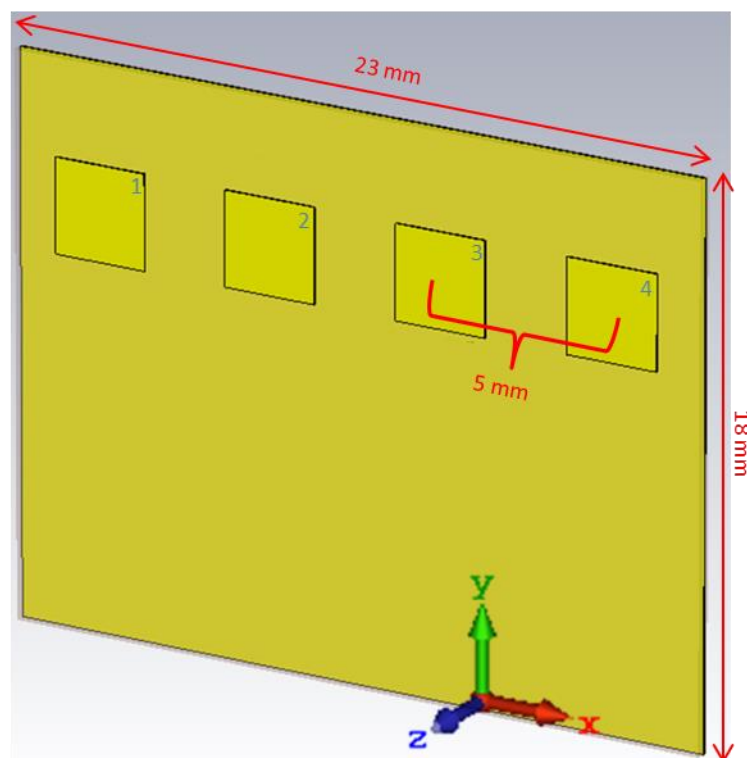


Figure 2.9 28 GHz 4 element linear antenna array on FPC

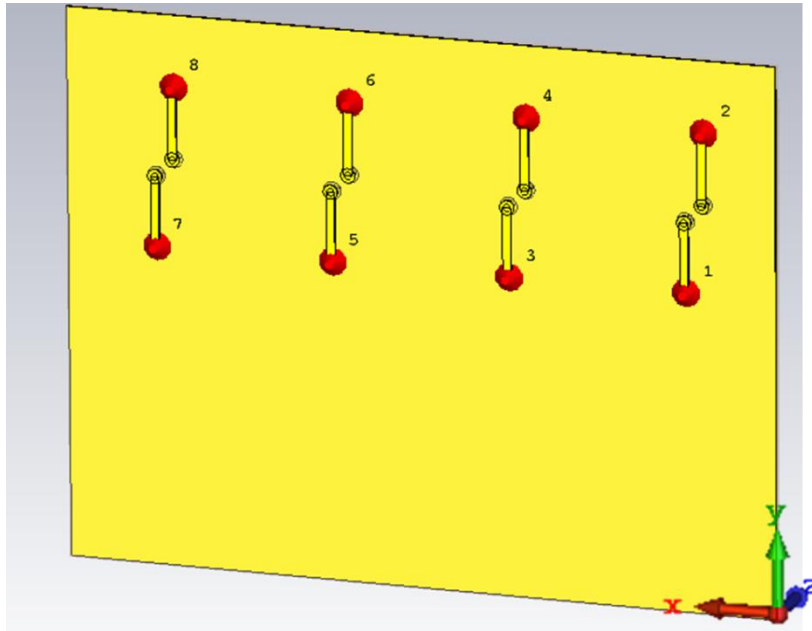


Figure 2.10 28 GHz 4 element linear antenna array feed locations

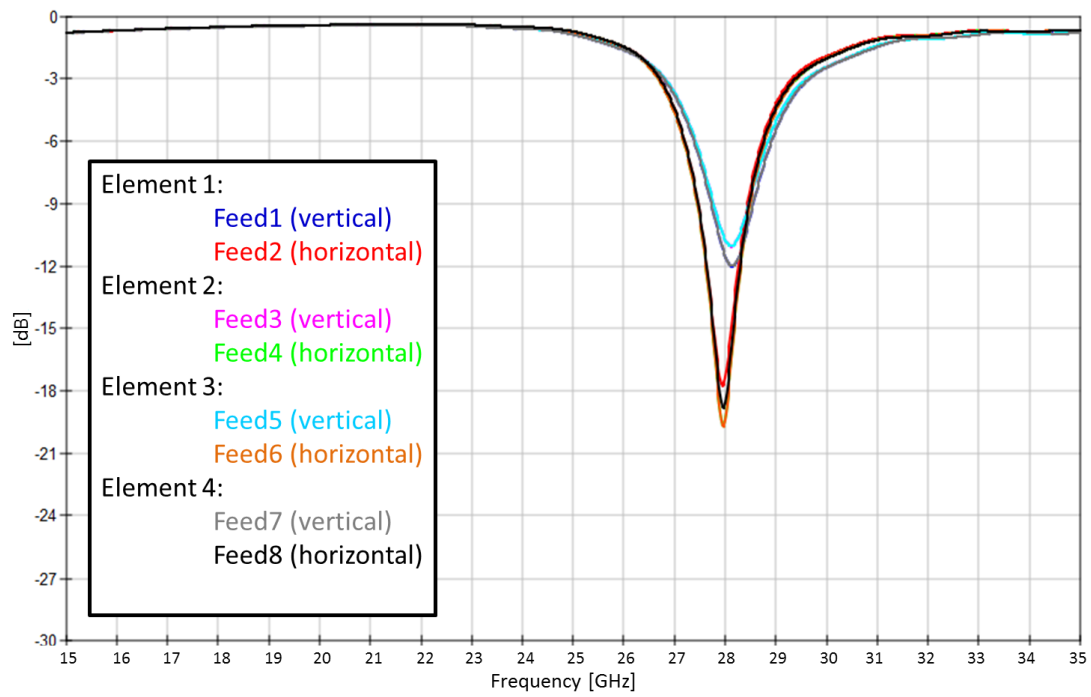


Chart 2.13 Return loss of all elements of the 28 GHz 4 element linear antenna array

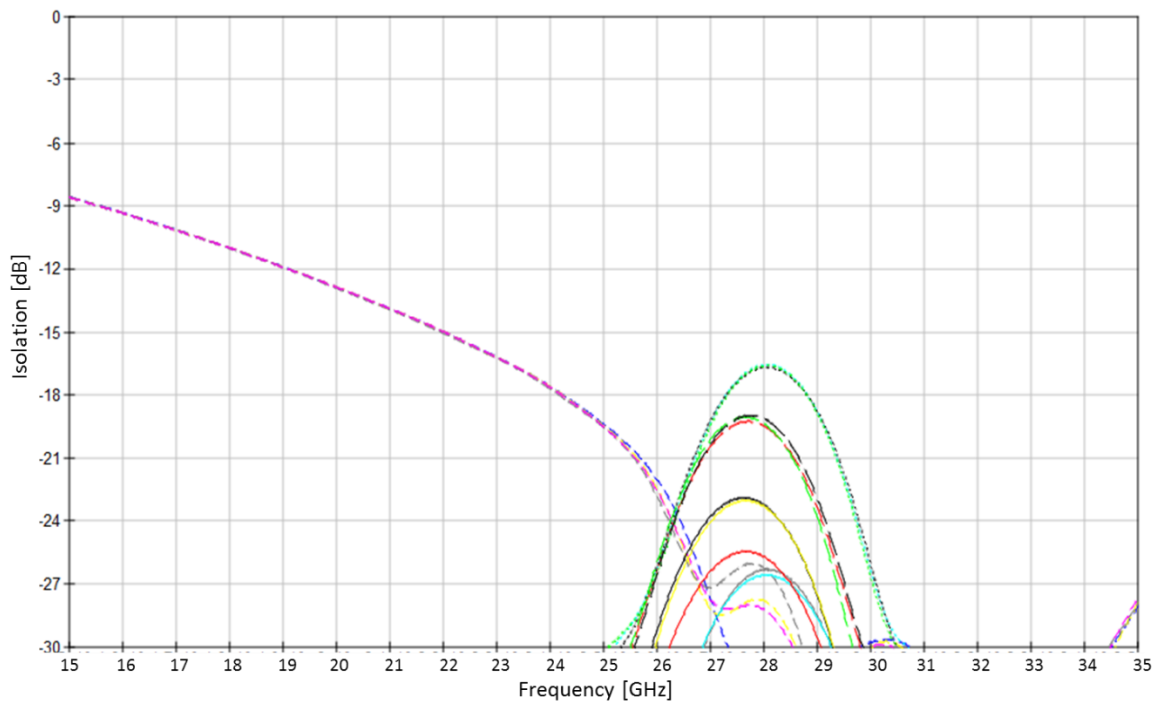


Chart 2.14 Isolation between all elements of the 28 GHz 4 element linear antenna array.

In the chart 2.14 the isolation between all the ports are plotted. The short dashed lines are the isolation between the each patch's vertical and horizontal polarization feeds, whereas the dotted lines are the isolation of the vertical polarization feeds with adjacent elements (feeds 1-3, 3-5, 5-7) and the long dashed lines are the isolation of the horizontal polarization feeds with adjacent elements (feeds 2-4, 4-6, 6-8). The poorest isolation is with the adjacent vertical feeds with -16 dB which is sufficient isolation between the different elements. The in element isolation between the two polarization feeds has slightly deteriorated from the single unit feed but is still has sufficient minimum isolation of 24 dB between the two polarization feeds at 28 GHz [35].

In charts 2.15 to 2.18 the combined, or the antenna array's, peak gain and gain cuts of the 4 element linear antenna array are shown for both vertical and horizontal polarization feeds. To get the combined results the vertical (feeds 1, 3, 5, and 7) and horizontal (feeds 2, 4, 6, and 8) feeds are combined separately in CST microwave studio post-processing with zero phase shift between the ports together to get the array gain as the elements are simulated in CST with individual ports. These results represent the optimal performance of the antenna array without any losses due the feeding network which is needed in real products.

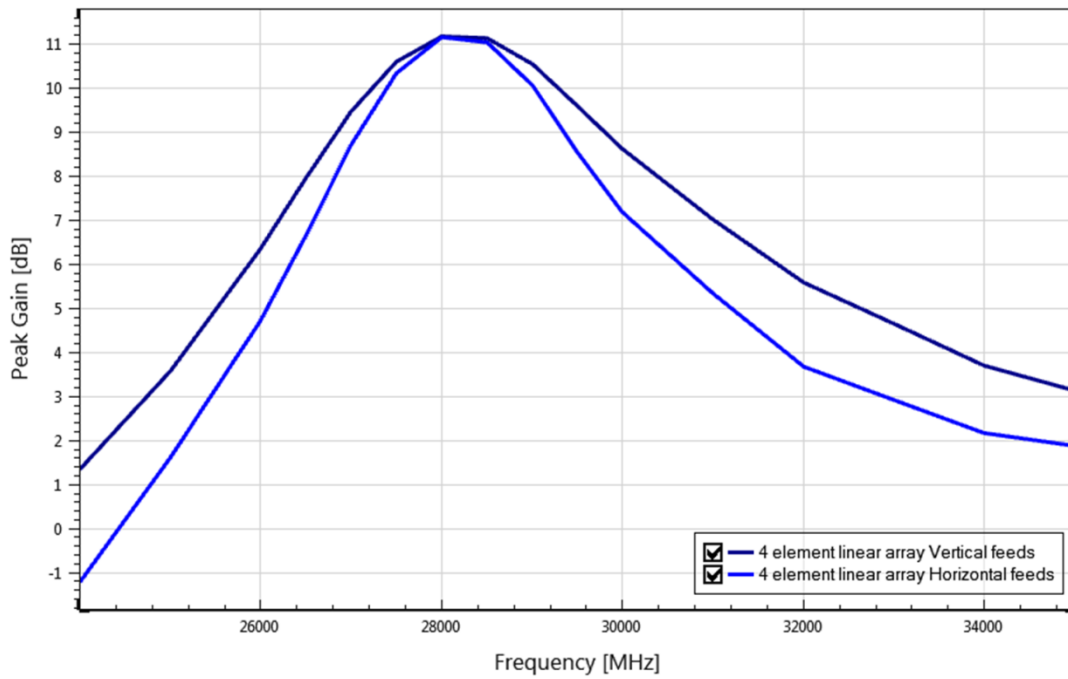


Chart 2.15 The peak gain of combined vertical and horizontal feeds of the 4 element linear antenna array

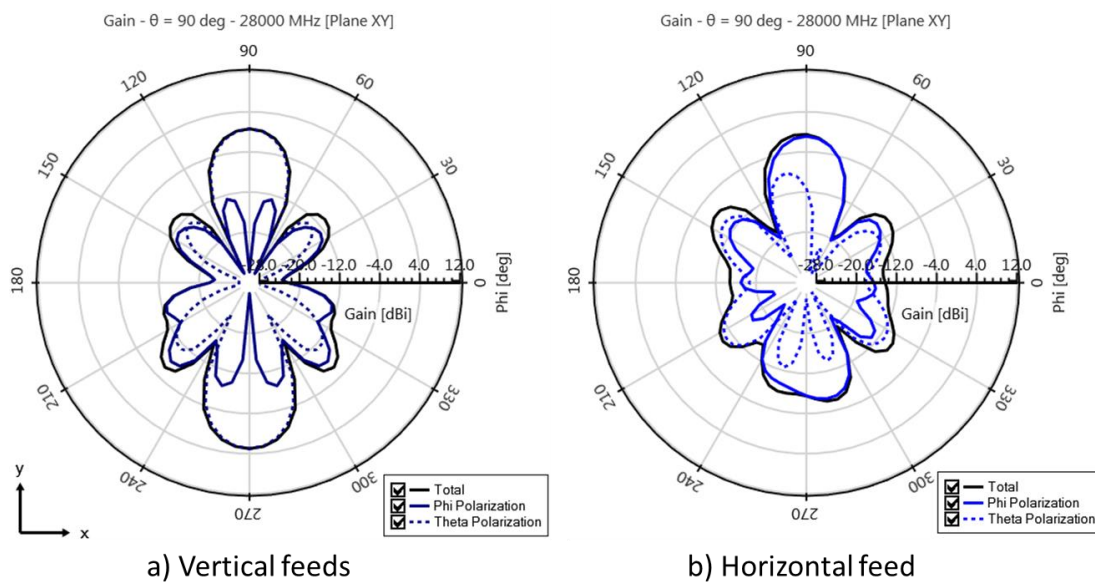
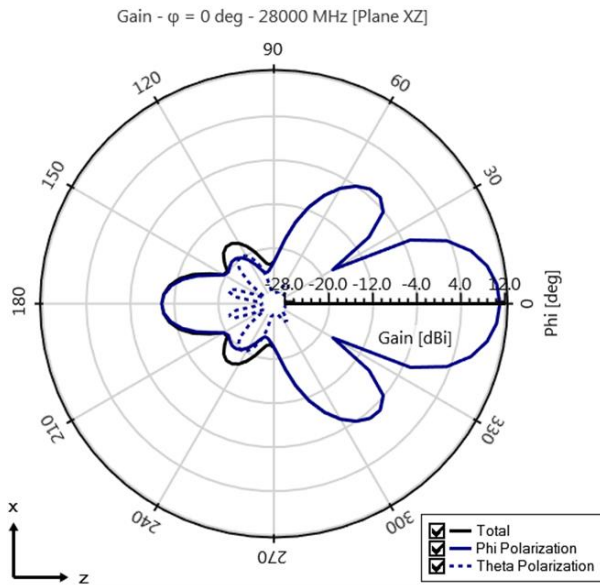
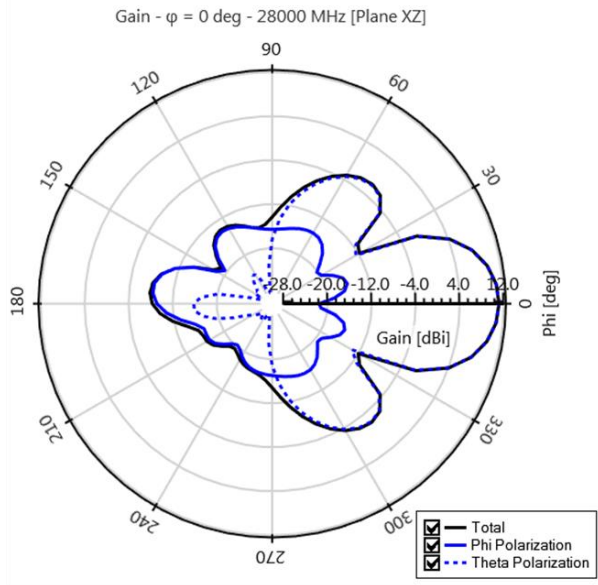


Chart 2.16 The XY-cut of the gain pattern of the 4 element linear antenna array's both polarization ports at 28 GHz

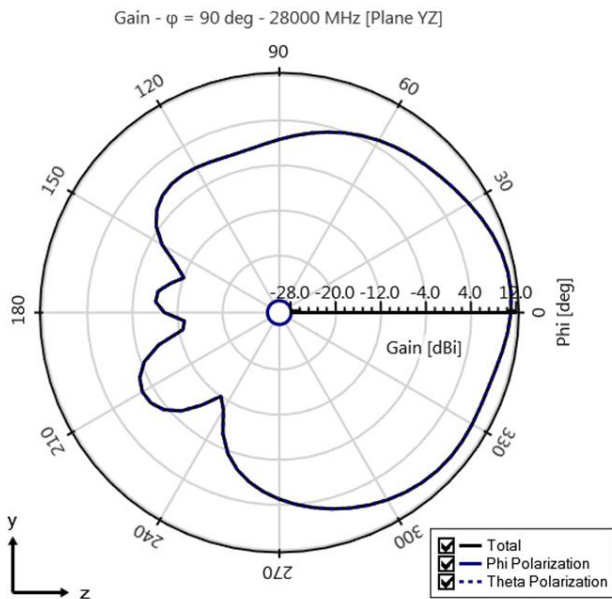


a) Vertical feeds

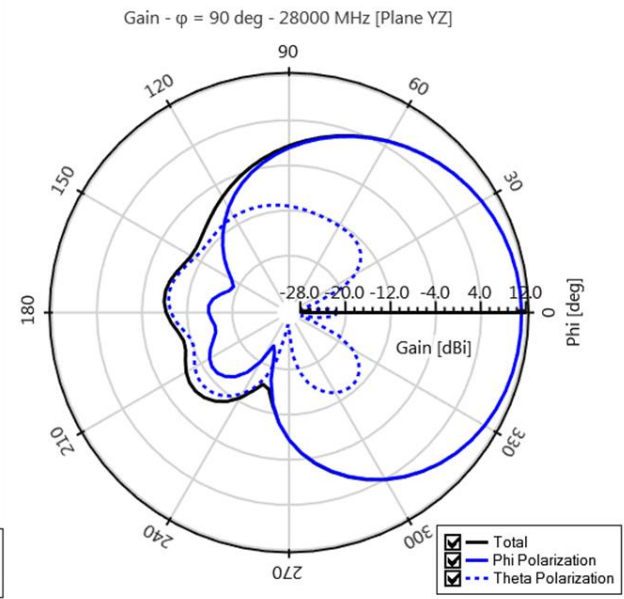


b) Horizontal feed

Chart 2.17 The XZ-cut of the gain pattern of the 4 element linear antenna array's both polarization ports at 28 GHz



a) Vertical feeds



b) Horizontal feed

Chart 2.18 The YZ-cut of the gain pattern of the 4 element linear antenna array's both polarization ports at 28 GHz

Unlike with the unit element gain patterns the difference between the vertical and horizontal polarization is not evident in the total gain patterns of the two feeds in the chart 2.16. With

more closer look and comparing the charts 2.16-2.18 to charts 2.10-2.12 we can observe that the phi and theta components of the vertical feed unit element and the 4 element array are behaving same way in the different cuts and are clearly different than the horizontal feed phi and theta components. In fact the dominant component is the opposite between vertical and horizontal feeds both in unit element and in the full array. This confirms that the dual polarization performance is preserved in the full antenna array design.

Although the distance between the antenna elements in the designed antenna arrays is smaller than the minimum requirement of one wavelength for linear arrays to minimize the side lobe levels the both polarizations have side lobes visible in the XZ gain-cut in chart 2.17. Although the side lobe levels are 16 dB lower than the main lobe a tighter spacing of the elements were tried during the array design with 3D EM simulations. The comparison of the final design 5 mm element spacing to 3.75 mm element spacing ( $\sim \frac{2}{3} - \lambda$ ) are shown in the below charts 2.19-2.22. As seen from the results the side lobe levels shrinks with the 3.75 mm spacing compared to the wider spacing. But so does the peak gain and the peak gain bandwidth. As the designed array is limited with the peak gain compared to the gain requirements discussed earlier in this chapter the wider spacing is kept to maximize the gain of the antenna array.

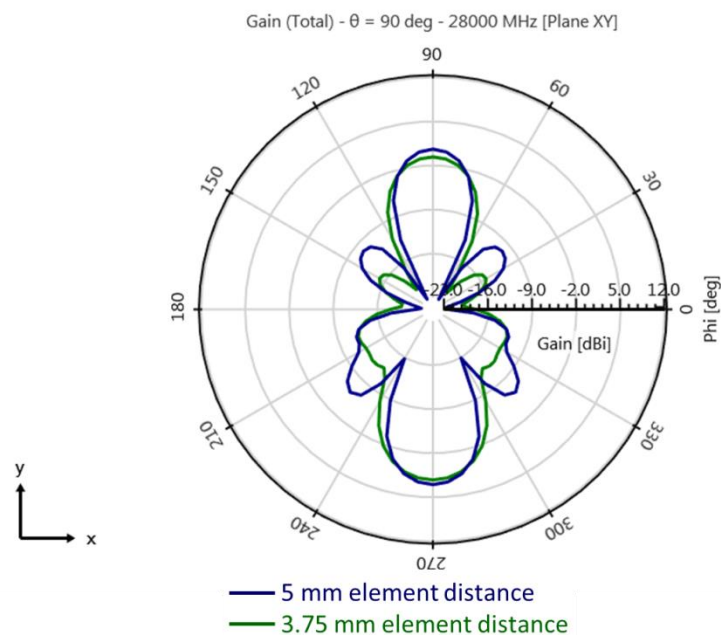


Chart 2.19 XY-cut of the gain patterns of 4 element linear antenna array with element spacing of 5 and 3.75 mm distances (vertical polarization feed) at 28 GHz



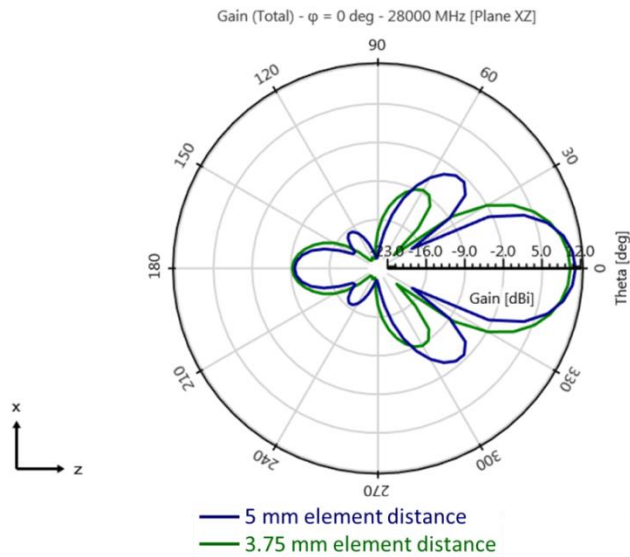


Chart 2.20 XZ-cut of the gain patterns of 4 element linear antenna array with element spacing of 5 and 3.75 mm distances (vertical polarization feed) at 28 GHz

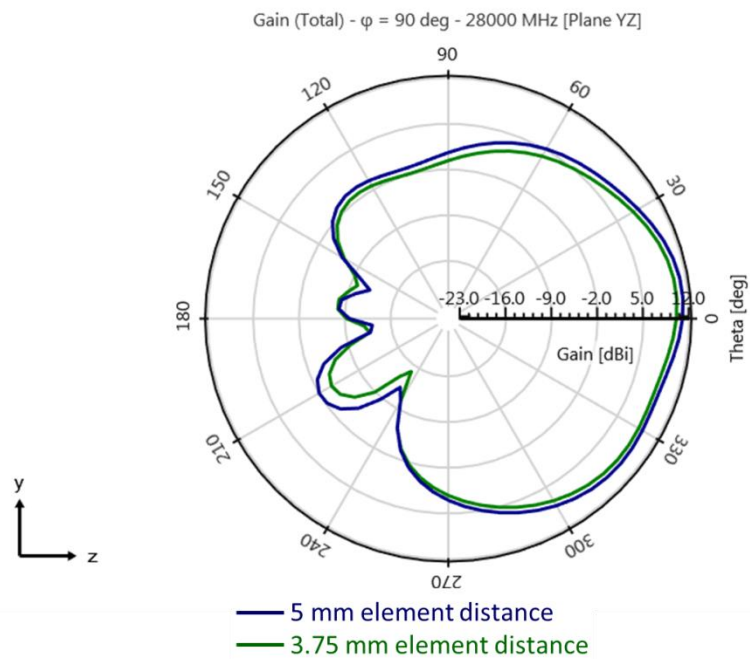


Chart 2.21 YZ-cut of the gain patterns of 4 element linear antenna array with element spacing of 5 and 3.75 mm distances (vertical polarization feed) at 28 GHz

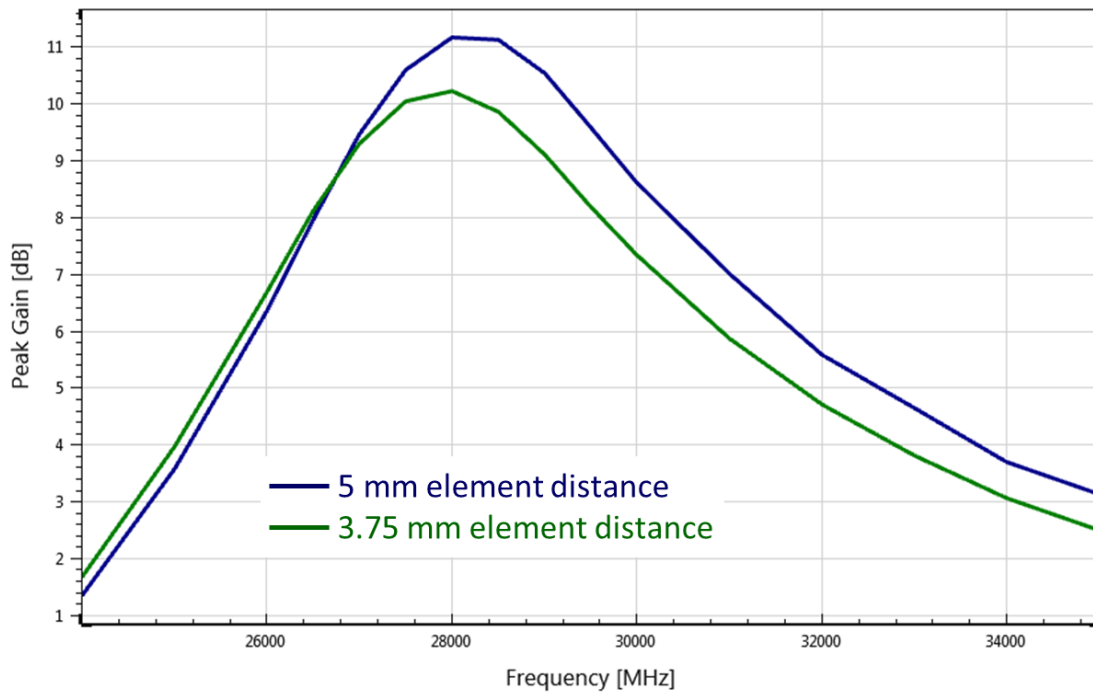


Chart 2.22 The peak gain of combined vertical feeds of the 4 element linear antenna array with 5 and 3.75 mm element spacing.

### II.2.3.3 Design of antenna array in FR-4 substrate

Before designing the full low cost FPC array with the feeding network, two 28 GHz antenna arrays with low cost FR-4 substrate were simulated and measured in AVX/Ethertronics 5G measurement system to verify the simulation results.

For this study planar antenna array is used instead of linear array, but the number of the elements is kept same (4 elements). The change to planar array is done to help the layout of the individual fed antenna array with the restricted space.

Two versions of the planar four element array were designed, one with individual feed lines for each element and polarizations and second with combined feed networks per polarization. The two arrays designed are shown in the figures 2.11 and their feeding networks in 2.12. The sizes of the antenna elements are slightly reduced to accommodate the changed permittivity. Also the stack up of the array has been modified to be better suitable for FR-4 manufacturing, shown in figure 2.13. The feeding network, shown in figure 2.12 a), for the individual feeds has equal length for each transmission line, whereas for the combined feed the length of the transmission lines, shown in figure 2.12 b), are equal for both polarization, port 1 for vertical polarization and port 2 for horizontal polarization. The 3 dB power divider for the combined feed is shown in figure 2.14 and the insertion loss from port 1 (common port) to port 2 and port 3 is shown in chart 2.23. The power divider has a  $\frac{\lambda}{4}$

length long low impedance ( $35.4 \Omega = \frac{50\Omega}{\sqrt{2}}$ ) transmission line which converts the combined impedance of the two parallel  $50 \Omega$  transmission lines to the  $50 \Omega$  impedance of the common port (port1) [34]. The T-line power divider is not as efficient as a Wilkinson power divider, but is much easier to integrate with the stripline transmission line structure as no external impedances are needed [16]. The designed 3 dB power divider is working well at frequency range in interest having only 0.5 dB more losses than an ideal 3 dB power divider.

Also the land pattern for the connector used to connect the array to the measurement system is shown in the figure 2.15. The 2.92 mm, also known as V-connector, connector designed by Anritsu is a connector especially designed for mmWave frequencies up to 65 GHz.

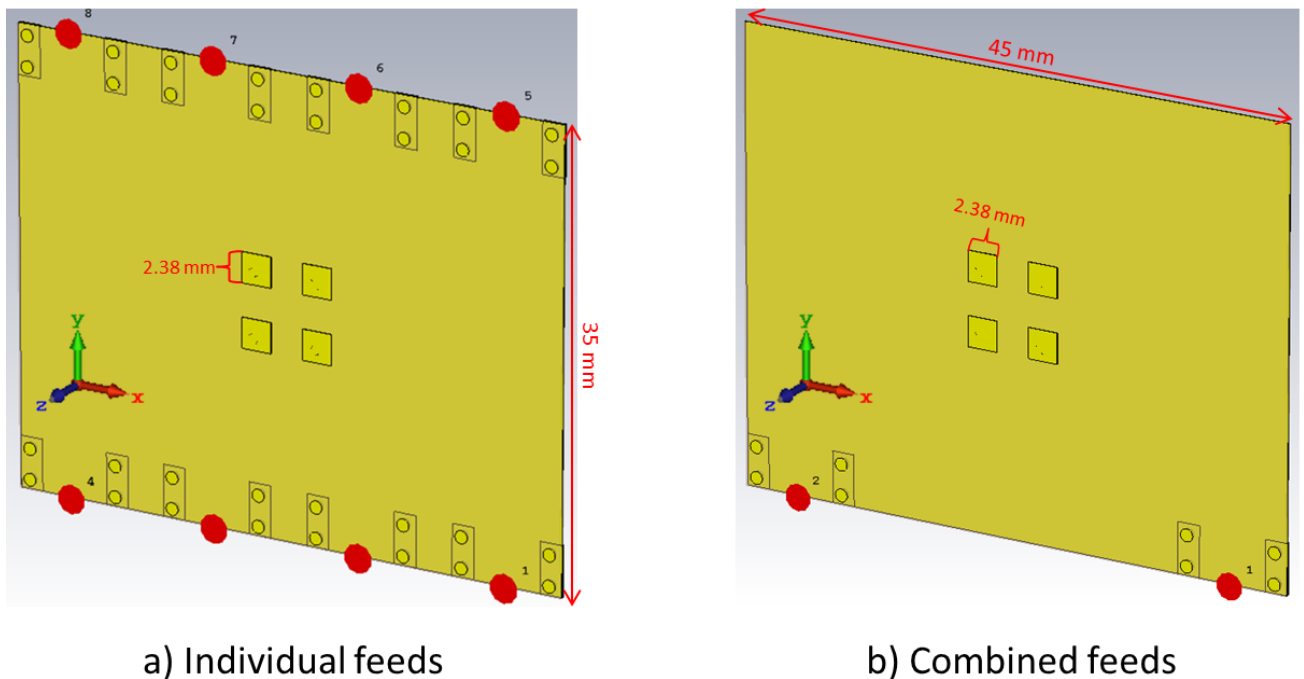


Figure 2.11 2x2 FR-4 planar antenna arrays

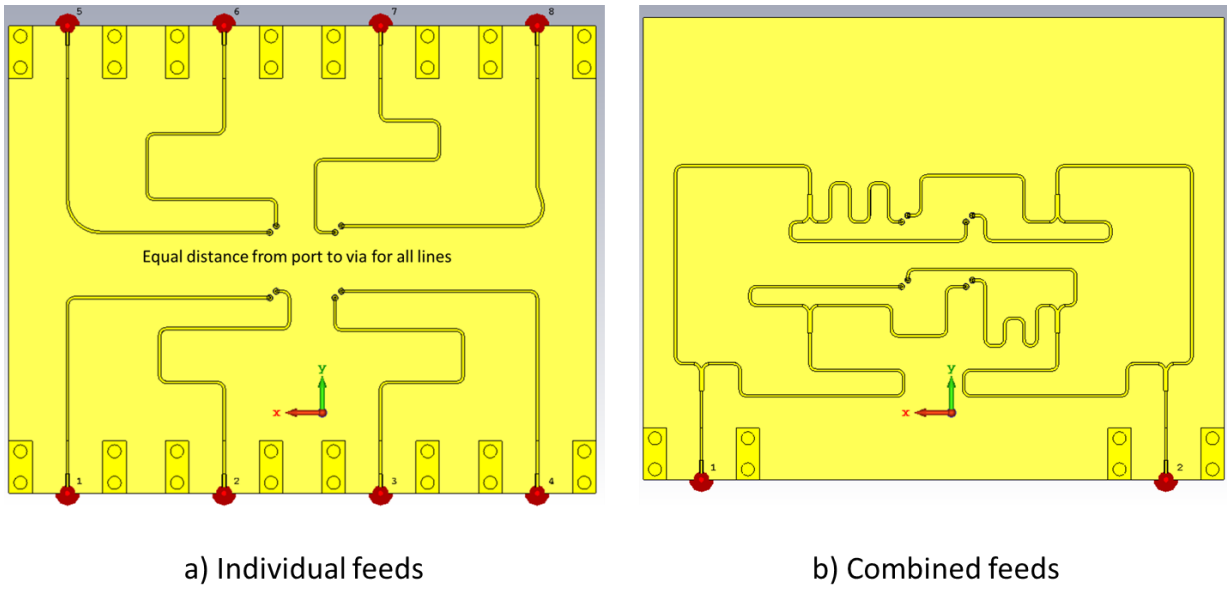


Figure 2.12 2x2 FR-4 planar antenna array feeding networks

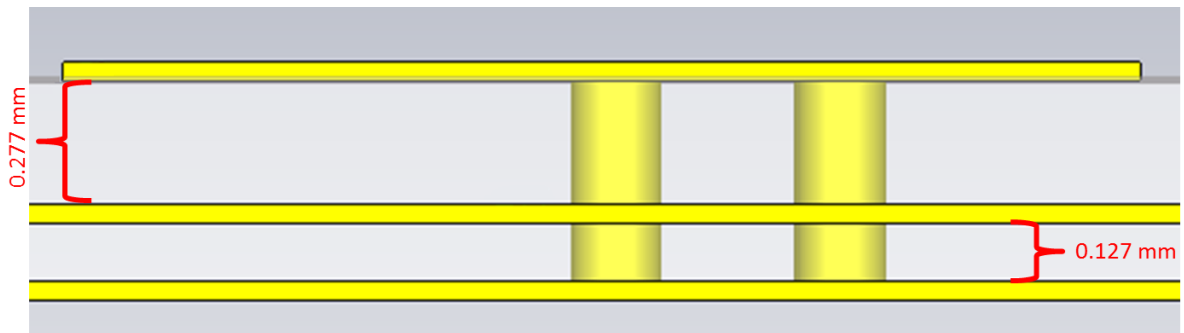


Figure 2.13 The stack up of the FR-4 antenna arrays

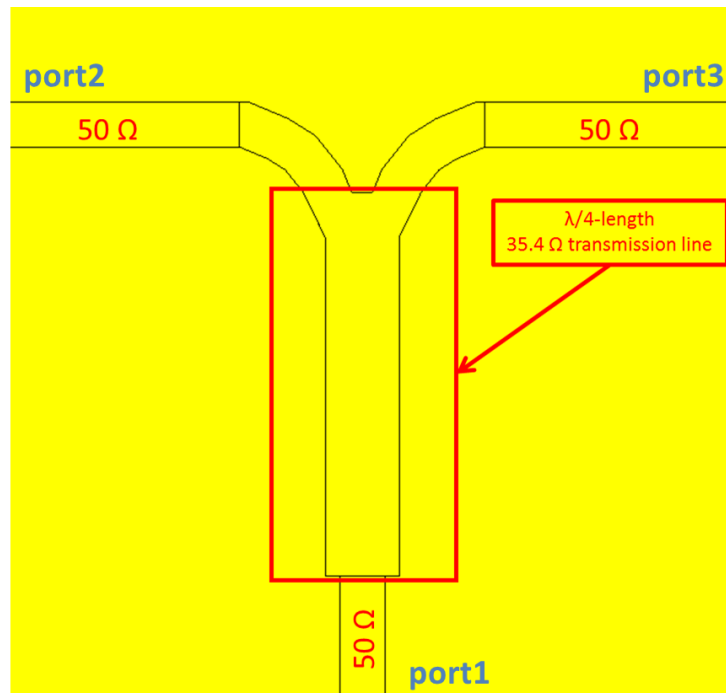


Figure 2.14 The 3 dB power divider used in combined feeds feed network

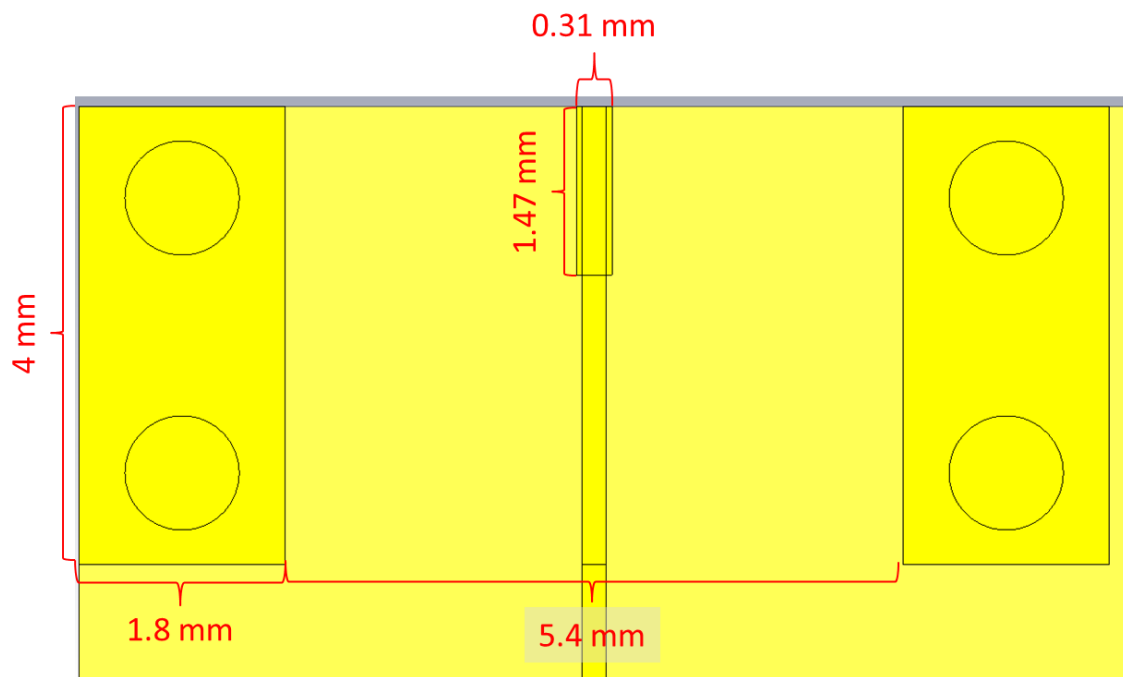


Figure 2.15 The 2.92 mm (V-connector) connector's land pattern in CST simulations

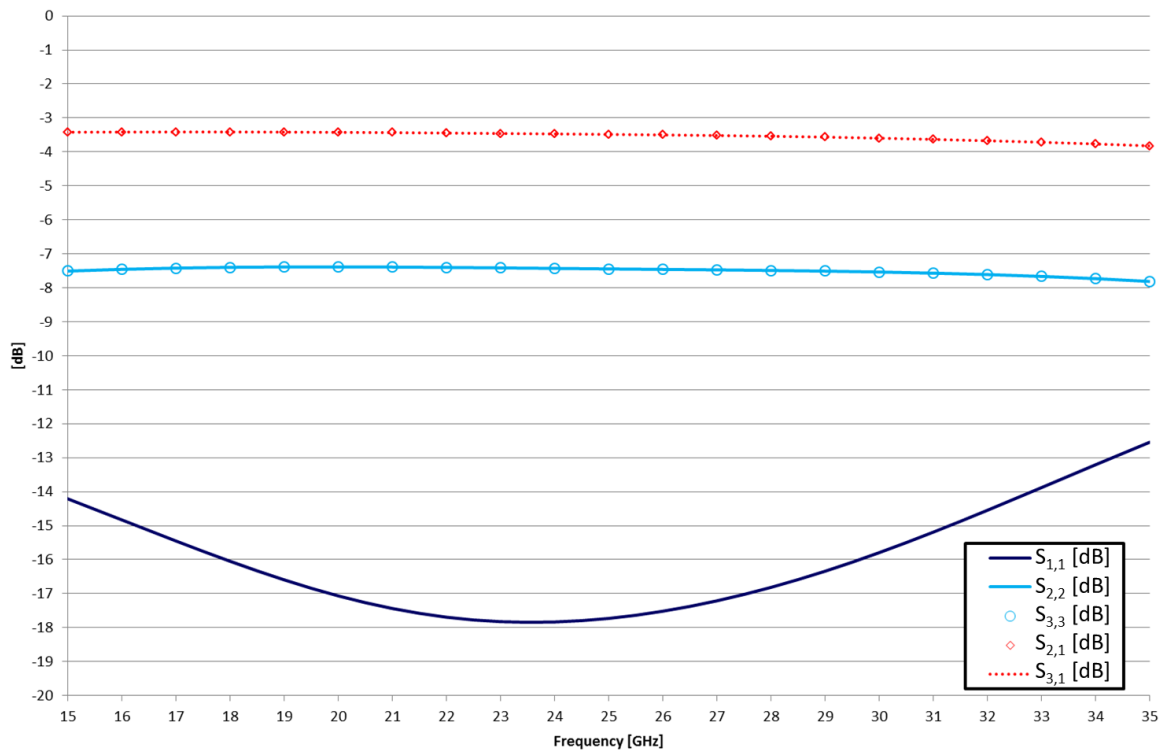


Chart 2.23 Insertion loss and input matching of the power divider of the combined feed array

For planar antenna arrays the elements spacing should not be more than half of the wavelength of the operated frequency for minimizing the side lobe levels [32]. To find out the best spacing for maximizing the gain a same study of the element spacing was carried out with the FR-4 planar array with individual feeds as it was done with the linear FPC array. In addition with the FR-4 substrate also element placement of  $\frac{\lambda}{2}$  was studied (2.5 mm in FR-4 is  $0.48 \lambda$  to be exact). In chart 2.24 the peak gain results of the study are shown for the combined vertical ports for the individual feed array. As it was with the linear array the highest peak gain is achieved with the 5 mm spacing, the lowest peak gain with the 2.5 mm spacing. It can be also seen that placing the element this close to each other the resonant frequency is tuned lower in frequency due the loading of the adjacent elements. Placing elements further away increase the peak gain and unlike with the linear array the side lobe levels do not increase as the placing distance increases as can be seen from the chart 2.25 where the gain patterns in XZ-plane of the three arrays with different element spacing are shown. Although this study was done with the individual feed array they are valid also for the combined feed array as the phase shift between the ports is same for both of the arrays.

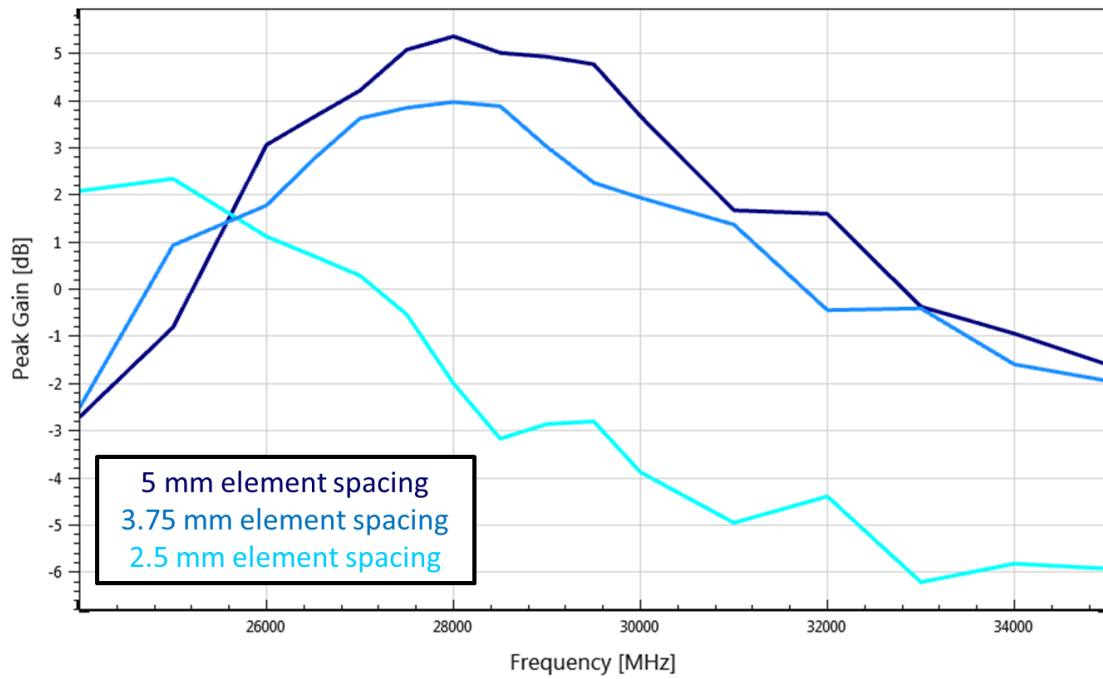


Chart 2.24 The peak gain of combined vertical ports with different element spacing

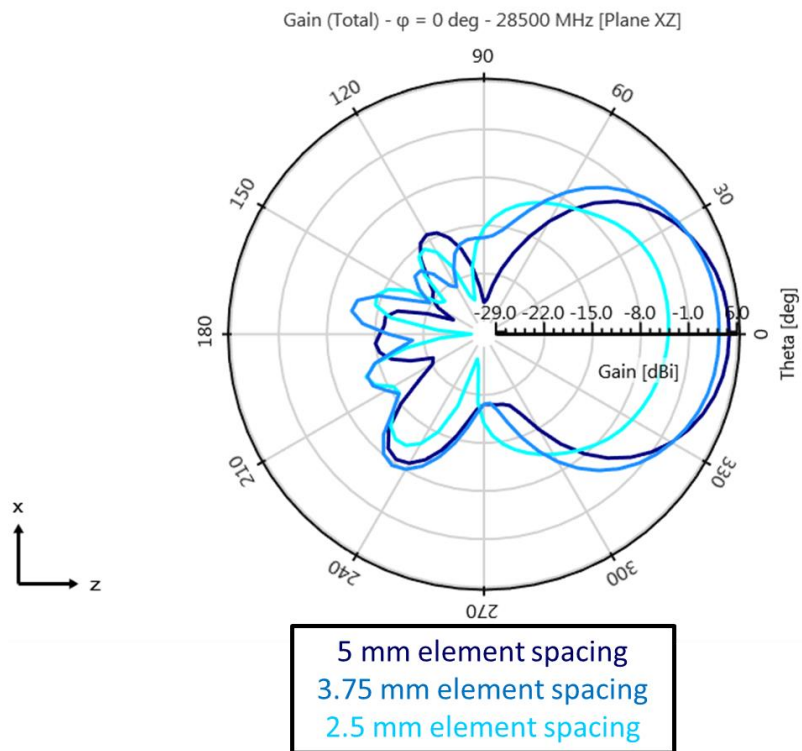


Chart 2.25 The XZ gain-cut of the combined vertical ports with different element spacing

After the optimal spacing for the elements is confirmed the two arrays can be designed in CST. An extra caution has to be taken when designing the feeding network for the combined feeds network. All the transmission lines have to be exactly in same length for optimum array performance and to be able to achieve the equal length lines some of the transmission lines have to be meandered as we can see from the figure 2.12 b).

In charts 2.26 to 2.28 the return loss and the isolation between all the ports are plotted for both the individual feed (8 port) and combined feeds (2 port) models. As we can see from the charts 2.26 and 2.28 the both array's return losses have periodical minimums. These minimums appears to the return loss as the length of the transmission lines, both in individual and combined feeds, are multiple wavelengths long. Because these periodical resonances it is slightly difficult to see the antennas resonances from the return loss of the individual feeds, but with comparing the isolation with the resonance at 28 GHz can be confirmed. The antenna resonance is more clearly visible for the combined feed array although it has too periodical minimums just like the individual feed array.

In the charts 2.29 to 2.35 the peak gain and the gain pattern cuts of the both arrays for both polarizations are visualized. Just like in the linear array case the combined peak gain and gain patterns of the individual feeds (8port) are calculated in the CST post-processing without any phase shift between the antennas, for the vertical polarization the ports 1-3-5-7 are combined and ports 2-4-6-8 are combined for the horizontal polarization. No results combining is done for the combined feed (2port) array as the vertical and horizontal polarization feeds are already combined in the model with feeding network.

The 3 dB gain difference between the individual and the combined feed peak gain results is due the longer feeding network design with non-ideal power dividers in the combined feed array. Otherwise the two arrays have similar shape of the peak gain curves. The combined feed array's peak gain is just 3 dB lower than the individual feed array's. The vertical and horizontal polarization feeds work correctly and the strongest component ( $\phi/\theta$ ) changes between the polarization feeds as we can see from the charts 2.32 to 2.35. If we compare the 2.33 to 2.32 and 2.35 to 2.34 we notice that the back lobe levels are relatively higher for the combined feed. This can be explained by the longer feed network lines which are radiating to the back side of the array.



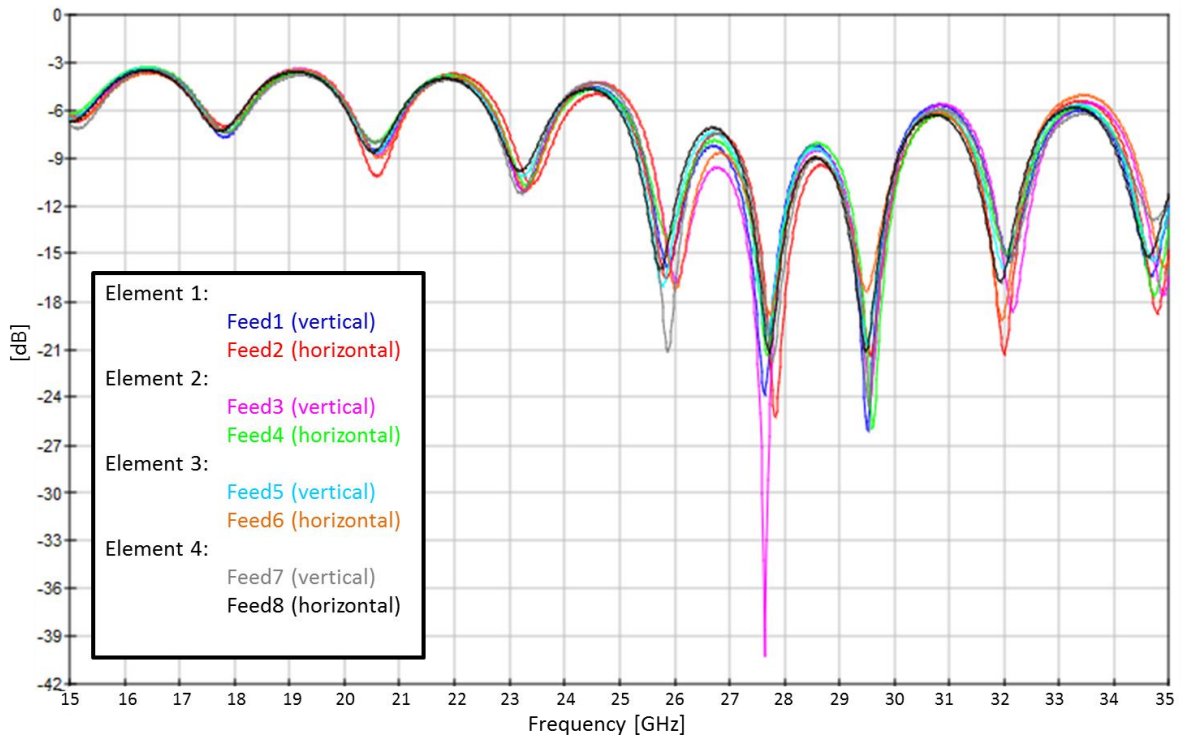


Chart 2.26 The simulated return loss of the 2x2 FR-4 antenna array with individual feeds

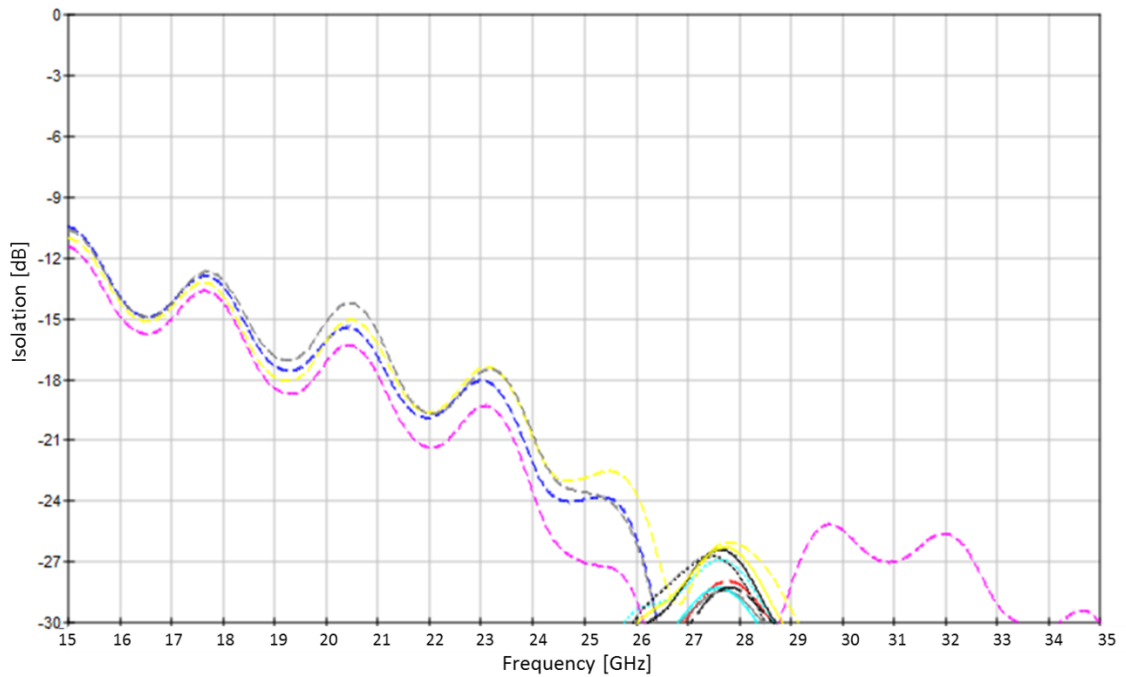


Chart 2.27 The isolation between all the feeds of the 2x2 FR-4 array with individual feeds

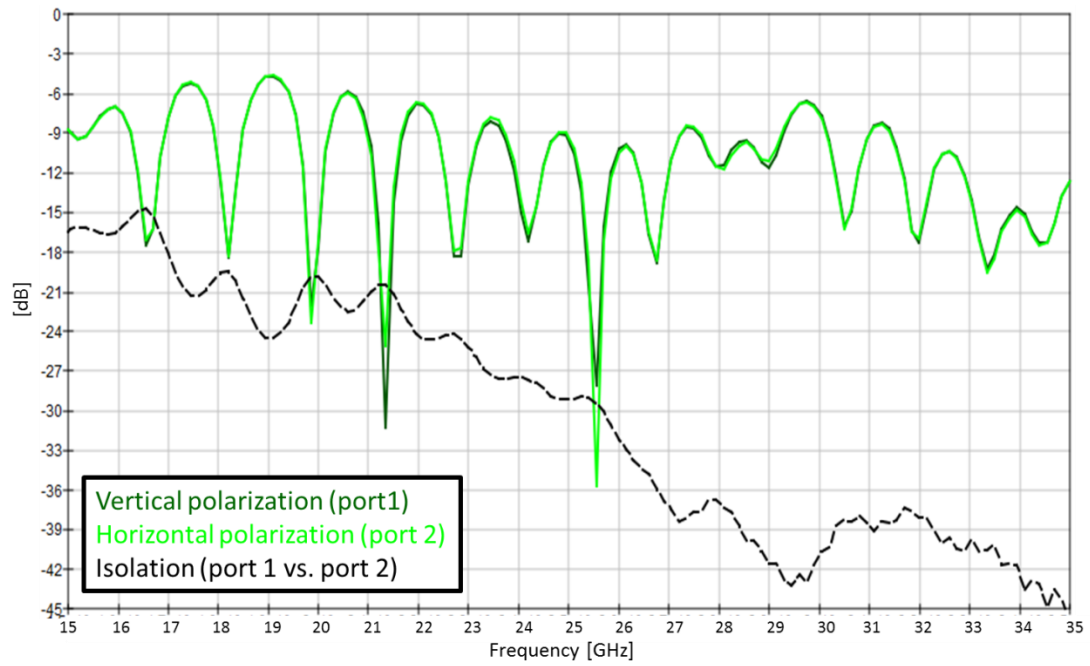


Chart 2.28 The return loss and isolation of the 2x2 FR-4 antenna array with combined feeds

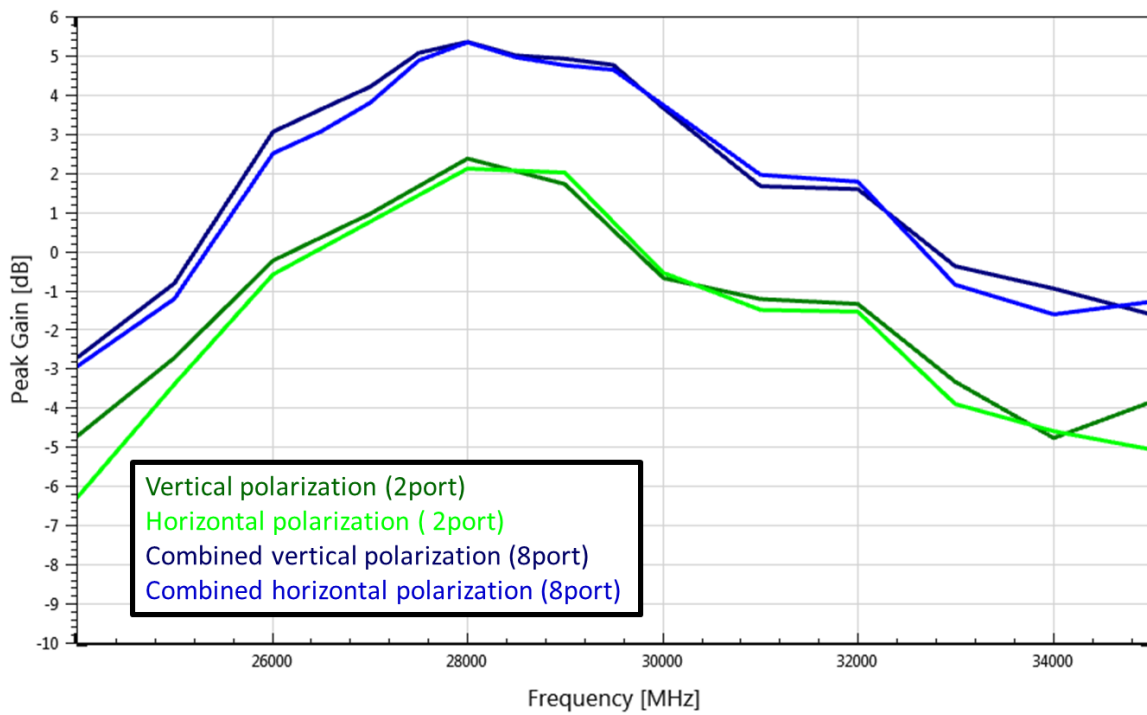
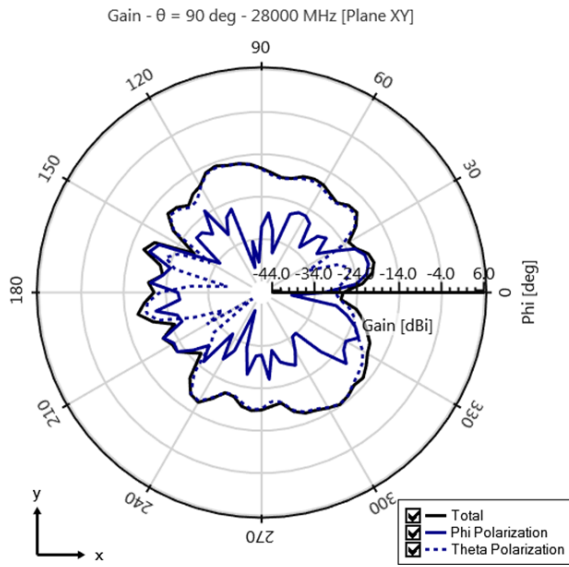
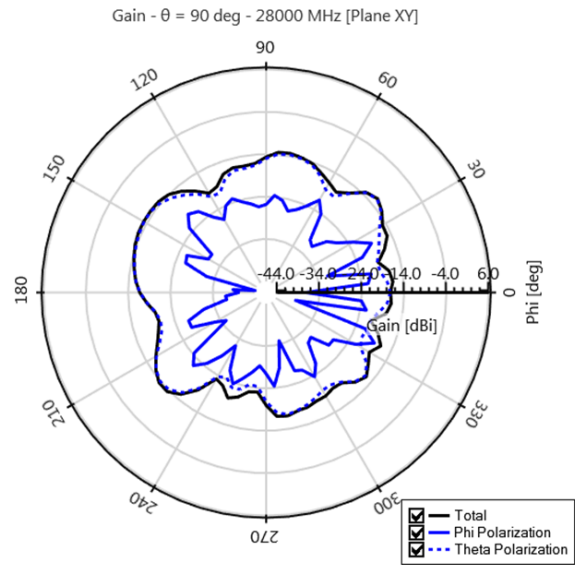


Chart 2.29 The peak gain of both FR-4 antenna arrays

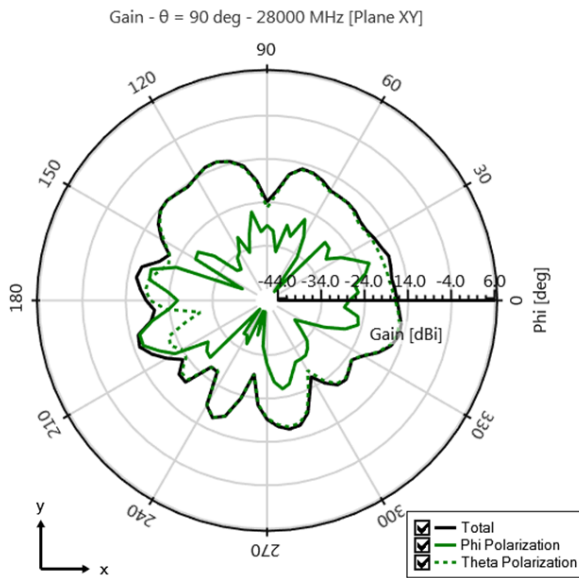


a) Vertical feed

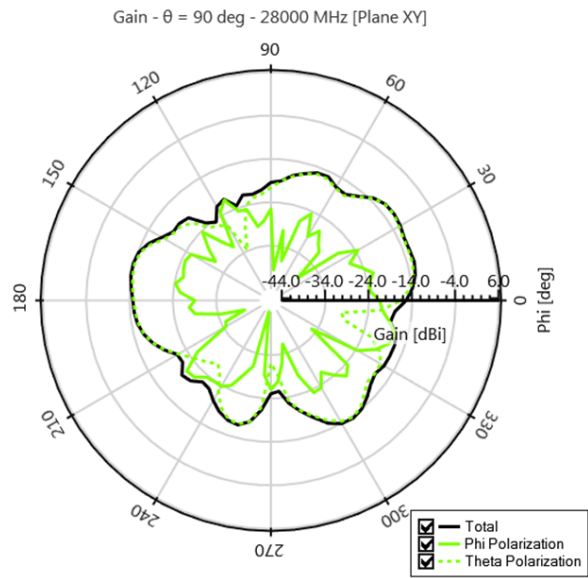


b) Horizontal feed

Chart 2.30 The XY-cut of the gain patterns for both polarizations of the FR-4 antenna array with individual feeds at 28 GHz

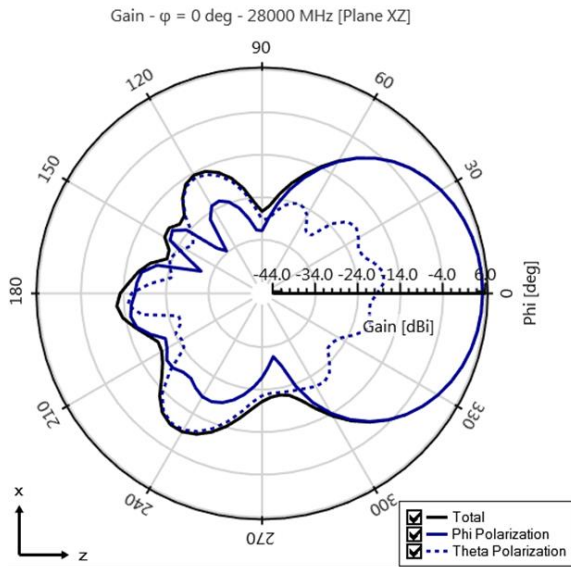


a) Vertical feed

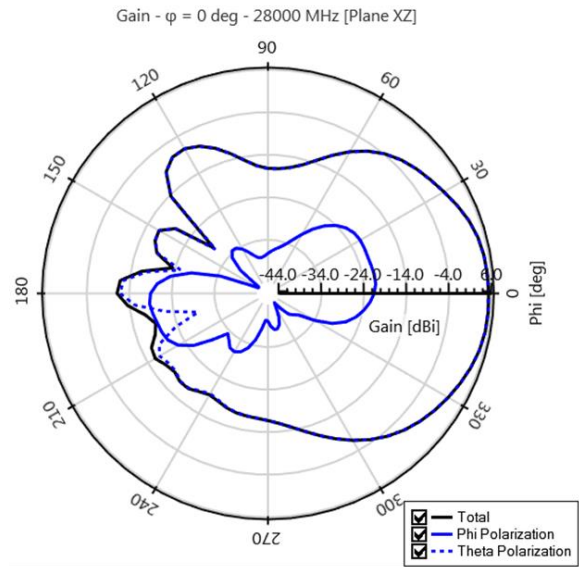


b) Horizontal feed

Chart 2.31 The XY-cut of the gain patterns for both polarizations of the FR-4 antenna array with combined feeds at 28 GHz

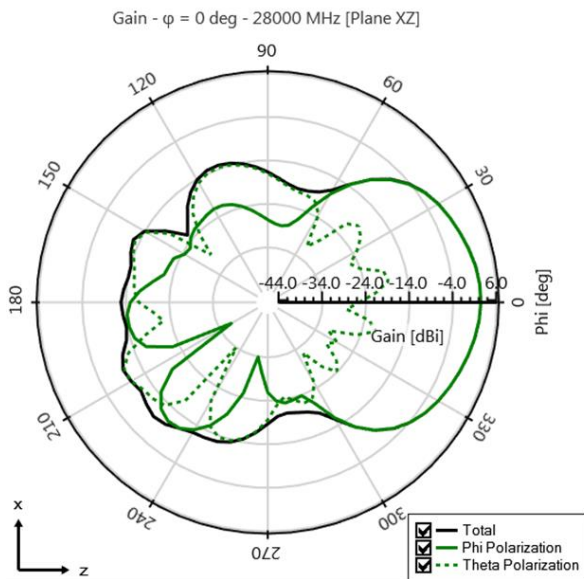


a) Vertical feed

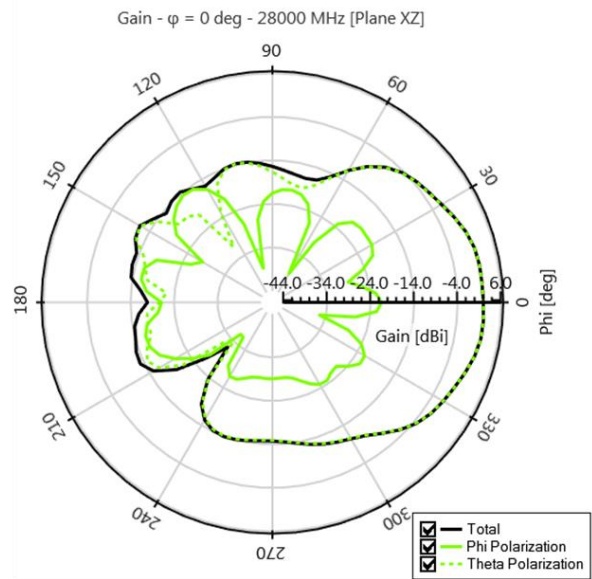


b) Horizontal feed

Chart 2.32 The XZ-cut of the gain patterns for both polarizations of the FR-4 antenna array with individual feeds at 28 GHz

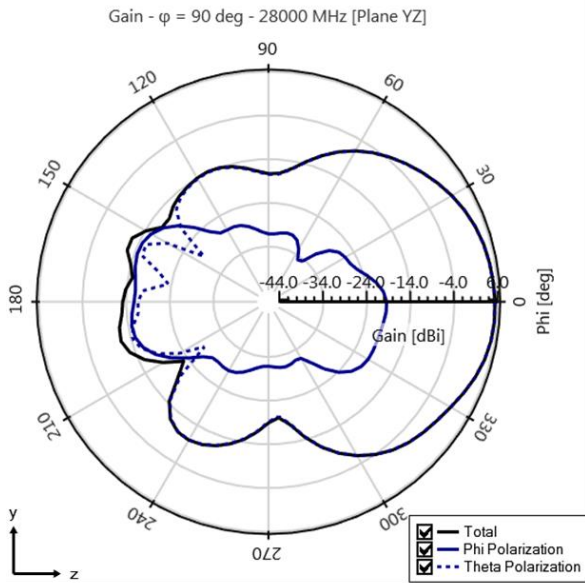


a) Vertical feed

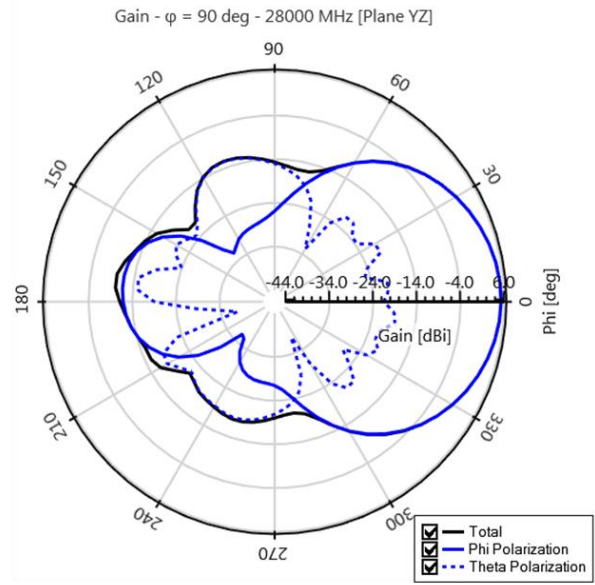


b) Horizontal feed

Chart 2.33 The XZ-cut of the gain patterns for both polarizations of the FR-4 antenna array with combined feeds at 28 GHz

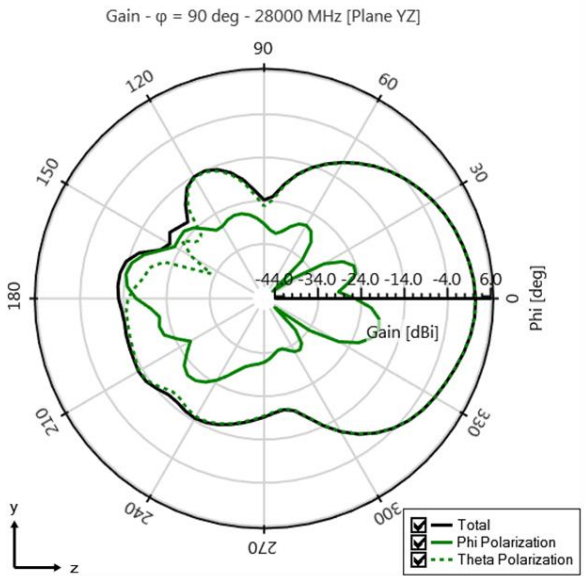


a) Vertical feed

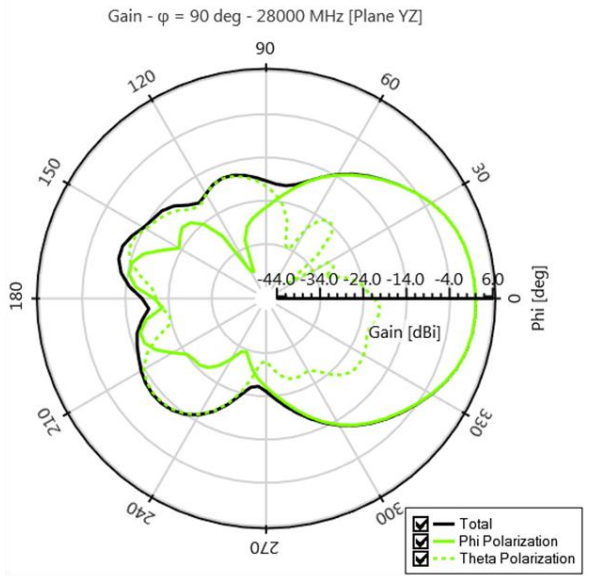


b) Horizontal feed

Chart 2.34 The YZ-cut of the gain patterns for both polarizations of the FR-4 antenna array with individual feeds at 28 GHz



a) Vertical feed



b) Horizontal feed

Chart 2.35 The YZ-cut of the gain patterns for both polarizations of the FR-4 antenna array with combined feeds at 28 GHz

After the arrays design have been finalized in the CST 3D EM simulations the sample antennas were manufactured on FR-4 PCB. In the figure 2.16 the manufactured combined

feed antenna array is shown with the 2.92 mm connectors. The individual feed array was manufactured also but not measured as only two pieces of 50  $\Omega$  loads were available for the 2.92 mm connector during the time of the measurements.

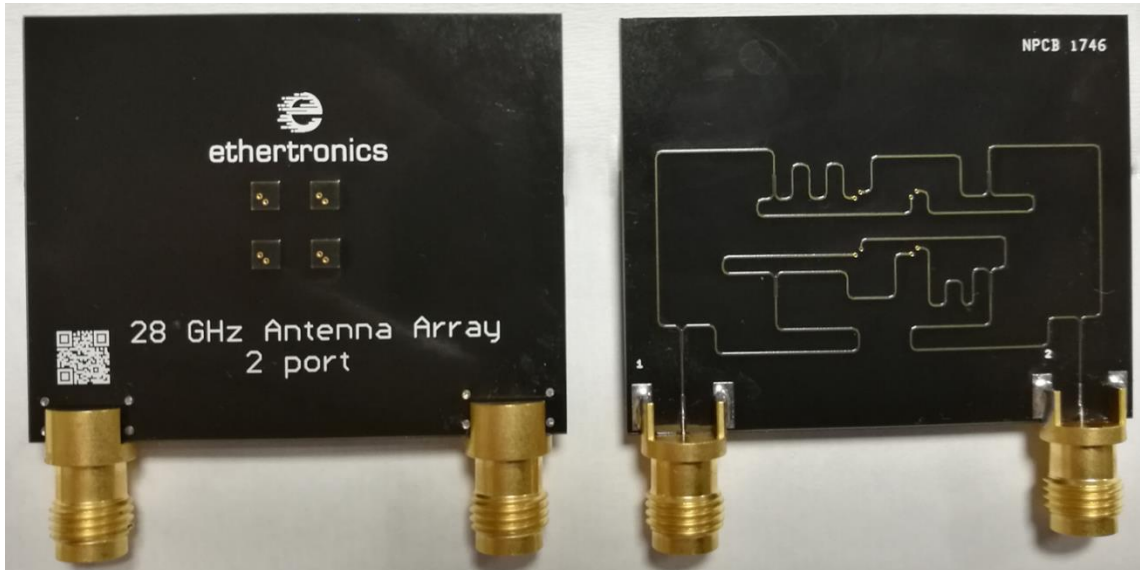
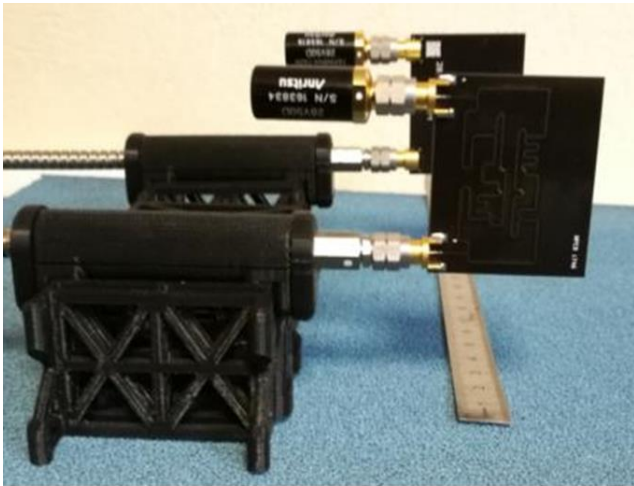


Figure 2.16 Front(patch side)- and back(feed network)-view of the manufactured FR-4 antenna array.

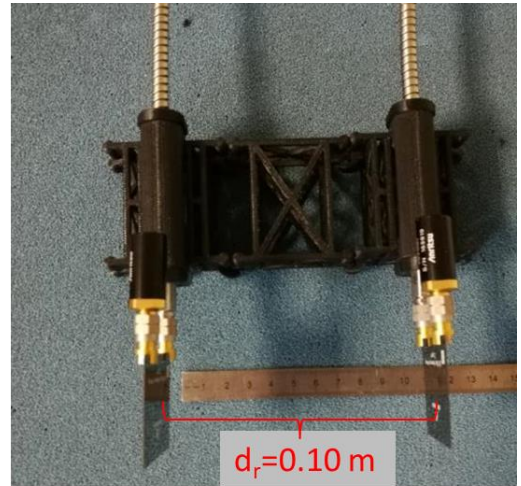
At the time when the FR-4 based patch antenna arrays were manufactured the AVX/Ethertronics mmWave 5G measurement system was not yet finished, and the array performance had to be tested with very rudimentary gain measurement setup, shown in Figures 2.17 and 2.18. The two antenna arrays were placed 10 cm from each other over on RF absorber and the  $S_{2,1}$  between the two arrays was measured with the Anritsu VectorStar MS4647B vector network analyzer. The “gain” was calculated with a formula  $\text{Gain} = (FSPL(f) + S_{2,1}(dB))/2$ , where  $FSPL(f)$  is the Free Space Path Loss (dB) given by the equation 2.7 [28].

$$FSPL = 20\log_{10}(d_r) + 20\log_{10}(f) + 20\log_{10}\left(\frac{4\pi}{c}\right) \quad (2.7)$$

where  $d_r$  is the distance between the two antennas, and  $c$  is the speed of light in vacuum



a)



b)

Figure 2.17 The gain measurement setup a) side and b) top views

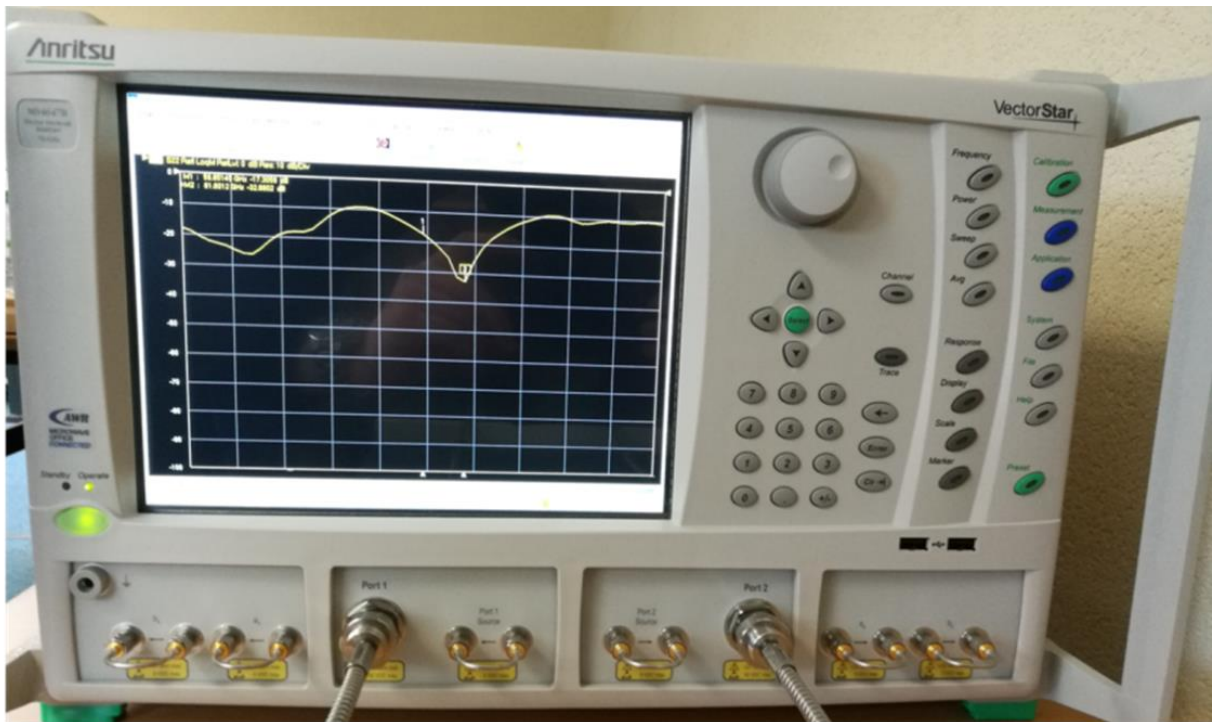


Figure 2.18 The Anritsu VectorStar MS4647B millimeter wave VNA

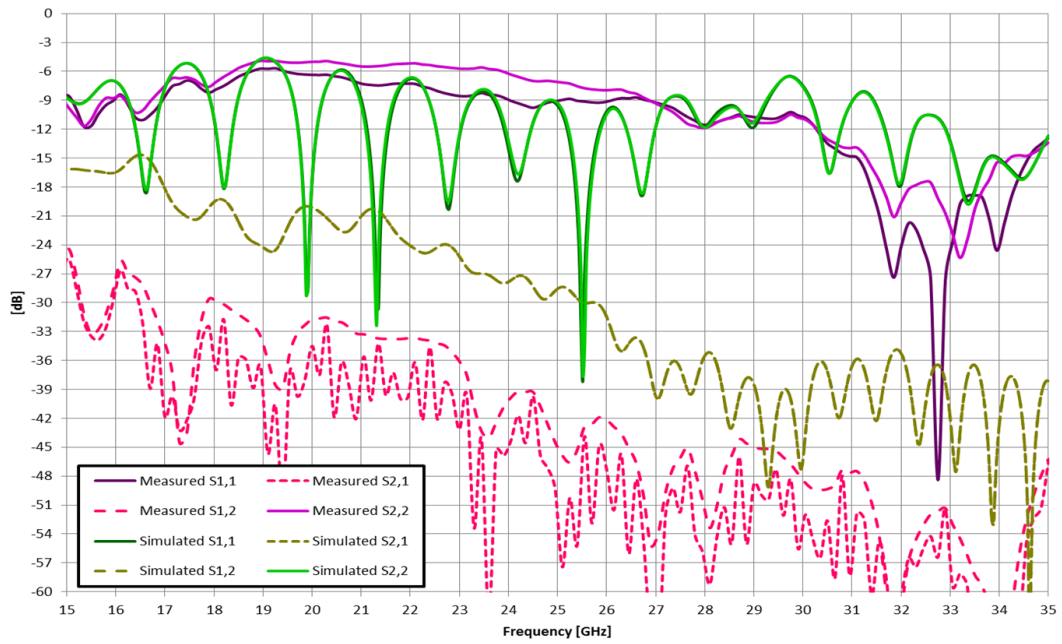


Chart 2.36 The return loss and isolation of the measured and simulated combined feed FR-4 antenna array

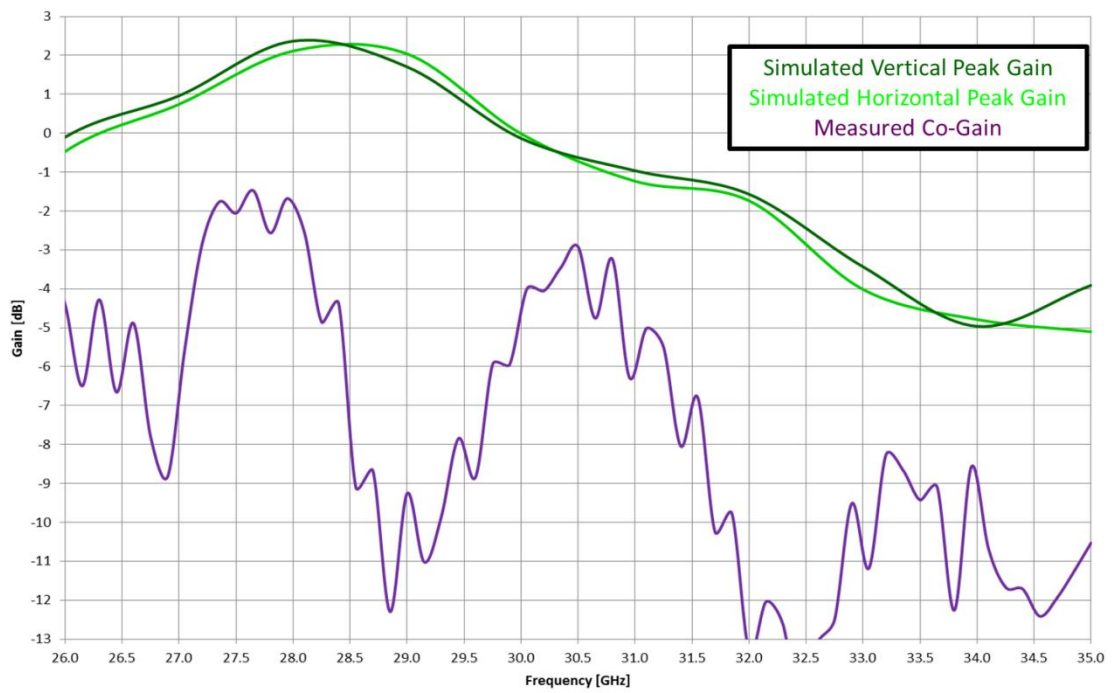


Chart 2.37 The Simulated Peak Gains and the Co-Gain of the measured combined feed FR-4 antenna array

In the charts 2.36 the measured antenna return loss is compared to the simulated results of the combined feed antenna array. The resonance of the antenna is same frequency both in



the simulation and measurements but there are very limited periodical resonances in the measured results. Also the isolation between the two polarizations is 10 dB better in the measurement compared to the simulated isolation. Both the improved isolation and the lack of the periodic resonances due the long feeding network can be partially explained with the slightly higher losses of the real FR-4 substrate compared to the simulated FR-4 substrate. The little bit higher losses of the measured FR-4 dampens the ringing and increase the isolation.

In the chart 2.37 the measured co-polarization “gain” (e.g. co-polarization gain = vertical polarization vs. vertical polarization) of the FR-4 antenna are shown. The peak gain of the co-polarization of the cross-polarization are 200 MHz lower than the simulated peak gains of the vertical and horizontal in polarizations. The peak co-gain value is 4 dB lower than in simulations, but as the measurement setup is very rudimentary the gain values between the simulation and measurements are not comparable in magnitude. But based on the measurement results one can assume that the manufactured antenna arrays are working roughly in the frequency they were designed in the CST simulations.

#### **II.2.3.4 Low loss FPC antenna array**

After confirming that the manufactured antenna array is correlating with the simulation model the design of the low cost antenna array can be started. To minimize the needed transmission lines in the design a combined feed approach from the FR-4 antenna array is chosen and to connect the antenna arrays to the centralized FEM (Front End Module) a cavity stripline from the chapter 2.2.2 is used to minimize the losses in the array system.

The design is started with the simplified model only including the antenna array and excluding the transmission lines. This way the simulation times can be kept in a reasonable level and after the antenna array design is finalized the transmission lines can be added to complete the model.

In the figure 2.19 the designed four element linear antenna array with combined feeds in FPC is presented. The antenna array is combinations of the linear element array of figure 2.9 and 2.12 b) where the element location is from the figure 2.9 and the feed network from figure 2.12 b). The length of the transmission lines for all the elements is same for both polarizations and the power divider is T-line power divider presented in figure 2.14 with the length and width adjusted to the permittivity of the FPC PI substrate.

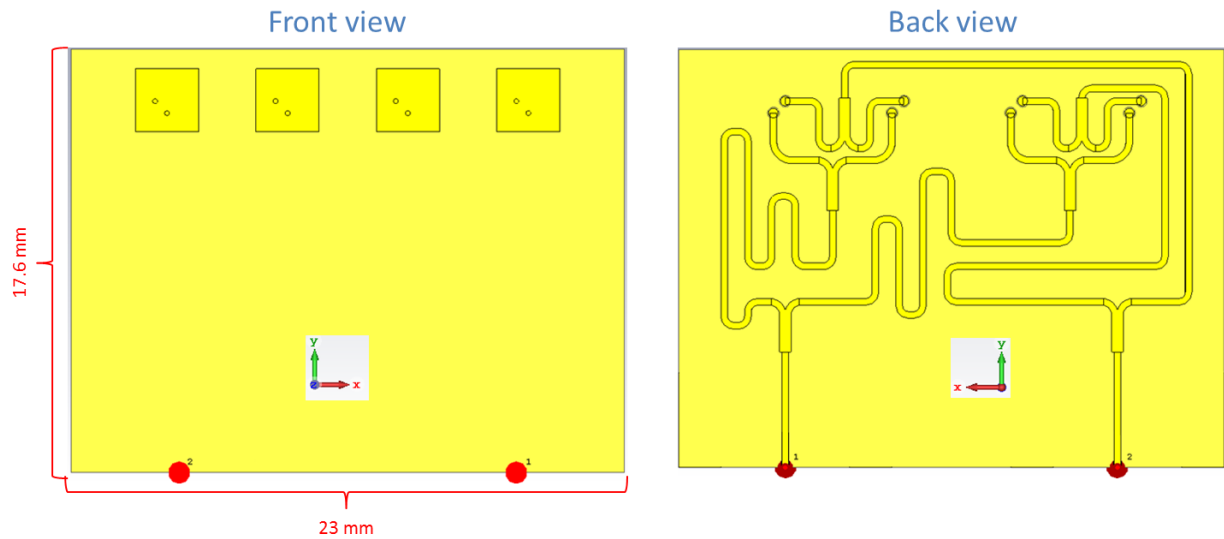


Figure 2.19 Antenna array element of the low cost antenna array

In the chart 2.38 the return loss of both polarization feeds and the isolation between the feeds are presented. The antenna array is matched with - 6 dB or better return loss in the 28 GHz band, also the isolation between the two polarizations is well below -20 dB.

The peak gain, gain cuts, and the 3D radiation patterns of both polarizations of the antenna array element are shown in the charts 2.39 to 2.43. From the gain-cuts patterns the dual polarization behavior can be confirmed. The dominant mode of the phi or theta component is changing between the polarization feeds as in the earlier designs. The vertical polarization has back lobe and side lobe levels of -10 dB and -19 dB respectively. The vertical polarization's back lobe and side lobe levels are slightly deteriorated from the vertical polarization and -8 and -16 dB.

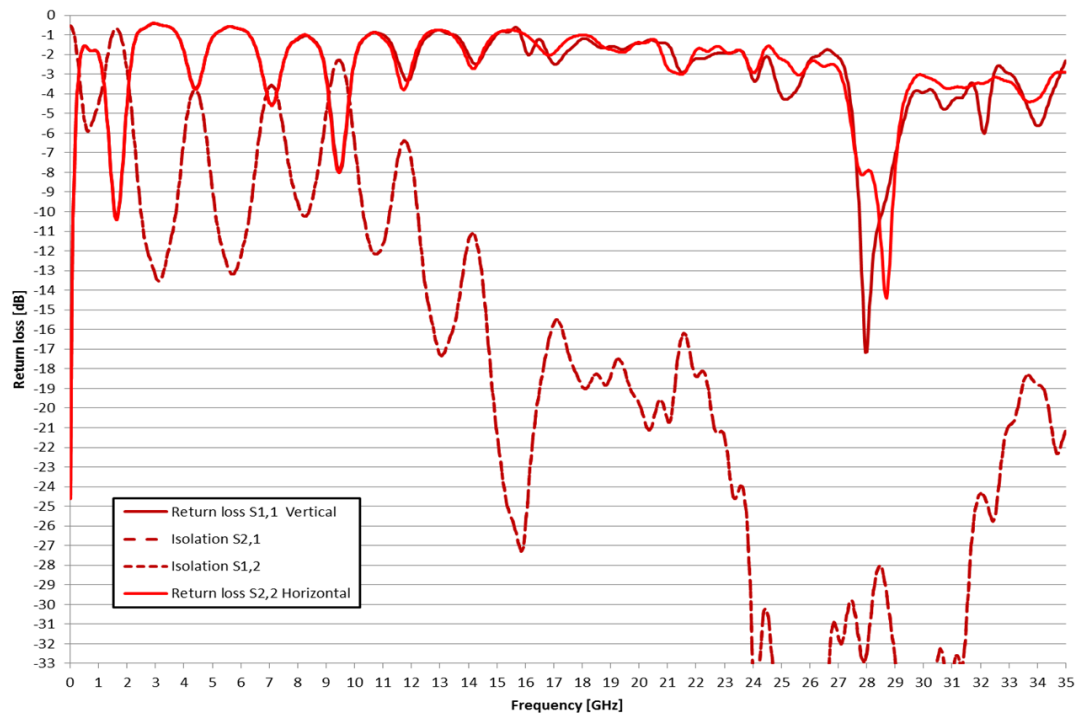


Chart 2.38 The return loss of both polarization feeds and the isolation of the FPC antenna array element

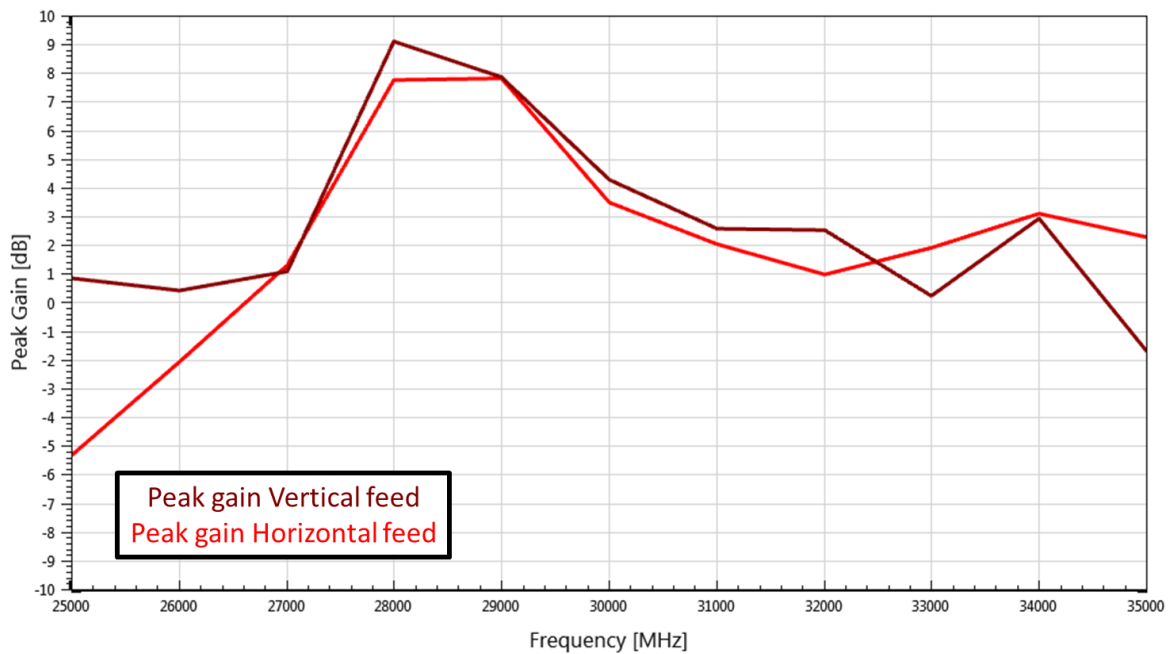


Chart 2.39 The peak gain of both polarization of the FPC antenna array element

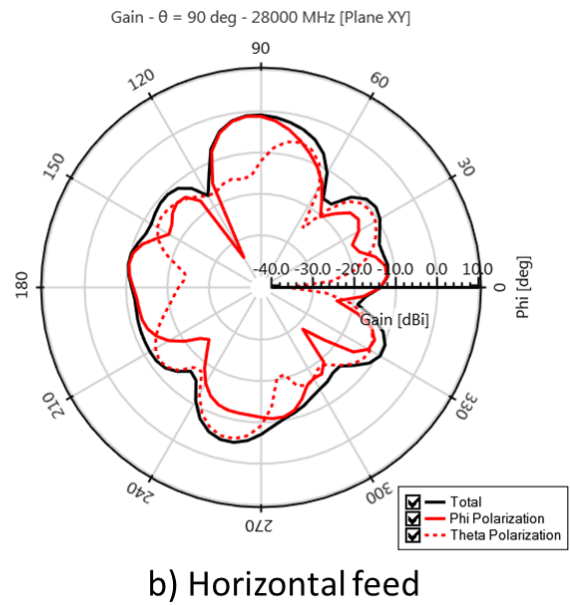
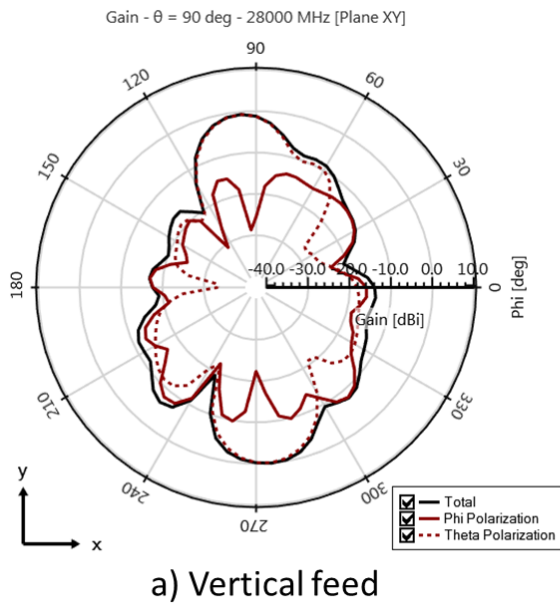


Chart 2.40 The XY-cut of the gain patterns for both polarizations of the low cost antenna array element at 28 GHz

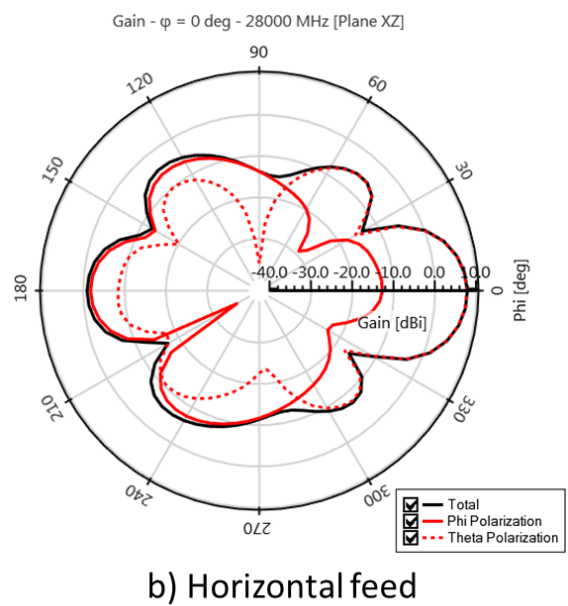
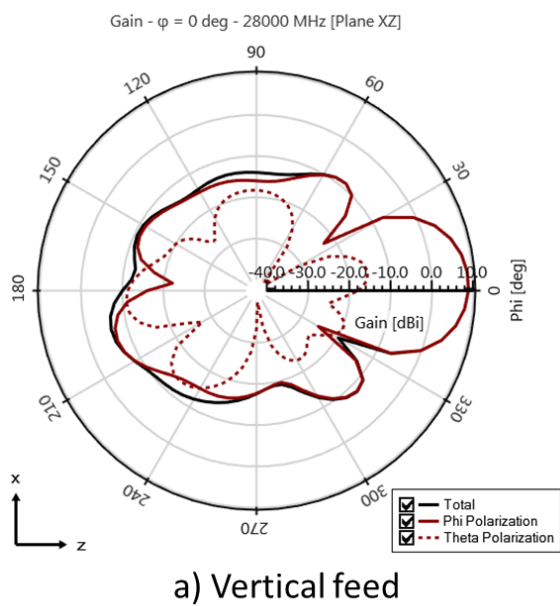


Chart 2.41 The XZ-cut of the gain patterns for both polarizations of the low cost antenna array element at 28 GHz

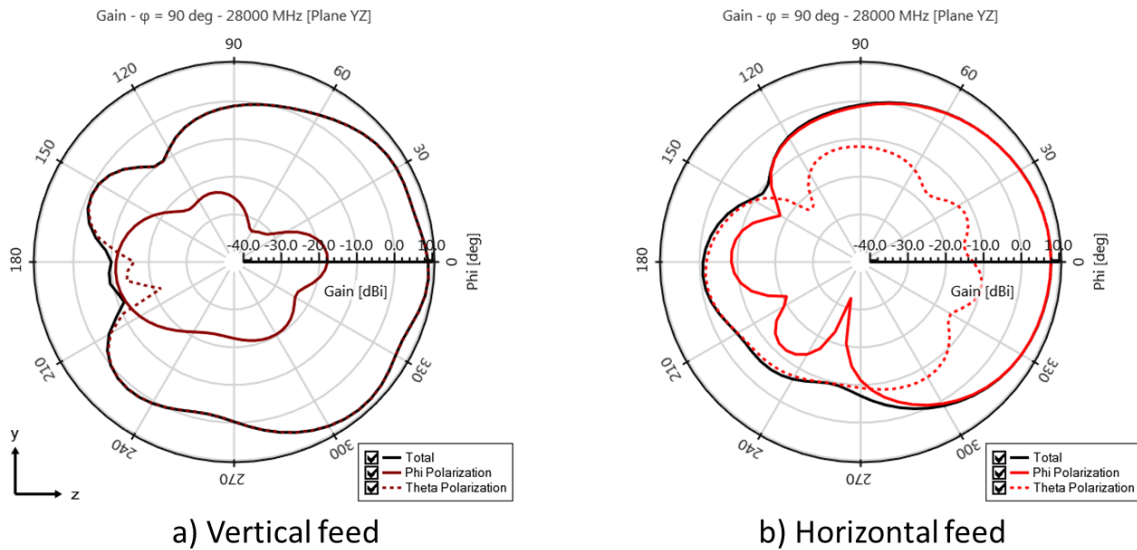


Chart 2.42 The YZ-cut of the gain patterns for both polarizations of the low cost antenna array element at 28 GHz

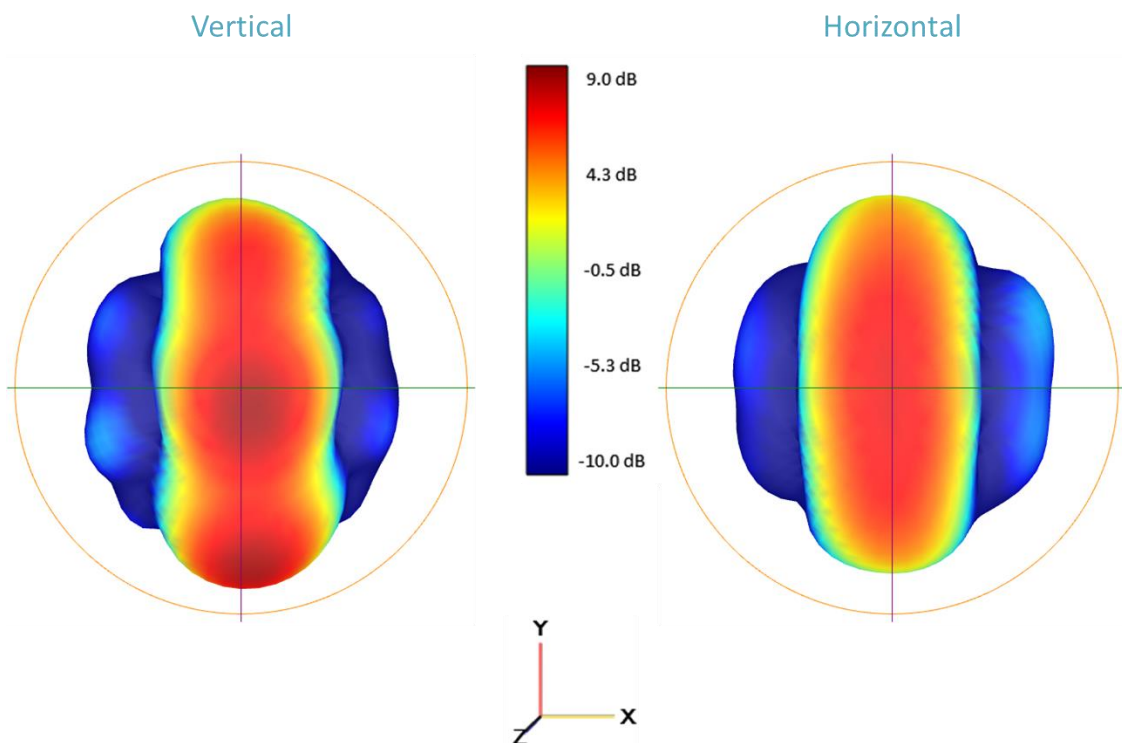


Chart 2.43 The 3D radiation patterns for both polarizations of the low cost antenna array element at 28 GHz

Before merging the antenna array with the transmission lines the last step of the antenna array design is to verify that the designed array element is manufacturable with the FPC

manufacturing technology. A tolerance study to the antenna array element presented in figure 2.19 is performed, changing the copper dimensions in the feed network and antenna patch layer and observing the effect to the array's resonance frequency. Also the effect of the PI substrate permittivity variation is taken in account.

Based on a commercial design guide for FPC circuits a  $\pm 50 \mu\text{m}$  variation for the copper conductor width is chosen [36]. This variation is a worst case scenario for plated and non-plated copper for up to  $40 \mu\text{m}$  thick copper layers. For the FPC permittivity variation a five percent variation is assumed. For the copper dimension variations uniform change in X- and Y-axis is assumed. The nominal length of the feed lines is kept constant and only the widths of the lines are changed. The feed via locations are assumed to be constant as their location is dependent from the drilling accuracy, not from the accuracy of the lithography process which the copper dimensions are dependent.

In the charts 2.44 to 2.48 the effect of the copper conductor tolerance and PI permittivity variance to the array's resonance frequency are presented. In chart 2.44 only top copper side (antenna patch) dimensions were changed while the bottom copper side (feeding network) was kept constant and in chart 2.45 the top was kept constant while the bottom layer copper dimensions were changed. In the chart 2.46 the top copper is enlarged by  $50 \mu\text{m}$  while the bottom copper is varied by  $\pm 50 \mu\text{m}$  and in chart the 2.47 the top copper is decreased and the bottom copper varied. The findings of the charts are summarized in table 2.3 for both polarizations.

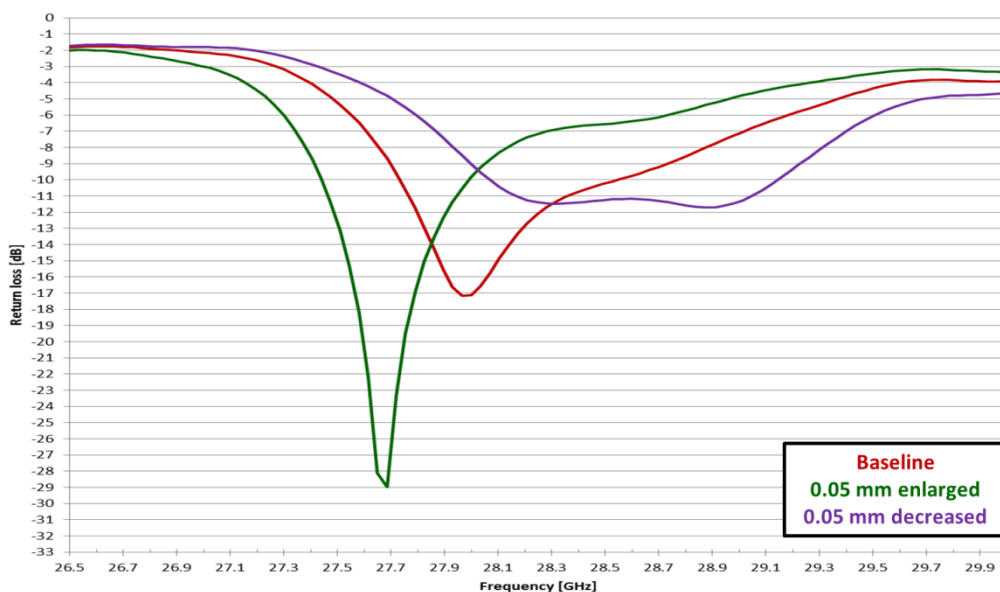


Chart 2.44 Copper manufacturing tolerance impact to resonance frequency only on top copper (antenna patch side)

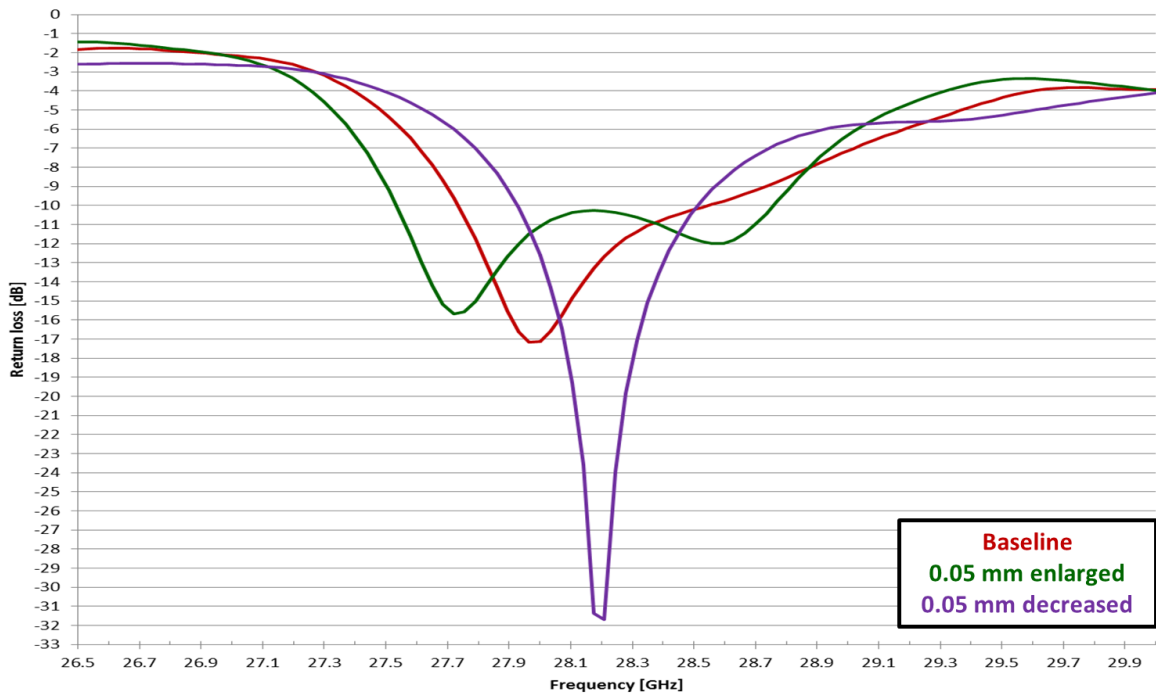


Chart 2.45 Copper manufacturing tolerance impact to resonance frequency only on bottom copper (feed network side)

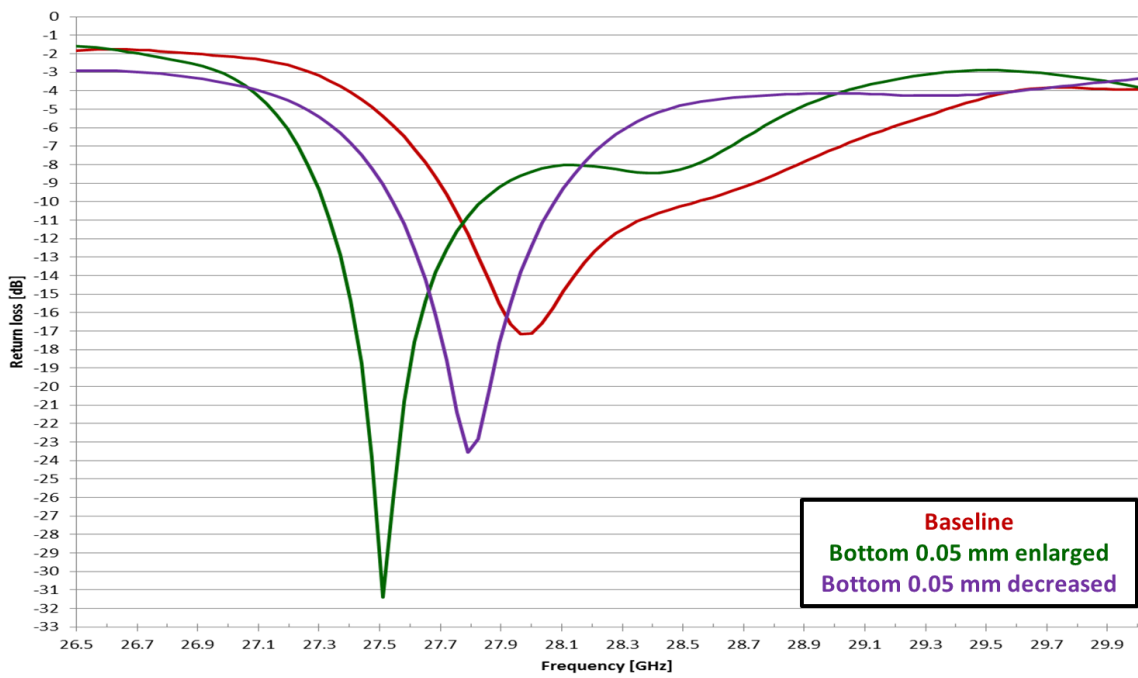


Chart 2.46 Copper manufacturing tolerance impact to resonance frequency on bottom copper and top copper enlarged

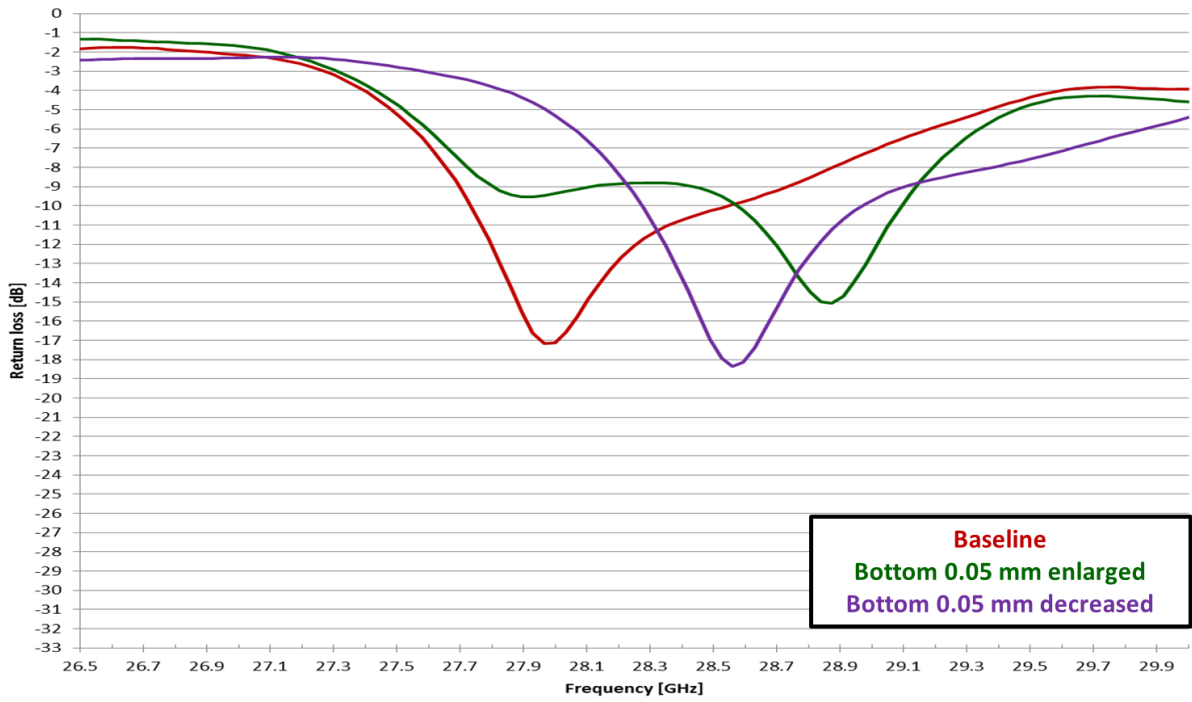


Chart 2.47 Copper manufacturing tolerance impact to resonance frequency on bottom copper and top copper decreased

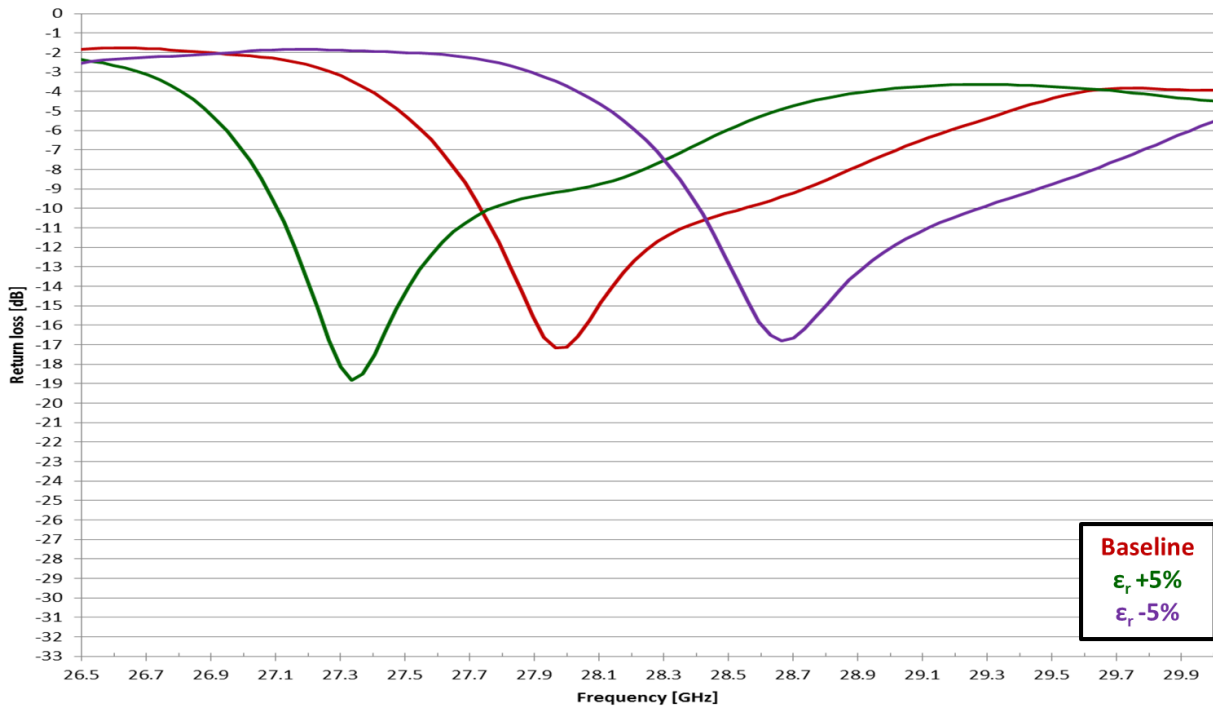


Chart 2.48 PI substrate manufacturing tolerance impact to resonance frequency



Table 2.3 Summary of the manufacturability test

Change compared to base line	Impact to resonance frequency [GHz]	
	Port 1	Port 2
The top layer dimension + 0.05 mm	0.3	0.3
The top layer dimension - 0.05 mm	0.3	0.3
The bottom layer dimension + 0.05 mm	0.2	0.2
The bottom layer dimension - 0.05 mm	0.2	0.2
The top & bottom layer dimension + 0.05 mm	0.4	0.4
The top & bottom layer dimension - 0.05 mm	0.4	0.4
PI substrate dielectric constant + 5%	0.5	0.5
PI substrate dielectric constant - 5%	0.5	0.5

As expected changing the antenna's dimensions and the substrate's permittivity have the biggest impact to the array's resonance frequency. The feeding network variation does have small impact to the resonance frequency but is mainly affecting the characteristic impedance of the feeding network, and thus the input matching of the antenna array. The detuning due the manufacturing tolerances is same for both polarization feeds as the feeding network length is same for both polarization and the change of the patch dimensions is same for both polarizations due the square patch. The combined effect of the metal layers variation with 0.4 GHz maximum shift of the resonance frequency is still in the manageable range, but in the worst case, when the permittivity and the copper dimensions move to same direction, the almost 1 GHz frequency shift is large enough to detune the antenna out of the frequency band in interest. Thus extra care is needed in mass-production and 100% RF test for the antenna array is recommended.

After the mass-production manufacturability of the antenna array is tested and the risks understood the merge of the antenna array and the transmission lines for the low cost millimeter antenna array can be started. In the figures 2.20 to 2.23 the metallic layers of the low cost antenna array are presented. The FPC antenna array consists of 3 separate antenna arrays as shown in the figure 2.20. The full FPC length, from Array1 to Array3, is 160 mm simulating the length of the modern smart phone, and the array element dimensions are the same as for the array in figure 2.9. The array is designed so that the Array1 and Array3 are in the top and bottom end of the mobile phone and the middle array element, Array2, is located middle of the phone top of the battery. To protect the transmission lines from the phone's battery and other metallic structures a stripline transmission line with air cavity to minimize the transmission line losses is chosen. Based on the cavity transmission

line simulations presented in the subchapter II.2.2 the cavity height is set to same as the thickness of the bottom substrate. The FPC arrays have wider air cavity than the simulated cavity transmission lines. This due the manufacturing tolerances of the FPC, with the wider air cavity the center conductor is guarantee to be in the air cavity. The center conductors of the stripline transmission lines are shown in the figure 2.22 and the air cavity cut-outs in the PI substrate are shown in figure 2.23. A PI substrate without the air cavity cut-outs is shown for reference in figure 2.24. The center conductors are sandwiched between metal layers 2 and 16 shown in the figure 2.21 and 2.25. The transmission lines are connected to the patch element with vias through the metallic layer 2. The whole stack up of the low cost antenna array, with and without the air cavity, is shown in figure 2.26. Except the air cavity the two antenna arrays are otherwise identical. The adhesive is modelled in the simulations as polyimide i.e. the adhesive layer effect to the total layer thickness between the copper layers is taken in account but the unknown electrical properties are not.

The RF test connector layout is shown in figure 2.27 in more details. Each array element has its own test connector and the polarization of the array element is chosen by a 0603 (0201 in imperial) sized 0  $\Omega$  SMT (Surface-Mount Technology) resistor. For measuring the isolation between the two polarizations of a single array element “cross connection line” can be used to re-route the second polarization to other array element test connector.

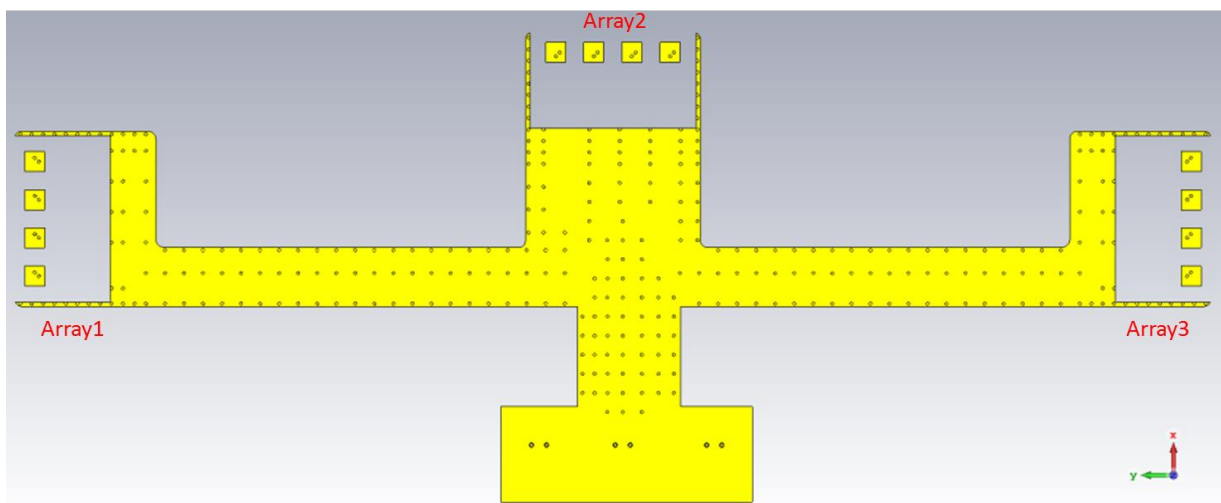


Figure 2.20 Top layer (antenna patch) of the low cost antenna array (bottom view, metal layer 1)

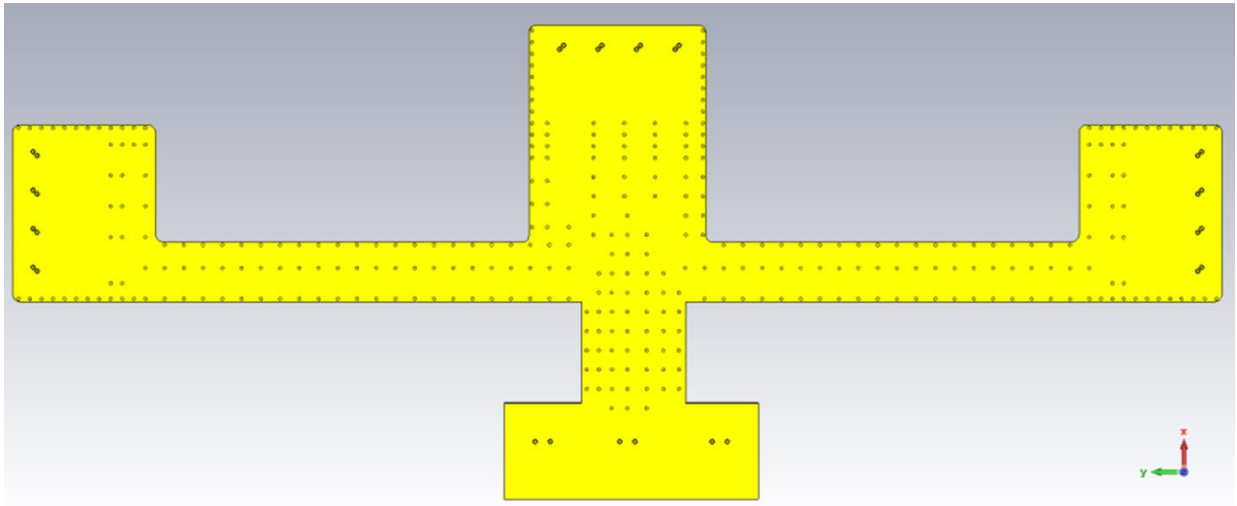


Figure 2.21 Ground plane layer of the low cost antenna array (bottom view, metal layer 2)

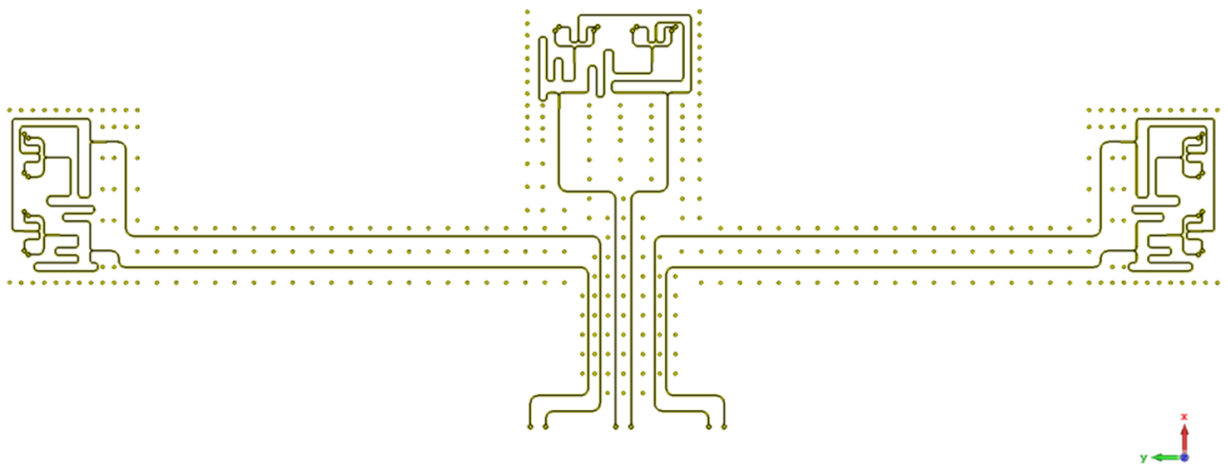


Figure 2.22 Stripline layer of the low cost antenna array (bottom view, metal layer 3)

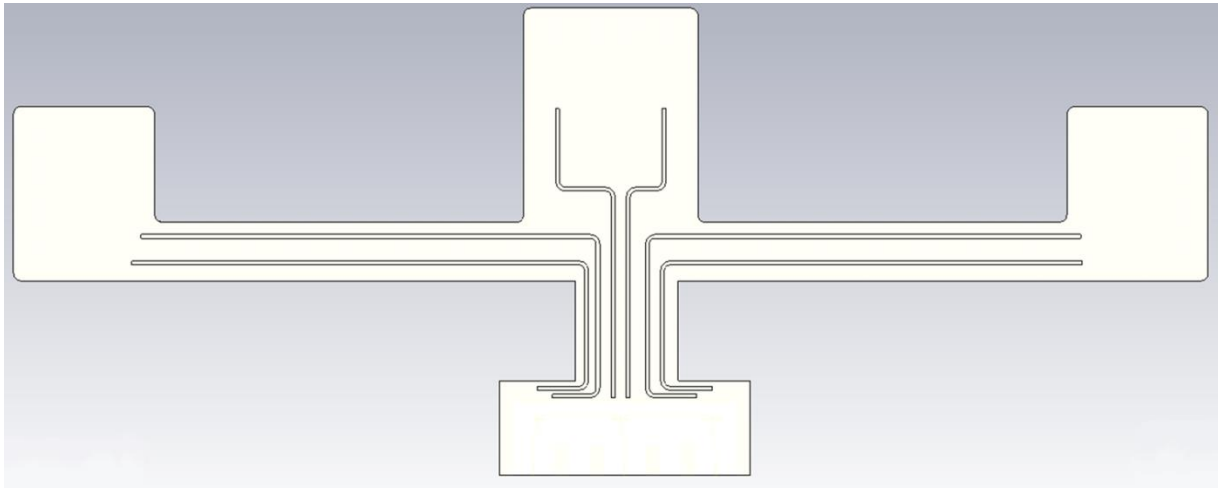


Figure 2.23 PI substrate layer of the low cost antenna array with the air cavity (bottom view)

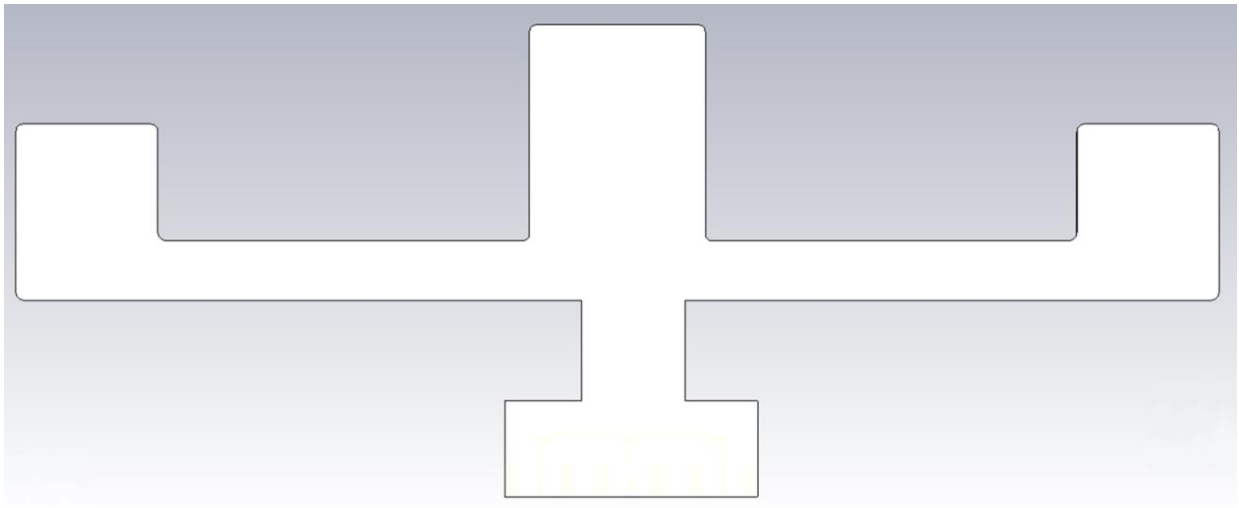


Figure 2.24 PI substrate layer of the low cost antenna array without the air cavity (bottom view)

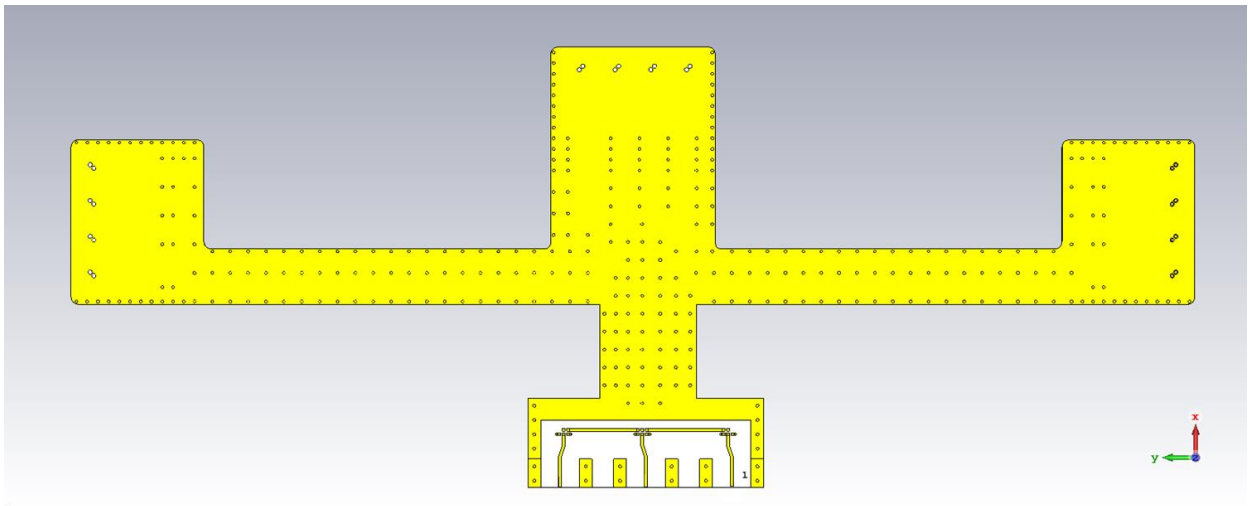


Figure 2.25 Bottom layer of the low cost antenna array (bottom view, metal layer 16)



Figure 2.26 The stack up of the low cost antenna array with and without the air cavity

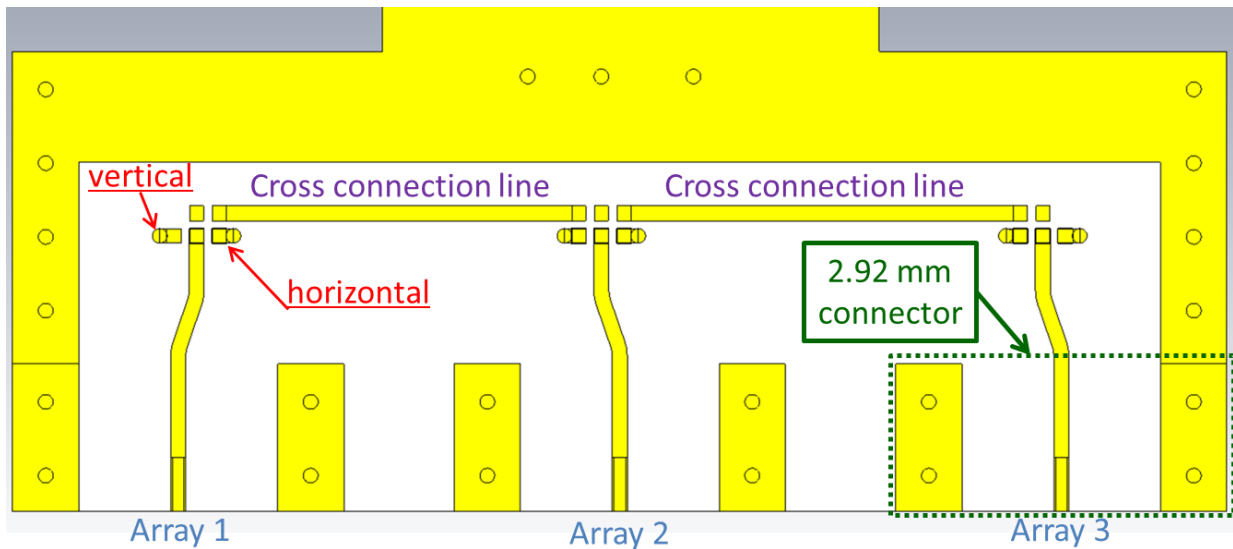


Figure 2.27 The array's RF test port location and polarization selection in low cost antenna array (bottom view)

In figures 2.28 and 2.29 the manufactured low cost antenna array's top and bottom layers are shown for the array with the air cavity transmission lines. As we can see from the both pictures the copper foil of the layers 1, 3, and 16 have slightly collapsed on the area where the PI substrate is left out to form the air cavity for the transmission line. This collapse of the metal layers will change the distance between the center line and the metal ground layers, affecting the characteristic impedance of the stripline and possible increase the transmission line losses as the electromagnetic fields couples more to the copper ground planes, as shown previously in this chapter.

Also noticeable from the figures 2.28 and 2.29 is the missing gold plating on the patch antennas on the array elements. The gold plating is applied only on coppers areas where soldering is required as the nickel metal used in ENIG (Electroless Nickel Immersion Gold) gold plating induce more losses than the solder mask used in PCB and FPC production [37].

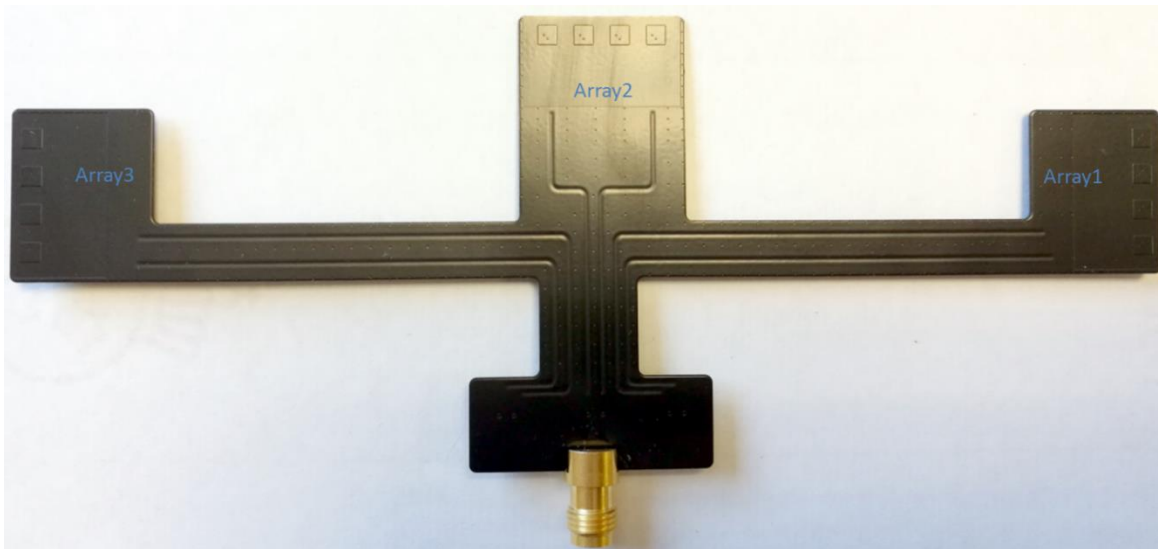


Figure 2.28 The manufactured low cost antenna array, top layer (top view, with air cavity)

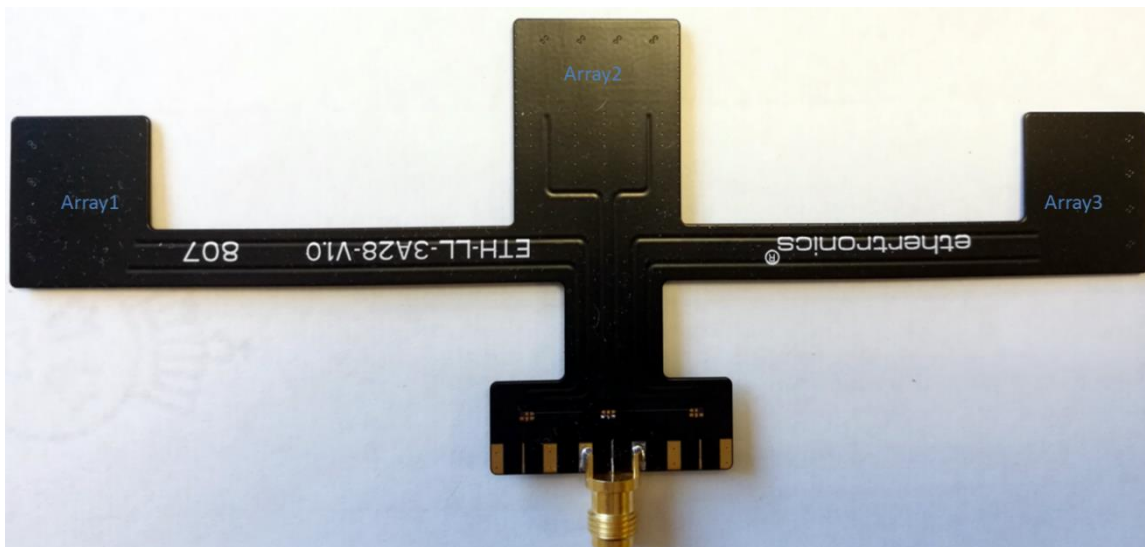


Figure 2.29 The manufactured low cost antenna array, bottom layer (bottom view, with air cavity)

In addition to the return loss measurements the FCP antenna arrays were also measured in the AVX/Ethertronics mmWave 5G measurement system is shown in the figures 2.30 and 2.31. The AVX/Ethertronics mmWave anechoic chamber has two measurements bands, one for 28 GHz band and second for 60 GHz band, covering the frequency range from 26-40 GHz for the first band and 50-70 GHz for the second band. For the passive efficiency and gain measurements Anritsu VectorStar MS4647B vector network analyzer is used which has a measurement range from 10 MHz -70 GHz. For measurements four horn antennas are used, as can be seen from the figure 2.31, two per frequency band one for each polarization.

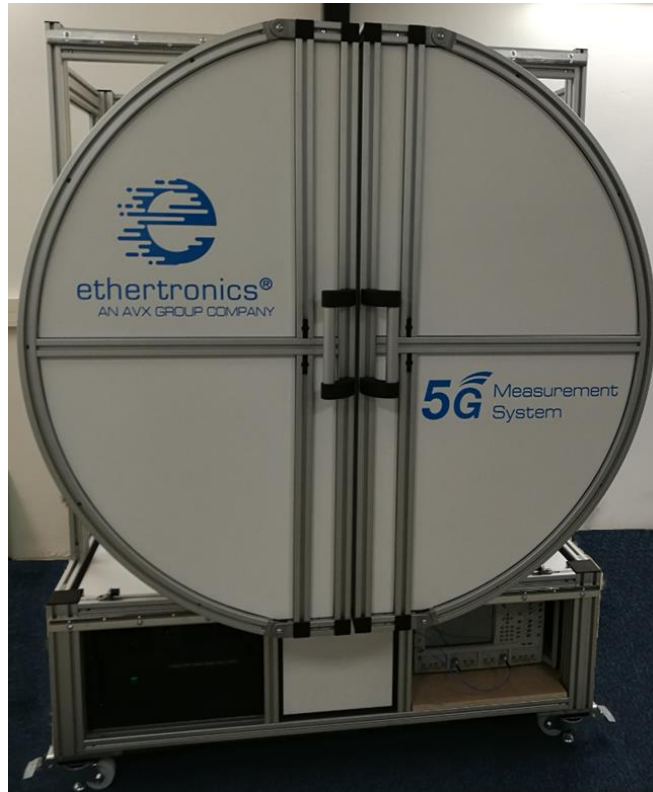


Figure 2.30 AVX/Ethertronics 5G measurement system for mmWave antennas

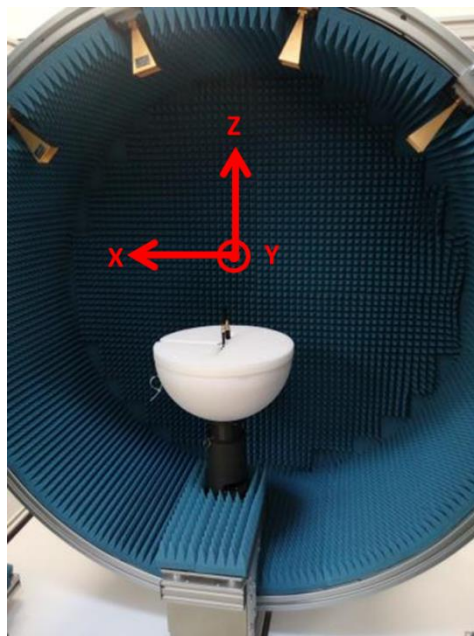


Figure 2.31 The coordinate system and the test horns inside the AVX/Ethertronics 5G measurement system



In chart 2.49 the return losses of the array element 2 (Array2) with and without the air cavity stripline are shown for both simulated and measured arrays. On the simulated results (with dashed lines) both polarization of the antennas have resonances at 28 GHz. If the simulated return loss results of the full array are compared to the simulated results of the single array, shown in chart 2.38, the resonance frequency of the arrays is same but the matching of the antenna elements in the array with the stripline are not as good as the matching of the elements with only the array element. This is main caused by the vias at the patch elements and in the RF test connectors that are through the whole stack up of the FPC. These extra long via stubs cause discontinuity in the transmission line and have effect to the characteristic impedance of the line, thus affecting the antenna matching.

When we study the measured results of the full antenna array we see that the resonance frequency of the both, with and without the air cavity stripline, measured arrays are tuned significantly lower in frequency than their simulated counterparts. The 3 GHz de-tuning witnessed in the measurements is three times more than the maximum de-tuning due the manufacturing tolerance study let us expect. This de-tuning poses a problem for measuring the gain of the antenna arrays as the resonance frequency of the arrays, at 25 GHz, is lower than the measurement range of the AVX/Ethertronics 5G measurement system as we can see from the peak gain results on the chart 2.50. Thus the real performance of the arrays, even if significantly de-tuned in frequency, cannot be verified.

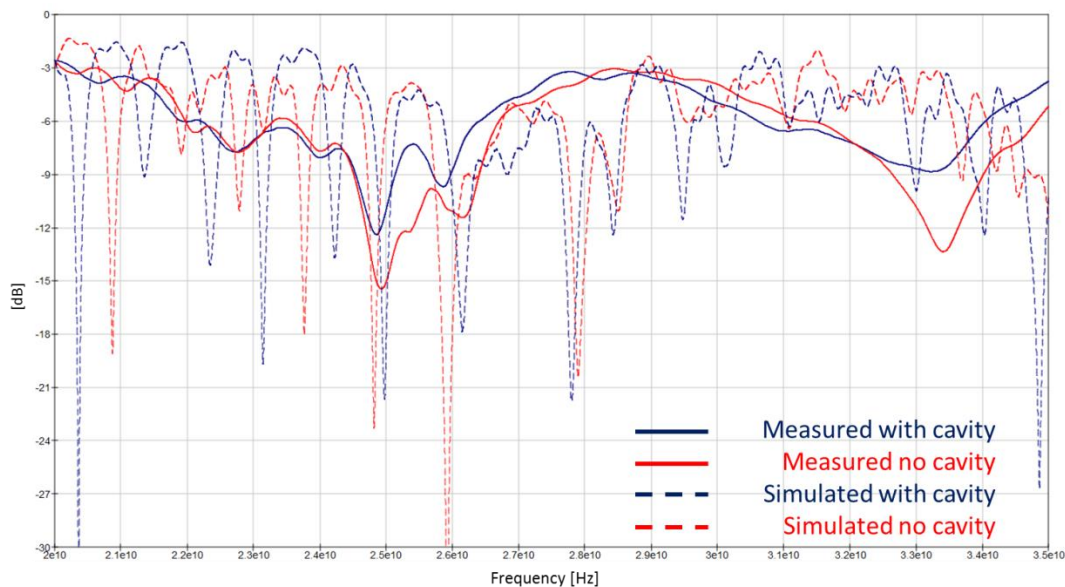


Chart 2.49 The return loss of the array 2 in simulations and measurements

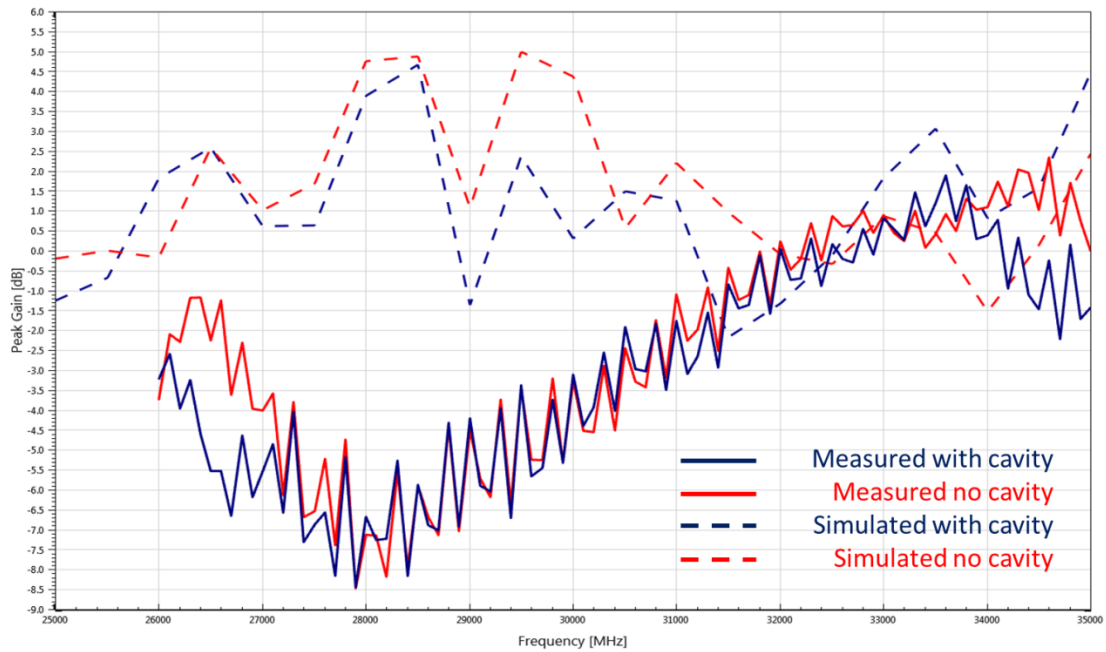


Chart 2.50 The peak gain of the array 2 in simulations and measurements

The de-tuning of resonance frequency of the manufactured low-cost antenna arrays is something very un-expected in its magnitude. Some de-tuning was expected as the simulation models are always an ideal case without any variation due the manufacturing process or materials. And as the FPC manufacturing process tolerance study did not forecast more than 0.9 GHz shift (in worst case), 3 GHz de-tuning was not expected.

If the air-cavity sample would have been de-tuned alone, the inaccuracy could have been pointed out to the collapsed air cavities and their affect to characteristic impedance transmission lines. But as the array without the air cavity transmission line is also de-tuned, although slightly less, the root cause of the de-tuning is not only due the collapsed cavity. One explanation could have been that due the several resonances on the simulated return loss the correct resonance frequency of the low cost antenna array has not been correctly identified and instead of radiating at 28 GHz the real resonance frequency would have been between 26 and 27 GHz. The simulation results of the array element alone and the simulated peak gain results of the full low cost antenna array presented on chart 2.50 does not support this theory. The simulated peak gain of the full array occurs at the 28 GHz as does the return loss and the peak gain of the simulated array element in the charts 2.38 and 2.39.

Thus either the 5% variance for permittivity of the FPC substrate is not large enough for taken in account the manufacturing process or the simulation model of the full array is not correctly taken in account all the effects of the array structure and materials used in millimeter wave frequencies, such as the surface roughness of the copper foil in used in the FPC arrays.

### **II.3 Conclusions**

It has been shown through electromagnetic simulations that it is possible to reduce the losses of a stripline transmission line by introducing an air cavity. This result made it possible to consider using a centralized mmWave antenna architecture, where the antenna arrays are connected to the RF FEM (Front End Module) and/or MCU/Baseband (Micro Control Unit) via RF-lines, for the three antenna array network inside a mobile device. Two combined feed antenna arrays in FR-4 substrate and FPC substrate were designed, manufactured and tested around 28 GHz. The obtained measurement results show offset of the operating frequency around 25 GHz. Unfortunately, the three antenna array FPC is too large and complicated test vehicle to be able to analyze and comment results, both in simulations and prototype measurements.

## References:

- [1] Cisco, "Cisco Visual Networking Index: Global Mobile Data Traffic Forecast Update, 2017–2022", February 2019 (Acquired July 2019 at <https://www.cisco.com/c/en/us/solutions/collateral/service-provider/visual-networking-index-vni/mobile-white-paper-c11-738429.pdf>).
- [2] Samsung, "Samsung 5G Vision", August 2015 (Acquired July 2018 at <https://www.samsung.com/global/business/networks/insights/white-paper/5g-vision/>).
- [3] P. Smulders, H. Yang, and I. Akkermans, "On the Design of Low-Cost 60 GHz Radios for Multigigabit-per-Second Transmission Over Short Distances", IEEE Communication magazine, December 2007.
- [4] T. S. Rappaport et al., "Millimeter Wave Mobile Communication for 5G Cellular: It Will Work!", IEEE Access, Vol. 1, 2013
- [5] A. I. Sulyman et al., "Radio Propagation Path loss Models for 5G Cellular Networks in the 28 GHz and 38 GHz Millimeter-Wave Bands", IEEE Communication Magazine, September 2014.
- [6] G. R. Maccartney, T. S. Rappaport, M. K. Samimi, and S. Sun, "Millimeter-Wave Omnidirectional Path Loss Data for Small Cell 5G Channel Modelling", IEEE Access, Vol. 3, 2015.
- [7] A. I. Sulyman et al., "Directional Radio Propagation Path Loss Models for Millimeter-Wave Wireless Networks in the 28-, 60-, and 73-GHz Bands", IEEE Transactions on Wireless Communications, Vol. 15, No. 10, October 2016.
- [8] ITU Radio Regulations, Chapter II Article 5, 2016 edition

- [9] 3GPP TS 38.101-1 V15.2.0, "3rd Generation Partnership Project; Technical Specification Group Radio Access Network; NR; User Equipment (UE) radio transmission and reception; Part 1: Range 1 Standalone", 3GPP Technical Specification, Release 15, June 2018.
- [10] 3GPP TS 38.101-2 V15.2.0, "3rd Generation Partnership Project; Technical Specification Group Radio Access Network; NR; User Equipment (UE) radio transmission and reception; Part 2: Range 2 Standalone", 3GPP Technical Specification, Release 15, June 2018.
- [11] FCC Public Notice, "Auctions of Upper Microwave Flexible Use Licenses for Next Generation Wireless Services", FCC 18-109, August 3<sup>rd</sup> 2018.
- [12] FCC Public Notice "Winning Bidders Announced for Auction of 28 GHz Upper Microwave flexible Use Service Licenses (AUCTION 101)", FCC DA 19-484, June 3<sup>rd</sup> 2019.
- [13] FCC Public Notice "Auction of 24 GHz Upper Microwave Flexible Use Service Licenses Closed Winning Bidders Announced for Auction 102", FCC DA 19-485, June 3<sup>rd</sup> 2019.
- [14] T. Seki et al, "A 60-GHz Multilayer Parasitic Microstrip Array Antenna on LTCC Substrate for System-on-Package", IEEE Microwave and Wireless Components Letters, Vol. 15, No. 5, May 2005.
- [15] S. Pinel, I. K. Kim, K. Yang, and J. Laskar, "60 GHz Linearly and Circularly Polarized Antenna Arrays on Liquid Crystal Polymer Substrate", Proceedings of the 36<sup>th</sup> European Microwave Conference, September 2006.
- [16] A. E. I. Lamminen, J. Saily, and A. R. Vimpari, "60-GHz Patch Antennas and Arrays on LTCC with Embedded-Cavity Substrate" IEEE Transactions on Antennas and Propagation, Vol. 56, No. 9, September 2008.

- [17] J. Xu, Z. N. Chen, X. Qing, and W. Hong, "Bandwidth Enhancement for a 60 GHz Substrate Integrated Waveguide Fed Cavity Array Antenna on LTCC", IEEE Transactions on Antennas and Propagation, Vol. 59, No. 3, March 2011,
- [18] S. B. Yeap, Z. N. Chen, and X. Qing, "Gain-Enhanced 60-GHz LTCC Antenna Array with Open Air Cavities", IEEE Transactions on Antennas and Propagation, Vol. 59, No. 9, September 2011.
- [19] Y. Li et al, " Axial Ratio Bandwidth Enhancement of 60-GHz Substrate Integrated Waveguide-Fed Circularly Polarized LTCC Antenna Array", IEEE Transactions on Antennas and Propagation, Vol. 60, No. 10, October 2012.
- [20] K.-S. Chin, W. Jiang, W. Che, C.-c. Chang, and H. Jin, "Wideband LTCC 60-GHz Antenna Array with a Dual-Resonant Slot and Patch Structure", IEEE Transactions on Antennas and Propagation, Vol. 62, No. 1, January 2014.
- [21] W. Liu, Z.-N. Chen, X. Qing, "60-GHz Thin Broadband High-Gain LTCC Metamaterial-Mushroom Antenna Array", IEEE Transactions on Antennas and Propagation, Vol. 62, No. 9, September 2014.
- [22] H. Jin, W. Che, K.-S.- Chin, and W. Yang, " High-Gain Low-Cross-Polarization 60 GHz LTCC Patch Antenna Array with Differential-Fed and Soft-Surface Structures", IEEE Asia-Pacific Microwave Conference (APMC), 2015.
- [23] W. E. McKinzie et al "60-GHz  $2 \times 2$  LTCC Patch Antenna Array With an Integrated EBG Structure for Gain Enhancement", IEEE Antennas and Wireless Propagation Letters, Vol. 15, 2016.
- [24] H.-K. Du et al, "Dual-polarized Patch Array Antenna Package for 5G Communication Systems", 11<sup>th</sup> European Conference on Antennas and Propagation (EUCAP), 2017.
- [25] M. Stanley, Y. Huang, T. Loh, Q. Xu, H. Wang, H. Zhou, "A High Gain Steerable Millimeter-Wave Antenna Array for 5G Smartphone Applications", 11<sup>th</sup> European Conference on Antennas and Propagation (EUCAP), 2017.

- [26] B. Yu, K. Yang, C.-Y.-D. Sim, and G. Yang, "A Novel 28 GHz Beam Steering Array for 5G Mobile Device With Metallic Casing Application", IEEE Transactions on Antennas and Propagation, Vol. 66, No. 1, January 2018.
- [27] David M. Pozar "Microstrip Antennas", Proceedings of IEEE. Vol. 80, No. 1, January 1992.
- [28] David M. Pozar "Microwave Engineering", John Wiley & Sons, 4<sup>th</sup> Edition 2012.
- [29] Dupont, "DUPONT™ KAPTON® SUMMARY OF PROPERTIES", 2017 (Acquired September 2019 at <https://www.dupont.com/content/dam/dupont/products-and-services/membranes-and-films/polyimide-films/documents/DEC-Kapton-summary-of-properties.pdf>).
- [30] J. A. Weldon "Flex for 5G – Why Materials Matter", Application note, Dupont, 2018 (Acquired September 2019 at [http://www.ocipcdc.org/archive/Jonathan\\_Weldon\\_Flex\\_for\\_5G\\_Why\\_Materials\\_Matter\\_03292018.pdf](http://www.ocipcdc.org/archive/Jonathan_Weldon_Flex_for_5G_Why_Materials_Matter_03292018.pdf)).
- [31] F. David, "Etude de composants micro-coaxiaux à fort facteur de qualité pour applications en bande Q/V" PhD Dissertation, Université de Limoges, 2017.
- [32] Constantine A. Balanis "Antenna Theory, Analysis and Design", John Wiley & Sons, Third edition, 2005.
- [33] H. Tanaka, F. Okado, "Precise Measurements of Dissipation Factor in Microwave Printed Circuit Boards", IEEE Transactions on Instrumentation and Measurement, Vol. 38, No. 2, April 1989.
- [34] J. R. James, P. S. Hall, "Handbook of Microstrip Antennas", Peter Peregrinus Ltd., 1969.

- [35] S. Gupta, M. Ramesh, and A. T. Kalghatgi, "Parametric Studies on Isolation in Probe-Fed Dual Polarized Microstrip Antennas", The European Conference on Wireless Technology, 2005.
- [36] Minco, "Minco Flex Circuit Design Guide", (Acquired 2017 at [www.minco.com](http://www.minco.com)).
- [37] Rogers Corp. "Design Right the First Time: Understanding how Dielectric Constant (Dk) Test Methods Affect Time to Market", Webinar, 2017.



## General Conclusions

---

In this thesis a frequency tunable filters for sub 6 GHz bands and a low cost millimeter wave (mmWave) antenna arrays were investigated for the upcoming 5G NR (Fifth Generation New Radio) mobile devices. The thesis has been divided into two parts and so are the general conclusions for this thesis. The first part of this chapter is concentrated on the frequency agile filter and the second part to the mmWave antenna array.

### Part I: Frequency agile filter

For the frequency agile filter a filter based on combline structure was studied using commercial RF SP4T (Radio Frequency, Single Pole – Four Through) switch, based on SOI CMOS (Silicon On Insulator, Complementary Metal-Oxide-Semiconductor) transistors, as tuning elements. The resonators are formed by stripline and microstrip line sections connected by vias. The frequency agile combline filter was designed in 3D EM (Three Dimensional Electromagnetic) full wave simulation software (CST) with LTCC (Low Temperature Co-fired Ceramic) ceramic substrate. In addition to the filter structure also the full control and power line network for the RF switches were integrated into the filter. The final designed filter included all the necessary connections inside the LTCC block to be able to operate the frequency agile filter without any external components other than the control traces in the mobile device PCB (Printed Circuit Board) as demonstrated with the prototype measurements.

The combline filter structure used in this thesis is well known and the basic operation theory is well studied. In this thesis two new concepts are introduced for the frequency agile combline filter; commercial SP4T RF switch as a tuning device and parallel resonator load for center frequency and bandpass bandwidth controls.

Bandpass bandwidth controlled frequency agile filters have been studied previously. The bandwidth control has been achieved using non-resonant transmission lines between the resonant transmission lines, distributed capacitive and corrugated couplings lines, mixed electrical and magnetic coupling structures, and inductors for input/output coupling. Excluding the use of inductors for input and output coupling the previously studied solutions requires complex design of coupling or decoupling lines which shape, size, and spacing are critical to their performance. This increase the complexity of the filter and except the non-resonant transmission lines does not give full freedom to optimize the bandpass bandwidth to each resonance frequency as they offer only constant bandwidth over the whole frequency range. In this thesis the passband bandwidth control is implemented to combline filter with lumped inductor in parallel with the tuning capacitor used to tune the resonance frequency of

the combine filter. The lumped inductor eliminates the complexity of the non-resonant transmission lines, distributed capacitive and corrugated couplings lines, mixed electrical and magnetic coupling structures and simplifies the filter design. In addition to the simplification the parallel load also enables resonance frequency independent bandwidth control for all the resonance frequencies. The lumped inductors as a passband bandwidth controller have been demonstrated both in theoretical synthesis and in 3D EM simulations in this thesis.

In the simulation ideal inductors and capacitors were used to model the tuning circuitry. It was assumed that the high-Q RF lumped inductors and capacitors would have only a minor effect to the insertion loss of the filter and that the losses of the RF switch would have the biggest impact to the filter losses. In the prototype measurements it was quickly find out that the inductor parallel the capacitor had 3dB more losses compared to the measurement results with capacitor only. Thus the first assumption was proven wrong on the part of the inductor and realistic models, such as S-parameter models, from component suppliers have to be used in the 3D EM simulations so that the filter performance can be modelled realistically in the simulation tools. Such component models are readily available from lumped RF component suppliers, such as AVX and muRata, webpages.

Varactors and MEMS (Micro Electro Mechanical Systems) switches and capacitor banks are commonly used in the frequency agile filter research as the tuning device to change resonance frequency of the filter. The downside of using them is their need of high control voltages, up to 100 V, which are difficult to provide in a battery powered mobile devices. To mitigate the need of the high control voltages, commercial SP4T RF switch was studied as a tuning device for the frequency agile combine filter in this thesis. Commercial SP4T RF switches use 3V as a power and control voltage which makes them an ideal tuning device for frequency agile filter mobile device applications. In this thesis Ethertronics EC 686 SP4T RF switch, based on SOI CMOS technology, is used as a tuning device. The EC 686 supports different communication protocols for controlling the state of the switch. The digital SPI and MIPI protocols are the most convenient for multi switch configurations as the switch state data is communicated in series format, thus minimizing the number of control lines needed.

In the 3D EM simulations the switch landing pattern and the transmission lines from the switch to the tuning components were modelled on the two top copper layers of the LTCC ceramic block and the switch and the tuning components as a RF ports inside the simulator. In the post-processing the tuning component ports were modelled as inductors and capacitors, and the RF switch was modelled with the  $R_{ON}$  resistance of the switch provided from the datasheet of the EC 686. Although this permitted to take in account the ohmic losses of the switch in the EM simulations it was found out in the prototype measurements that it didn't modelled correctly the RF switch affect to the filter's performance. As seen from the 1<sup>st</sup> chapter prototype measurements, adding the RF switch to the manufactured filter destroyed the filters insertion loss and frequency agility performance. This was not expected as the same switch has been used successfully on several antenna frequency tuning circuits. The performance drop witnessed is most likely because of the RF IC (Integrated Circuit) packaging and/or the IC internal routing and placement of the transistors. Especially the IC internal routings are not practical to integrate into the 3D EM simulations. As the dimensions inside the CMOS IC are in nanometer scale and the modelling and meshing becomes

challenging with a normal work desktop computer. Also for all the commercial RF switches the layout of the transistors are company confidential information and are not available for designers outside the company. Thus more extensive studies are needed to understand better why the frequency tunability was lost with the CMOS RF switch before they can be used in commercial frequency agile combline filters as a tuning device.

#### **For the future work on the frequency agile filter:**

- A re-simulation of the combline filter should be done using more realistic component models for the parallel load inductors and capacitors. The spacing of the combline resonators inside the LTCC block can be optimized to minimize the losses induced by the parallel load inductor.
- Also other methods to implement the parallel load inductor than the lumped components should be investigated to minimize the losses due the inductor.
- The CMOS RF switch impact to the combline filter should be investigated further as discussed already in this general conclusion. The transistor level modelling inside the 3D EM simulations is most likely too complicated task. But the impact of the CMOS RF switch packaging should be possible to carry out. A re-simulation of the combline filter should be done using realistic model for switch integrating capacitors and resistances. The values of the elements of the equivalent circuit could be validated by making measurements on the switch in the operating frequency band of the filter. Also others manufacturers CMOS switches and different switch types (e.g. SPDT) should be tested to confirm this thesis findings of the CMOS switch to the filters performance. There is no need to test MEMS or varactor as these have been already proven a successful tuning device for combline filters.

## Part II: Low cost mmWave antenna array

In the second part of the thesis, a low cost mmWave antenna array was studied on polyimide (PI) substrate used in commercial flexible printed circuits (FPC) boards. Also a low loss transmission line topology, based on strip line, was studied for a centralized mmWave RF architecture, where all the antenna arrays are connected with RF transmission lines to one central RF IC which takes care of the filtering, down/up converting, and digitalization/ analogization of the in/out-coming signal and distributing the signals to different antenna arrays.

To reduce the transmission line losses in centralized mmWave RF architecture low loss shielded RF lines are needed. In the sub 6 GHz frequency range coaxial RF-cables are commonly used in mobile devices, but the PCB connectors used with sub 6 GHz RF-cables won't work in the mmWave frequencies. Thus integrated transmission lines, such as strip lines, are an interesting transmission line topology for mmWave devices. Although strip lines are more lossy than the microstrip lines they provide better isolation from the RF interference and metal structures inside the mobile devices. One way to mitigate the losses of the stripline is to introduce an air cavity over the center conductor of the stripline. With the introduction of the air cavity the electromagnetic fields are travelling in low loss air instead of the more lossy substrate material, such as FR-4.

Similar technique has been studied before in higher frequencies (above 33 GHz) with rectangular co-axial cables using additive micro-fabrication techniques by François David in his PhD dissertation "Etude de composants micro-coaxiaux à fort facteur de qualité pour applications en bande Q/V". In addition to the substrate material also the rectangular shape used in the David's thesis are not attractive for consumer mobile devices. Thus a new study was done using polyimide substrate and stripline topology, also the frequency range used in this study, 0-35 GHz, is more appropriate for the 5G mmWave frequencies.

For the 3D EM simulations two different stack-ups were studied with two different widths of air cavities over the central conductor. Based on the E- and H-field results in 28 GHz it was expected that the reduced height stack-up stripline, where the center conductor has non-equal distance to the two ground planes, would have had lower insertion losses compared to the "normal", equal distance, stack-up striplines. With the reduced height stack-up the E- and H-fields were more concentrated in the air cavity region, compared to the equal distance stack-up, and thus higher percentage of the electromagnetic-field would traverse in lower loss medium. But the insertion loss results showed that this assumption was not correct and the copper conductor losses, albeit of optimistic conductivity parameters, overruled the benefits gained from concentrating the fields in the air cavity region.

Based on the simulation results the width of the air cavity is not as critical a parameter as the stack-up of the stripline for the air-cavity, as long as the width of the air-cavity is larger than the width of the center conductor.

Overall this new study confirms the findings on the "Etude de composants micro-coaxiaux à fort facteur de qualité pour applications en bande Q/V" in lower frequencies and shows that

with introducing an air-cavity in to a stripline the losses of the stripline transmission line can be reduced. The reductions of the losses are significant with longer length of transmission line, 2-3 dB in 150 mm length stripline. As the size of the consumer mobile phones have been increased the air-cavity stripline can bring clear benefits for low cost mmWave antenna arrays.

After the performance of the air-cavity stripline at 28 GHz on polyimide was confirmed a low cost antenna array was designed on polyimide substrate. The antenna array consist of four co-linear patch antennas with dual polarization feeds, one for vertical and one for horizontal polarization. The antenna element spacing and the power divider network was optimized in CST for maximum peak gain performance. Also the manufacturability of an mmWave antenna array on polyimide was tested with parametric simulations on 3D EM simulator. The copper layer manufacturing tolerance and the permittivity fluctuation ( $\epsilon_r \pm 5\%$ ) was taken account on the parametric simulations. The manufacturability simulations indicated that the permittivity is the most sensitive parameter, i.e. it had the biggest impact, to the antenna resonance frequency. In a worst case scenario, when the substrate permittivity change enhances the frequency detuning due copper dimension change, a 1 GHz frequency shift is possible. Thus extra cautions is needed during the manufacturing of the antenna arrays on polyimide and if possible try to minimize these effects during the design process.

Based on the air-cavity stripline and antenna array simulations a prototype antenna array was designed with three separate antenna arrays on single large FPC, one array in the middle and two at the adjacent ends of the FPC. Two sets of arrays were manufactured, one with the air-cavity striplines and one with normal stripline stack-up i.e. without air-cavity. Unfortunately both of the samples were detuned in frequency (around 25 GHz) out of the measurement range of the AVX/Ethertronics 5G mmWave chamber (26-40 GHz) and thus no reliable antenna performance results were acquired.

Upon the visual inspection it was observed that the top ground plane layer of the air-cavity line was partially collapsed over the center conductor on the prototype antenna array with the air-cavity stripline and a clear indentation was visible throughout the length of the stripline with the air-cavity. Due the collapse of the top ground plane the characteristic impedance of the stripline is no longer optimal. And as the electromagnetic fields are coupling stronger to the ground plane also the insertion losses are higher. The collapse of the top ground plane metal is not the only reason why the antenna array was tuned out of the band, as the antenna array without the air-cavity was also, although not as much as the array with the cavity, de-tuned lower in frequency. It is not clear what caused the de-tuning of the array. One culprit could be higher than expected permittivity of the adhesive layer which was modelled as a normal polyimide layer in the 3D EM simulations.

### **For the future work on the low cost mmWave antenna array:**

- The air-cavity stripline's mechanical structure has to be redesigned so that the drooping of the top layer ground plane can be eliminated or at least minimized. This can be achieved by adding support structures inside the air-cavity. A balanced trade-off between the support and the removal of the substrate should be studied.
- After a mechanical solution for the air-cavity has been found new study for the air-cavity transmission line has to be done to verify the possible benefits compared to traditional stripline transmission line.
- The dielectric properties ( $\epsilon_r$  and  $\tan\delta$ ) of the multi-layer substrate should be reliably characterized around the 28 GHz in order to introduce them into the electromagnetic simulations.
- A simplified antenna array with a modified air-cavity transmission line should be designed and manufactured on polyimide. The three antenna array FPC is too large and complicated test vehicle to be able to get good and reliable test results, both in simulations and prototype measurements.

## Table of Charts

---

Chapter I. Frequency Agile Filters for Mobile Devices .....	15
Chart 1.1 Reflection and transmission responses of the filters with $d$ and $w_g$ optimized for GSM 1800 band (a) and for LTE 7 band (b).....	29
Chart 1.2 Wideband response of the simulated filter .....	33
Chart 1.3 Wide band response of the combline filter with optimized parallel load component values ..	34
Chart 1.4 Passband responses for a) GSM 1800 and b) LTE 7 for the optimized filter .....	34
Chart 1.5 The tuning range of the basic combline filter .....	36
Chart 1.6 Parallel load impact to combline filter bandwidth .....	43
Chart 1.7 Parallel load impact to combline filter bandwidth with transmission response .....	43
Chart 1.8 Bandpass bandwidth optimization with parallel inductor.....	44
Chart 1.9 Verification of the $R_{on}$ simulation model .....	45
Chart 1.10 The CMOS switch $R_{on}$ effect to the filter's insertion loss (in dB).....	46
Chart 1.11 RF-path effect to filter's resonance frequency. Where T denotes the capacitance in pF and L the inductance in nH for each parallel load.....	47
Chart 1.12 All the filter states simulated with their optimized RF-path, where T and L are the parallel load capacitance in pF and inductance in nH, respectively. And the R is the $R_{ON}$ resistance of the RF switch in $\Omega$ .....	48
Chart 1.13 CST simulations versus measurements of the frequency agile filter .....	53
Chart 1.14 All the RF-states of the measured filter .....	53
Chart 1.15 Measured filter performance without the inductive load.....	54
Chart 1.16 Measured performance of frequency agile filter without the three EC 686 .....	56
Chart 1.17 Measured performance of frequency agile filter without the three EC 686 and the inductive loads.....	57
Chart 1.18 Simulation comparison of ideal and realistic lossy (with realistic Q-values) components effect to filter performance a) return loss and b) insertion loss .....	58
Chapter II. Low Cost Millimeter Wave Antenna Arrays .....	63
Chart 2.1 Input matching of the transmission lines .....	73
Chart 2.2 Insertion losses per mm of the transmission lines .....	74
Chart 2.3 Insertion losses of the full length transmission lines .....	74
Chart 2.4 Losses due to the copper in the transmission lines .....	75
Chart 2.5 Losses due to the dielectric in the transmission lines .....	75
Chart 2.6 Isolation between the feeding probes of 28 GHz square patch .....	79
Chart 2.7 The return loss and isolation of the designed unit element of the 28 GHz antenna array .....	80

Chart 2.8 The total efficiency of the unit element's both polarization ports .....	80
Chart 2.9 The peak gain of the unit element's both polarization ports.....	81
Chart 2.10 The XY-cut of the gain pattern of the unit element's both polarization ports at 28 GHz .....	81
Chart 2.11 The XZ-cut of the gain pattern of the unit element's both polarization ports at 28 GHz .....	82
Chart 2.12 The YZ-cut of the gain pattern of the unit element's both polarization ports at 28 GHz .....	82
Chart 2.13 Return loss of all elements of the 28 GHz 4 element linear antenna array .....	84
Chart 2.14 Isolation between all elements of the 28 GHz 4 element linear antenna array.....	85
Chart 2.15 The peak gain of combined vertical and horizontal feeds of the 4 element linear antenna array .....	86
Chart 2.16 The XY-cut of the gain pattern of the 4 element linear antenna array's both polarization ports at 28 GHz .....	86
Chart 2.17 The XZ-cut of the gain pattern of the 4 element linear antenna array's both polarization ports at 28 GHz .....	87
Chart 2.18 The YZ-cut of the gain pattern of the 4 element linear antenna array's both polarization ports at 28 GHz .....	87
Chart 2.19 XY-cut of the gain patterns of 4 element linear antenna array with element spacing of 5 and 3.75 mm distances (vertical polarization feed) at 28 GHz .....	88
Chart 2.20 XZ-cut of the gain patterns of 4 element linear antenna array with element spacing of 5 and 3.75 mm distances (vertical polarization feed) at 28 GHz .....	89
Chart 2.21 YZ-cut of the gain patterns of 4 element linear antenna array with element spacing of 5 and 3.75 mm distances (vertical polarization feed) at 28 GHz .....	89
Chart 2.22 The peak gain of combined vertical feeds of the 4 element linear antenna array with 5 and 3.75 mm element spacing. ....	90
Chart 2.23 Insertion loss and input matching of the power divider of the combined feed array .....	94
Chart 2.24 The peak gain of combined vertical ports with different element spacing.....	95
Chart 2.25 The XZ gain-cut of the combined vertical ports with different element spacing.....	95
Chart 2.26 The simulated return loss of the 2x2 FR-4 antenna array with individual feeds .....	97
Chart 2.27 The isolation between all the feeds of the 2x2 FR-4 array with individual feeds .....	97
Chart 2.28 The return loss and isolation of the 2x2 FR-4 antenna array with combined feeds.....	98
Chart 2.29 The peak gain of both FR-4 antenna arrays .....	98
Chart 2.30 The XY-cut of the gain patterns for both polarizations of the FR-4 antenna array with individual feeds at 28 GHz .....	99
Chart 2.31 The XY-cut of the gain patterns for both polarizations of the FR-4 antenna array with combined feeds at 28 GHz.....	99
Chart 2.32 The XZ-cut of the gain patterns for both polarizations of the FR-4 antenna array with individual feeds at 28 GHz .....	100
Chart 2.33 The XZ-cut of the gain patterns for both polarizations of the FR-4 antenna array with combined feeds at 28 GHz.....	100



Chart 2.34 The YZ-cut of the gain patterns for both polarizations of the FR-4 antenna array with individual feeds at 28 GHz .....	101
Chart 2.35 The YZ-cut of the gain patterns for both polarizations of the FR-4 antenna array with combined feeds at 28 GHz.....	101
Chart 2.36 The return loss and isolation of the measured and simulated combined feed FR-4 antenna array .....	104
Chart 2.37 The Simulated Peak Gains and the Co-Gain of the measured combined feed FR-4 antenna array .....	104
Chart 2.38 The return loss of both polarization feeds and the isolation of the FPC antenna array element.....	107
Chart 2.39 The peak gain of both polarization of the FPC antenna array element.....	107
Chart 2.40 The XY-cut of the gain patterns for both polarizations of the low cost antenna array element at 28 GHz .....	108
Chart 2.41 The XZ-cut of the gain patterns for both polarizations of the low cost antenna array element at 28 GHz .....	108
Chart 2.42 The YZ-cut of the gain patterns for both polarizations of the low cost antenna array element at 28 GHz .....	109
Chart 2.43 The 3D radiation patterns for both polarizations of the low cost antenna array element at 28 GHz .....	109
Chart 2.44 Copper manufacturing tolerance impact to resonance frequency only on top copper (antenna patch side).....	110
Chart 2.45 Copper manufacturing tolerance impact to resonance frequency only on bottom copper (feed network side).....	111
Chart 2.46 Copper manufacturing tolerance impact to resonance frequency on bottom copper and top copper enlarged .....	111
Chart 2.47 Copper manufacturing tolerance impact to resonance frequency on bottom copper and top copper decreased.....	112
Chart 2.48 PI substrate manufacturing tolerance impact to resonance frequency .....	112
Chart 2.49 The return loss of the array 2 in simulations and measurements .....	121
Chart 2.50 The peak gain of the array 2 in simulations and measurements .....	122

## Table of Figures

---

Chapter I. Frequency Agile Filters for Mobile Devices .....	15
Figure 1.1 Block diagram of multiband transceiver [1].....	16
Figure 1.2 Side view of general CMOS N-FET transistors [15] .....	20
Figure 1.3 Series a) and series-shunt b) SP4T switch topologies .....	21
Figure 1.4 Equivalent-circuit models of series a) and series-shunt b) SP4T RF switches, where $RSE$ and $CSE$ stands for ON ( $R_{ON}$ ) resistance and OFF ( $C_{OFF}$ ) capacitance of the series branches, respectively, $RSH$ and $CSH$ stands for ON ( $R_{ON}$ ) resistance and OFF ( $C_{OFF}$ ) capacitance of the shunt branches, respectively [15].....	22
Figure 1.5 The block diagram of the Ethertronics EC 686 SP4T RF switch [14].....	23
Figure 1.6 Topology of 3rd order combline filter .....	27
Figure 1.7 Topology of the new proposed filter.....	30
Figure 1.8 Simulation model to determine the values of $L_1$ and $C_1$ .....	31
Figure 1.9 EC 686 QFN-16 package pin description [14] .....	37
Figure 1.10 Perspective projection of the designed frequency agile filter with three EC868 in CST.....	38
Figure 1.11 Ceramic layer stack up of the frequency agile filter .....	38
Figure 1.12 The top metallic layers of a) the ceramic layer 9 and b) the ceramic layer 8 .....	39
Figure 1.13 The top metallic layers of a) the ceramic layer 7 b) the ceramic layer 6 .....	40
Figure 1.14 The top metallic layers of a) the ceramic layer 5 and b) the ceramic layer 4 .....	40
Figure 1.15 The top metallic layers of a) the ceramic layer 3 and b) the ceramic layer 2 .....	41
Figure 1.16 The top metallic layers of a) the ceramic layer 1 and b) the ceramic layer 0 .....	41
Figure 1.17 The bottom metallic layer of the ceramic layer 0 .....	42
Figure 1.18 The updated filter CST model to take in account the CMOS $R_{on}$ resistance .....	45
Figure 1.19 The manufactured LTCC block for the frequency agile combline filter.....	49
Figure 1.20 The evaluation board for the filter measurements .....	50
Figure 1.21 The control PCB and the connections to the evaluation PCB .....	50
Figure 1.22 The view of the control software for controlling the MIPI switches from computer.....	51
Figure 1.23 The tunable filter on the evaluation board with three EC 686.....	52
Figure 1.24 Frequency agile filter with only capacitive tuning loads with the EC 686 switches .....	54
Figure 1.25 Frequency agile filter without the EC 686 .....	55
Figure 1.26 Frequency agile filter without the RF-switches and inductive loads .....	56

Chapter II. Low Cost Millimeter Wave Antenna Arrays .....	63
Figure 2.1 a) A centralized and b) a distributed mmWave antenna architecture .....	66
Figure 2.2 Geometry of stripline transmission line.....	68
Figure 2.3 Transmission line topologies for the CST simulation .....	69
Figure 2.4 E-field distributions in the transmission lines at 28 GHz.....	71
Figure 2.5 H-field distributions in the transmission lines at 28 GHz .....	72
Figure 2.6 Dual polarized patch antenna with the simulation coordinates.....	76
Figure 2.7 The stack up of the 28 GHz dual polarized FPC patch antenna .....	77
Figure 2.8 Location of the feeding pins for dual polarization patch antenna .....	78
Figure 2.9 28 GHz 4 element linear antenna array on FPC.....	83
Figure 2.10 28 GHz 4 element linear antenna array feed locations .....	84
Figure 2.11 2x2 FR-4 planar antenna arrays .....	91
Figure 2.12 2x2 FR-4 planar antenna array feeding networks .....	92
Figure 2.13 The stack up of the FR-4 antenna arrays .....	92
Figure 2.14 The 3 dB power divider used in combined feeds feed network .....	93
Figure 2.15 The 2.92 mm (V-connector) connector's land pattern in CST simulations .....	93
Figure 2.16 Front(patch side)- and back(feed network)-view of the manufactured FR-4 antenna array. ....	102
Figure 2.17 The gain measurement setup a) side and b) top views .....	103
Figure 2.18 The Anritsu VectorStar MS4647B millimeter wave VNA .....	103
Figure 2.19 Antenna array element of the low cost antenna array .....	106
Figure 2.20 Top layer (antenna patch) of the low cost antenna array (bottom view, metal layer 1)....	114
Figure 2.21 Ground plane layer of the low cost antenna array (bottom view, metal layer 2) .....	115
Figure 2.22 Stripline layer of the low cost antenna array (bottom view, metal layer 3) .....	115
Figure 2.23 PI substrate layer of the low cost antenna array with the air cavity (bottom view) .....	116
Figure 2.24 PI substrate layer of the low cost antenna array without the air cavity (bottom view) .....	116
Figure 2.25 Bottom layer of the low cost antenna array (bottom view, metal layer 16) .....	117
Figure 2.26 The stack up of the low cost antenna array with and without the air cavity.....	117
Figure 2.27 The array's RF test port location and polarization selection in low cost antenna array (bottom view) .....	118
Figure 2.28 The manufactured low cost antenna array, top layer (top view, with air cavity) .....	119
Figure 2.29 The manufactured low cost antenna array, bottom layer (bottom view, with air cavity) ...	119
Figure 2.30 AVX/Ethertronics 5G measurement system for mmWave antennas .....	120
Figure 2.31 The coordinate system and the test horns inside the AVX/Ethertronics 5G measurement system .....	120

## Table of Tables

---

General Introduction .....	5
Table I. Filter performance comparison .....	7
Table II. Millimeter-Wave antenna comparison .....	8
Chapter I. Frequency Agile Filters for Mobile Devices .....	15
Table 1.1 Mechanical and electrical specifications for frequency agile filter in mobile devices.....	16
Table 1.2 Frequency bands for tunable filter .....	17
Table 1.3 List of different filter technologies for tunable filters .....	18
Table 1.4 Comparison of filter technologies to mechanical specifications (Table 1.1) .....	18
Table 1.5 The characteristics of EC 686 RF Switch [14] .....	23
Table 1.6 Element values of Chebyshev lowpass filter ( $g_0 = 1, \Omega c = 1 \text{ rad/s}$ ), $LAr = 0.1 \text{ dB}$ .....	26
Table 1.7 Calculated external quality factor $Q_e$ and inter-resonator coupling factor $k$ .....	27
Table 1.8 Simulated $Q_e$ and $k$ for the GSM 1800 and LTE 7 with $d$ and $wg$ optimized for GSM 1800 band.....	28
Table 1.9 Simulated $Q_e$ and $k$ for the GSM 1800 and LTE 7 with $d$ and $wg$ optimized for LTE 7 band	29
Table 1.10 Values of $L_1$ and $C_1$ for different tapped feed locations for GSM 1800 and LTE 7 Rx bands.....	32
Table 1.11 Filter characteristics, $d = 2000 \mu\text{m}$ and $wg = 400 \mu\text{m}$ .....	33
Table 1.12 Filter characteristics for the optimized parallel load combine filter, $d = 2000 \mu\text{m}$ and $wg = 280 \mu\text{m}$ .....	35
Table 1.13 Final mechanical dimensions of the simulated filter.....	49
Chapter II. Low Cost Millimeter Wave Antenna Arrays .....	63
Table 2.1 3GPP millimeter wave bands in Release 15 [10].....	64
Table 2.2 Center conductor widths .....	70
Table 2.3 Summary of the manufacturability test.....	113